

Shape Stability and Bundling of Ultrathin Nanowires

**Dissertation
zur Erlangung des Grades
des Doktors der Ingenieurwissenschaften
der Naturwissenschaftlich-Technischen Fakultät
der Universität des Saarlandes**

**von
Simon Bettscheider**

**Saarbrücken
2022**

Tag des Kolloquiums	08. November 2022
Dekan	Prof. Dr. Ludger Santen
Berichterstatter	Prof. Dr. Tobias Kraus Prof. Dr. Martin H. Müser Prof. Dr. Norman A. Fleck
Vorsitz	Prof. Dr.-Ing. Stefan Diebels
Akademischer Mitarbeiter	Dr. Martin Brinkmann

Abstract

Ultrathin nanowires are promising nanoscale materials. They can reach length-to-diameter aspect ratios exceeding 1000, making them suitable building blocks for optoelectronic devices such as transparent conducting films. An organic ligand shell surrounds their inorganic core, provides colloidal stability, and guides their one-dimensional growth.

Two unresolved issues limit their application. Nanowires can agglomerate into elongated bundles, but efficient use of this superstructure is difficult since we do not yet understand the bundling mechanisms. Furthermore, nanowires are prone to the Plateau-Rayleigh instability: thin wires tend to fragment into discrete spheroidal particles to reduce their surface energy, limiting their lifetime and reliability.

This thesis investigates superstructure formation and nanowire stability and the link between both topics. Bundles are shown to emerge in non-polar solvents for entropic reasons. Solvent or unbound ligand molecules align in proximity to the ligand shell, thus losing entropy. Bundling decreases this loss in entropy by reducing contact with the bulk solvent. The structural stability of nanowires is enhanced or degraded by the ligand shell, depending on the relationship between free energy and local surface curvature. Kinetic barriers in ad- and desorbing ligands and rearrangement of surface atoms slow down the break-up. Bundling further stabilizes the wires by confining the space available to them.

Zusammenfassung

Ultradünne Nanodrähte, bestehend aus einem anorganischen Kern und einer organischen Ligandenhülle, können Aspektverhältnisse von über 1:1000 erreichen und sind potenzielle Materialien für optoelektronische Technologien wie transparente Elektroden.

Einer breiteren Anwendung stehen zwei Herausforderungen entgegen. Nanodrähte können zu Bündeln agglomerieren, aber eine effiziente Nutzung dieser Superstruktur ist schwierig, da unser Verständnis der zugrundeliegenden Bündelungsmechanismen unvollständig ist. Zudem sind Nanodrähte instabil: gemäß der Plateau-Rayleigh-Instabilität zerbrechen sie zur Reduktion ihrer Oberflächenenergie in kleinere Nanopartikel, was ihre Langzeit-Anwendung verhindert.

Sowohl Formstabilität und Superstruktur als auch der Zusammenhang zwischen beiden Themen wurden in dieser Dissertation untersucht. Bündel entstehen in unpolaren Lösemitteln, weil sich Lösemittelmoleküle oder freie Liganden parallel zur Ligandenhülle ausrichten und dabei Entropie verlieren. Durch die Anordnung in Bündeln wird der Kontakt zum Lösemittel reduziert, sodass der Entropieverlust geringer ausfällt. Die Formstabilität von Nanodrähten wird von der Ligandenhülle verbessert oder verschlechtert, je nach Zusammenhang zwischen freier Energie und Oberflächenkrümmung. Kinetische Barrieren in der Ad- und Desorption von Liganden und der Reorganisation der Oberfläche verlangsamen den Zerfall. Bündel verbessern die Formstabilität, indem sie den für die Nanodrähte verfügbaren Raum begrenzen.

Publications and Contributions

This thesis contains four publications that have been published in peer-reviewed journals. The contribution of each co-author is described below within the taxonomy CRediT (Contributor Roles Taxonomy) [1–3].

Publication 1 H. Gao, S. Bettscheider, T. Kraus, M.H. Müser, Entropy Can Bundle Nanowires in Good Solvents, *Nano Lett.* 19 (2019) 6993–6999. <https://doi.org/10.1021/acs.nanolett.9b02379>.

- *Hongyu Gao*: Methodology; Software; Formal analysis; Investigation; Writing - Original Draft; Visualization.
- *Simon Bettscheider*: Validation; Formal analysis; Investigation; Writing - Original Draft; Writing - Review & Editing; Visualization.
- *Tobias Kraus*: Conceptualization; Writing - Review & Editing; Project administration; Funding acquisition.
- *Martin H. Müser*: Conceptualization; Methodology; Writing - Review & Editing; Project administration; Funding acquisition.

Publication 2 S. Bettscheider, B. Kuttich, L.F. Engel, L. González-García, T. Kraus, Bundling of Nanowires Induced by Unbound Ligand, *J. Phys. Chem. C* 125 (2021) 3590–3598. <https://doi.org/10.1021/acs.jpcc.0c10919>.

- *Simon Bettscheider*: Conceptualization; Methodology; Validation; Formal analysis; Investigation; Writing - Original Draft; Writing - Review & Editing; Visualization.
- *Björn Kuttich*: Methodology; Software; Formal analysis; Writing - Original Draft; Writing - Review & Editing; Supervision.
- *Lukas F. Engel*: Investigation; Writing - Original Draft; Writing - Review & Editing.
- *Lola González-García*: Conceptualization; Writing - Review & Editing; Supervision.
- *Tobias Kraus*: Conceptualization; Methodology; Writing - Review & Editing; Supervision; Project administration; Funding acquisition.

Publication 3 S. Bettscheider, T. Kraus, N.A. Fleck, On the geometric stability of an inorganic nanowire and an organic ligand shell, J. Mech. Phys. Solids. 123 (2019) 3–19. <https://doi.org/10.1016/j.jmps.2018.07.017>.

- *Simon Bettscheider*: Methodology; Software; Validation; Formal analysis; Investigation; Writing - Original Draft; Visualization.
- *Tobias Kraus*: Conceptualization; Writing - Review & Editing; Supervision; Project administration; Funding acquisition.
- *Norman A. Fleck*: Conceptualization; Methodology; Software; Formal analysis; Writing - Original Draft; Writing - Review & Editing; Supervision; Project administration; Funding acquisition.

Publication 4 S. Bettscheider, T. Kraus, N.A. Fleck, Stabilization of ultrathin nanowires by self-assembly into bundles, Acta Mater. 231 (2022) 117799. <https://doi.org/10.1016/j.actamat.2022.117799>.

- *Simon Bettscheider*: Methodology; Validation; Formal analysis; Investigation; Writing - Original Draft; Visualization.
- *Tobias Kraus*: Conceptualization; Writing - Review & Editing; Supervision; Project administration; Funding acquisition.
- *Norman A. Fleck*: Conceptualization; Methodology; Formal analysis; Writing - Original Draft; Writing - Review & Editing; Supervision; Project administration; Funding acquisition.

Acknowledgments

This doctoral dissertation would not be the same without the help of many intelligent and talented people who supported me prepare this thesis. I am grateful for those helping minds.

My supervisor *Prof. Dr. Tobias Kraus* introduced me to the topic of ultrathin nanowires and sparked my interest in the subject. He advanced the project by making many resourceful comments in our many discussions. He challenged and supported me in learning about colloidal nanoparticles and the experimental and theoretical methods we used to study them. He initiated our collaboration with Prof. Dr. Norman A. Fleck at the University of Cambridge and made several research visits to Cambridge possible, thus ensuring that I can work with both experimental and theoretical methods. That I often participated in renowned conferences and summer schools was a matter of course for him. What was outstanding is the fact that Prof. Dr. Tobias Kraus always gave me the trust and freedom to develop and pursue my own ideas and research questions. I thank him for supervising me throughout my work on the topic.

Prof. Dr. Norman A. Fleck welcomed me for several short research visits to the University of Cambridge. I am grateful he mentored me closely in our work on the Plateau-Rayleigh instability. He taught me that it takes endurance and focus on dealing with questions in solid mechanics. He also trained me to break problems into elementary physical equations and express complex ideas in plain and clear sentences.

My second reviewer *Prof. Dr. Martin H. Müser* collaborated with us in investigating the bundling of ultrathin nanowires. I thank him for providing insights into molecular dynamics simulations and suggesting that entropy might be the leading cause of bundle formation.

The directors of INM, the Leibniz Institute for New Materials, *Prof. Dr. Eduard Arzt* and *Prof. Dr. Aránzazu del Campo* created a work environment that fosters excellent science, for which I am thankful. Even during the Covid-19 pandemic, they quickly put in place measures that allowed me to continue my scientific endeavors safely and efficiently.

I thank all coauthors, group members, and colleagues for their friendly and productive collaboration. In particular, I would like to mention *Lukas F. Engel* and *Roman Buchheit* for countless discussions on our research questions, *Dr. Louis V. Weber* for many measurements on the transmission electron microscope, *Dr. David Doblás Jiménez* for introducing me to small-angle X-ray scattering and data analysis with Python, *Dr. Björn Kuttich* for assistance in the analysis and interpretation of scattering data, *Dr. Lola González-García* for her original and practical ideas and hands-on advice, *Anna Zimmermann* for the introduction to nanowire and nanoparticle synthesis, *Indra Backes* for Raman measurements, *Robert Drumm* for thermogravimetric analyzes, *Dr. Bart-Jan Niebuur*, *Dr. Thomas Kister*, and *Dr. Philipp Loew* for proofreading and reviewing my thesis, and my Bachelor's and Master's students *Peter Spies* and *Tobias Knapp* for their curiosity, perseverance, and willingness to learn.

I thank my early mentor *Prof. Dr. Andreas Rosenkranz* for encouraging me to study Materials Science and Engineering and introducing me to experimental research. Likewise, I thank the supervisors of my Master's thesis, *Asst. Prof. Dr. Jamie A. Booth* and *Dr. René Hensel*, who taught me how to use continuum mechanics to tackle research questions, thereby preparing me for this PhD project.

Many thanks go to the team and the founders of *Stiftung der Deutschen Wirtschaft* (Foundation of German Business), who supported me financially and foremost intellectually. Thanks to them, I participated in many interdisciplinary workshops and seminars that helped me think outside the box and see the bigger picture.

I am particularly grateful to my parents, friends, and my partner. My *parents* supported me during my undergraduate and graduate studies and allowed me to pursue whatever I found most exciting and inspiring. My *friends* regularly showed me that there is life outside the academic campus bubble. My *partner* was constantly at my side, gave resourceful advice, and supported me in writing well-structured and comprehensible texts.

The latex template for this dissertation was written by *Prof. Dr. Steve Gunn*, *Dr. Sunil Patel*, *Vel*, and *Johannes Böttcher* and is licensed under [CC BY-NC-SA 3.0](https://creativecommons.org/licenses/by-nc-sa/3.0/).

Contents

Abstract	iii
Zusammenfassung	iii
Publications and Contributions	iv
Acknowledgments	vi
List of Abbreviations	xi
1 Introduction	1
2 State of the Art	5
2.1 Synthesis and applications of nanowires	5
2.1.1 Synthesis and growth mechanisms	5
2.1.2 Applications of ultrathin ligand-coated nanowires	9
2.2 Colloidal stability and self-assembly of nanowires into bundles	11
2.2.1 Colloidal interactions of non-polar nanoparticles in non-polar solvents	11
2.2.2 Self-assembly of ultrathin nanowires into bundles	18
2.3 The Plateau-Rayleigh instability of nanowires	20
2.3.1 Phenomenological introduction to the Plateau-Rayleigh instability	21
2.3.2 Chemical potential and surface energies as driving forces	22
2.3.3 Factors influencing the shape stability	26
2.3.4 Influence of the ligand shell	32
2.4 Knowledge gaps in the state of the art and the goal of this dissertation	36
3 Results	39
3.1 Publication 1: Entropy can bundle nanowires in good solvents	40
3.2 Publication 2: Bundling of nanowires induced by unbound ligand	58
3.3 Publication 3: On the geometric stability of an inorganic nanowire and an organic ligand shell	76
3.4 Publication 4: Stabilization of ultrathin nanowires by self-assembly into bundles	94
4 Discussion	117
4.1 Mechanisms of bundle formation	117
4.2 Shape stability of ligand-coated nanowires	120
4.3 Influence of bundling on shape stability	122
5 Conclusion and Outlook	127
Bibliography	131

List of Abbreviations

AuNR	(ultrathin) gold nanorod
AuNW	(ultrathin) gold nanowire
Covid-19	coronavirus disease 2019, also known as severe acute respiratory syndrome coronavirus 2 (SARS-CoV-2)
DNA	deoxyribonucleic acid
e.g.	exempli gratia (Latin for “for example”)
et al.	et alia (Latin for “and others”)
fcc	face-centered cubic
i.e.	id est (Latin for “that is”)
MD	molecular dynamics
mRNA	messenger ribonucleic acid
OAm	oleylamine
PDF	pair-distribution function
PDMS	polydimethylsiloxane
PEG	poly(ethylene glycol)
(P(S-<i>b</i>-S-N₃))	poly(styrene- <i>b</i> -azidostyrene)
PVP	polyvinylpyrrolidone
SANS	small-angle neutron scattering
SAXS	small-angle X-ray scattering
TEM	transmission electron microscopy
TOP	trioctylphosphine
TOPO	trioctylphosphine oxide
UV-vis	ultraviolet–visible spectroscopy
vdW	van der Waals
XRD	X-ray diffraction

Chapter 1

Introduction

Nanoparticles, that is, objects with at least one dimension in the range of 1 nm to 100 nm [4–6], can be found throughout our daily life. ZnO and TiO₂ nanoparticles are used in sunscreen, silver nanoparticles in antimicrobial soaps, and semiconductor quantum nanodots in television screens [7]. We also rely on nanoparticles in our fight against the Covid-19 pandemic. Lipid nanoparticles encapsulate and deliver mRNA vaccines to our cells, which enzymes would otherwise digest [8, 9]. Gold nanoparticles are used as optical markers in Covid-19 rapid antigen tests, emitting red color due to their surface resonance plasmons and making the test and control lines visible [10–12].

Nanoparticles come in all shapes, and an exciting type is nanowires. Nanowires are nanoparticles of cylindrical shape; they are particular in that they can reach length-to-diameter aspect ratios well above 1000 [13, 14]. This large aspect ratio allows nanowires to form percolating networks at lower volume fractions than spherical particles [15–17], making them suitable building blocks in various applications. Nanowires have been used to make transparent conductive electrodes in touchscreens [18–20], sensors for biochemical molecules [21–23], and catalysts in hydrogen production [24–27]. They can be made from various materials, including polymers, metals, and semiconductors (see section 2.1.1 for a complete list), and different synthesis routes are available [28–30]. Nanowires with diameters below 10 nm are called “ultrathin” [14, 31, 32]. Ultrathin nanowires are commonly produced by wet chemical synthesis and consist of an inorganic core surrounded by an organic ligand shell. The ligand assists in the one-dimensional growth and renders the nanowires colloidally stable [14].

Given the small size of ultrathin nanowires, their properties are dominated by phenomena at their surface. Therefore, the structure and superstructure of the nanowires are mainly determined by interfacial energies and the ligand shell. Understanding how these surface characteristics govern structure and superstructure is the core objective of this dissertation. This thesis combines a general analytical study

with experiments on ultrathin nanowires made from gold (AuNWs). They consist of a gold core of diameter of 1.7 nm surrounded by a ligand shell of oleylamine (OAm) of a similar thickness and reach lengths of up to 6 nm [13, 33–39].

Once synthesized, ultrathin nanowires exist as a colloidal dispersion and can be freely dispersed or agglomerated into elongated bundles [14, 40–43]. Our control of this *superstructure* and the *colloidal stability* is still limited since we do not yet understand the mechanisms responsible for bundle formation. To date, it is known that nanowires inside bundles typically assemble in a close-packed hexagonal lattice, and the diameter of the bundles was reported to range from 70 nm to 400 nm [42, 44]. AuNWs capped with the ligand OAm spontaneously assemble in bundles during synthesis, each nanowire being surrounded by a bilayer of the ligand [44, 45]. When AuNWs are washed after synthesis, they are surrounded by only a monolayer, reducing the distance between the wires [45–47]. The interwire distance can also be tuned by the concentration of ligand [45], the type of ligand [47], and the type of solvent [45]. Loubat et al. [44] proposed that bundles form due to van der Waals forces between their cores, while Reiser et al. [45] argued that osmotic pressure and supramolecular forces drive bundling. Surprisingly, AuNWs bundle in *n*-hexane, but no bundles were observed in chemically similar cyclohexane [45]. This unexplained effect demonstrates that the underlying mechanisms of bundling in nanowires are not yet understood. We need further insight into the molecular origins of bundling to understand its driving forces.

The key challenge concerning the *structure* of nanowires is their limited *shape stability*. Nanowires tend to break down into discrete spheroidal particles [48–52]. Their shape is thermodynamically unfavorable because a cylinder has a greater surface area and surface energy than a sphere of equal volume [48–52]. Depending on the application, this instability may be exploited, for example, when creating strings of spherical particles [53, 54], or it must be prevented, as in the case of transparent conductive electrodes [18–20]. The instability is called Plateau-Rayleigh instability after its discoverers [55, 56]; it is also known as shape, geometric, morphological, or Rayleigh instability [48, 49, 57–60]. The Plateau-Rayleigh instability occurs in solids and liquids and can be observed at home: water running out of a faucet flows initially in a continuous jet and eventually breaks into discrete droplets. The break-up time scales with the wire radius to the fourth power, making thin wires much more susceptible to this instability than thicker ones [61, 62].

Research on the Plateau-Rayleigh instability of nanowires dealt with understanding and preventing the instability. It is known that anisotropy in surface energy, the presence of a substrate, confinement, and mechanical stresses can hinder the instability. For example, sapphire nanowires along specific crystallographic axes outlived

those along other axes by more than a factor of 10, likely because stable equilibrium facets bound the long-lived nanowires [60, 63]. Wetting substrates in contact with the nanowires suppressed the instability [64], and nanowires confined by a shell or matrix were stable longer than bare nanowires [65, 66].

The instability is less well understood in ultrathin nanowires surrounded by a ligand shell. Some ligands can improve while others impair stability [47, 65, 67, 68], a denser and stiffer ligand shell appears to be beneficial [66, 69, 70], and removal of the ligand shell seems to deteriorate stability [71]. To date, the link between the molecular properties of the ligand shell and the shape stability of the nanowires is not well understood. It remains unclear why and how the ligand shell stabilizes or destabilizes nanowires. We do not yet understand why some ligands improve and others degrade stability, whether the influence is energetic or kinetic, and whether there exist optimum ligand properties that maximize stability.

The goal of this dissertation is to investigate the colloidal and shape stability of ultrathin, ligand-capped nanowires on several length scales. Both topics are governed by interfacial energies and properties of the ligand shell. Bundling and its molecular origins shall be studied in AuNWs experimentally and by molecular dynamics (MD) simulations. The simulations are suitable for investigating the molecular length scale, while the experiments assess the micro- and macroscale. Regarding shape stability, a framework shall be developed that incorporates the effects of the ligand shell into the theory of the Plateau-Rayleigh instability. This framework will allow relating molecular-scale properties of the ligand shell to the microscopic issue of wire stability. Last, the connection between colloidal and shape stability will be addressed by studying whether and to what extent bundling influences shape stability. Experiments on bundled and freely dispersed AuNWs shall provide qualitative insights, and an analytical continuum model shall be used to rationalize the experimental findings.

The thesis is organized as follows. Chapter 2 reviews the current state of the art of ultrathin nanowires, bundling and underlying colloidal interactions, and the Plateau-Rayleigh instability. The results are presented in Chapter 3 in the form of four peer-reviewed publications. [Publication 1](#) and [Publication 2](#) study the mechanisms that drive bundling in AuNWs. [Publication 3](#) investigates the Plateau-Rayleigh instability in ligand-capped nanowires. [Publication 4](#) deals with whether the bundling influences the Plateau-Rayleigh instability in nanowires. The results are discussed in light of the current state of the art in Chapter 4. Conclusions are presented, and an outlook on further research routes is given in Chapter 5.

Chapter 2

State of the Art

2.1 Synthesis and applications of nanowires

Nanowires can be produced via various physical and chemical routes, including the vapor-liquid-solid mechanism [29, 30], optical or electron beam lithography [29], electrospinning [30], or electrochemical filling of aluminum oxide templates [28, 30]. Ultrathin nanowires are commonly synthesized by reducing a metal or semiconductor salt in the presence of a shape-directing ligand in dispersion [14, 31, 32].

2.1.1 Synthesis and growth mechanisms

To date, ligand-coated ultrathin nanowires have been produced from the metals gold [33–37], silver [72], ruthenium [73], samarium [74], the alloy iron-platinum [75], and the semiconductors antimony sulfide [76], bismuth sulfide [77], cadmium selenide [41], and copper sulfide [42]. The synthesis involves dissolving the metal or semiconductor salt, adding a shape-directed organic ligand such as OAm [34], oleic acid [31], or polyvinylpyrrolidone (PVP) [27], a reduction agent such as triisopropylsilane [43], ascorbic acid [78], or dimethylmethanamide [24], and seeds if necessary. The product is then purified to eliminate excess ligands and by-products [32, 45]. The resulting nanowires consist of an inorganic core surrounded by a mono- or bi-layer of ligands, see Fig. 2.1. They are dispersed as colloids and can self-assemble into hexagonal agglomerates, see Section 2.2.2.

It is not yet fully understood why and how nanowires grow. At least four theories exist to explain their one-dimensional growth: oriented attachment of spherical nanoparticles, lamellar or cylindrical micelles as templates, preferential adsorption of ligands, and self-assembly of polymeric strands. All four theories will be introduced in the following paragraphs and reviewed with respect to AuNWs with the ligand OAm, the example material of this dissertation.

The theory that nanowires form by oriented attachment of spherical particles has been proposed by Halder and Ravishankar [33], who were the first to report on the

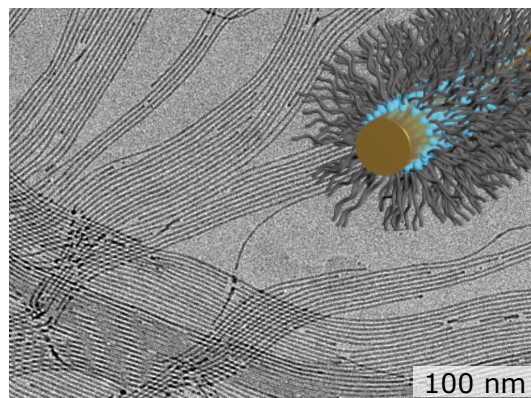


FIGURE 2.1: Transmission electron micrograph of AuNWs. The inset shows a schematic rendering of the AuNWs; they consist of a gold core with a diameter of 1.7 nm and a ligand shell of OAm of similar thickness. Micrograph adapted and reprinted with permission from [45]. CC BY-NC 3.0.

formation of AuNWs with a diameter of roughly 2 nm. They observed that the synthesis initially produced spherical gold nanoparticles with a diameter of 2 nm and that some of the forming nanostructures branched at (111) crystal facets [33]. According to their theory, spheroidal nanoparticles combined at (111) facets. The crystal surface of the resulting strands then smoothed so that the (111) facets required for further growth only remained at the two ends of the strands, thus forming highly uniform nanowires (compare to Fig. 2.2A) [33]. Such oriented attachment was also observed in Pt nanowires [79] and 10 nm wide, kinked Au nanowires [80]. Pschunder et al. [81] studied the growth of 2 nm thin AuNWs *in situ* by small-angle X-ray scattering (SAXS) and supported the theory of oriented attachment: the scattering of the first 3 h fitted a model of flat disks with a diameter of 2.6 nm. The authors claimed that nanowires form because these disks aggregate in one direction and shrink in diameter, see Fig. 2.2A [81].

Several newer experimental observations are hard to reconcile with oriented attachment, at least for the case of highly uniform AuNWs with a diameter of only 2 nm. Pazos-Pérez et al. [37] claimed that 2 nm wide AuNWs must form via another mechanism since they lack any kinks or branches. Observation of the formation of these ultrathin AuNWs *in situ* by SAXS by Loubat et al. [44] revealed that spherical particles do form during the synthesis but are not consumed during nanowire growth [44]. The spherical particles might only act as seeds [44]. The discrepancy between the SAXS studies of Loubat et al. [44] and Pschunder et al. [81] might be explained by the fact that the form factor of monodisperse flat disks fitted by Pschunder et al. [81] can result in scattering signals similar to those of polydisperse spheres.

Huo et al. [34] and Pazos-Pérez et al. [37] proposed that lamellar micelles or reverse cylindrical micelles template the one-dimensional growth of AuNWs, a theory

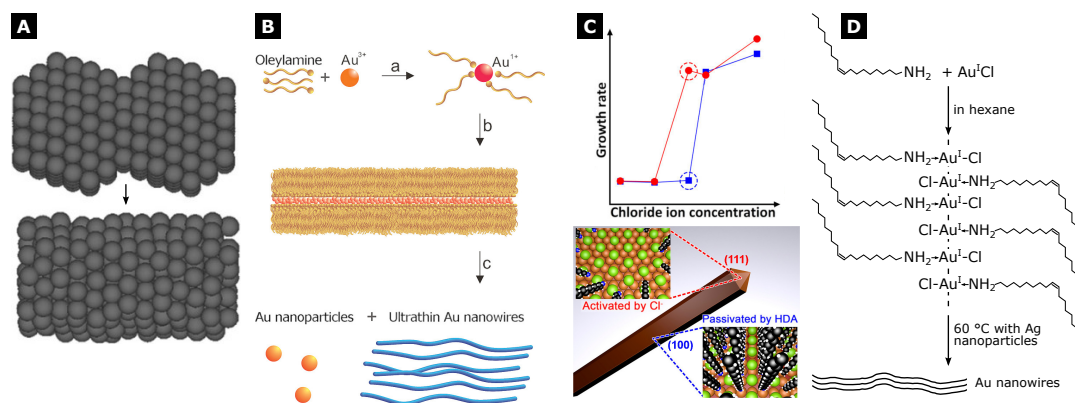


FIGURE 2.2: Proposed growth mechanisms of ultrathin nanowires. (A) oriented attachment of spherical or disk-like particles, (B) growth inside lamellar or cylindrical micelles, (C) preferential adsorption of ligands promotes crystal growth along specific facets, (D) the metal salt precursor (here $\text{Au}^{\text{I}}\text{Cl}$) and the ligand (here OAm) form polymeric strands that then self-assemble into elongated wires. (A) Adapted and reprinted with permission from [33]. © 2007 Wiley-VCH Verlag GmbH and Co. KGaA. (B) Adapted and reprinted with permission from [34]. © 2008 American Chemical Society. (C) Adapted and reprinted with permission from [82]. © 2018 American Chemical Society. (D) Adapted and reprinted with permission from [36]. © 2008 American Chemical Society.

also suggested for the growth of FePt nanowires [75]. In their synthesis, $[\text{Au}^+ \text{-OAm}]$ complexes formed a lamellar mesostructure with each layer of Au^+ being separated by a bilayer of OAm [34]. They believed that Au^+ was gradually reduced within this lamellar template so that one-dimensional nanowires could form [34], see Fig. 2.2B. Similarly, Wang et al. [35] and Pazos-Pérez et al. [37] suggested that OAm forms reverse cylindrical micelles in which Au^+ is slowly reduced.

Several observations call into question the theory of lamellar growth. Loubat et al. [83] compared the synthesis involving the lamellar $[\text{OAm-Au}^{\text{I}}\text{Cl}]$ phase with a direct one-pot synthesis [83]. The first only yielded 2% while the second produced 75% of AuNWs, indicating that the lamellae are not essential for nanowire growth [83]. In addition, the lamellar spacing of 4.8 nm remained constant during the first synthesis, indicating that the lamellae always consisted of Au monolayers and never contained thicker Au nanowires [83]. The growth of AuNWs must have occurred outside the lamella. It is also unclear how *two*-dimensional Au planes inside lamella could induce the growth of *one*-dimensional Au nanowires. Experimental results opposing the growth theory inside reverse cylindrical micelles include the observation by Miyajima et al. [84] that ultrathin AuNWs synthesized in the water phase are surrounded by a ligand monolayer only. The double layer in non-polar solvents appears not to be necessary for nanowire growth.

Preferential adsorption of ligands is another explanation for one-dimensional growth. Amines preferentially adsorb on (100) planes of Au surfaces, which could

explain nanowire growth in the [111] direction [85]. Likewise, hexadecylamine adsorbs preferentially on (100) over (111) Cu surfaces when Cl^- ions are present, thus explaining the growth of 30 nm to 300 nm wide Cu nanowires, as shown in Fig. 2.2C [82, 86]. The presence of Cl^- ions is also relevant in synthesizing AuNWs; they increase their length [84]. The efficiency of the ligand layer in shielding growth depends on the ligand length. The interaction energy between ligands increases with increasing ligand length, raising the energy necessary to remove a ligand from a shell [85, 86], which explains why Cu nanowires only formed with ligands with twelve or more carbon atoms [86].

Preferential adsorption cannot explain why nanowires form with a specific and highly uniform diameter, and it is unlikely that the concept alone can explain the formation of AuNWs. The Cu nanowires studied by Kim et al. [82] possessed a pentagonally twinned structure that induced mechanical stresses [82, 86]. These stresses might hinder further growth in the radial direction [82, 86]. Yet, for nanowires without these stresses in the crystal structure, there must be other forces that set the nanowire diameter. In addition, AuNWs also formed in the absence of preferential absorption but with the help of an interface [87]. Wang et al. [75] synthesized 6 nm wide AuNWs from spherical seeds. Nanowires formed because growth occurred only at the interface between the spherical seed and a substrate; all other surfaces of the seeds were capped with aromatic thiols, which are known to adsorb fairly equally on all gold facets [87]. Without such an interface, other theories must explain the one-dimensional growth.

Lu et al. [36] rationalized that organometallic $[\text{OAm}-\text{Au}^{\text{I}}\text{Cl}]$ complexes form due to aurophilic interactions in the initial stage of the synthesis and that these complexes form polymeric strands with a backbone of Au^{I} and side chains of OAm, see Fig. 2.2D. These polymeric strands could aggregate into elongated bundles that eventually transform into nanowires when Au^{I} is reduced to Au^0 [36]. Atomic pair distribution functions (PDF) extracted from *in-situ* high-energy X-ray diffraction (XRD) of the synthesis supported this theory [88]. The PDFs revealed a nearest neighbor distance larger than that of bulk gold during the first hours of the synthesis, indicating the formation of polymeric strands [88]. Furthermore, the crystal structure of the resulting AuNWs was not face-centered cubic (fcc) but identical to α -Mn (topologically close-packed) [88]. Such a crystal structure is incompatible with crystal growth along the [111] axis of an fcc crystal. The authors argued that the α -Mn crystal structure emerged because the morphology of the polymeric strands prevented Au from organizing in an fcc crystal structure [88]. The mechanical stresses in the α -Mn crystal structure were believed to prevent further radial growth of the AuNWs, thus setting their highly uniform diameter [88]. Recently, other $[\text{FeCl}]$

organometallic complexes were also found to aggregate into nanostructures [89], supporting the notion that such a growth mechanism could be possible.

In summary, all but one theory for one-dimensional growth is inconsistent with the details of AuNW formation. Oriented attachment of spherical particles does not seem a plausible explanation for one-dimensional growth because AuNWs do not exhibit any branching and because spherical particles are not consumed during nanowire growth. Micellar templates are unlikely an explanation either: two-dimensional lamellae cannot explain one-dimensional growth; one-dimensional inverse cylindrical micelles appear not to be necessary for AuNW formation. The growth of Cu nanowires can be explained by preferential adsorption and mechanical stresses caused by their pentagonally twinned crystal structure. Yet, AuNWs do not possess the same crystal structure. The currently most coherent and plausible growth mechanism of ultrathin AuNWs is the self-assembly of polymeric [OAm–Au^ICl] strands into wires with an α -Mn crystal structure.

2.1.2 Applications of ultrathin ligand-coated nanowires

Ultrathin, ligand-coated nanowires have been employed as transparent electrodes [18, 90–94], sensors for (bio-)chemical moieties [21–23], in wastewater treatment [95], and other applications [43, 96–103]). Three examples will be highlighted in the following. They exploit the small percolation threshold of AuNWs, the photothermal conversion efficiency of W₁₈O₄₉ nanowires, and the superior number of active sites and improved charge transport of Pt nanowires over spherical Pt nanoparticles.

Gong et al. [104] employed AuNWs in a pressure sensor to measure the pulse at a human wrist. The pressure sensor was the size of a fingertip and consisted of two layers of polydimethylsiloxane (PDMS) surrounding a tissue paper impregnated with AuNWs. The bottom PDMS layer contained integrated, meandering electrodes; the fingertip-sized tissue paper was dip-coated ten times in a colloidal dispersion of AuNWs, resulting in a sheet resistance of 2.5 M Ω /sq. When the sensor was compressed, the PDMS and tissue layers deformed so that more AuNWs came into contact with the integrated electrodes, and the sensor's electrical resistance decreased. The layers recovered their original shape upon unloading, and the electrical resistance increased. The sensitivity of the sensor, defined as the ratio of change in current ΔI to no-load current I_0 to change in applied pressure ΔP , was $(\Delta I/I_0)/\Delta P = 1.14 \text{ kPa}^{-1}$, about an order of magnitude more sensitive than other flexible pressure sensors of similar size discussed in the literature [105–108]. The sensor could resolve pressures as low as 13 Pa, corresponding to the weight of a 13 μL water droplet. When mounted to a human wrist, the pressure sensor allowed

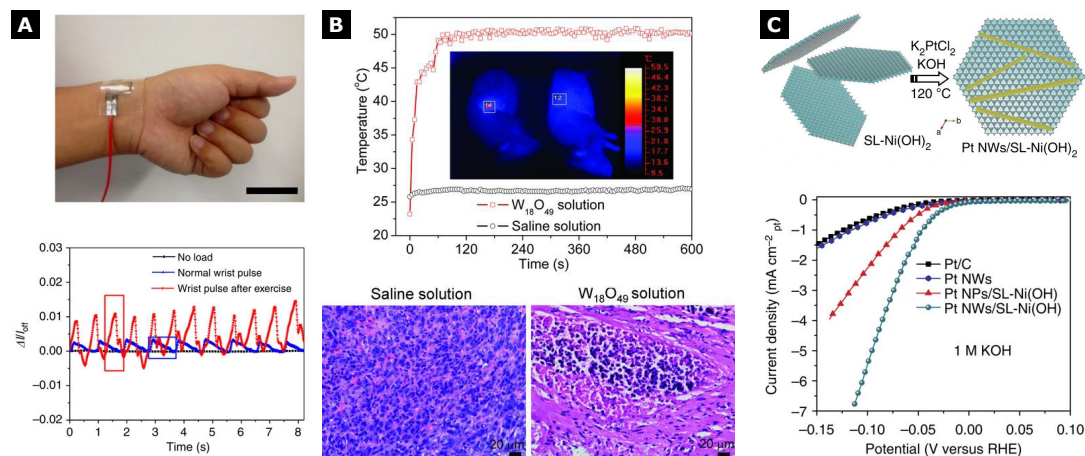


FIGURE 2.3: Application examples of ultrathin nanowires. (A) AuNWs embedded in tissue between two PDMS layers serve as a pressure sensor. The pressure sensor was sensitive enough to detect the pulse on a human wrist. Adapted and reprinted with permission from [104]. © 2014 Macmillan Publishers Limited. (B) Ultrathin $W_{18}O_{49}$ nanowires were injected into tumors in mice. Excitation of the tumor spots with a laser increased the temperature of the tissue due to the photothermal conversion by the $W_{18}O_{49}$ nanowires, killing the tumor cells. In the control group injected with saline solution, laser irradiation did not increase the temperature and left the tumor unaltered. Adapted and reprinted with permission from [110]. © 2013 Wiley-VCH Verlag GmbH und Co. KGaA. (C) Ultrathin platinum nanowires were used for water electrolysis. When placed on single-layered $Ni(OH)_2$ nanosheets, they outperformed commercial nanoscale catalysts and spherical Pt nanoparticles on single-layered $Ni(OH)_2$ nanosheets in the hydrogen evolution reaction under basic conditions. Adapted and reprinted with permission from [24]. © 2015 Macmillan Publishers Limited.

to read the pulse at the radial artery, and the sensitivity of the sensor was sufficient to read further details such as the arterial stiffness of the subjects. A similar sensor was built by Ho et al. [109] to detect facial expressions. Nanowires outperformed spherical nanoparticles in these pressure sensors because they formed percolating networks that responded linearly to ΔP with high sensitivity.

Chen et al. [110] injected ultrathin $W_{18}O_{49}$ nanowires into mice to photothermally ablate cancer cells. The ultrathin $W_{18}O_{49}$ nanowires showed low cytotoxicity in cell proliferation tests over periods of 24 h. Dispersions of $W_{18}O_{49}$ nanowires were injected into 5 mm to 10 mm large tumors; saline dispersions were injected into the control group. Upon irradiation with laser light with a wavelength of 980 nm, the surface temperature of the tumor increased from 26 °C to 27.5 °C in the control group and 26 °C to 50 °C in the treatment group, a rise caused by the localized surface plasmon resonances of the $W_{18}O_{49}$ nanowires. *Ex vivo* examination of the cancer cells revealed that the increase in temperature in the treatment group was sufficient to kill most of the tumor cells, while no change was observed in the control group. The benefit of using ultrathin $W_{18}O_{49}$ nanowires over other photothermal materials was that they were cheap to manufacture and showed excellent photothermal conversion efficiency with near-infrared light.

Yin et al. [24] synthesized ultrathin Pt nanowires on single-layered Ni(OH)₂ nanosheets for the electrolysis of water. The nanowires had diameters of 1.8 nm and lengths of 10 nm to 50 nm. Their combination with single-layered Ni(OH)₂ nanosheets (activity of 2.48 mA/cm²) outperformed commercial nanoscale catalysts (activity of 0.296 mA/cm²) and Pt nanoparticles on single-layered Ni(OH)₂ nanosheets (activity of 1.06 mA/cm²) in the hydrogen evolution reaction under basic conditions. Compared to the commercial system, the Pt nanowires on single-layered Ni(OH)₂ nanosheets performed better because the Ni(OH)₂ nanosheets activated the HO–H bond. Compared to the nanoparticle-based system, the nanowires showed an increased activity because the nanowire shape provided more active sites and improved the charge transport. The nanowire-nanosheet combination also showed higher stability in long-term tests because the nanowire shape and the presence of the nanosheets suppressed the dissolution of the catalyst. Degradation only occurred if the nanowires fragmented into shorter segments. Other reports on the use of nanowires as catalysts are plentiful [26, 78, 111–133].

2.2 Colloidal stability and self-assembly of nanowires into bundles

Colloidal stability and self-assembly are two sides of the same coin. Colloidal stability describes whether particles in a solvent aggregate and precipitate (“colloidally unstable”) or remain finely dispersed or form temporary reversible agglomerates (“colloidally stable”) [134]. Ordered superstructures resulting from aggregation are often called “self-assembled” structures [135–142]. Whether a colloid is stable depends on the interaction potential between the particles [134–142]. The following sections review interaction potentials relevant to AuNWs and summarize current knowledge on the colloidal stability of ultrathin nanowires.

2.2.1 Colloidal interactions of non-polar nanoparticles in non-polar solvents

Several reviews summarize colloidal interactions [135–142]. Since many if not most ultrathin nanowires, including the AuNWs investigated in this dissertation, are capped by non-polar hydrocarbon ligands and are dispersed in non-polar solvents [43, 74–77], the following section will limit attention to the forces found in such non-polar colloidal systems.

The section will not treat interactions triggered by external stimuli such as external magnetic fields [143] or the presence of a substrate [144] and will neither discuss

specific interactions such as DNA origami bonds [145] or covalent bonds found in cross-linked ligands [146].

Van der Waals forces

Van der Waals (vdW) forces occur between permanent, induced, and spontaneous dipoles in atoms, molecules, and bodies [134, 147]. Langbein [148] expressed the vdW interaction energy U between two parallel cylinders of radius R at a distance x , neglecting retardation screening, as

$$U = -\frac{2A_{121}}{3x} \sum_{i,j=1}^{\infty} \frac{\Gamma^2(i+j+\frac{1}{2})}{i!j!(i-1)!(j-1)!} \left(\frac{R}{x}\right)^{2(i+j)}, \quad (2.1)$$

where Γ is the Gamma function and A_{121} is the reduced Hamaker constant for the cylinders of material 1 and Hamaker constant A_1 interacting through a medium 2 of Hamaker constant A_2 , which can be approximated as [134]

$$A_{121} = (\sqrt{A_1} - \sqrt{A_2})^2. \quad (2.2)$$

The interaction potential can be approximated by

$$U = -\frac{3\pi^3 R^4 A_{121}}{8x^5} \quad (2.3)$$

at large distances and by

$$U = -\frac{\sqrt{R} A_{121}}{l^{3/2}} \quad (2.4)$$

at small distances, where $l = x - 2R$ is the surface-to-surface separation [147].

The interaction potential (2.1) between the metal cores of two AuNWs is plotted in Fig. 2.4. This interaction potential neglects contributions from the ligand shell, which is justified if ligand and solvent possess similar dielectric properties, as in OAm-capped AuNWs in alkane solvents [44, 149].

The vdW forces between two colloidal particles are, with few exceptions, attractive [134, 147]. If the vdW force dominates the interaction potential, two particles will approach each other until a repulsive force balances the vdW force. As will be seen in the next section, this can be the repulsion of the ligand shell.

Ligand-ligand and ligand-solvent forces

While ligand-ligand and ligand-solvent interactions in particles capped by oligomer ligands have only been studied relatively recently, those in polymer ligands have

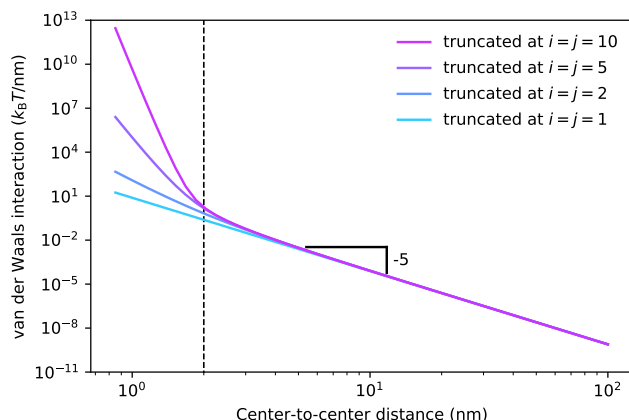


FIGURE 2.4: The van der Waals interaction between the cores of two AuNWs (diameter of 1.7 nm) aligned in parallel and dispersed in alkanes following (2.1). The theory derived by Langbein [148] is valid for center-to-center distances greater than 2 nm corresponding to a surface separation of 0.3 nm (dashed line). Hamaker constants of 1.96×10^{-19} J for gold and 4.69×10^{-20} J for hydrocarbon were obtained from Ref. [147] p. 64.

been researched for over half a century and are better understood [134, 150]. This section, therefore, focuses on the models developed for polymer ligands.

The solubility of the ligand in the solvent determines the ligand conformation. In a theta solvent, a polymeric ligand adopts the conformation of a random walk and behaves independently of the solvent, as shown in Fig. 2.5A [134, 150, 151]. The excess free energy of mixing the polymer and the theta solvent is zero (Flory-Huggins interaction parameter $\chi = \frac{1}{2}$)¹. In a good solvent ($\chi < \frac{1}{2}$), the interaction between the polymeric ligand and the solvent is favorable, the polymeric ligand adopts an extended conformation, and solvent molecules interdigitate into the ligand shell and solvate the ligand, see Fig. 2.5A [134, 150, 151]. The degree of ligand solvation depends on the chain length, surface coverage, surface curvature, and combination of ligand and solvent [152]. In a poor solvent ($\chi > \frac{1}{2}$), the polymeric ligand shrinks or collapses to reduce contact with the solvent [134, 150, 151]. Various intermolecular forces can drive this reduction in contact, depending on the combination of ligand and solvent; examples are vdW forces, ionic interactions, or hydrogen bonds [150].

When two ligand-grafted nanoparticles approach each other in a good solvent, repulsive forces occur. They are called “steric”, “overlap” or “entropic” repulsive forces [134, 150, 153, 154] and are often used to stabilize the colloid against vdW attraction of the core [155–157]. Once the ligand shells come into contact with each other, the space available to the ligands shrinks, the solvent is forced to leave the ligand shell, and the entropy of mixing and the conformational entropy of the ligands decrease [152, 158–160]. If the ligand shells are further compressed, “elastic” forces

¹For a definition of the Flory-Huggins interaction parameter, see for example Ref. [151]

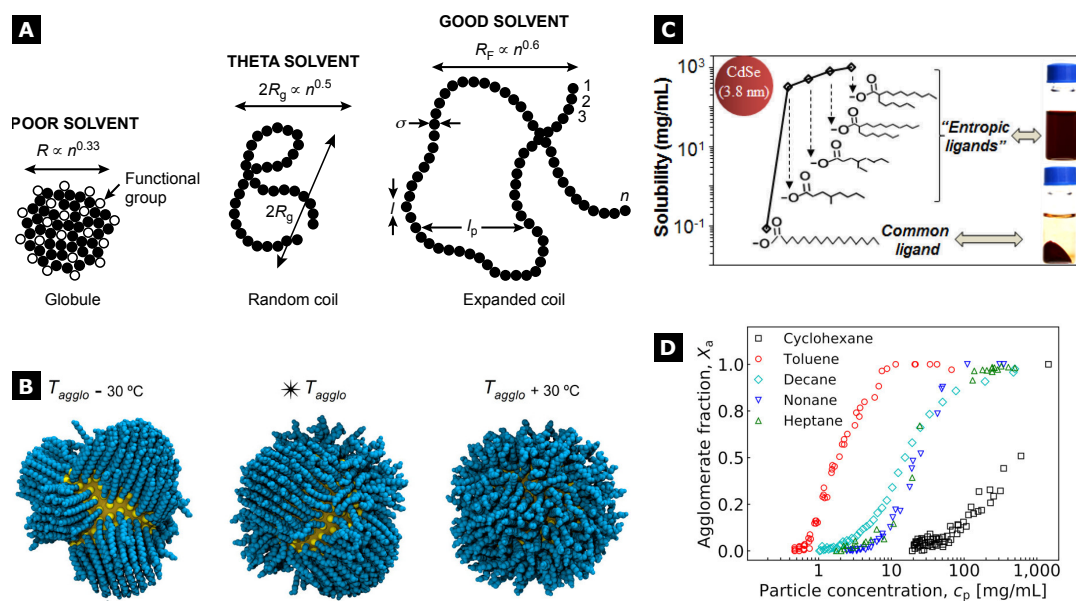


FIGURE 2.5: Ligand-ligand and ligand-solvent forces in non-polar nanoparticles. (A) The conformation of polymers in a solvent depends on solubility. In a poor solvent, the polymer coil shrinks and collapses; in a theta solvent, the free energy of mixing is zero; in a good solvent, the polymer chain extends into the solvent. Adapted and reprinted with permission from [150]. © 2011 Elsevier Inc. (B) Order-to-disorder transition in the hexadecanethiol ligand shell of gold nanoparticles. Below the transition temperature, the ligands agglomerate into ordered bundles. Adapted and reprinted with permission from [157]. © 2020 American Chemical Society. (C) The solubility of nanoparticles depends on the shape of the ligand. Nanoparticles with branched (“entropic”) ligands are more soluble than those with linear ligands. Adapted and reprinted with permission from [165]. © 2016 American Chemical Society. (D) Agglomerated fraction of octadecanethiol-stabilized gold nanoparticles as a function of particle concentrations. Solvents that hinder the ordering of the ligand shell, such as cyclohexane, improve solubility. Adapted and reprinted with permission from [166]. © 2019 American Chemical Society.

occur and oppose any further approach of the particles [158, 159]. These repulsive steric forces approximately scale exponentially with the interparticle spacing [150].

In a poor solvent (sometimes called anti-solvent or non-solvent), attractive forces can agglomerate nanoparticles. The enthalpy of mixing favors ligand-ligand over ligand-solvent interactions. The repulsive entropic force (due to solvation) no longer exists, and the ligand shell shrinks [152, 158–160]. The shell no longer balances the vdW force, making the interaction attractive at larger distances [152, 158–160]. Only at short distances do repulsive elastic forces set in once two shells touch and compress each other. Depending on the solubility in the poor solvent, ligands prefer to be next to other ligands, resulting in a short-ranged attractive force between the shells of two particles. The net attraction in poor solvents is exploited when washing nanoparticles [152, 161, 162] and nanowires [45, 88] and was also used to assemble superlattices [163, 164].

Ligand shell order-to-disorder transitions

Recent research suggests that the picture above of polymer chains interacting with solvent does not always hold for small nanoparticles (core diameter < 10 nm) passivated by oligomer ligands. Oligomer ligands can undergo order-to-disorder transitions, and these transitions affect the interaction potential between nanoparticles. The transitions were already known in self-assembled monolayers on macroscopic substrates [167, 168] and were found in ligand monolayers on nanoparticles, too [155–157, 169–174]. At high temperatures, the ligand shell is disordered and well solvated; at lower temperatures, the ligands align in ordered domains or bundles, as shown in Fig. 2.5B [155–157, 169–172, 175]. In the disordered phase, the ligand shell is repulsive because the entropy of mixing and elastic compression of the shell oppose the agglomeration of the particles (see the previous section). The disordered phase is also associated with better solubility of the particles [176, 177]. In the ordered phase, the behavior is inverse, and the ligand shell is attractive due to vdW forces between the ligands [155–157, 169–172]. Monego et al. [157] quantified enthalpic and entropic contributions to the disorder-to-order transition in Au nanoparticles covered by hexadecanethiol (diameter of 4 nm) and CdSe nanoparticles covered by hexadecanethiol (diameter of 5.8 nm). When transitioning from the disordered to the ordered state, the system gained internal energy because the ligands could arrange at their preferred dihedral angles and paid the penalty for the reduced vdW interaction between ligand and solvent and the reduced conformational entropy of the ligands [157]. The contributions from the solvent's mixing entropy and conformational entropy were negligible [157].

Several factors influence the order-to-disorder transition temperature: nanoparticle facets size, ligand length, ligand shape, ligand surface coverage, type of solvent, and the presence of a neighboring ligand shell. The order-to-disorder transition shifts to lower temperatures when the surface curvature increases [169–171]. The influence of curvature vanishes the longer the ligand is compared to the particle size [171]. Increasing the ligand chain length increases the order-to-disorder transition temperature [156, 171]. Introducing unsaturated or branched ligands (Fig. 2.5C) in the shell or mixing different ligands in the shell distorts the order so that the disordered state is reached at lower temperatures [165, 172, 178]. In addition, the transition temperature broadens with increased steric complexity in the shell. For example, increasing the fraction of oleate in a combined shell of oleate and octadecylphosphonate from 0% to 70% decreased the transition temperature from 300 K to 150 K, as simulated for CdSe and CdS nanoparticles (diameter of 5 nm) [172]. The transition temperature decreases if reducing the ligand surface coverage leads to less

favorable ligand packing. For example, octadecyl ligands on CdS nanorods underwent the order-to-disorder transition at 365 K at 100 % surface coverage and 312 K at 75 % surface coverage, with the smaller surface coverage requiring alternating arrangements of ligands in the monolayer [170]. Solvents lower the transition temperature if they solvate the ligand well and hinder its ordering. This correlation explains why cyclohexane is a better solvent for nanoparticles covered by alkyl ligands than linear alkane solvents (Fig. 2.5D) [157, 166] and why smaller solvents with otherwise similar solubility parameters seem to provide increased colloidal stability [178]. Finally, the proximity of another ligand-capped nanoparticle can increase order and the transition temperature [169].

Because direct observation of the ligand shell can be difficult in experiments, much of the insight into the order-to-disorder transitions was obtained in combination with MD simulations. Among the experimental toolkit, the broadening of ^1H NMR resonances was used to assess ligand solvation, with broad NMR lines correlating with poor solvation [179]. Small-angle neutron scattering (SANS) could indicate which fraction of the ligand shell is tightly packed [180].

Indirect experimental insight stems from studies of colloidal stability. Kister et al. [155] distinguished a shell-dominated and a core-dominated regime in the agglomeration of gold nanoparticles passivated by hexadecanethiol in *n*-hexane (core diameter of 4 nm to 10 nm). Larger particles agglomerated by vdW attraction of the cores. In this core-dominated regime, the ligand shell was disordered during agglomeration and would only order at temperatures below the agglomeration temperature [155]. Smaller particles agglomerated by ligand-ligand attraction once the ligand shell was ordered (the order-to-disorder transition temperature approximately was the same as the agglomeration temperature) [155]. In this ligand-dominated regime, shorter ligands enhance colloidal stability since they order at lower temperatures. Which regime dominated could be estimated: vdW interactions between the cores dominated when they exceeded approximately $1/3k_{\text{B}}T$ at the distance where the shells started to touch (k_{B} is the Boltzmann constant and T is the temperature) [155].

Depletion forces

Depletion forces arise in dispersions containing colloidal particles and a second species of smaller particles or molecules [134, 139, 150, 181]. These smaller particles or molecules (the “depletants”) cannot enter the volume directly next to the larger particles (the “excluded volume”), which is thus depleted of the smaller species, see Fig. 2.6A. When two larger particles approach, their excluded volumes overlap so

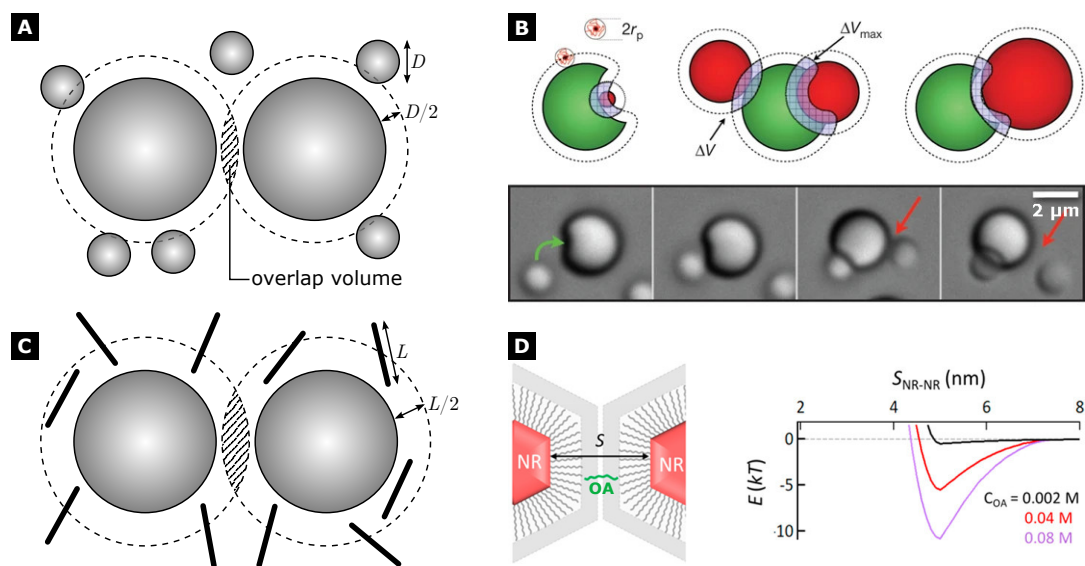


FIGURE 2.6: The depletion force in colloidal nanoparticles. (A) Depletion forces occur in mixtures of larger and smaller particles. The center of the smaller particles of diameter D cannot enter the excluded volume of width $D/2$ around the larger particles. (B) In a lock-and-key particle system, the depletion force drives the keys into the locks because this combination maximizes the overlap volume. Adapted and reprinted with permission from [182]. © 2010 Macmillan Publishers Limited. (C) Rod-shaped depletants of length L must align parallel to the particle surface and lose entropy when their centers enter the excluded volume of width $L/2$. (D) Ligand-coated nanorods were assembled by adding oleic acid (OA) to the dispersion. Analytical calculations of the interaction potential show that the minimum in the interaction potential increases with increasing concentration of oleic acid. The calculations considered the attractive vdW, repulsive steric, and attractive depletion forces and treated oleic acid as a prolate spheroid. Adapted and reprinted with permission from [183]. © 2019 American Chemical Society.

that overall more volume becomes available to the depletants, increasing their translational degrees of freedom and hence their entropy. A net attractive force arises between the larger particles if this increase in entropy outweighs the entropic penalty paid for agglomeration of the larger particles. This is typically the case if the depletants outnumber the larger particles [134, 139, 150, 181]. Explained in simpler terms: There is a gradient in the concentration of depletants between the “overlap volume” and the bulk solvent. This gradient in concentration gives rise to an osmotic pressure, which pushes the larger particles together and induces their agglomeration [134, 139, 150, 181].

The magnitude of the depletion force is proportional to the overlap volume, which changes with particle shape [181]. Varying the particle shape also allows for making the depletion force directional. For example, Sacanna et al. [182] created a lock-and-key particle system consisting of larger spherical particles with a cavity (“lock”) and smaller particles fitting precisely into the cavities (“key”). Their assembly could be triggered by adding depletants. The keys self-assembled in the locks because this configuration maximized the overlap volume, see Fig. 2.6B [182].

The exclusion mechanism can be geometric (the depletants do not fit into the excluded volume) or entropic (the depletants lose entropy within the excluded volume). Entropic reasons are relevant for anisotropic, e.g., rod-shaped depletants [184–190]. They can enter the excluded volume but must orient parallel to the particle surface, thus losing rotational entropy, see Fig. 2.6C [184–190]. The resulting depletion potential is proportional to the length-to-diameter aspect ratio of the rod-shaped depletants. The concept has been used to purify rod-shaped viruses, for example [191].

Macromolecules can induce depletion forces [134, 150, 181], and recent research suggests that smaller linear molecules can act as depletants, too. For example, ligand-coated semiconductor nanorods could be assembled into hexagonal arrays when oleic acid was added to the dispersion [192]. Adding linearly-shaped molecules (e.g., oleic acid or OAm) to dispersions of drying nanoparticles improved the crystallinity of the emerging superlattices [183, 192–195]. Analytical calculations of the interaction potential demonstrated that such an enhanced crystallinity might stem from the added molecules inducing an attractive depletion force, thus deepening the well in the particles' interaction potential, see Fig. 2.6D [183]. The nanoparticles in these studies were coated with ligands in the size range of the depletants, suggesting that ligand molecules could induce depletion forces, too. Likewise, solvent molecules can order in the proximity of nanoparticle surfaces and might induce depletion forces. Although the ordering of solvent molecules is well known around charged particles in polar solvents [134] and has also been observed in non-polar solvents [196], it has not yet been reported to induce depletion forces.

2.2.2 Self-assembly of ultrathin nanowires into bundles

Ultrathin nanowires can self-assemble into elongated bundles [14, 40–43]. Such nanowire bundles were observed in ultrathin nanowires made from FeP [40], CdSe [41], Cu₂S [42], Bi₂S₃ [14], CsPbBr₃ [197], and Au [43–45]. Bundles formed with thicknesses ranging from 70 nm in Au nanowires [44] to 400 nm in Cu₂S nanowires [42], and were observed both in dispersion and after drying [14, 40–43, 71].

The solvent and the type and amount of ligand influence the bundling of AuNWs. Freshly synthesized AuNWs assembled into bundles with a hexagonal lattice and a lattice spacing of 9.2 nm to 9.9 nm, implying that each nanowire was surrounded by a bilayer of OAm, as depicted in Fig. 2.7A [44, 45]. The formation of these bundles took approximately 2 h to 3 h [44, 45], a long time associated with the considerable length of the nanowires that slows diffusion and self-organization [44]. SAXS revealed an equilibrium between bundled and dispersed AuNWs at about 40% of AuNWs being contained in bundles in a freshly synthesized sample. The

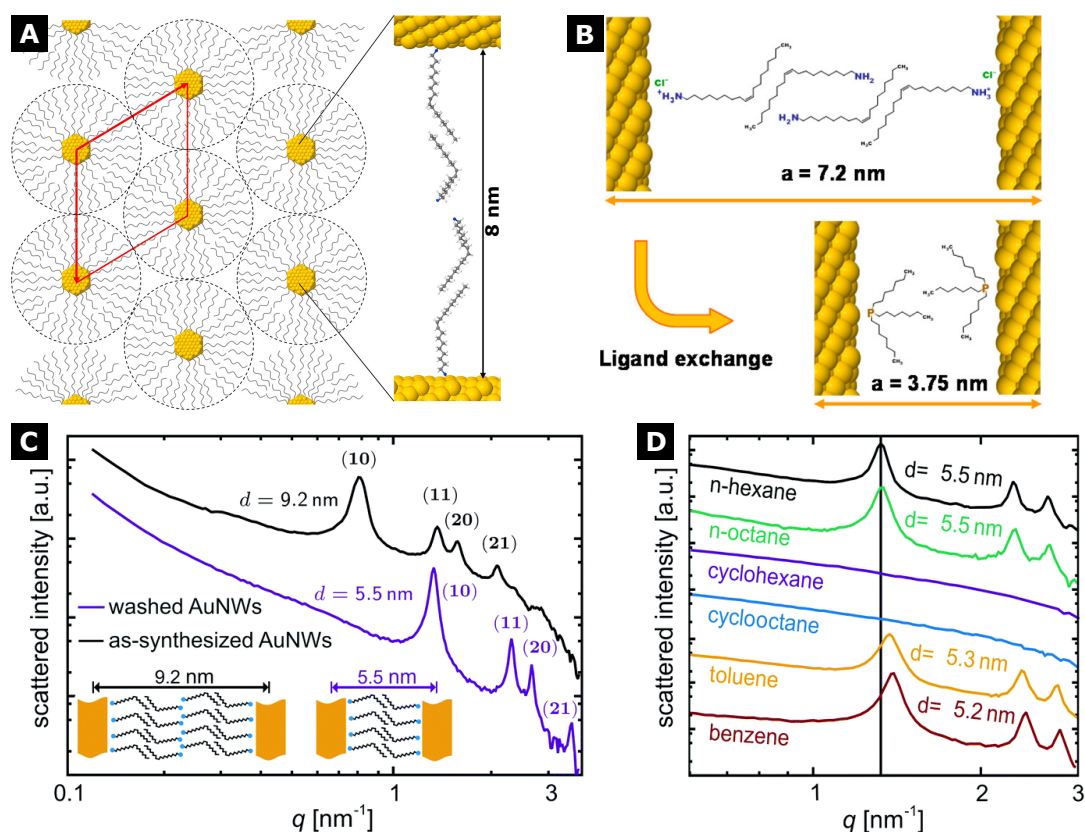


FIGURE 2.7: Self-assembly of AuNWs into bundles. (A) AuNWs self-assemble into hexagonal bundles during synthesis, with each nanowire being surrounded by a double layer of the ligand OAm. Adapted and reprinted with permission from [44]. © 2014 American Chemical Society. (B) Exchanging the ligand from OAm to TOP reduces the center-to-center distance in dried AuNWs from 7.2 nm to 3.75 nm. Adapted and reprinted with permission from [47]. © 2017 American Chemical Society. (C) Washing of AuNWs after synthesis reduces the spacing so that each nanowire is surrounded by a monolayer of the ligand OAm. Adapted and reprinted with permission from [45]. CC BY-NC 3.0. (D) The center-to-center distance of bundled AuNWs dispersed in arenes (toluene and benzene) is shorter than in linear alkanes (*n*-hexane and *n*-octane). No bundle formation was observed in cyclic alkanes (cyclohexane and cyclooctane). Adapted and reprinted with permission from [45]. CC BY-NC 3.0.

underlying mechanism of bundling was believed to be vdW attraction of the gold cores, with an interaction energy of $5k_{\text{B}}T$ for a pair of AuNWs [44].

Reducing the amount of ligand in the system by purifying AuNWs reduced the center-to-center distance to 7.2 nm for one purification cycle and 5.5 nm for two purification cycles, which corresponds to each nanowire being surrounded by a monolayer of OAm (see Fig. 2.7C) [45–47]. The center-to-center distance also decreased upon adding free ligand and increased by adding solvent, thus lowering the ligand concentration [45]. The dependence of the center-to-center distance on the ligand concentration was explained with osmotic pressure: increasing the ligand concentration increases the osmotic pressure in the bulk solvent so that some solvent is removed from within the bundles, and the bundles tighten [45].

Exchanging the type of ligand from OAm to shorter ligands resulted in tighter

bundles. The center-to-center distance of dried AuNWs decreased from 7.2 nm to 3.8 nm with trioctylphosphine (TOP) and to 6.6 nm with trioctylphosphine oxide (TOPO), as shown in Fig. 2.7B [47]. TOP and TOPO are molecules of similar size, but TOP resulted in significantly tighter bundles than TOPO because the phosphine head group bound more strongly to gold than the phosphine oxide group, so fewer OAm remained in the shell.

The purity of the ligand plays a role in nanowire self-assembly. AuNWs can self-assemble on amphiphilic, templated substrates in nematic and ribbon phases [144, 198]. AuNWs synthesized with pure 9-*cis*-octadeceneamine only showed one transition from the ribbon to the nematic phase. AuNWs synthesized with technical grade OAm, containing 9-*trans*-octadeceneamine and saturated alkyl amines as impurities, exhibited two additional order-to-disorder transitions [198].

Solvents influence bundling, too. No bundles were observed in AuNWs dispersed in cyclic alkanes (cyclohexane and cyclooctane), see Fig. 2.7D, which was explained by the less flexible cyclic alkanes not being able to interdigitate into the ligand shell the same way that linear alkanes do [45]. Bundles formed in arenes (toluene and benzene) with slightly tighter center-to-center distance than in *n*-hexane (5.2 nm to 5.3 nm versus 5.5 nm), which was attributed to the π - π -interactions rendering the solvent less compatible to the alkyl tail of OAm (Fig. 2.7D) [45]. The densest bundles were observed in alcohols such as ethanol with a center-to-center distance of 3.6 nm, likely due to differences in the polarity of the solvent and the ligand shell [199].

To summarize, it is known that ultrathin, ligand-coated nanowires can self-assemble into elongated bundles. Solvent and type and amount of ligand modulate bundle formation and lattice constant. The colloidal interactions that drive the bundling are still unclear. VdW forces [44] and osmotic pressure [45] have been postulated to cause bundling, but we lack clear evidence to support any of the theories. Further systematic experiments and simulations on the molecular length scale are needed to elucidate the dominating interactions.

2.3 The Plateau-Rayleigh instability of nanowires

The shape of a cylinder is thermodynamically unfavorable. The resulting instability was first discovered for fluids by Plateau [55] in 1873 and Rayleigh [56] in 1878 and is named “Plateau-Rayleigh”, “Rayleigh”, “morphological”, “geometric”, or “shape instability”. The phenomenon was described for solids by Nichols and Mullins [61] in 1965. The instability is driven by a reduction in surface energy: a cylinder of radius R_0 splits into an array of spheres of radius $R_s \geq (3\pi/2)^{\frac{1}{3}}R_0$, which have a

smaller overall surface area and hence surface energy [61, 62]. In metals, the fragmentation evolves by surface diffusion, which is driven by a gradient in chemical potential.

The Plateau-Rayleigh instability is more severe for smaller structures. The break-up time scales with a nanowire's radius to the fourth power, as will be shown in the following sections. In the past two decades, the emergence of one-dimensional nanostructures with sizes well below 100 nm has renewed interest in the Plateau-Rayleigh instability.

This section presents prototypical examples of the Plateau-Rayleigh instability in one-dimensional nanomaterials, briefly derives the underlying theory, summarizes the current state of the art, and discusses the most recent literature dealing with the instability in ligand-coated nanowires.

2.3.1 Phenomenological introduction to the Plateau-Rayleigh instability

Researchers around Toimil-Molares investigated the break-up of Cu, Au, and Pt nanowires with diameters ranging from 25 nm to 74 nm, see Fig. 2.8A [48–50]. Li et al. [52] investigated the break-up of ultrathin gold nanoribbons on the atomic scale via high-resolution transmission electron microscopy (TEM), see Fig. 2.8B. And Wang, Huang, and He [200] observed diblock copolymer micelles (average diameter of 43 nm and lengths of about 25 μm) breaking up within 10 days, a time period allowing to study intermediate morphologies, see Fig. 2.8C.

The Plateau-Rayleigh instability begins with small irregularities in the surface, as those seen in the high-resolutions TEMs in Fig. 2.8B at 0 min and 10 min [48, 49, 52]. Such irregularities may be present in the surface from its creation on or may form due to thermal fluctuations. They cause the material to reorganize into thinner and thicker cross sections that repeat periodically, see Fig. 2.8B at 20 min and Fig. 2.8C at 2 h. The periodicity is set by the fastest growing perturbation that dominates the Plateau-Rayleigh instability (derived in the following section) [61, 62]. The amplitude of the perturbations increases because atoms diffuse from the thinned to the thickened sections, see for example the evolution in Fig. 2.8B from 20 min to 50 min and Fig. 2.8C from 2 h to 5 days [51]. Eventually, the cylinder pinches off into discrete spheroidal particles, see again Fig. 2.8.

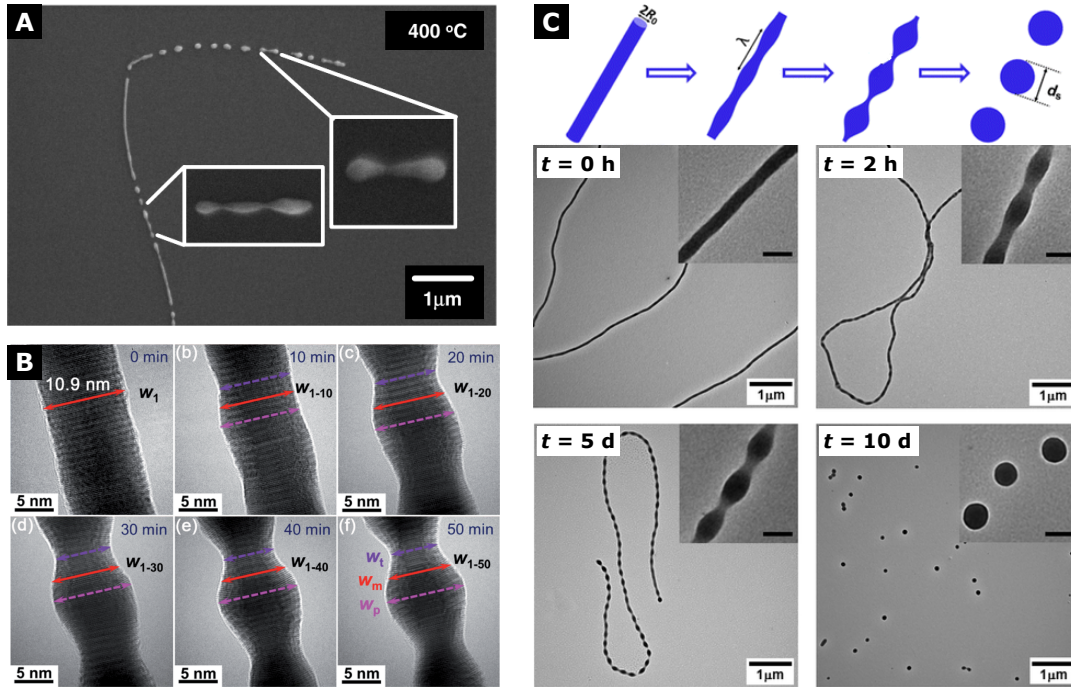


FIGURE 2.8: Prototypical examples of the Plateau-Rayleigh instability in one-dimensional nanostructures. (A) AuNW with a diameter of 25 nm decays into spheroidal nanoparticles. The insets show transient states in the shape instability. Adapted and reprinted with permission from [49]. © 2006 IOP Publishing Ltd. (B) Gold nanoribbon with a width of 11 nm develops a perturbation in its radius. The perturbation will lead to break-up into spherical particles. Adapted and reprinted with permission from [52]. CC BY-NC 3.0. (C) Schematic and TEMs of a cylindrical micelle made from diblock copolymers (average diameter of 43 nm) decaying into spherical micelles. The scale bar in the insets corresponds to 100 nm. Adapted and reprinted with permission from [200]. © 2014 American Chemical Society.

2.3.2 Chemical potential and surface energies as driving forces

The basic theory of the Plateau-Rayleigh instability will now be discussed². Consider a non-perfect cylinder whose radius R is perturbed with amplitude a and wavelength λ as shown in Fig. 2.9. The radius of the cylinder is described as

$$R(z, t) = R_0 + \Delta R(t) + a(t) \cos(kz), \quad (2.5)$$

with axial coordinate z , time t , and wavenumber $k = 2\pi/\lambda$. The term ΔR is required to conserve volume. In the following analysis, it is assumed that the perturbation amplitude is small ($a \ll R_0$) so that terms of $\mathcal{O}(a^3)$ and higher order can be neglected [201]. The volume-conserving term ΔR can be derived by comparing the volume V

²The only two textbooks known to the author that treat the Rayleigh-Plateau instability are Refs. [201] and [202]. Since they only treat specific variants of the topic, a brief and complete introduction is given here.

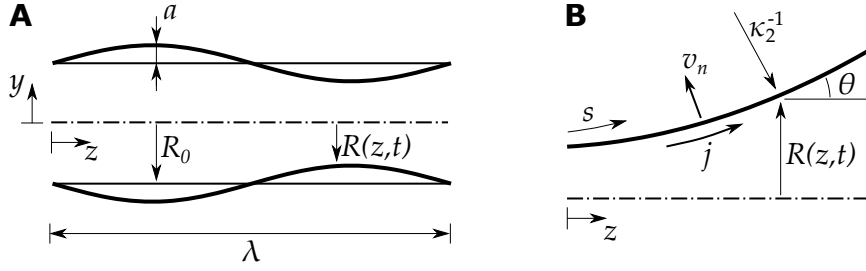


FIGURE 2.9: Geometry of a perturbed cylinder. (A) Cylinder of initial radius R_0 perturbed with a harmonic perturbation of wavelength λ and amplitude a . (B) Geometry along the surface line of the cylinder.

of the perturbed cylinder over one wavelength,

$$V = \pi R_0^2 \lambda \left(1 + 2 \frac{\Delta R}{R_0} + \frac{1}{2} \frac{a^2}{R_0^2} \right), \quad (2.6)$$

with that of a non-perturbed cylinder over one wavelength of $V_0 = \pi R_0^2 \lambda$, so that the term ΔR equates to

$$\frac{\Delta R}{R_0} = -\frac{1}{4} \frac{a^2}{R_0^2}. \quad (2.7)$$

Energetics

In order to determine whether the cylinder breaks into smaller spheres, the change in Gibbs free energy ΔG of the cylinder caused by the perturbation must be considered. The perturbation changes the surface area A_s and its overall surface energy [201]. The change in Gibbs free energy is defined as $\Delta G = \gamma \Delta A_s$, where γ is the specific surface energy. The surface of the cylinder A_s over one perturbation wavelength is given by

$$A_s = \int_0^\lambda 2\pi R \, ds \quad (2.8)$$

with s being the arc length along the surface. Assuming $a \ll R_0$ allows to write $ds = (1 + (ka)^2 \sin^2(kz)/2) \, dz$ so that

$$A_s = 2\pi R_0 \lambda \left(1 + \frac{1}{4} \frac{a^2}{R_0^2} \left((kR_0)^2 - 1 \right) \right). \quad (2.9)$$

Now compare with the surface area of the non-perturbed cylinder over one wavelength, $A_s^0 = 2\pi R_0 \lambda$, to find the change in Gibbs free energy of

$$\Delta G = \frac{\pi}{2} R_0 \lambda \gamma \left(\frac{a^2}{R_0^2} \right) \left((kR_0)^2 - 1 \right). \quad (2.10)$$

It can be seen from (2.10) that the perturbation decreases the Gibbs free energy ($\Delta G < 0$) and consequently leads to break-up if

$$kR_0 < 1 \quad \text{or} \quad \lambda > 2\pi R_0, \quad (2.11)$$

the result obtained experimentally by Plateau [55] and analytically by Rayleigh [56].

Kinetics via a variational principle

The perturbation growth rate can be found using a variational principle with functional $\Pi(\dot{A}, \mathbf{j}_s) = \Delta\dot{G} + \Psi$ that depends on the rate of change in surface area \dot{A} and the surface diffusive flux \mathbf{j}_s , where Ψ is the dissipation potential caused by surface diffusion [203, 204]. The dot symbol denotes differentiation with respect to time and a bold symbol denotes a vector. A valid solution must give a stationary value of Π ,

$$\delta\Pi = \delta(\Delta\dot{G}) + \delta\Psi = 0. \quad (2.12)$$

The first term $\delta(\Delta\dot{G})$ can be obtained directly from (2.10). The dissipation potential Ψ of a diffusive flux of magnitude j_s is defined as

$$\Psi = \int_{A_s} \frac{j_s^2}{2\mathcal{D}_s} dA, \quad (2.13)$$

where the surface diffusion parameter \mathcal{D}_s is defined as $\mathcal{D}_s = \delta_s D_s \Omega_s / (k_B T)$, with δ_s being the layer height over which surface diffusion occurs, D_s being the surface diffusivity, and Ω_s being the volume of an atom [205]. The diffusive flux j_s along the surface is related to the normal velocity of a volume element [203, 204] by

$$\nabla_s \cdot \mathbf{j}_s + v_n = 0. \quad (2.14)$$

Since the in-plane is faster than the out-of-plane diffusion and any cylinder section will remain circular, it is sufficient to consider surface diffusion only along the z -direction so that the term $\nabla_s \cdot \mathbf{j}_s$ simplifies to $\partial j_s / \partial z$ with first-order accuracy in a [62, 204]. The velocity into a surface element v_n is given by $v_n = \dot{R}$. With first-order accuracy in \dot{a} , the diffusive flux hence equates to,

$$j_s = -\frac{\dot{a}}{k} \sin(kz) \quad (2.15)$$

Inserting (2.15) into the definition of the dissipation potential (2.13) gives

$$\Psi = \frac{\pi^2 R_0 \dot{a}^2}{\mathcal{D}_s k^3}. \quad (2.16)$$

Upon substitution of (2.16) into the variational functional (2.12), the perturbation growth rate is obtained as

$$\frac{\dot{a}}{a} = \frac{\gamma \mathcal{D}_s k^2}{R_0^2} \left(1 - (kR_0)^2 \right). \quad (2.17)$$

This perturbation growth rate allows the same conclusions as drawn by the analysis of (2.10): a wire is unstable against perturbations of wavelength $\lambda > 2\pi R_0$. In addition, (2.17) allows to determine the fastest growth rate and pinch-off time.

Kinetics via chemical potential

An alternative way to derive this perturbation growth rate is to consider the gradient in chemical potential due to locally different surface curvatures [56, 61, 62]. This gradient in chemical potential induces surface diffusion so that the instability evolves. The chemical potential μ of a surface atom is related to the mean surface curvature κ_m via

$$\mu = 2\Omega\gamma\kappa_m, \quad (2.18)$$

where the mean curvature is defined as $\kappa_m = (\kappa_1 + \kappa_2)/2$ with $\kappa_1 = \cos(\theta)/R$ and $\kappa_2 = -\partial\theta/\partial s$ being the two principal surface curvatures [62]. Neglecting terms of $\mathcal{O}(a^2)$ and higher order, these curvatures are $\kappa_1 = 1/R_0 - (a/R_0^2) \cos(kz)$ and $\kappa_2 = ak^2 \cos(kz)$. Fick's law [203] relates a gradient in chemical potential to a diffusive flux

$$j_s = -\frac{\mathcal{D}_s}{\Omega} \nabla_s \mu. \quad (2.19)$$

The surface flux j_s is related to the outward normal velocity of the surface v_n via (2.14), so the problem can be stated as

$$v_n = 2\mathcal{D}_s\gamma \frac{\partial^2 \kappa_m}{\partial z^2}. \quad (2.20)$$

Differentiating (2.20) and using $v_n = \dot{R} = \dot{a} \cos(kz)$ allows to determine the perturbation growth rate as

$$\frac{\dot{a}}{a} = \frac{\mathcal{D}_s \gamma k^2}{R_0^2} \left(1 - (kR_0)^2 \right). \quad (2.21)$$

This result is the same as obtained in (2.17), this time motivated by the gradient in chemical potential that arises due to locally varying surface curvatures.

Fastest growth rate and pinch-off time

The fastest-growing perturbation wavenumber maximizes \dot{a} and is given by

$$k_{\max}R_0 = \frac{1}{\sqrt{2}} \quad \text{or} \quad \lambda_{\max} = 2\sqrt{2}\pi R_0. \quad (2.22)$$

It leads to a growth rate of $(\dot{a}/a)_{\max} = \gamma\mathcal{D}_s/(4R_0^4)$ [62, 201]. With this information, the time required for pinch-off can be calculated. More precisely, one can approximate the time required for a perturbation of initial amplitude a_0 to grow to an arbitrary amplitude a_p necessary for pinch-off (say, for example, $a_p = 0.9R_0$), which gives

$$t_p = 4 \log \left(\frac{a_p}{a_0} \right) \frac{R_0^4}{\gamma\mathcal{D}_s}. \quad (2.23)$$

The scaling of t_p with R_0^4 explains why the Plateau-Rayleigh instability is more severe in small cylindrical structures such as ultrathin nanowires [201]. Take a nanowire with a thickness of 100 nm which breaks up within 100 d. A nanowire with the same properties and a diameter of only 2 nm breaks up in less than 2 s.

2.3.3 Factors influencing the shape stability

The Plateau-Rayleigh theory predicts that the stability of a nanowire depends on the surface diffusion parameter \mathcal{D}_s , the radius of the nanowire R_0 , and the surface energy γ . While this model accurately describes many real cases, recent research has shown that additional factors influence shape stability in some systems. Among these factors are crystallographic and surface energy anisotropy, the presence of substrates, and confinement by a matrix or shell. These factors will be reviewed in the following section.

Crystallographic and surface energy anisotropy

The surface energy of crystalline solids is anisotropic and depends on crystallographic orientation [206]. The change in Gibbs free energy caused by an evolving perturbation, therefore, not only depends on the surface area but also the orientation of the perturbed surface. Cahn [206] was the first to consider this effect by assuming the surface energy γ to be a function of the surface inclination θ (see Fig. 2.9B). The critical perturbation wavenumber k_c given in (2.11) then reads [206]

$$k_c R_0 = \left(1 + \frac{1}{\gamma} \left(\frac{\partial^2 \gamma}{\partial \theta^2} \right) \right)^{-\frac{1}{2}}. \quad (2.24)$$

Crystalline facets could potentially render the term $\partial^2\gamma/\partial\theta^2$ singular around $\theta = 0$ and make the nanowire stable against perturbations of any wavelength [206].³ The fastest growing perturbation wavenumber is $k_{\max} = k_c/\sqrt{2}$, which is consistent with (2.22) for the isotropic case [57].

The surface energy depends on only one angle in the model of Cahn [206]. In reality, it depends on the orientation of the surface in three dimensions, which was considered by Gurski and McFadden [207]. The cylinder's cross section was not necessarily circular but could take any equilibrium shape determined by the anisotropy. Gurski and McFadden [207] found that whether anisotropy stabilizes or destabilizes a nanowire still depended on the magnitude and sign of the anisotropy [207].

Experimental evidence on the influence of anisotropy was provided by the group of Glaeser, who extensively studied the Plateau-Rayleigh instability in cylindrical pores in sapphire [60, 63, 208]. Such pores can occur naturally around cracks; Glaeser [208] created them at precise crystallographic orientations on a sapphire surface by photolithography and electron beam etching (see Fig. 2.10A). Note that the Plateau-Rayleigh instability occurs regardless of whether the cylinder shape is concave (a void pore in a matrix) or convex (a solid wire in air). From an experimental point of view, the concave shape was advantageous, as it allowed observation of the instability in an inert atmosphere [208]. The spacing of the emerging spherical pores in the (0001) plane was 3 to 5 times larger on the $[11\bar{2}0]$ than on the $[1\bar{1}00]$ axis, indicating that the crystallographic orientation influences shape stability [208]. Note that the pore spacing correlated with the pinch-off time. For channels etched into the $(10\bar{1}0)$ plane, the trend was opposite: channels along the $[11\bar{2}0]$ axis were an order of magnitude more stable (break-up time of 468 h versus 2 h to 10 h in all other orientations), see Fig. 2.10C-D [60, 63]. The stable $[11\bar{2}0]$ channels were bound by (0001), $(\bar{1}012)$, and $(10\bar{1}1)$ facets, which are equilibrium facets of the Wulff shape and therefore pin the wire shape in a local energetic minimum [60, 63].

Similar experiments with convex shapes were carried out by Kim and Thompson [209]. Strips with widths of 130 nm (e-beam lithography) and 2 μm to 4 μm (photolithography) were patterned in a single-crystalline nickel thin film and placed on magnesium oxide and sapphire substrates. Their observation confirmed that nanowires bound by equilibrium facets are more stable. The break-up time was up to four times longer than predicted by the Plateau-Rayleigh theory, which was attributed to the surface energy anisotropy and the presence of a substrate [209].

The continuum analysis and experiments were complemented by kinetic Monte

³The nanowire may still be unstable against perturbations of larger perturbation amplitude on the order of the nanowire radius.

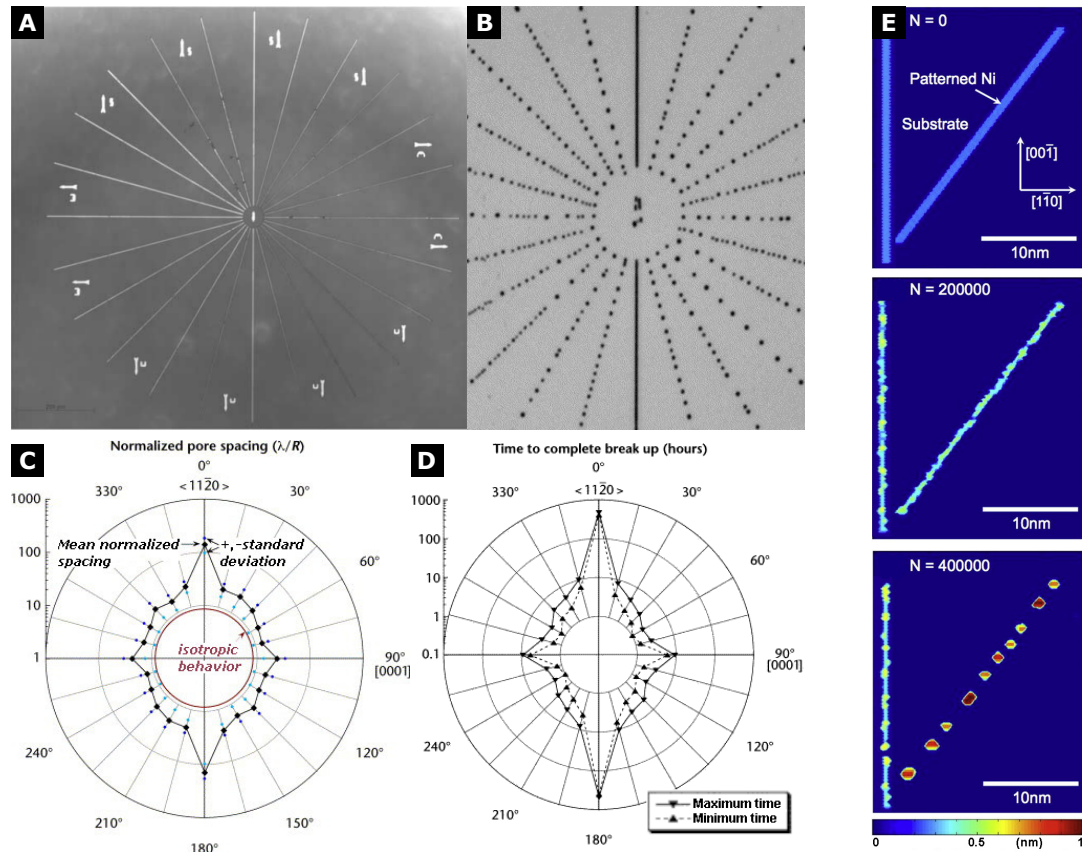


FIGURE 2.10: Influence of crystallographic and surface energy anisotropy on the Plateau-Rayleigh instability. (A) Channels of varying crystallographic orientations etched into the $(10\bar{1}0)$ plane of sapphire. The width of the channels was $3\ \mu\text{m}$ and that of the image approximately $1\ \text{mm}$. (B) The same channels as in (A) annealed at $1700\ \text{°C}$ for 8 h. Most channels have broken up into spherical pores except the vertical ones oriented along the $\langle 11\bar{2}0 \rangle$ axis. (C) Polar plot of the pore spacing normalized by effective radius. The isotropic behavior predicted by the Plateau-Rayleigh theory is marked in red. (D) The break-up time correlates with the pore spacing and manifests that channels along the $\langle 11\bar{2}0 \rangle$ orientation were stable for longer periods than other orientations. Parts (A) to (D) are adapted and reprinted with permission from [60]. © 2005 Elsevier B.V. (E) Kinetic Monte Carlo simulations of two Ni strips with different crystallographic orientations. The strip along the $[00\bar{1}]$ orientation was stable for longer periods than the other one. Adapted and reprinted with permission from [209]. © 2014 Elsevier Ltd. and Acta Materialia Inc.

Carlo simulations that qualitatively showed that equilibrium facets could delay morphological changes (see Fig. 2.10E) [209–211]. Simulations of Gorshkov and Privman [210, 211] treated nanowires with the fcc crystal structure common to noble metals. Surface atoms were allowed to move by random diffusion with probabilities set by the free energy in the local neighborhood of an atom. Additionally, the atoms were in equilibrium with their gas and allowed to desorb and adsorb from the wire surface. At temperatures close to the melting temperature, the systems were well described by the classic Plateau-Rayleigh theory. At lower temperatures, the influence of bounding facets was more pronounced such that the evolution deviated from the Plateau-Rayleigh theory: particle spacings twice the predicted value were observed

[210, 211]. In summary, there is plentiful evidence from theory, simulation, and experiment showing that anisotropic surface energies influence the shape stability of nanowires.

Presence of a substrate

There is sound evidence from continuum analysis that the presence of a substrate stabilizes nanowires [64, 204, 212, 213]. For liquids, Dussan [214] and Davis [215] showed that the presence of a substrate reduces the critical perturbation wavenumber k_c from 1 to $\sqrt{3/4}$ and increases stability, regardless of the contact angle. McCallum et al. [64] were the first to analyze the analogous problem in solids and confirmed these results. They considered an infinite cylindrical line in contact with a flat substrate. The shape of the cylinder could evolve by surface diffusion and was subjected to a perturbation along the cylinder axis. The radius R was a function of both the axial and cylindrical coordinates, as shown in Fig. 2.11A. The resulting critical and fastest-growing perturbation wavenumbers are plotted in Fig. 2.11B. Both vanish at small contact angles, meaning that a fully wetting cylinder is linearly stable against any perturbation [64].

The analysis by McCallum et al. [64] was extended to include crystallographic and surface energy anisotropy [212] and grooves on the substrate [204, 213]. A small contact angle close to 0° (non-wetting) can stabilize the nanowire if crystallographic anisotropy induces pinning of the contact line and hence hinders the evolution of the shape [212]. Gill [204] included a V-shaped groove in the substrate and simplified the model by McCallum et al. [64] by making the radius a function of the axial coordinate only. This simplification yielded the same result (within a deviation of 6%) as obtained for a flat substrate. The V-shaped groove generally stabilized the nanowire; the nanowire became stable against perturbations of any wavelength if the sum of the groove and the contact angle (here defined on the outside of the nanowire) exceeded π [204]. Boussinot and Brener [213] analyzed the influence of an arbitrarily shaped groove. In line with the findings by Gill [204], a Gaussian-shaped groove stabilized the wire when it was sufficiently deep and the contact angle sufficiently small (wetting), and a V-shaped groove when it was sufficiently deep or when the triple line was pinned.

These findings from continuum analysis are consistent with experimental evidence [209, 216–218]. Polymer strips on different substrates broke into spherical particles whose spacing depended on contact angle [217]. These strips with widths between $0.8\ \mu\text{m}$ and $2.5\ \mu\text{m}$ were placed on plain and SiN_x enriched Si wafers and annealed at $160\ ^\circ\text{C}$. The spacing of the resulting particles was larger than expected by

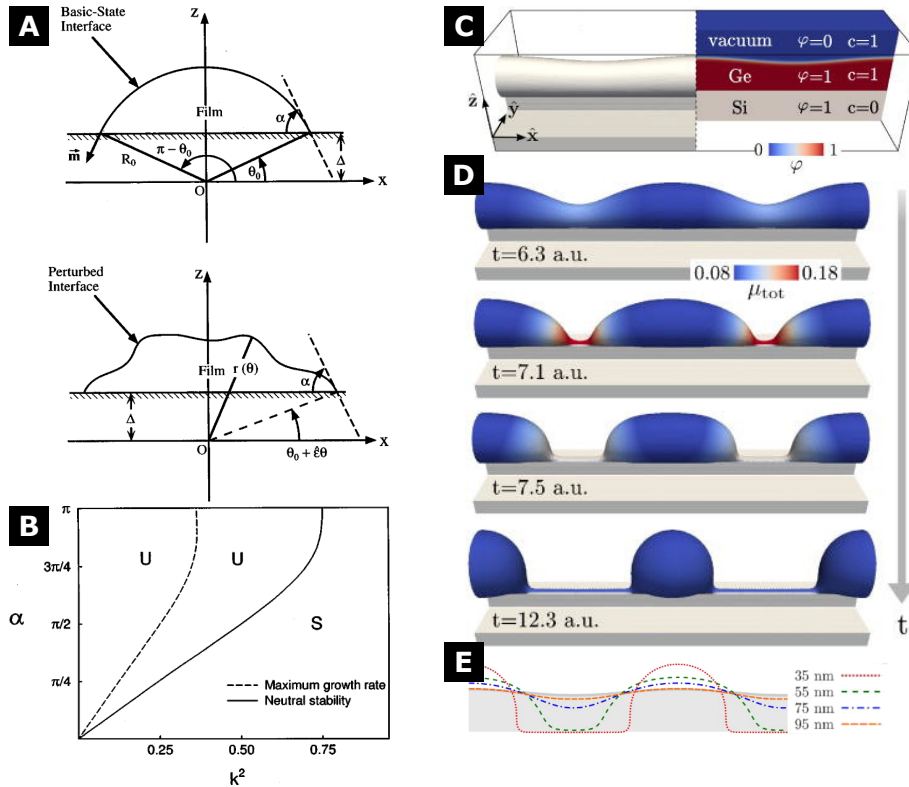


FIGURE 2.11: Continuum models and simulations of nanowire stabilization on substrates. (A) Cylindrical wire on a flat substrate in a non-perturbed and perturbed state. (B) The critical and fastest-growing perturbation wavenumbers k as a function of contact angle α . For small contact angles (wetting), the nanowire is stable against a larger range of perturbation wavenumbers. (C) Phase field simulation cell consisting of Si ridge, Ge nanowire, and vacuum. (D) Evolution of shape and chemical potential μ_{tot} for a perturbed Ge nanowire with time. The chemical potential is highest in the thinned regions, inducing diffusion that leads to a break-up. (E) Contours of the nanowire shape for different widths of the Si ridge at an arbitrary time point. The wider the ridge, the less change in shape. Parts (A) and (B) are adapted and reprinted with permission from [64]. © 1996 American Institute of Physics. Parts (C) to (E) are adapted and reprinted with permission from [216]. © 2018 AIP Publishing LLC.

classic Plateau-Rayleigh theory and correlated well with the contact angle on the two substrates [217]. In an experiment carried out by Salvalaglio et al. [216], the width of the substrate was systematically varied. To this end, Ge strips were prepared by epitaxial growth on Si ridges. The diameter of the Ge strips was held constant at 150 nm while the width of the Si ridges (height of 30 nm) was varied between 35, 55, and 95 nm. The wider these Si ridges, the longer it took the Ge nanowires to break up into distinct particles, implying that the substrate stabilized the wires. Illustrative phase-field studies (Fig. 2.11C-E) considering diffusion along the free surface of the Ge nanowire and fixed contact with the Si substrate confirmed this observation [216]. All of these findings confirm that a wetting substrate stabilizes nanowires or at least delays the Plateau-Rayleigh instability.

Confinement by a matrix or shell

When a template confines the nanowire shape, the template limits how the shape can evolve. For example, when Shin, Yu, and Song [219] deposited Sn nanowires electrochemically into cylindrical pores in an anodic aluminum oxide (AAO) template, the nanowires did not break up into spherical particles but into nanorods. The volume of these nanorods was slightly larger than that predicted for spheres resulting from the break-up of free-standing nanowires. Since volume correlates with break-up time [201], it can be concluded that the confinement increased the shape stability.

If the nanowire wets the confining walls and does not completely fill the confined space, the Plateau-Rayleigh instability can invert: spherical voids form instead of spherical nanoparticles [217, 220–222]. Such an inversion was observed in polymer strips in a rectangular channel [217, 223] and polymer nanotubes within cylindrical pores [220–222]. The polymer strips (widths from 0.8 μm to 3 μm and height of 125 nm) were formed by pressing a patterned PDMS stamp on a polystyrene film. The widths of the strips were confined by the PDMS walls, and their height could evolve freely. Upon annealing, spherical voids formed in the strips until the strips broke up into shorter fragments [217, 223]. The hollow polymer nanotubes (outer diameter from 100 nm to 400 nm and length of about 60 μm) were formed by filling AAO pores with poly(methyl methacrylate) or polystyrene [220–222]. When annealed, the shape of these hollow nanotubes became unstable and spherical voids formed. The pinch-off time was longer for nanotubes with denser, stiffer polymers [222].

A coating can confine nanowires [65, 66]. For example, AuNWs were coated with a silica shell, which increased their shape stability [65]. To this end, AuNWs were first made dispersible in ethanol by exchanging the ligand OAm for 3-mercaptopropionic acid. The silica coating was then created by adding tetraethoxysilane. The resulting shell had a thickness of 6 nm to 18 nm around the nanowire gold core of 2 nm. While AuNWs in OAm ligand broke up within 1 min of electron beam irradiation, those in silica shells did not change their shape within 10 min. Likewise, OAm-capped AuNWs broke up when heated at 150 $^{\circ}\text{C}$ for 3 h while those in silica remained stable [65] (Fig. 2.12A). It remained unclear whether this stability increase is to be attributed to the confinement of the shell, the larger overall radius, or a lower surface diffusivity.

Evidence for stabilization by confinement is also provided by the experiments

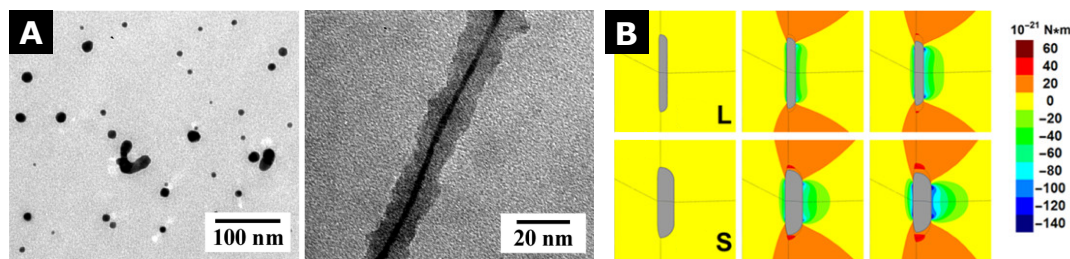


FIGURE 2.12: The Plateau-Rayleigh instability of confined nanowires. (A) AuNWs surrounded by the ligand OAm broke up into spheroidal particles (left) after 3 h of heating at 150 °C, whereas silica-coated AuNWs remained stable (right). Adapted and reprinted with permission from [65]. © 2014 American Chemical Society. (B) Mechanical stresses in an epoxy matrix around a long (L) and short (S) nanorod of the same diameter, caused by the nanorods changing shape. Adapted and reprinted with permission from [66]. © 2018 American Chemical Society.

of Kennedy et al. [66]. They embedded PEG-coated gold nanorods (AuNRs; diameters from 10 nm to 20 nm and aspect ratios from 2.5 to 5.5) in an epoxy matrix and cross-linked the matrix. The samples were heated to temperatures between 120 °C and 200 °C, and the shape of the AuNRs was tracked by transmission extinction spectroscopy. In the initial stage, the change in shape followed the Plateau-Rayleigh instability. In the second stage, the rate of change slowed, and the shape stabilized. This effect was more pronounced in stiffer polymer matrices (see Fig. 2.12B for a visualization of the stresses), indicating a relation between shape stability and confinement.

Mechanical stresses between the nanowire and a confining shell influence the Rayleigh-Plateau instability, too. Schmidt, McIntyre, and Gösele [224] analyzed shape stability in core-shell nanowires with a misfit strain between core and shell subjected to axisymmetric and higher-order perturbations. In core-shell nanowires with a positive misfit parameter (e.g., Ge shell on Si core), the zeroth-order perturbation always grew fastest, eventually leading to break-up. Higher-order modes could dominate in nanowires with a negative misfit parameter (e.g., Si shell on a Ge core) when the shell was relatively thin. The misfit strain could even render thinner nanowires more stable than thicker ones and counterbalance the strong scaling of the pinch-off time with nanowire radius [224]. To sum up, there is experimental and computational evidence that confining the nanowire shape by a matrix or shell improves the nanowire's shape stability.

2.3.4 Influence of the ligand shell

The synthesis of ultrathin nanowires involving the reduction of metal or semiconductor salts requires a shape-directing ligand [33–37]. This shape-directing ligand might also influence the shape stability of one-dimensional nanomaterials. About

a dozen articles have been published on this topic since the wet chemical synthesis of ultrathin nanowires was introduced [47, 65–71, 225–228]. These range from mere speculation [90, 229, 230] to more systematic and insightful studies [47, 65, 66, 69, 70, 227].

The shape stability of ligand-coated nanowires has been studied in the context of transparent and flexible electrodes. Maurer et al. [71] created thin films of Au-NWs (diameter of 1.6 nm) by dip-coating a glass substrate. The thin films were plasma-treated to (partially) remove the OAm ligand shell. Transmission electron micrographs taken after one week showed that films without plasma treatment kept their morphology, while those with short plasma treatment (60 s) disintegrated into spheroidal nanoparticles. Maurer et al. [71] concluded that the partial removal of the ligand shell by plasma treatment of the thin films accelerates the Plateau-Rayleigh instability. Tomioka et al. [225] created electrodes from silver nanowires (diameters of 68 nm and 220 nm) surrounded by the ligand PVP. In their case, plasma treatment of 30 s improved the shape stability of the electrodes, and they concluded that the removal of PVP must have lowered the surface energy of the silver nanowires.

Covering such nanowire electrodes with additional ligands can increase their shape stability [226]. For example, Kwan, Le, and Huan [226] covered silver nanowires (diameter of 100 nm) with a mixture of graphene oxide and ascorbic acid and observed that their electrical resistance at elevated temperatures of 573 K increased at a slower rate than the resistance of uncovered electrodes. It is unclear whether this effect was due to the graphene oxide layer or the ascorbic acid acting as a ligand.

Other studies directly manipulated the ligand shell. Nough et al. [47] exchanged the ligand OAm surrounding ultrathin AuNWs (diameter of 1.6 nm) with TOP and TOPO. The nanowires stabilized by OAm completely broke up into spheroidal nanoparticles after storage at room temperature for a duration of 13 d while those stabilized by TOP and TOPO maintained their cylindrical shape, see TEMs in Fig. 2.13A.

Not all ligand exchanges were successful. Nanowires broke into spheroidal nanoparticles when attempting to exchange the ligand with thiols such as 1-dodecanethiol or 3-mercaptopropanoic acid [47, 65, 67]. Interestingly, break-up with 3-mercaptopropanoic acid was only observed at large ligand concentrations [65]. Maturi et al. [68] managed to exchange OAm for the thiol ethyl 11-(4-mercaptobenzamido) undecanoate, which increased the shape stability in tetrahydrofuran at 25 °C. These findings clearly show that the type of ligand matters and can either stabilize or destabilize the nanowire shape. Yet, it remains unclear which properties of the ligand determined the shape stability (e.g., adsorption chemistry and bond strength, ligand tail steric, compatibility with solvent, stronger bundling of nanowires, etc.).

Similar findings were made by Imura et al. [65] and Wu et al. [227]. Imura et al.

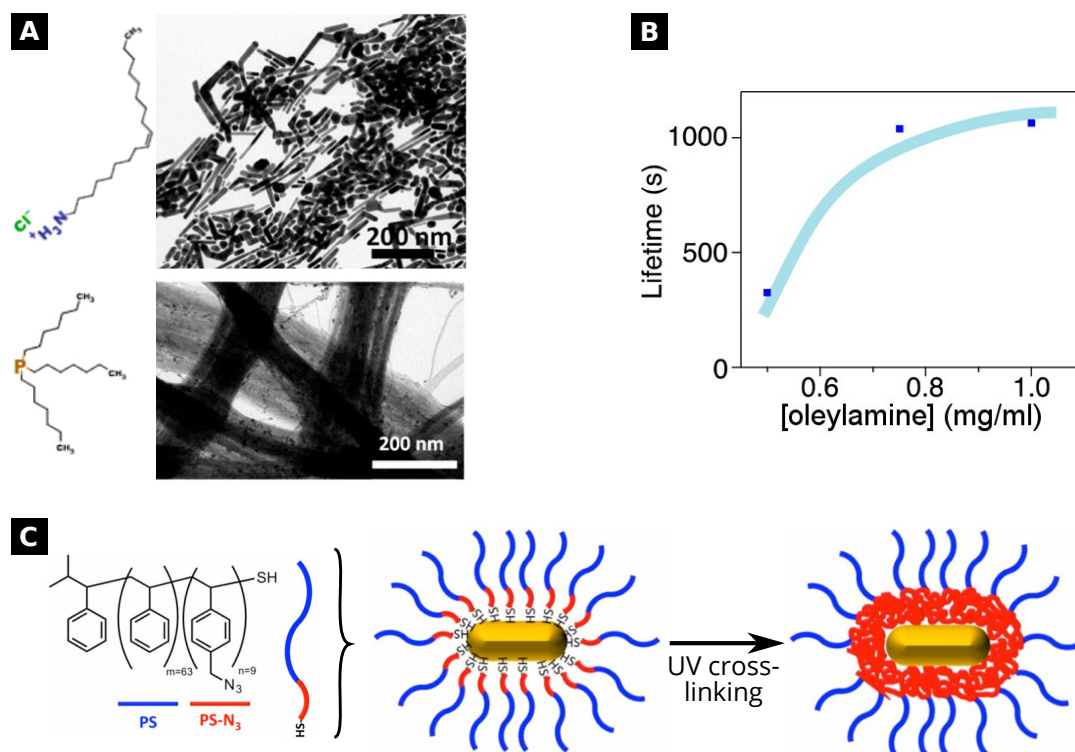


FIGURE 2.13: Known influences of the ligand shell on the Plateau-Rayleigh instability of ultrathin nanowires and nanorods. (A) Exchanging the ligand oleylammonium chloride on AuNWs with trioctylphosphine increased shape stability. Adapted and reprinted with permission from [47]. © 2017 American Chemical Society. (B) Increasing the ligand concentration in dispersion rendered the ligand shell around AuNRs denser and the AuNRs more stable. Adapted and reprinted with permission from [69]. © 2016 American Chemical Society. (C) Stiffening the ligand shell by cross-linking the ligands slowed surface diffusion and the rate of shape change. Adapted and reprinted with permission from [70]. © 2015 Wiley Periodicals, Inc.

[65] synthesized ultrathin AuNWs with a custom-made, water-soluble, long-chain amidoamine ligand and observed shape stability in dependence of pH. AuNWs remained stable under basic but not acidic conditions. They attributed this difference in stability to a change in the ligand shell structure induced by protonation of the ligand [65].

Additionally, the ligand (or at least the surface chemistry) might also influence the crystal structure of the nanowire core and, therefore, indirectly influence the shape stability. Wu et al. [227] synthesized ultrathin AuNWs (diameter of 2 nm) following two different recipes; the prevailing recipe using OAm [33–37] and an adapted recipe using CO gas. Electron beam bombardment and heating of the dispersion at 60 °C revealed that the AuNWs made with CO gas were more stable. Wu et al. [227] argued that the increase in stability stems from the AuNWs made with CO gas being bound by stable 111 crystal facets whereas 100 crystal facets bound the others. The stable 111 facets must have emerged thanks to the synthesis, the adsorption chemistry between ligand and core, or both [227].

Relatively direct evidence of the stabilizing effect of the ligand shell can also be found in the MD simulations run by Huber et al. [228]. They investigated whether adsorbing model ligands (*n*-aminopentane with tunable adsorption energies) onto AuNWs (diameter of 2 nm and length of 40 nm) influences the melting point depression known in various nanostructures [231, 232]. An uncovered nanowire melted at approximately 750 K. Adsorbing a monolayer of the model ligand onto the AuNWs increased the melting temperature by 200 K to 300 K, given that the adsorption energy was at least 4.5 kcal/mol. The effect of an increased melting temperature was attributed to the ligand suppressing the surface diffusion of gold atoms, which would also slow down the Plateau-Rayleigh instability.

The density of the ligand shell also influences shape stability. Takahata et al. [69] observed the break-up of AuNRs (diameter of 2 nm and length of 6 nm) with a ligand shell of OAm. The AuNRs were dispersed in chloroform enriched with varying amounts of OAm, heated to temperatures from 70 °C to 100 °C, and their shape evolution was followed by TEM and ultraviolet-visible spectroscopy (UV-vis). The AuNRs in dispersions with an amount of 1.0 mg/mL of added OAm were stable three times as long as those with an amount of only 0.5 mg/mL (Fig. 2.13B). Takahata et al. [69] argued that increasing the ligand concentration shifts the chemical equilibrium between unbound and adsorbed ligands so that the density of the ligand shell increases. Such a denser ligand shell then enhances the shape stability of AuNRs [69].

Finally, the mechanical stiffness of the ligand shell is known to influence the shape stability. Danielsen, Choi, and Composto [70] observed that cross-linking the ligand shell slowed the rate at which AuNRs change their shape. They grafted AuNRs (diameter from 8 nm to 15 nm and aspect ratio of 3) with poly(ethylene glycol) (PEG) and poly(styrene-*b*-azidostyrene) (P(S-*b*-S-N₃)) and dispersed them in a polymer matrix. The inner shell of the P(S-*b*-S-N₃) covered AuNRs was cross-linked by exposure to ultraviolet light (Fig. 2.13C). All samples were exposed to increased temperatures (150 °C and 200 °C), and changes in shape were monitored. The AuNRs with non-cross-linked shells changed their shape more rapidly. Kennedy et al. [66] carried out a similar experiment (already discussed in Section 2.3.3). Both groups concluded that an increase in the mechanical stiffness of the nanorods' surroundings (i.e., ligand shell or polymer matrix) slowed the surface diffusion of Au atoms and hence slowed the Plateau-Rayleigh instability.

To summarize, there is some evidence in the literature suggesting that the ligand shell influences the Plateau-Rayleigh instability in one-dimensional nanostructures and stabilizes their shape. More specifically, it is known that the type of ligand, the ligand shell density, and the mechanical stiffness of the ligand shell influence the

shape stability of ultrathin nanorods and nanowires. The mechanistic understanding of why and how this stabilization occurs is limited. For example, we do not yet understand why TOP rendered AuNWs more stable and 1-dodecanethiol less stable in the experiments of Nough et al. [47]. Is this for energetic or kinetic reasons? Moreover, is shape stability governed by the adsorption chemistry and bond strength, the ligand tail steric, the ligand-induced agglomeration of particles, or the compatibility with the solvent? Answering these questions requires further research on the shape stability of one-dimensional nanostructures.

2.4 Knowledge gaps in the state of the art and the goal of this dissertation

The above review identified knowledge gaps regarding the bundling and shape stability of ultrathin nanowires. The goal of this dissertation is to investigate the shape stability of ultrathin, ligand-coated nanowires, elucidate the mechanisms that induce the bundling of these nanowires, and assess whether bundling influences the shape stability.

Bundling is known to occur in various solvents and nanowire materials, but we do not understand why, see Fig. 2.14A. An especially intriguing example is AuNW in alkanes, where bundling was observed in *n*-hexane but not in cyclohexane. We do not yet understand the underlying physical and chemical mechanisms that elucidate the phenomena.

More specifically, we do not know the nature and strength of the interaction that drives bundling. Is the interaction driven by core-core, ligand-ligand, or ligand-solvent interactions? Is the driving force enthalpic or entropic? Is the ligand shell compressed or well-solvated inside bundles? What role plays the structure of the ligand shell, and are order-to-disorder transitions in the ligand shell such as those observed in other nanoparticle systems of similar size of importance (Section 2.2.1)? What determines the difference in interwire spacing observed in various solvents and with various ligand shells? These questions are unanswered for ultrathin nanowires in general, with AuNWs only being the most prominent example.

Our limited knowledge of the bundling mechanisms is an issue because it limits the proper processing of the nanowires. Some applications, such as stamp imprinting of AuNWs into transparent electrodes, require precise control over whether nanowires are bundled or freely dispersed [92, 233]. The ability to control the structure of a colloid is generally key to the industrial use of colloids, for example, in

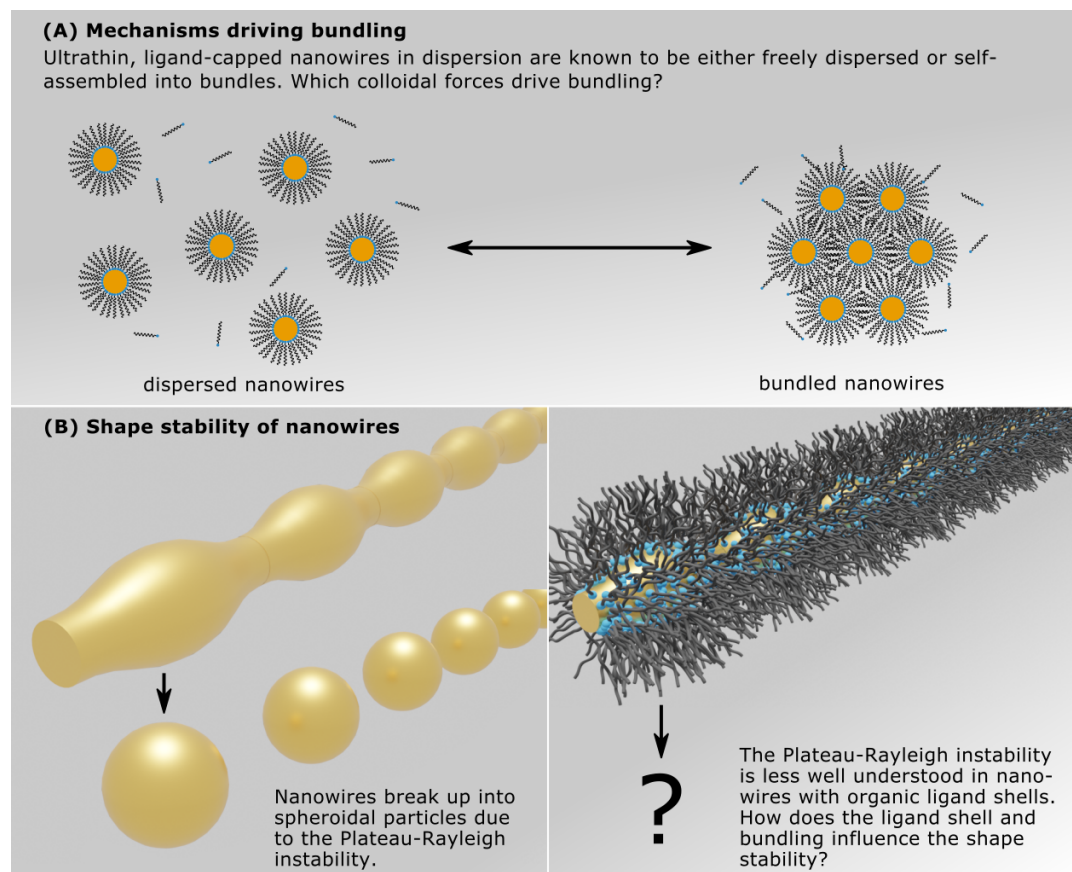


FIGURE 2.14: Knowledge gaps in the state of the art and goal of this dissertation. (A) The underlying mechanisms of bundling shall be elucidated. (B) The influence of the ligand shell and bundling on the Plateau-Rayleigh instability of ultrathin nanowires shall be studied.

paints [234]. Understanding the fundamental interactions that determine the structure of a colloid is the first step in that direction.

The first goal of this dissertation is to resolve the bundling mechanism of OAm-capped AuNWs in alcohols and alkanes. This example material was chosen for three reasons. First, it has shown interesting and inexplicable behavior as reported in the literature [44, 45]. Second, its synthesis is established and reliable. Third, it also serves as the material in the experiments on the Plateau-Rayleigh instability and allows for studying the link between colloidal and shape stability. The study of other core materials, ligands, and solvents is beyond the scope of this dissertation.

The strategy to answer these questions involves systematic experimentation using SAXS combined with MD simulations. SAXS allows probing the structure of nanowires in dispersion, including the size and lattice constant of bundles. The experiments are suitable to screen a large part of the available parameter space and modulate macroscopically available parameters such as the type of solvent, the

nanowire concentration, or the ligand concentration. The simulations allow obtaining detailed insight into the colloid on a molecular length scale and studying phenomena such as the ordering of the ligand shell and solvent. They will allow linking bundling to molecular-scale phenomena.

The second goal of this dissertation is to deepen our understanding of the Plateau-Rayleigh instability in ligand-capped nanowires. This goal is essential because any long-term use of the nanowires that relies on their cylindrical shape will remain impossible until we better understand and eventually control their break-up. The literature review shows a decent understanding of the instability in nanowires with bare metal surfaces, whereas the instability is less well understood for nanowires with an organic ligand shell, see Fig. 2.14B. For bare metal nanowires, factors such as anisotropy in the crystal structure and surface energy, the presence of a substrate, and confinement have been investigated. The few studies on ligand-capped nanowires show that the ligand shell influences shape stability, depending on the type of ligand and the density and mechanical stiffness of the ligand shell. However, it is unclear why and how these properties affect the Plateau-Rayleigh instability. We do not understand why some ligands improve and others impair shape stability (see Section 2.3.4). Is this due to the bond between core and ligand, the tail steric and packing of the ligands, or the interaction between the ligand and the solvent? Which properties would make a perfect ligand? Will the colloidal structure—whether the nanowires are bundled or freely dispersed—impact the shape stability?

The strategy for a better understanding of nanowire shape stability is to develop a continuum model that applies to various core materials and ligands and can be compared to experimental data from SAXS, TEM, and other sources. To this end, a linear perturbation analysis shall be extended to include the effects of the ligand shell. Whether bundling influences the Plateau-Rayleigh instability shall be studied experimentally by SAXS and theoretically by extending the continuum model to bundled nanowires. SAXS, along with TEM, is a suitable tool since it allows for probing the colloidal structure (bundled versus freely dispersed nanowires) and the shape of the colloids (nanowires versus spheroidal nanoparticles) at the same time. The continuum model shall be extended by incorporating the constraining effects of bundles, allowing linking experimental observation with the theoretical prediction.

Chapter 3

Results

3.1 Publication 1: Entropy can bundle nanowires in good solvents

Reprinted with permission from:

H. Gao, S. Bettscheider, T. Kraus, M.H. Müser, Entropy Can Bundle Nanowires in Good Solvents, *Nano Lett.* 19 (2019) 6993–6999. <https://doi.org/10.1021/acs.nanolett.9b02379>.

© 2019 American Chemical Society.

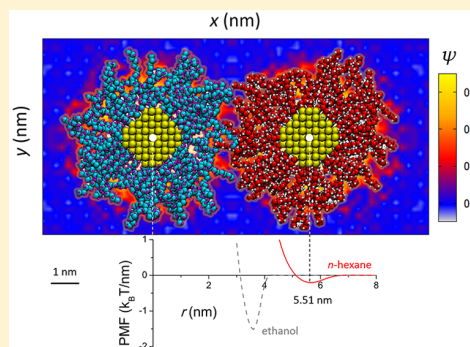
Entropy Can Bundle Nanowires in Good Solvents

Hongyu Gao,[†] Simon Bettscheider,^{‡,§} Tobias Kraus,^{‡,§} and Martin H. Müser^{*,†}[†]Department of Materials Science and Engineering, Saarland University, Campus C6 3, 66123 Saarbrücken, Germany[‡]INM – Leibniz Institute for New Materials, Campus D2 2, 66123 Saarbrücken, Germany[§]Colloid and Interface Chemistry, Saarland University, Campus D2 2, 66123 Saarbrücken, Germany

S Supporting Information

ABSTRACT: Surfaces with surface-bound ligand molecules generally attract each other when immersed in poor solvents but repel each other in good solvents. While this common wisdom holds, for example, for oleylamine-ligated ultrathin nanowires in the poor solvent ethanol, the same nanowires were recently observed experimentally to bundle even when immersed in the good solvent *n*-hexane. To elucidate the respective binding mechanisms, we simulate both systems using molecular dynamics. In the case of ethanol, the solvent is completely depleted at the interface between two ligand shells so that their binding occurs, as expected, via direct interactions between ligands. In the case of *n*-hexane, ligands attached to different nanowires do not touch. The binding occurs because solvent molecules penetrating the shells preferentially orient their backbone normal to the wire, whereby they lose entropy. This entropy does not have to be summoned a second time when the molecules penetrate another nanowire. For the mechanism to be effective, the ligand density appears to best be intermediate, that is, small enough to allow solvent molecules to penetrate, but not so small that ligands do not possess a clear preferred orientation at the interface to the solvent. At the same time, solvent molecules may be neither too large nor too small for similar reasons. Experiments complementing the simulations confirm the predicted trends.

KEYWORDS: Gold nanowires, bundle stability, agglomeration, nonpolar solvent, potential of mean force, molecular dynamics



Ultrathin gold nanowires (AuNWs) are chemically synthesized particles that exist as colloidal dispersions in apolar solvents.^{1–3} They consist of a metal gold core with a diameter as small as 1.7 nm, which is surrounded by a shell of oleylamine (OA) molecules of similar thickness. The nanowires form when gold chloride salts are reduced in the presence of OA. Their length depends on reaction time; values of up to 6.4 μm have been reported.⁴ The large aspect ratio of the wires above 10^3 and their limited bending stiffness lead to an unusual type of agglomeration: the wires can spontaneously self-assemble into bundles. This was first observed in the original synthesis of AuNWs^{5,6} and studied in more detail by Loubat et al.⁷ The bundles that formed in the presence of excess OA from synthesis exhibited a hexagonal arrangement of 10–100 parallel AuNWs that were separated by two double layers of OA at a wire–wire distance of 9.7 nm.

Nanowire bundling has interesting technological implications. For example, Liz-Marzan and co-workers used the formation of AuNW networks to create disordered, conductive meshes at a gas–liquid interfaces, which they deemed suitable as transparent conductive electrodes.⁸ Maurer et al. used an elastomer stamp to direct the bundling wires into regular meshes, which were applicable for touch-screen devices,^{9,10} while Gong et al. casted electrode patterns of nanowire bundles onto a glove to create a wearable strain sensor.¹¹ It is even possible to extrude or “spin” the wires into macroscopic fibers

with mechanical properties that depend on the degree of shear alignment.¹²

While much phenomenology is known about the bundling of nanowires, our present understanding of the bundling mechanism is rather limited. For example, Reiser et al.¹³ systematically altered the solvent and showed that purified AuNWs in *n*-hexane packed more densely (wire–wire distance of 5.5 nm) than as-synthesized AuNWs with only two sheets of OA in between their gold core surfaces.¹³ Even tighter bundles were identified by Reiser et al.¹² when AuNWs were dispersed in polar solvents such as ethanol. Tighter bundles also formed when the ligand OA was replaced by the shorter trioctylphosphine as demonstrated by Nouh et al.¹⁴ No ordered bundling was observed when purified AuNWs were redispersed in apolar cyclohexane.¹³

Little is known about the molecular origin of the exact spacing and its dependence on the solvent and its quality. Most importantly, it is not understood why AuNWs sometimes bundle in good solvents and sometimes do not. The shape of the wires apparently plays a role. Spherical gold nanoparticles coated with OA are stable against agglomeration in *n*-hexane even if the gold cores are as large as 12 nm.^{15–18} Reiser and

Received: June 12, 2019

Revised: September 18, 2019

Published: September 19, 2019

coauthors suggested a “supramolecular” origin of bundling.¹³ Despite its appeal, this argument is somewhat vague.

The binding mechanism in our system of interest can certainly not be fully explained in terms of usually successful coarse-graining approaches casting the effect of good solvents as two-body repulsion between monomers.¹⁹ We believe that it belongs to the cases where an effective modeling of intricate solvent-induced phenomena requires the solvent to be treated explicitly. Examples include cononsolvency,²⁰ nanoparticles in binary solvent mixtures,²¹ and an almost perfectly suppressed interdigitation of solvated hydrophobic and solvated hydrophilic polymer brushes.²² We therefore run large-scale, explicit-solvent simulations of our system of interest. In order to acquire reliable potentials of mean force (per unit length) between two nanowires in good and poor solvents alike, the umbrella sampling strategy was adopted.

Methodology. Molecular dynamics (MD) simulations were carried out based on a representative model system shown in Figure 1, where two identical AuNWs, each grafted

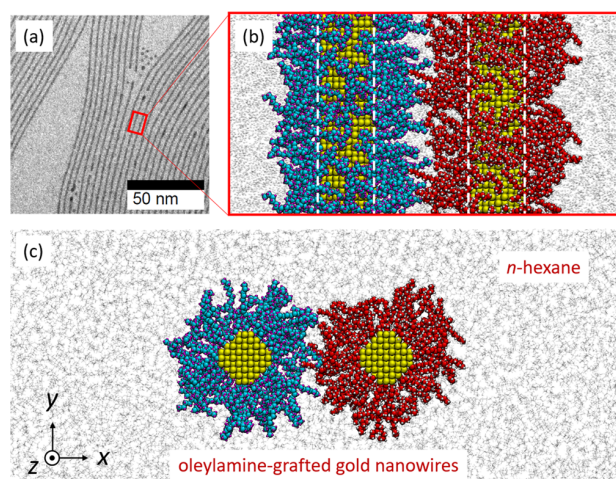


Figure 1. (a) TEM micrograph of bundled ultrathin AuNWs. (b,c) Projections of representative MD configurations for near-equilibrium spacings onto (b) the xz -plane and (c) the xy -plane. n -Hexane is the solvent in both cases. (Au: gold; OA C/H: blue/purple on the left wire and red/white on the right wire; and n -hexane: gray). Periodic box dimensions are $l_x = 24.6$ nm, $l_y = 9.0$ nm, and $l_z = 3.3$ nm.

with 62 ligand molecules (OA), were embedded in a n -hexane (or an ethanol) solvent. The central cylindrical Au wires with 0.85 nm radius and 3.01 nm length were treated as rigid bodies throughout the simulation, because bending, for example, induced by thermal fluctuations, is negligible on the nanometer scale. Both NWs were oriented parallel to the z -axis, one was fixed in space, while the other one was free to move along the x - and z -axes as well as to rotate about its symmetry axis. As mentioned again further below, periodic boundary conditions were used in all three spatial dimensions to eliminate wire-end effects.

To effectively deduce pairwise interactions between bundled AuNWs, only two NWs were included. While three-wire (and higher-order wire) interactions may slightly change the interactions between wires on a triangular lattice, significant many-body interactions require the soft shell to be small compared to the rigid core.²³ Moreover, the simulations are already very demanding for dimers because of the used realistic

all-atom force field. This is why it is scarcely feasible at this point to reliably compute the expectedly small many-wire corrections to construct accurate many-wire free-energy surfaces.

Ligands were randomly distributed on the Au wire surfaces with a mean grafting density of approximately 3.8 ligands/nm², which falls into the range of typical experimental values.^{24,25} When a new anchoring site was drawn, a constraint ensured that the new site had a distance of at least 0.47 nm to all pre-existing anchoring atoms, so that nearest-neighbor Au atoms could not be simultaneously anchoring sites. Periodic boundary conditions were applied at the boundaries of the simulation domain (Figure 1) in all three spatial directions. This way, the wires had neither beginning nor end. The size of the simulation cell was 24.6 nm in x and 9 nm in y direction. This geometry certainly provides a sufficiently large buffer to suppress any noticeable interaction between the wire pair and its periodic images, at least for the given maximum distance of the wires of $\Delta x_{\max} \approx 8$ nm.

A key assumption of our model is that the amine end of a ligand is connected to the Au surface by a strong permanent bond. Such an arrangement should not affect the results very much as long as bonds between the amine groups and the front gold atoms are sufficiently strong²⁶ so that the coverage density remains constant. Due to the lack of well-tested interatomic potentials between gold atoms and amine groups, and due to the close-packed structure of gold atoms on the surface, we took the liberty of describing the bonds between them with the same set of parameters as between two methylene groups. This imposes no preferred bond angles on the gold atoms, but a tetrahedral bond angle on the amine group. As the ligands are relatively long, we do not expect it to be important to work with a more realistic bond angle on the amine group.

The wire–wire radial distribution function $g(r)$ —from which the potential of mean force $F(r)$ follows—was obtained by monitoring the thermal fluctuations of the interwire spacing after equilibration had occurred. This was done with umbrella sampling. Specifically, in order to acquire good statistics for all (relevant) distances, a harmonic biasing potential

$$V_{\text{bias}} = \frac{k}{2}(r - r_s)^2 \quad (1)$$

was applied, where k is the spring constant and r_s the equilibrium distance between the center of masses of the two wires. The effect of the biasing spring was subtracted from the construction of the “real” two-body (free) energy through

$$F(r) = F_0(r_s) - k_B T \ln g(r, r_s) - V_{\text{bias}}(r, r_s) \quad (2)$$

where $F_0(r_s)$ is an offset, T is the temperature of the system, $g(r, r_s)$ is the radial distribution function for the given value of r_s , and k_B is the Boltzmann constant. For reasons of completeness, it shall be mentioned that the spring constant was finalized as $k = 0.07$ N/m after multiple attempts on its effectiveness. Moreover, six different equilibrium spring positions r_s were investigated, where adjacent ones were separated by 0.4–0.6 nm.

The temperature and pressure of the system were maintained at 330 K and 1 bar, respectively, using an isothermal–isobaric (NPT) ensemble with an integration time step of 1 fs. The temperature was slightly (10%) higher than that in the experiment (i.e., room temperature) so as to achieve better sampling by reducing the viscosity of the solution. Since both investigated solvents are far away from a

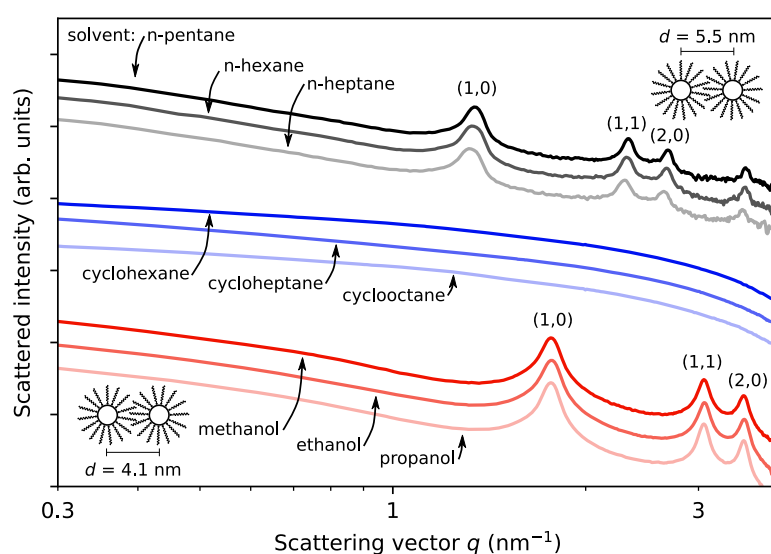


Figure 2. SAXS signals for AuNWs dispersed in linear alkanes (upper, gray curves), cycloalkanes (middle, blue curves), and alcohols (lower, red curves) with the lattice indices indicated above the corresponding Bragg reflection peaks. Wire–wire distances of 5.5 and 4.1 nm are found for the linear alkanes and alcohols, respectively. In cycloalkanes, ordering is not observed.

phase transition and no order–disorder transition has been reported on grafted OA (signs of any such transformation are missing in the simulations), $F(r)$ should only weakly depend on temperature. Thus, results for $F(r)$ at the laboratory temperature of $T \approx 300$ K must be similar to those at the simulation temperature of $T = 330$ K.

For each value of r_s , the system was found to have equilibrated within the first 1 ns of simulation time. Each equilibration was followed by another 200 ns simulation, over which data were collected for postprocessing. Interactions within the system were described using the all-atom OPLS force field.²⁷ The used parameters are provided in the [Supporting Information \(SI\)](#). All the simulations were carried out using the open-source MD code LAMMPS.²⁸

We evaluated the spacing of the wires experimentally using a previously published method in order to verify the measured values and to extend the range of solvents. Details can be found in the [SI](#).

Results and Discussion. Experimental Results of Nano-wire Spacing. In order to qualitatively assess the structure of AuNWs in the two solvents, small-angle X-ray scattering (SAXS) measurements were performed 24 h after redispersion in the desired solvent. Given the results of Reiser et al.,¹³ this period is sufficient for the AuNWs to reach their equilibrium arrangement. The SAXS curves shown in [Figure 2](#) for linear alkanes and alcohols show distinct Bragg peaks. No Bragg reflections can be observed for AuNWs dispersed in cycloalkanes. (The measurements in here were taken at a nominal Au concentration of 30 mmol L⁻¹. For lower concentrations, small reflection peaks could be observed. We plan to investigate this phenomenon in upcoming work.) The relative position of these peaks reveals that the wires condense into a hexagonal lattice. We calculate the lattice parameter, that is, the wire–wire distance by extracting the q -vector of the local maxima in the SAXS curves and applying [eq. 2 in the SI](#). In alkanes, wire–wire distances of 5.42, 5.47, and 5.52 nm arose for *n*-pentane, *n*-hexane, and *n*-heptane, respectively. For alcohols, we found a unique (within experimental uncertainties of 0.01 nm) value of 4.11 nm for methanol, ethanol, and 1-

propanol. (Measurements of AuNWs in ethanol were already performed in earlier work.¹² The SAXS data that we report here match the previously published data. Note that the analysis of the SAXS data in ref 12 of the wire–wire distance in ethanol contains a typo and was incorrectly stated as 3.5 nm, where the correct value is 4.1 nm, consistent with the analysis reported here.)

A comparison with the size of the AuNWs can help to interpret this result. The AuNWs have a core diameter of approximately 1.7 nm and a shell of OA molecules that have a length of ca. 2 nm in their fully stretched configuration (see the [first](#) section of the paper). Two layers of fully extended OA between the gold cores yield a wire–wire distance of 5.7 nm, which is close to the value measured in alkanes. A single layer of OA would result in a wire–wire distance of 3.7 nm, which is close to the value that we found for the alcohols. This suggests that the OA ligands barely interdigitate when in contact with *n*-hexane, but almost fully interdigitate when dispersed in ethanol. The degree of interdigitation in linear alkanes depends on the alkane length and increases by about 1 Å from *n*-pentane to *n*-heptane. This is on the order of magnitude of a C–C bond, for a solvent length increase by two C–C bonds. Further experiments and simulations are planned to investigate this interesting trend.

Because the AuNWs are fragile and can be prone to Rayleigh–Plateau instabilities,^{29–32} we investigated their quality after the SAXS experiments by transmission electron microscopy (TEM). Results demonstrating the stability of the AuNWs are shown in [Figure S1](#) of the [Supporting Information](#).

Potential of Mean Force and Interwire Distance. Equilibrium MD simulations based on the model system shown in [Figure 1](#) were carried out at each given equilibrium spring length r_s . As discussed in the [Methodology](#) section, separate simulations with different r_s can be effective in exploring the phase space that is poorly sampled in thermal equilibrium. Averaging over 200 ns is sufficient to achieve reliable statistics for each value of r_s . A probability density distribution of dynamic interwire spacing, $\text{Pr}(r)$, can thus be

determined as data points shown in Figure 3, with peaks close to r_s .

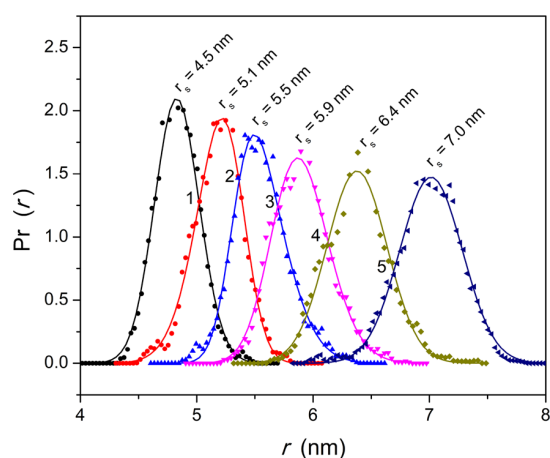


Figure 3. Probability densities of interwire distance in *n*-hexane for cases of varied spring equilibrium distances (differentiated by colors). MD results are shown with symbols, to which $\text{Pr}(r)$ (solid curves) were fitted with a SND function.

For each value of r_s , the normalized $\text{Pr}(r)$ was fitted with a skew normal distribution (SND) function,³³ defined by

$$\text{Pr}_{\text{SND}}(r, \sigma, \mu, \alpha) \equiv \frac{2}{\sigma} \cdot \phi\left(\frac{r - \mu}{\sigma}\right) \cdot \Phi\left[\frac{\alpha(r - \mu)}{\sigma}\right] \quad (3)$$

where $\phi(x) \equiv \exp(-x^2/2)/\sqrt{2\pi}$ is the standard Gaussian, $\Phi(x) \equiv [1 + \text{erf}(x/\sqrt{2})]/2$ is a cumulative distribution function, $\text{erf}(x/\sqrt{2})$ is the error function, and α is a shape parameter, which is greater (or less) than zero if the distribution is right (or left) skewed. SND is better for our purpose than conventional Gaussians because the asymmetry (or skewness) of a distribution can be captured in leading order. Both the MD-derived $\text{Pr}(r)$ (data points) and the results from SND fitting (solid curves) are shown in Figure 3 for *n*-hexane; the corresponding fitting parameters are listed in Table 1. For a given value of r , the data set, for which the fit to

Table 1. Fitted SND Parameters

	r_s (nm)					
<i>n</i> -hexane	4.7	5.1	5.5	5.9	6.4	7.0
μ (nm)	4.75	5.37	5.32	5.70	6.36	6.99
σ (nm)	0.21	0.28	0.32	0.32	0.26	0.27
α (-)	0.57	-1.58	2.05	1.26	0.10	0.13
	r_s (nm)					
ethanol	3.15	5.1	3.95	4.35		
μ (nm)	3.15	3.41	3.73	4.02		
σ (nm)	0.19	0.23	0.18	0.17		
α (-)	1.79	2.74	1.53	1.37		

$\text{Pr}(r, r_s)$ turned out largest, was selected to be the relevant data set at the value of r in the construction of the combined $F(r)$.

A potential of mean force (PMF) for the wire–wire separation was deduced from the various $\text{Pr}(r)$ according to eq 2. Note that, for reasons of simplicity, the abbreviation PMF is used, irrespective of whether or not the energy is normalized to length. The offsets $F_0(r_s)$ were chosen such that the

combined $F(r)$ was a smooth function in r while obeying the boundary condition $F(r \rightarrow \infty) \rightarrow 0$. The ultimate PMF was obtained by fitting the combined $F(r)$ with the following function:

$$W(r) = V_{\text{rep}} \exp\left(-\frac{r}{\rho_{\text{rep}}}\right) - V_{\text{adh}} \left[1 - \text{erf}\left(\frac{r - r_{\text{adh}}}{\rho_{\text{adh}}}\right)\right] \quad (4)$$

where V , ρ , and r_{adh} are fitting parameters. This potential outperformed all other tested two-body potentials. For example, fits to the data using eq 4 resulted in lower standard deviations (27% and 68% lower in the cases of *n*-hexane and ethanol, respectively) compared to Mie potentials with the form of $V(r) = \epsilon[n(\zeta/r)^m - m(\zeta/r)^n]/(m - n)$, where ϵ is the binding energy, ζ is the equilibrium distance, and m and n are adjustable parameters.

Figure 4 shows the PMFs for both solvents, *n*-hexane and ethanol. The NWs immersed in good solvents reveal a

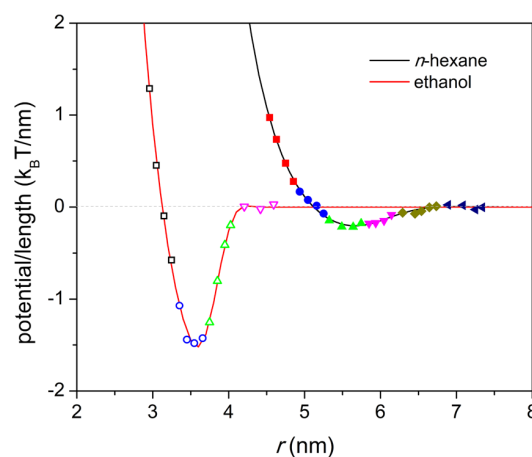


Figure 4. PMF per unit length for wire–wire interaction in *n*-hexane and ethanol (data points—converted MD results with colors identifying various r_s s, solid lines—fitted PMFs). Fitting parameters can be found in Table 2. Note that $k_B T$ in this graph refers to the thermal energy at room temperature and not to $T = 330$ K used in the simulations.

distinctly smaller minimum in $W(r)$ at a larger separation r_{min} compared to the poor solvent. The observed trends reflect those seen in reported data and a small set of new experiments, which was conducted to accompany the simulations and to assess the effect of solvents on interwire distance. In the experiments, the wires were carefully purified according to the protocols established in the literature (see experimental details in the SI and e.g., refs 13, 14, and 34) to exclude effects of excess OA, which is known to strongly affect spacing. Care was taken not to desorb too much OA, which would reduce the ligand shell density and could also affect the spacing. The distances between the wires were then reconstructed in different solvents using SAXS, radial integration, and fitting.

The simulations find $\leq 15\%$ smaller spacings between NWs in ethanol than the experiments, specifically, 3.55 nm versus 4.10 nm (see Figure 2). For *n*-hexane, the spacings even turn out almost identically, that is, 5.51 nm (simulations) and 5.50 nm (experiments). Discrepancies of the order 20% between simulations and experiments are expected most notably because of differences in the grafting densities. The

value of 3.8 ligands/nm² used in the simulations falls within the range of experimental estimates (2–8 ligands/nm²),^{25,35,36} which suffer from a large degree of currently unavoidable uncertainty.³⁶ This uncertainty cannot be eliminated experimentally because there is no technique available that would provide the ligand density of individual wires and because it is unknown how broad the standard deviation of the density over many wires is. Inaccuracies in the simulations result from the simplified treatment of the Au–N bond between the ligand and the core and, more generally, from small imprecisions in the used potential energy surface, which is scarcely ever exact. Thus, the extremely good agreement for the NW spacing in *n*-hexane is certainly fortuitous to some degree. We would yet argue that the simulations certainly reproduce the trends correctly for the right reason. This does not only include the location of the (free-) energy minima but also their depths. Spheres with a radius *R* similar to that of the simulated wires agglomerate in the poor solvent ethanol, while they are stable against agglomeration in *n*-hexane.¹⁷ This is consistent with our values for the depth of the free-energy line density of wires with $R \approx 1.6$ nm, which is $1.52 k_B T/\text{nm}$ for ethanol but only $0.20 k_B T/\text{nm}$ for *n*-hexane.

Table 2. Fitted PMF Parameters

	V_{rep} ($k_B K/\text{nm}$)	ρ_{rep} (nm)	V_{adh} ($k_B K/\text{nm}$)	r_{adh} (nm)	ρ_{adh} (nm)
<i>n</i> -hexane	7.23×10^6	0.47	65.78	6.02	0.55
ethanol	1.55×10^6	0.42	398.03	3.84	0.25

Molecular Morphology. In order to understand the underlying molecular origins of bundling in both solvents,

we studied the morphology of both ligand and solvent molecules. To this end, the systems were simulated at their equilibrium interwire distance over a period of 20 ns.

Snapshots of the MD simulations are shown in Figure 5a,b. They indicate that the ligand shells strongly interdigitate in the case of ethanol but barely touch in *n*-hexane. This can be seen more clearly in the quantitative contour plots in Figure 5c–f, which show the density of ligand (c,d) and solvent (e,f) atoms projected onto the *xy*-plane.

The polar solvent ethanol is completely expelled from the interface between the two nanowires (Figure 5e), and the interdigitated ligands within the interface exhibit the largest atom densities throughout the simulations (see Figure 5c and Figure S2 in the SI). The two-dimensional (2D) radius of gyration (R_g) of the ligands is shorter in ethanol ($R_g = 4.69$ Å) than in the good solvent *n*-hexane ($R_g = 4.93$ Å). Note that the surface-to-surface separation of the nanowires is only about 1.9 nm, approximately the length of one OA ligand molecule. Bundling in ethanol is driven by minimizing the interfacial area between polar and apolar phases.

In the apolar solvent *n*-hexane, Figure 5d,f reveals that the ligand shells of two neighboring nanowires do not touch. There is enough space in between the ligand shells for at least one layer of *n*-hexane molecules. Furthermore, solvent molecules penetrate the shell (Figure 5f), which is in line with the notion that *n*-hexane is a good solvent for OA grafted nanowires. For the case of *n*-hexane, the formation of bundles cannot be explained by “classic” colloidal interaction potentials such as the interplay between attractive van der Waals forces and repulsive steric forces.^{37–39} The increased equilibrium separation between the wires cannot be due to swelling by the

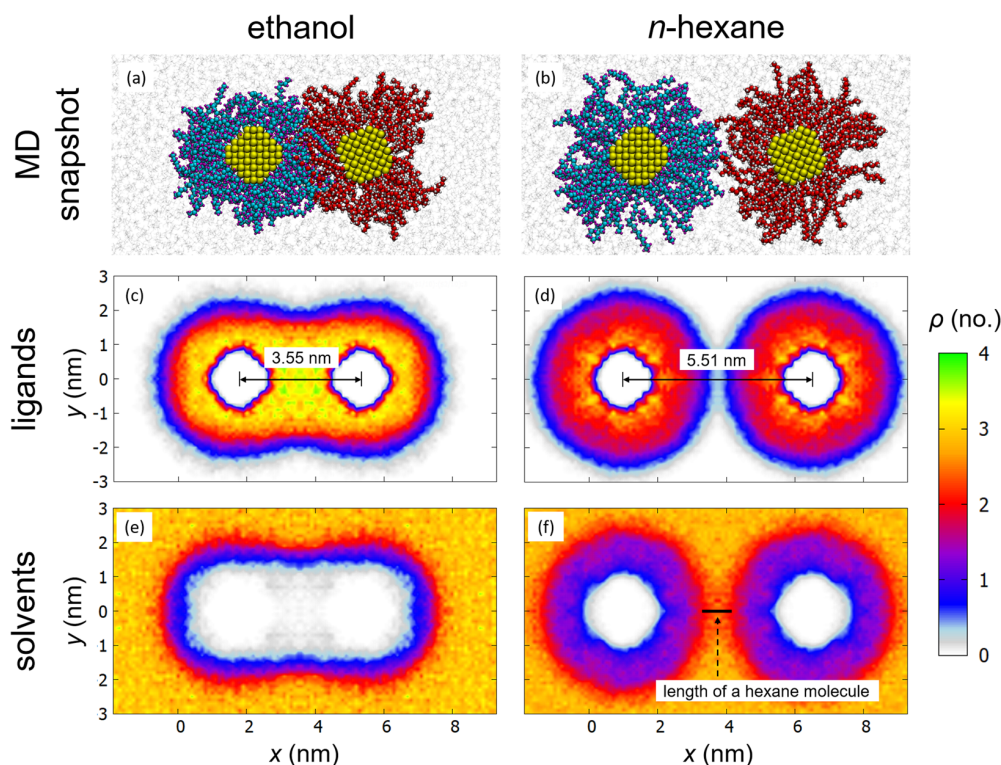


Figure 5. Representative snapshots of the MD simulations in (a) ethanol and (b) *n*-hexane and projected atom number densities of (c,d) the ligands and (e,f) the solvent molecules; ρ is with respect to each bin with dimensions of $0.1 \times 0.1 \times l_z$ nm³.

good solvent, either. Replacing ethanol with *n*-hexane leads to a swelling of the ligand shells by $<2 \text{ \AA}$, which certainly does not explain the increase of almost 1.5 nm that we observe.

To elucidate the role of *n*-hexane molecules in between two nanowires, we studied their degree of order with Herman's orientation function ψ_i , defined as

$$\psi_i = \frac{3}{2} \left\langle (\hat{n}_{\text{EE}}^i \times \hat{n}_{\text{COM}}^i)^2 - \frac{1}{3} \right\rangle$$

where \hat{n}_{EE} is a unit vector from one end-carbon to the other end-carbon of a solvent molecule, and \hat{n}_{COM} is a unit vector from the center of the closer nanowire to the center of that molecule. This defines ψ ranging from -0.5 to 1 , where $\psi = -0.5$ when the director \hat{n}_{EE} is perpendicular to \hat{n}_{COM} and $\psi = 1$ when $\hat{n}_{\text{EE}} \parallel \hat{n}_{\text{COM}}$. Random orientation as it occurs in the liquid phase leads to $\psi = 0$. However, other distributions may also lead to $\psi = 0$.

Figure 6 shows ψ obtained for *n*-hexane by averaging over the *z*-direction and a period of 20 ns. In the bulk solvent, *n*-

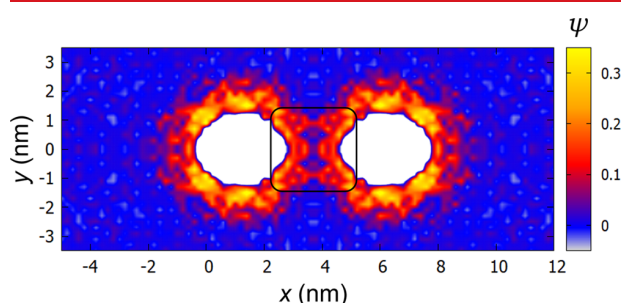


Figure 6. Contour plot of the orientational order parameter ψ evaluated for *n*-hexane molecules and projected onto the *xy*-plane. A value of ψ exceeding zero indicates a preferential orientation perpendicular to the nearest wire surface, while negative values indicate a preferential parallel orientation.

hexane molecules are randomly distributed. Within the ligand shell and in its direct proximity, $\psi_i > 0$, indicating that *n*-hexane molecules have a tendency to align their backbone normal to the Au surface. Oriented solvent molecules “bridge” the space in between the nanowires that is highlighted by the black frame in Figure 6.

Ordering of the solvent is associated with a decrease in entropy. This decrease in entropy must be the reason for bundle formation. Nanowires bundle in *n*-hexane because they can “share” ordered solvent. If the nanowires remained dispersed, solvent would have to be ordered around each nanowire and the decrease in entropy would scale linearly with the length and number of nanowires. By forming bundles, solvent in between the nanowires only needs to be ordered once, and the system can keep a larger fraction of solvent in an disordered, high-entropy state.

Conclusions. It is rare to find that local solvent ordering induces the agglomeration of colloidal particles. In classical theory, the “combinatorial” (purely entropic) contribution to the total free energy of solvent and ligand molecules in a dispersion is assumed to always increase with decreasing particle separation, because removing solvent from stabilizing shells decreases entropy. This is usually the dominating stabilizing term for nonaqueous dispersions.⁴⁰

The line contact between the very thin wires used here makes it possible for solvent molecules to “bridge” two ligand

shells along many micrometers. The persistence length of the wires is on the order of $10 \mu\text{m}$ and keeps them locally parallel. The free energy gain associated with the entropic bundling mechanism is on the order of $0.2 k_{\text{B}}T/\text{nm}$. This is sufficient to stabilize dimers of wires that are longer than 100 nm. This bridging over a line contact is geometrically impossible for small spheres. A similar mechanism may exist in planar contacts, although the constraints of packing may reduce the order in a hypothetical single solvent layer between two planes, depending on the ligand structure. It would be interesting to explore this possibility in apolar dispersions of 2D materials such as nanoplatelets.⁴¹ Aside from the contact having to be elongated for the mechanism to be effective, an intermediate density of the ligands near the outer shell appears to be beneficial. If the ligand shell was too dense, only a few solvent molecules could interdigitate into the shell and the entropy loss due to ordering of the solvent would be negligible. On the other hand, if the ligand shell was too sparse, the ligands would supposedly not possess a preferential alignment and hence might not order the solvent.

The existence of this bundling mechanism has several practical implications. Local order is sensitive to the exact molecular structure of the solvent, and one would expect large differences in colloidal stability for solvents that have similar bulk properties but different molecular structures such as *n*-hexane and cyclohexane. This should make it possible to precisely tune the spacing between wires and thus control their coupling, for example, to control the fluorescence of semiconductor nanowires,^{42,43} tune charge carrier tunneling between metal nanowires,⁴⁴ or modulate the mechanical properties of fibers made from nanowires.¹²

If bundling is undesirable, it will be useful to perturb the order of the solvent layer and suppress entropic bundling. Recent results on the stability of spherical nanoparticles suggest that this may be possible by using suitable ligand molecules.⁴⁵

■ ASSOCIATED CONTENT

Supporting Information

The Supporting Information is available free of charge on the ACS Publications website at DOI: 10.1021/acs.nanolett.9b02379.

Experimental methods and chemicals used, OPLS-AA force field parameters, transmission electron micrographs of AuNWs after SAXS analysis, radial probability density distribution of ligands calculated from the MD simulations (PDF)

■ AUTHOR INFORMATION

Corresponding Author

*E-mail: martin.mueser@mx.uni-saarland.de. Phone: +49 681 302 57452. Fax: +49 681 302 57454.

ORCID

Hongyu Gao: 0000-0003-0695-0122

Simon Bettscheider: 0000-0001-6068-246X

Tobias Kraus: 0000-0003-2951-1704

Notes

The authors declare no competing financial interest.

ACKNOWLEDGMENTS

The authors gratefully acknowledge the Gauss Centre for Supercomputing e.V. (www.gauss-centre.eu) for funding this project by providing computing time through the John von Neumann Institute for Computing (NIC) on the GCS Supercomputer JUQUEEN at Jülich Supercomputing Center (JSC). H.G. thanks the Alexander von Humboldt Foundation for the research fellowship. S.B. thanks the Foundation of German Business for his Ph.D. scholarship. The authors would like to thank Lukas F. Engel for help with the synthesis of gold nanowires, Anna Zimmermann and David Doblas Jiménez for support in acquiring SAXS measurements, and Lola González-García for recording TEM micrographs. Vikrant Naik is acknowledged for fruitful discussions.

REFERENCES

- (1) Halder, A.; Ravishankar, N. *Adv. Mater.* **2007**, *19*, 1854–1858.
- (2) Huo, Z.; Tsung, C.-k.; Huang, W.; Zhang, X.; Yang, P. *Nano Lett.* **2008**, *8*, 2041–2044.
- (3) Wang, C.; Hu, Y.; Lieber, C. M.; Sun, S. *J. Am. Chem. Soc.* **2008**, *130*, 8902–8903.
- (4) Saitoh, M.; Kashiwagi, Y.; Chigane, M. *Soft Matter* **2017**, *13*, 3927–3935.
- (5) Lu, X.; Yavuz, M. S.; Tuan, H.-Y.; Korgel, B. A.; Xia, Y. *J. Am. Chem. Soc.* **2008**, *130*, 8900–8901.
- (6) Feng, H.; Yang, Y.; You, Y.; Li, G.; Guo, J.; Yu, T.; Shen, Z.; Wu, T.; Xing, B. *Chem. Commun.* **2009**, *0*, 1984–1986.
- (7) Loubat, A.; Impéror-Clerc, M.; Pansu, B.; Meneau, F.; Raquet, B.; Viau, G.; Lacroix, L.-M. *Langmuir* **2014**, *30*, 4005–4012.
- (8) Sánchez-Iglesias, A.; Rivas-Murias, B.; Grzelczak, M.; Perez-Juste, J.; Liz-Marzán, L. M.; Rivadulla, F.; Correa-Duarte, M. A. *Nano Lett.* **2012**, *12*, 6066–6070.
- (9) Maurer, J. H. M.; González-García, L.; Reiser, B.; Kanelidis, I.; Kraus, T. *Nano Lett.* **2016**, *16*, 2921–2925.
- (10) Maurer, J. H. M.; González-García, L.; Backes, I. K.; Reiser, B.; Schlossberg, S. M.; Kraus, T. *Adv. Mater. Technol.* **2017**, *2*, 1700034.
- (11) Gong, S.; Lai, D. T.; Wang, Y.; Yap, L. W.; Si, K. J.; Shi, Q.; Jason, N. N.; Sridhar, T.; Uddin, H.; Cheng, W. *ACS Appl. Mater. Interfaces* **2015**, *7*, 19700–19708.
- (12) Reiser, B.; Gerstner, D.; Gonzalez-Garcia, L.; Maurer, J. H. M.; Kanelidis, I.; Kraus, T. *ACS Nano* **2017**, *11*, 4934–4942.
- (13) Reiser, B.; Gerstner, D.; Gonzalez-Garcia, L.; Maurer, J. H. M.; Kanelidis, I.; Kraus, T. *Phys. Chem. Chem. Phys.* **2016**, *18*, 27165–27169.
- (14) Nouh, E. S. A.; Baquero, E. A.; Lacroix, L.-M.; Delpéch, F.; Poteau, R.; Viau, G. *Langmuir* **2017**, *33*, 5456–5463.
- (15) Wang, F.; He, C.; Han, M. Y.; Wu, J. H.; Xu, G. Q. *Chem. Commun.* **2012**, *48*, 6136–6138.
- (16) Sánchez-Iglesias, A.; Grzelczak, M.; Pérez-Juste, J.; Liz-Marzán, L. M. *Angew. Chem., Int. Ed.* **2010**, *49*, 9985–9989.
- (17) Lau, C. Y.; Duan, H.; Wang, F.; He, C. B.; Low, H. Y.; Yang, J. K. W. *Langmuir* **2011**, *27*, 3355–3360.
- (18) Peng, S.; Lee, Y.; Wang, C.; Yin, H.; Dai, S.; Sun, S. *Nano Res.* **2008**, *1*, 229–234.
- (19) Teraoka, I. *Polymer Solutions*; John Wiley & Sons, Inc.: New York, 2002.
- (20) Mukherji, D.; Marques, C. M.; Kremer, K. *Nat. Commun.* **2014**, *5*, 4882.
- (21) Rabani, E.; Egorov, S. A. *Nano Lett.* **2002**, *2*, 69–72.
- (22) de Beer, S.; Kutnyanszky, E.; Schön, P. M.; Vancso, G. J.; Müser, M. H. *Nat. Commun.* **2014**, *5*, 3781.
- (23) Fraser, B.; Denniston, C.; Müser, M. H. *J. Polym. Sci., Part B: Polym. Phys.* **2005**, *43*, 970–982.
- (24) Khanal, B. P.; Zubarev, E. R. *Angew. Chem., Int. Ed.* **2007**, *46*, 2195–2198.
- (25) Sebbby, K. B.; Mansfield, E. *Anal. Bioanal. Chem.* **2015**, *407*, 2913–2922.
- (26) Quek, S. Y.; Venkataraman, L.; Choi, H. J.; Louie, S. G.; Hybertsen, M. S.; Neaton, J. B. *Nano Lett.* **2007**, *7*, 3477–3482.
- (27) Jorgensen, W. L.; Maxwell, D. S.; Tirado-Rives, J. *J. Am. Chem. Soc.* **1996**, *118*, 11225–11236.
- (28) Plimpton, S. J. *Comput. Phys.* **1995**, *117*, 1–19.
- (29) Xu, J.; Zhu, Y.; Zhu, J.; Jiang, W. *Nanoscale* **2013**, *5*, 6344.
- (30) Lacroix, L.-M.; Arenal, R.; Viau, G. *J. Am. Chem. Soc.* **2014**, *136*, 13075–13077.
- (31) Takahata, R.; Yamazoe, S.; Warakulwit, C.; Limtrakul, J.; Tsukuda, T. *J. Phys. Chem. C* **2016**, *120*, 17006–17010.
- (32) Bettscheider, S.; Kraus, T.; Fleck, N. A. *J. Mech. Phys. Solids* **2019**, *123*, 3–19.
- (33) O'Hagan, A.; Leonard, T. *Biometrika* **1976**, *63*, 201–203.
- (34) Maurer, J. H. M.; González-García, L.; Reiser, B.; Kanelidis, I.; Kraus, T. *ACS Appl. Mater. Interfaces* **2015**, *7*, 7838–7842.
- (35) Huber, S. E.; Warakulwit, C.; Limtrakul, J.; Tsukuda, T.; Probst, M. *Nanoscale* **2012**, *4*, 585–590.
- (36) Smith, A. M.; Johnston, K. A.; Crawford, S. E.; Marbella, L. E.; Millstone, J. E. *Analyst* **2017**, *142*, 11–29.
- (37) Cölfen, H.; Mann, S. *Angew. Chem., Int. Ed.* **2003**, *42*, 2350–2365.
- (38) Ozin, G. A.; Hou, K.; Lotsch, B. V.; Cademartiri, L.; Puzzo, D. P.; Scotognella, F.; Ghadimi, A.; Thomson, J. *Mater. Today* **2009**, *12*, 12–23.
- (39) Bishop, K. J. M.; Wilmer, C. E.; Soh, S.; Grzybowski, B. A. *Small* **2009**, *5*, 1600–1630.
- (40) Napper, D. H. *Polymeric Stabilization of Colloidal Dispersions*; Academic Press Inc.: London, 1983.
- (41) Jana, S.; De Frutos, M.; Davidson, P.; Abécassis, B. *Sci. Adv.* **2017**, *3*, e1701483.
- (42) Fujiwara, M.; Toubaru, K.; Noda, T.; Zhao, H. Q.; Takeuchi, S. *Nano Lett.* **2011**, *11*, 4362–4365.
- (43) He, J.; Li, J.; Xia, J.; Tian, L.; Jin, B.; Zhou, S.; Sun, M.; Meng, X. *Adv. Mater. Interfaces* **2019**, *6*, 1801418.
- (44) Loubat, A.; Escoffier, W.; Lacroix, L.-M.; Viau, G.; Tan, R.; Carrey, J.; Warot-Fonrose, B.; Raquet, B. *Nano Res.* **2013**, *6*, 644–651.
- (45) Monego, D.; Kister, T.; Kirkwood, N.; Mulvaney, P.; Widmer-Cooper, A.; Kraus, T. *Langmuir* **2018**, *34*, 12982–12989.

Supporting Information

Entropy Can Bundle Nanowires in Good Solvents

Hongyu Gao,[†] Simon Bettscheider,[‡] Tobias Kraus,^{‡,¶} and Martin H. Müser*,[†]

[†]*Department of Materials Science and Engineering, Saarland University, Campus C6 3,
66123 Saarbrücken, Germany*

[‡]*INM - Leibniz Institute for New Materials, Campus D2 2, 66123 Saarbrücken, Germany*

[¶]*Colloid and Interface Chemistry, Saarland University, Campus D2 2, 66123 Saarbrücken,
Germany*

E-mail: martin.mueser@mx.uni-saarland.de

Phone: +49 681 302 57452. Fax: +49 681 302 57454

Contents

S1 Experimental methods	3
S1.1 Synthesis of ultrathin gold nanowires	3
S1.2 Characterization by transmission electron microscopy	4
S1.3 Characterization by small angle X-ray scattering and data analysis	4
S2 Simulations methods: OPLS-AA force field parameters	5
S3 Supporting experimental results: transmission electron micrographs of nanowires after scattering analysis	7
S4 Supporting simulation results: Radial probability density distribution of ligands	8
References	9

S1 Experimental methods

S1.1 Synthesis of ultrathin gold nanowires

Ultrathin AuNWs were prepared using an adapted protocol originally developed by Feng et al.¹ Gold(III) chloride hydrate (CAS number 7440-57-5; InChI and PubChem CID of all chemicals can be found in Table S1) was prepared by dissolving a gold ingot (99.99%, Degussa, Munich, Germany) in aqua regia. An amount of 39 mg $\text{HAuCl}_4 \cdot x\text{H}_2\text{O}$ (degree of hydration $x \approx 3$) was dissolved in a mixture of 6 mL *n*-hexane (99%, ABCR, Germany, CAS number 110-54-3) and 1.8 mL oleylamine (technical grade, 70%, Sigma-Aldrich, Steinheim, Germany, CAS number 112-90-3). Subsequently, 2.6 mL triisopropylsilane (98%, ABCR, Germany, CAS number 6485-79-6) were added as reducing agent. The solution was flushed with argon, vortexed for 5 min, and left undisturbed to react at room temperature for 16 h. The as-synthesized AuNWs were purified twice by adding an volumetric 2:1 excess of ethanol (99.8%, Sigma-Aldrich, Germany, CAS number 64-17-5), letting the AuNWs sediment under force of gravity, carefully removing the supernatant. After the first washing step, the AuNWs were re-dispersed in the same volume of *n*-hexane as the reaction volume. Finally and after the second washing step, the AuNWs were redispersed in their final solvent (linear alkane, cycloalkane, or alcohol).

Table S1: Chemical identifiers of the substances used to synthesize ultrathin gold nanowires.

Name	PubChem ID	CAS Number	InChI Key
Gold	23985	7440-57-5	PCHJSUWPFVWCPO-UHFFFAOYSA-N
Chlorauric acid	28133	1303-50-0	VDLSFRRYNGEBEJ-UHFFFAOYSA-K
Aqua regia	90477010	8007-56-5	NICDRCVJGXLKSF-UHFFFAOYSA-N
<i>n</i> -hexane	8058	110-54-3	VLKZOE-OYAKHREP-UHFFFAOYSA-N
Oleylamine	5356789	112-90-3	QGLWBTPVKHMHVM-KTKRTIGZSA-N
Triisopropylsilane	6327611	6485-79-6	ZGYICYBLPGRURT-UHFFFAOYSA-N
Ethanol	702	64-17-5	LFQSCWFLJHTTHZ-UHFFFAOYSA-N

S1.2 Characterization by transmission electron microscopy

In order to observe AuNWs by transmission electron microscopy (TEM), an amount of approximately 1 μL of dispersed AuNWs diluted to a concentration of 1.5 mmol L^{-1} was dried on a 400-mesh carbon coated copper grid (Plano, Germany), which was then introduced into a JEM 2010 microscope (JEOL, Germany) operated at an acceleration voltage of 200 kV.

S1.3 Characterization by small angle X-ray scattering and data analysis

The arrangement of AuNWs in different solvents was observed via small angle X-ray scattering (SAXS) 24 h after redispersion in the respective solvent at a nominal Au concentration of 30 mmol L^{-1} . Samples were introduced into a glass capillary with an inner diameter of 1.5 mm. The XEUSS 2.0 (XENOCSS SA, France) SAXS setup was equipped with a Cu K- α X-ray source and a PILATUS3 R 1M (DECTRIS, Switzerland) X-ray detector. The sample to detector distance was 560.07 mm and the setup was calibrated by measuring a glass capillary filled with silver behenate.

All samples were measured five times for a period of 300 s. The diffraction patterns were integrated with the software Foxtrot² and the resulting two-dimensional patterns were averaged over the five measurements. To correct for the background, the solvent signal was subtracted from the sample signal.

Wire-wire distances d were determined from the q -vector of Bragg peaks using the Miller indices h and k of a two-dimensional, hexagonal lattice according to

$$q_{hk} = \frac{4\pi}{\sqrt{3}d} \sqrt{h^2 + hk + k^2}, \quad (1)$$

as proposed by Förster et al.³

S2 Simulations methods: OPLS-AA force field parameters

Table S2: OPLS-AA non-bonded parameters

Mat.	Type	12-6 Lennard-Jones		Charge (e)
		σ (\AA)	ϵ (Kcal/mol)	
oleylamine	CT _{CH₃}	3.50	0.066	-0.222
	CT _{CH₂}	3.50	0.066	-0.148
	CM _{CH}	3.55	0.076	-0.160
	HC _{CH₃}	2.50	0.030	+0.074
	HC _{CH₂}	2.50	0.0263	+0.074
	HM _{CH}	2.50	0.030	+0.160
<i>n</i> -hexane	CT _{CH₃}	3.50	0.066	-0.180
	CT _{CH₂}	3.50	0.066	-0.120
	HC	2.50	0.030	+0.060
ethanol	CT _{CH₃}	3.50	0.066	-0.180
	CT _{CH₂OH}	3.50	0.066	+0.145
	OH	3.12	0.170	-0.683
	HC	2.50	0.030	+0.060
	HO	0.0	0.0	+0.418
gold	Au	2.934	0.039	0.0

Table S3: OPLS-AA bonded parameters

	Type	K_s (Kcal/mol-Å ²)	r_0 (Å)		
stretching	CT-CT	268.0	1.529		
	CT-HC	340.0	1.090		
	CT-CM	317.0	1.510		
	CM-CM	549.0	1.340		
	CM-HC	340.0	1.080		
	CT-OH	320.0	1.410		
	OH-HO	553.0	0.945		
	Type	K_b (Kcal/mol-rad ²)	θ_0 (degree)		
bending	CT-CT-CT	58.35	112.7		
	CT-CT-CM	63.0	111.1		
	CT-CT-OH	50.0	109.5		
	CT-CT-HC	37.5	110.7		
	CT-CM-CM	70.0	124.0		
	CT-CM-HC	35.0	117.0		
	CT-OH-HO	55.0	108.5		
	HC-CT-CM	35.0	109.5		
	HC-CT-OH	35.0	109.5		
	HC-CT-HC	33.0	107.8		
	HC-CM-CM	35.0	120.0		
		Type	K_{t1}	K_{t2}	K_{t3}
		(Kcal/mol-Å ²)			
torsional	CT-CT-CT-CT	1.3	-0.05	0.2	0.0
	CT-CT-CT-CM	1.3	-0.05	0.2	0.0
	CT-CT-CT-HC	0.0	0.0	0.3	0.0
	CT-CT-CM-CM	0.346	0.405	-0.904	0.0
	CT-CT-CM-HC	0.0	0.0	0.468	0.0
	CT-CT-OH-HO	-0.356	-0.174	0.492	0.0
	CT-CM-CM-CT	0.0	14.0	0.0	0.0
	CT-CM-CM-HC	0.0	14.0	0.0	0.0
	CM-CT-CT-HC	0.0	0.0	0.366	0.0
	CM-CM-CT-HC	0.0	0.0	-0.372	0.0
	OH-CT-CT-HC	0.0	0.0	0.468	0.0
	HC-CT-CT-HC	0.0	0.0	0.3	0.0
	HC-CT-CM-HC	0.0	0.0	0.318	0.0
	HC-CT-OH-HO	0.0	0.0	0.352	0.0
	HC-CM-CM-HC	0.0	14.0	0.0	0.0

S3 Supporting experimental results: transmission electron micrographs of nanowires after scattering analysis

Because the AuNWs are fragile and can be prone to Rayleigh-Plateau instabilities,⁴⁻⁷ we investigated their quality after the SAXS experiments by transmission electron microscopy (TEM). TEM micrographs for linear alkanes and cycloalkanes are shown in Fig. S1 and reveal elongated nanowires alongside a fraction of spherical particles. The latter could be a side product of the synthesis or might stem from decomposed nanowires due to the Rayleigh-Plateau instability. The fact that the fraction of nanowires prevails verifies that the SAXS patterns shown in Fig. S1 stem from bundled nanowires. The bundles of nanowires formed in alcohols were too dense to be examined by TEM, which is in line with the smaller interwire distance found by SAXS. Given that the SAXS pattern is alike to one found in linear alkanes, we can conclude that the pattern also stem from undamaged nanowires.

It should be noted that a TEM micrograph is ex-situ experimental data and cannot be used to draw conclusions on the system behaviour in solution. For acquiring TEM micrographs, the AuNW dispersion is diluted by a factor of 20, dried at air and then examined under vacuum. During drying, there are additional forces at play and nanowires that are finely dispersed in solution can be bundled in the dried state. The TEM micrographs are therefore not suitable to analyse the bundling behavior of AuNWs. Instead, they allow to draw conclusions on whether the objects measured by SAXS are any nanostructures or ultrathin nanowires, as is the case in here.

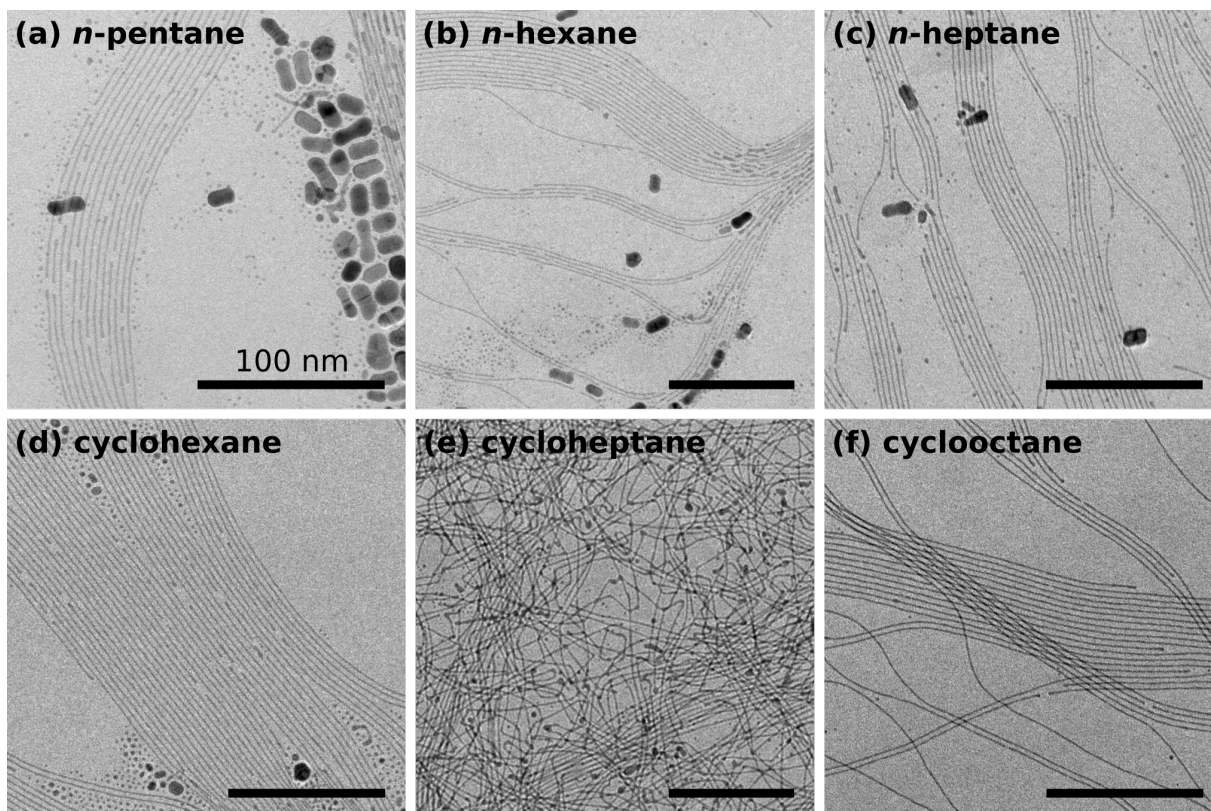


Figure S1: Transmission electron micrographs (TEM) of dried AuNWs on a carbon coated copper grid in (a) *n*-pentane, (b) *n*-hexane, (c) *n*-heptane, (d) cyclohexane, (e) cycloheptane, and (f) cyclooctane. All scale bars correspond to 100 nm.

S4 Supporting simulation results: Radial probability density distribution of ligands

To demonstrate that the increase of distance between NW in good solvents is not predominantly caused by a swelling of the ligands, we measured the probability density $\text{Pr}(r)$ of ligand carbon atoms for a single immersed NW. Here, $2\pi r \text{Pr}(r)\Delta r$ denotes the probability of a ligand carbon atom to be within a distance of $r \pm \Delta r/2$ from the NW's symmetry axis. Analysis of the resulting probability densities, which are shown in Fig. S2, reveals that the tail of the probability distribution in *n*-hexane are shifted slightly above 1 Å to the outside compared to ethanol.

To quantify the swelling induced by good solvents in terms a number of unit length rather

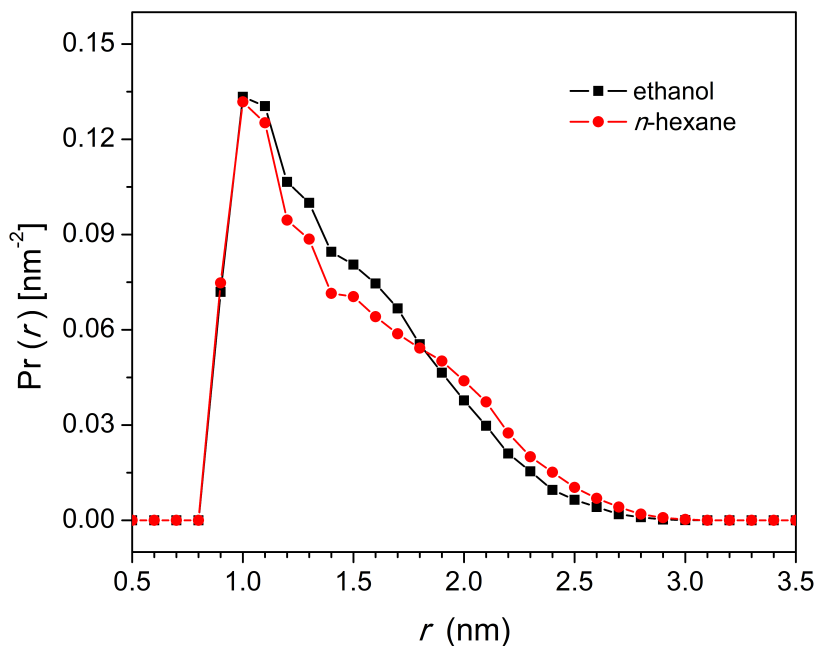


Figure S2: Radial probability density $\text{Pr}(r)$ of ligands in ethanol and *n*-hexane. Inset shows a schematic of how the parameters are defined.

than with a distribution function, we computed the root-mean square distance d of an end-group from the surface of the NW gold core and found values of $d = 12.7 \text{ \AA}$ for ethanol and 14.5 \AA for *n*-hexane.

References

- (1) Feng, H.; Yang, Y.; You, Y.; Li, G.; Guo, J.; Yu, T.; Shen, Z.; Wu, T.; Xing, B. Chem. Commun. **2009**, *0*, 1984–1986.
- (2) Girardot, R.; Viguier, G.; Pérez, J.; Ounsy, M. FOXTROT: A Java-based application to reduce and analyse SAXS and WAXS piles of 2D data at synchrotron SOLEIL. Proceedings of the canSAS-VIII. Tokai, Japan, 2015.
- (3) Förster, S.; Timmann, A.; Konrad, M.; Schellbach, C.; Meyer, A.; Funari, S. S.; Mul-

- vaney, P.; Knott, R. J. Phys. Chem. B **2005**, 109, 1347–1360.
- (4) Xu, J.; Zhu, Y.; Zhu, J.; Jiang, W. Nanoscale **2013**, 5, 6344.
- (5) Lacroix, L.-M.; Arenal, R.; Viau, G. J. Am. Chem. Soc. **2014**, 136, 13075–13077.
- (6) Takahata, R.; Yamazoe, S.; Warakulwit, C.; Limtrakul, J.; Tsukuda, T. J. Phys. Chem. C **2016**, 120, 17006–17010.
- (7) Bettscheider, S.; Kraus, T.; Fleck, N. A. J. Mech. Phys. Solids **2019**, 123, 3–19.

3.2 Publication 2: Bundling of nanowires induced by unbound ligand

Reprinted with permission from:

S. Bettscheider, B. Kuttich, L.F. Engel, L. González-García, T. Kraus, Bundling of Nanowires Induced by Unbound Ligand, *J. Phys. Chem. C.* 125 (2021) 3590–3598.
<https://doi.org/10.1021/acs.jpcc.0c10919>.

© 2021 The Authors. Published by American Chemical Society.

Bundling of Nanowires Induced by Unbound Ligand

Simon Bettscheider, Björn Kuttich, Lukas F. Engel, Lola González-García, and Tobias Kraus*

 Cite This: *J. Phys. Chem. C* 2021, 125, 3590–3598

 Read Online

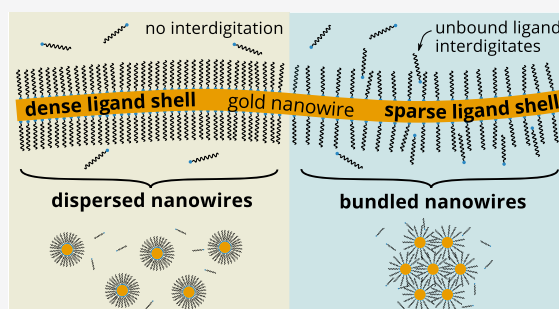
ACCESS |

 Metrics & More

 Article Recommendations

 Supporting Information

ABSTRACT: We report on the dilution-induced agglomeration of ultrathin gold nanowires (AuNWs) into regular bundles. Wires with a metal core diameter of 1.6–1.7 nm surrounded by a ligand shell of oleylamine formed stable colloids in *n*-hexane and cyclohexane. Dilution with pure solvent induced the self-assembly into bundles with a regular, hexagonal cross-section. Small-angle X-ray scattering and thermogravimetric analysis indicated that bundles formed only if the ligand shell was sufficiently sparse. Dilution with pure solvent shifts the chemical equilibrium and reduces the ligand density, thus enabling agglomeration. We show that agglomeration is driven not by van der Waals forces but by the depletion forces of linearly shaped molecules. Linear solvent molecules or small amounts of unbound ligand align normal to the nanowire if the ligand shell is sparse. The resulting reduction in entropy creates a driving force for the AuNWs to bundle such that the low-entropy domains overlap and the overall entropy is increased. Dilution-induced nanowire bundling is thus explained as a combined effect of ligand desorption and destabilization by depletion.



INTRODUCTION

Ultrathin nanowires are chemically synthesized, solid objects that form colloidal dispersions in suitable solvents. Such wires can be several micrometers long but a few nanometers in diameter, mechanically flexible, and mobile enough to align laterally. Attractive forces that act along the length of two adjacent wires can lead to unusual colloidal properties. Even weak attractive forces accumulate and lend the wires a strong tendency to assemble into elongated bundles. The colloidal stability of ultrathin nanowires thus differs from that of spheres with similar molecular structures and diameters.

Here, we discuss an unusual agglomeration mechanism of ultrathin gold nanowires (AuNWs) in alkanes. The wires agglomerate and form bundles upon dilution, a type of colloidal instability that has not yet been observed in other nanoparticle systems. For example, spherical nanoparticles with nonpolar ligand shells agglomerate at increasing particle concentrations with a solubility that depends on the solvent.¹ Apparently, the colloidal stability of AuNWs cannot be understood in similar terms.

We link the dilution-induced destabilization of AuNWs to the depletion of unbound ligand molecules. Such unbound (also called “free” or “solvated”) ligands are in a dynamic equilibrium with adsorbed (“coordinated” or “bound”) ligands.^{2,3} The number ratio between unbound and adsorbed ligands depends on the adsorption energy of the ligand, among other factors. Their role in the colloidal stability of ultrathin nanowires has not yet been discussed.

Ultrathin gold nanowires can be synthesized by reducing chloroauric acid in the presence of the ligand oleylamine. This

route was pioneered by Halder and Ravishanker in 2007⁴ and advanced by several research groups in 2008.^{5–8} The resulting nanowires consist of a gold core of diameter of 1.6 to 1.7 nm (corresponding to 6 to 7 gold atoms along the diameter) surrounded by an organic ligand shell of oleylammonium chloride of similar thickness. The wires reach typical lengths of 4 μm ,^{5,6} although up to 6.4 μm long wires have been observed.⁹

Large aspect ratios above 1:10³ and their electrically conductive cores make AuNWs appealing as nanoscale building blocks. For example, Gong et al.¹⁰ created monolayers of AuNWs on polydimethylsiloxane in order to create flexible electrodes for supercapacitors. Porter et al.¹¹ used striped phases of phospholipids to precisely align individual wires over micrometer-wide areas. Roy et al.¹² demonstrated that AuNWs are suitable as chemical sensors to detect CO, CH₃NH₂, and CH₃CHO. Reiser et al.¹³ spun AuNWs into free-standing macroscopic fibers with a mechanical strength that could be tuned by varying the alignment of the AuNWs. Many applications require control over nanowire bundling. For example, our group reported that the printing of AuNW meshes for flexible and transparent conductive electrodes

Received: December 7, 2020

Revised: January 25, 2021

Published: February 3, 2021



requires that the wires bundle inside the structuring stamp and not earlier.¹⁴

The formation of AuNW bundles has already been reported in the first synthesis papers,^{6,15} and some of its mechanisms are well understood. As-synthesized AuNWs carry a double layer of oleylammonium chloride/oleylamine and arrange into bundles with two-dimensional hexagonal packing cross-section at a center-to-center interwire distance of 9.5 nm.^{16,17} Purification decreased the interwire distance to 5.5 nm for AuNWs in *n*-hexane.¹⁷ No bundles were observed for AuNWs redispersed in cyclohexane.¹⁷ Tighter bundles form in polar solvents such as ethanol in order to reduce the AuNW–solvent interfacial area.¹⁸ The lattice constant of bundles has been tuned by modifying the ligand shell. For example, Nough et al. reduced the center-to-center distance from 5.5 to 3.8 nm by replacing oleylamine with the shorter trioctylphosphine. Molecular dynamics simulations showed that the driving force for bundling in linear alkanes such as *n*-hexane is entropic:¹⁸ solvent molecules close to the ligand shell align normal to the nanowire surface and lose entropy. Bundling excludes (“depletes”) solvent molecules from the ligand shells and decreases the loss in entropy.

In the following, we focus on the unexpected bundling of nonpolar AuNWs upon dilution. We find that AuNWs remain dispersed in nonpolar solvents at large nanowire concentrations but form bundles at smaller concentrations, whereas most colloidal systems become more stable at lower concentrations. Small-angle X-ray scattering and thermogravimetric analysis were used to assess the role of the amount of ligand present in the system. Our results indicate that a combination of ligand desorption and the depletion of unbound ligand can initiate bundling.

METHODS

Synthesis of Ultrathin Gold Nanowires. Materials.

Hydrogen tetrachloroaurate trihydrate (HAuCl₄·3H₂O) was synthesized following Schubert et al.²⁰ and was dried for at least 30 min on a Schlenk line (<1 mbar). Oleylamine (OAm), 80–90% C18, was purchased from Acros Organics and filtered with a syringe filter (Millex, 0.45 μm, hydrophobic PTFE). All other chemicals were used as received. Triisopropylsilane (TIPS), 98%, and *n*-hexane, ≥99%, were obtained from abcr. Absolute ethanol (EtOH), ≥ 99.8%, was provided by Fisher Scientific. Cyclohexane, ≥99.9%, was received from Carl Roth.

Synthesis. AuNWs were synthesized under ambient conditions using the protocols of Feng et al.¹⁵ and Nough et al.¹⁹ For a typical synthesis, 60 mg of the dry precursor HAuCl₄·3H₂O was quickly weighed into a 50 mL glass snap-on vial preflushed with Ar, and the sample was immediately covered with 9.9 mL of the solvent *n*-hexane. Then 2.04 mL of the ligand OAm was added, and the resulting mixture was thoroughly vortexed for 5 min (both under Ar) to achieve complete dissolution of the precursor. Subsequently, 3.06 mL of the reducing agent TIPS was added, and the obtained mixture was vortexed for 30 s (both under Ar). The solution was then kept still under Ar at 25 °C for 24 h without stirring. As the reaction progressed, the solution’s color evolved during the first hours from orange to bright yellow to pitch black as the precursor was being reduced, the AuNWs grew and consequently the light scattering changed.

Purification. Three different purification protocols were used (see main text), differing in the number of carried out cycles and whether precipitation was accelerated by

centrifugation. Each purification cycle consisted of adding two volumes of ethanol, precipitating the AuNWs either by sedimenting for 10 min or by centrifuging at 100 rcf for 1 min, followed by removal of the supernatant and resuspension in the desired solvent.

Transmission Electron Microscopy. Samples for observation in transmission electron microscopy were prepared by diluting the dispersion of AuNWs to a concentration of approximately 0.05 mg/mL and drying an amount of 3 μL on a carbon-coated copper grid (Plano, Germany). The samples were observed at an acceleration voltage of 200 kV in the JEM 2010 microscope (JEOL).

Thermogravimetric Analysis. Samples for thermogravimetric analysis were prepared by drying an amount of 1 mL of a dispersion of AuNWs at 2 mg/mL in a crucible made from aluminum oxide. To remove any moisture, the samples were dried in a vacuum oven overnight before being placed in the analyzer (Netsch STA 449 F3 Jupiter). The samples were heated from room temperature to 1000 °C at a rate of 10 °C/min under argon followed by an isothermal stage of 10 min under oxygen while the mass of the samples was continuously recorded.

The ratio of ligand molecules to gold atoms and the grafting density were determined assuming that the residual mass was pure gold and the loss pure oleylammonium chloride. We assumed an AuNW core diameter of 1.65 nm, consistent without our SAXS measurements and literature.^{5,7,16}

Small-Angle X-ray Scattering. The colloidal state of AuNWs was observed by small-angle X-ray scattering (SAXS). Samples were let rest at least 16 h before being filled into glass capillaries with an inner diameter of 1.5 mm for the SAXS measurement. The scattering setup (XEUSS 2.0, XENOCs,) used a Cu Kα source, and the scattered beam was captured by a detector (PILATUS3 R 1 M DECTRIS) at a distance of approx. 550 mm from the sample. The exact sample-to-detector distance was calibrated with a standard of silver behenate prior to each measurement. If not noted otherwise, each sample was measured for a total duration of 25 min. The two-dimensional scattering images were azimuthally integrated with the software Foxtrott (Synchrotron Soleil) to obtain scattering curves. To correct for the background, the respective solvent was subtracted from all scattering curves.

The (center-to-center) interwire distance *d* in bundled AuNWs was determined following Förster et al.²¹ using

$$q_{hk} = \frac{4\pi}{\sqrt{3}d} \sqrt{h^2 + hk + k^2} \quad (1)$$

where q_{hk} is the value of the q -vector of the Bragg scattering peak of two-dimensional hexagonal lattice with the Miller indices h and k .²¹

Analysis of the Ratio of Bundled and Dispersed Nanowires. The ratio of bundled and dispersed nanowires was obtained from small-angle X-ray scattering data using a scattering model. The scattering of single, well-dispersed nanowires can be approximated by the form factor of a cylinder with a variable diameter. Polydispersity is taken into account by convolution with a Schulz–Zimm distribution. The length of the cylinder is too large to be resolved by our SAXS instrument and will be assumed to be infinity, resulting in a power-law decay of intensity at the lowest measured scattering vectors q which is proportional to q^{-1} .^{16,22,23} Scattering from bundled nanowires was modeled by multiplying the cylindrical form factor with the structure factor of a 2D hexagonal lattice,

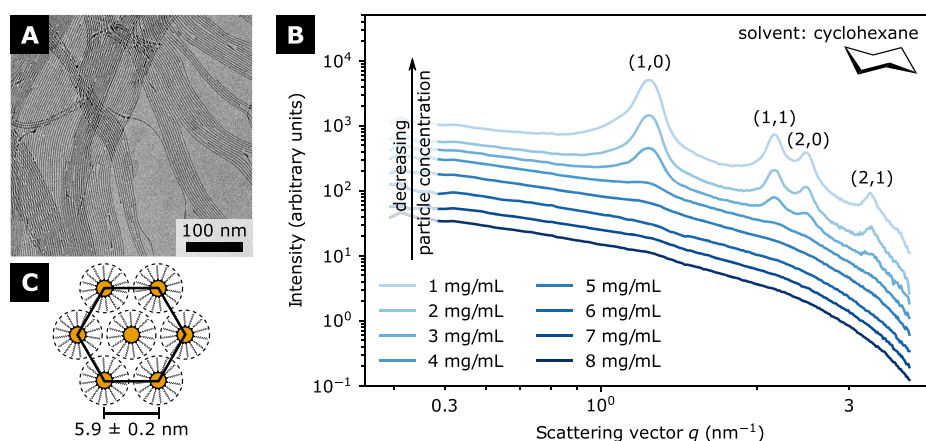


Figure 1. (A) Transmission electron micrograph (TEM) of ultrathin gold nanowires. (B) Radially integrated small-angle X-ray scattering (SAXS) curves of ultrathin gold nanowires in cyclohexane at different concentrations. The tuples indicate a two-dimensional hexagonal lattice; curves were shifted vertically for visibility. (C) Schematic of the hexagonal packing and center-to-center distances with mean and standard deviations of 82 samples.

which is the sum of Lorentzian functions at the respective positions of the Bragg-peaks. Disorder of the lattice due to thermal fluctuations for example was taken into account by a Debye–Waller factor.^{16,22,23} Concurrent scattering from both dispersed and bundled nanowires was modeled by a weighted sum in scattered intensity of both dispersed and bundled contributions, with the weighting factor allowing to determine the dispersed/bundled ratio.

RESULTS

Ultrathin gold nanowires with uniform core diameters and oleylamine (OAm) shells were prepared using a well-established synthesis in *n*-hexane, purified, and redispersed in cyclohexane.^{15,19} The resulting wires had diameters in the range of 1.6–1.7 nm and lengths exceeding 427 nm according to transmission electron microscopy (TEM); see Figure 1A. Small-angle X-ray scattering (SAXS) indicated full dispersion in cyclohexane (Figure 1B), without signs of bundling at large gold concentrations of $[\text{Au}] \gtrsim 5 \text{ mg/mL}$ (2.5 times above that during synthesis). Dilution of the dispersion with pure cyclohexane to concentrations $\lesssim 4 \text{ mg/mL}$ led to scattering peaks with a hexagonal arrangement (see Figure 1C) that have been reported for bundled AuNWs previously.^{13,16,17,19} Here, the center-to-center distance was $5.9 \pm 0.2 \text{ nm}$.

Dilution reduces the concentration of both wires and OAm in the dispersion. Since a dynamic equilibrium exists between adsorbed and unbound OAm,^{2,3} diluting will affect the ratio of adsorbed and unbound ligand and will decrease the ligand shell density (see illustration in Figure 2A). Oleylamine-coated gold nanowires are colloidal stabilized by the interactions between solvents and OAm shells.¹⁷ Changing the ligand density can therefore affect their stability, too. A rigorous analysis of the destabilizing mechanism of dilution requires the analysis of both OAm concentration in the solvent and ligand shell density.

The amount of OAm in freshly prepared AuNW dispersions depends on the purification protocol. The literature contains different approaches to remove the excess OAm after synthesis; they involve precipitation by ethanol (sometimes with the aid of centrifugation), removal of the supernatant, and resuspension. We used three different protocols to purify AuNWs after synthesis (Figure 2B): one cycle of centrifugation

at 100 rcf for 1 min (sample 1), two cycles of sedimentation for 10 min (sample 2), and two cycles of centrifugation at 100 rcf for 1 min (sample 3). Appropriate dilution ensured that the AuNW concentration remained constant for all three samples. The three resulting dispersions were then dried and analyzed for their organic content.

Thermogravimetric analyses in Figure 2C and Table 1 indicated distinct, but quantitatively different mass losses between 140 and 470 °C in argon and after oxygen introduction for all samples. The greatest loss of $52.2 \pm 5.2 \text{ wt\%}$ was observed for sample 1 (Figure 2B). It is reasonable to assume that all losses were due to the decomposition of OAm, which implies a ratio of 0.708 ± 0.148 ligands per gold atom, far below the 40 ligands per gold atom used in synthesis.^{15,16,24} This corresponds to a nominal ligand density of $17.3 \pm 3.6 \text{ ligands/nm}^2$, far above the values around 4–6 ligands/nm² that are often reported for gold nanoparticles.²⁵ Thus, sample 1 must have contained considerable amounts of unbound ligand. Sample 2 contained 0.216 ± 0.013 ligands per gold atom corresponding to an intermediate nominal density of $5.3 \pm 0.3 \text{ ligands/nm}^2$, while sample 3 only contained 0.183 ± 0.002 ligands per gold atom, corresponding to $4.5 \pm 0.1 \text{ ligands/nm}^2$ (Figure 2B). It is not possible at this stage to differentiate unbound from adsorbed OAm. It is clear, however, that samples 1–3 contained different total [OAm] values, and it is very likely that both the ligand density and the unbound OAm concentration were different for each sample.

We split and diluted the three samples 1–3 to observe the effects on colloidal nanowire stability. Each sample was split in eight aliquots, and pure cyclohexane was added to create series with gold concentrations [Au] in the range of 1 to 8 mg/mL. We let the samples equilibrate for at least 16 h and then used SAXS to detect bundling for the full series (Figure 2D–F). Clear scattering peaks from the diluted samples with the smallest $[\text{OAm}]/[\text{Au}] = 0.18$ (Figure 2D) indicated considerable bundling of up to 75% of AuNWs, while the samples with the greatest $[\text{OAm}]/[\text{Au}] = 0.71$ had no bundling visible in SAXS; see Figure 2F (we estimate the limit of detection for bundles at approximately 5%). Bundling in the sample with intermediate $[\text{OAm}]/[\text{Au}] = 0.22$ began at

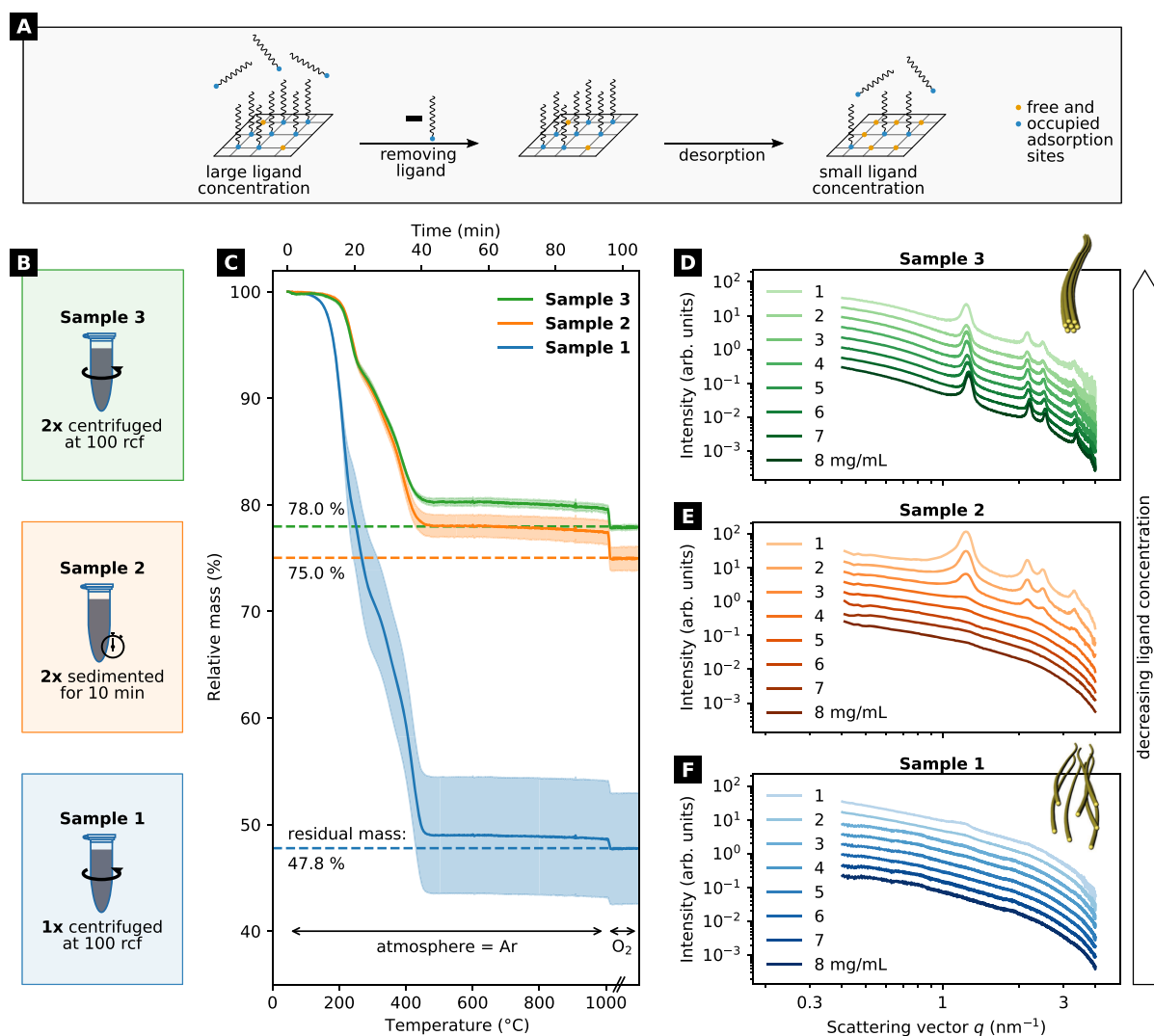


Figure 2. (A) Dilution and purification of AuNW dispersions shifts the adsorption equilibrium between free and adsorbed ligands to fewer adsorbed ligands and “removes” ligands from the particles into the solvent. The extent of removal depends on the exact protocol. (B) Purification of the as-synthesized samples involved precipitation by ethanol, removal of the supernatant, and resuspension. We tested three purification protocols that differed in the number of purification cycles and use of centrifugation. (C) Thermogravimetric analysis (TGA) of dried AuNWs prepared with different purification protocols indicated differences in organic content. The shaded areas indicate ± 1 standard deviation of three independently prepared samples. (D–F) Strong peaks in SAXS of sample 3 indicate that the AuNWs with the smallest OAm content agglomerated into hexagonal bundles (see inset) at all concentrations. Sample 2 did not exhibit such peaks until diluted to approximately 4 mg/mL. Sample 1, with the highest OAm content, did not agglomerate even upon maximal dilution. (The SAXS curves are shifted vertically for better visualization.)

Table 1. Amount of Ligand in the Three Different Samples as Obtained from the Thermogravimetric Analysis

sample name	purification protocol	residual mass (wt %)	amount of ligand ([OAm]/[Au])	nominal density (ligands/nm ²)
sample 1	centrifuged once	47.8 \pm 5.2	0.708 \pm 0.148	17.3 \pm 3.6
sample 2	sedimented twice	75.0 \pm 1.1	0.216 \pm 0.013	5.3 \pm 0.3
sample 3	centrifuged twice	78.0 \pm 0.2	0.183 \pm 0.002	4.5 \pm 0.1

a dilution of [Au] \approx 4 mg/mL and increased upon further dilution.

These results indicate a stabilizing effect of OAm that is reduced by dilution. We further investigated this correlation by adding pure OAm to the dispersions. Sample 2 was enriched with 1 mol of OAm for every mole of gold in order to reach [OAm]/[Au] = 1.2 at [Au] = 6 mg/mL. This did not initiate any bundling visible in SAXS (see Figure S3 in the Supporting

Information). Sample 3 was diluted to 2 mg/mL with pure cyclohexane, which initiated bundling. Subsequent addition of 0.031 to 2.0 mol OAm per mol gold led to deagglomeration of the AuNWs according to SAXS (Figure 3B).

We quantified the stabilizing effect of OAm using a SAXS scattering model (Figure 3B).^{16,22,23} The model fits provide the ratio of bundled and dispersed AuNWs (Figure 3C), the diameter of the bundles' cross sections (Figure 3D), and the

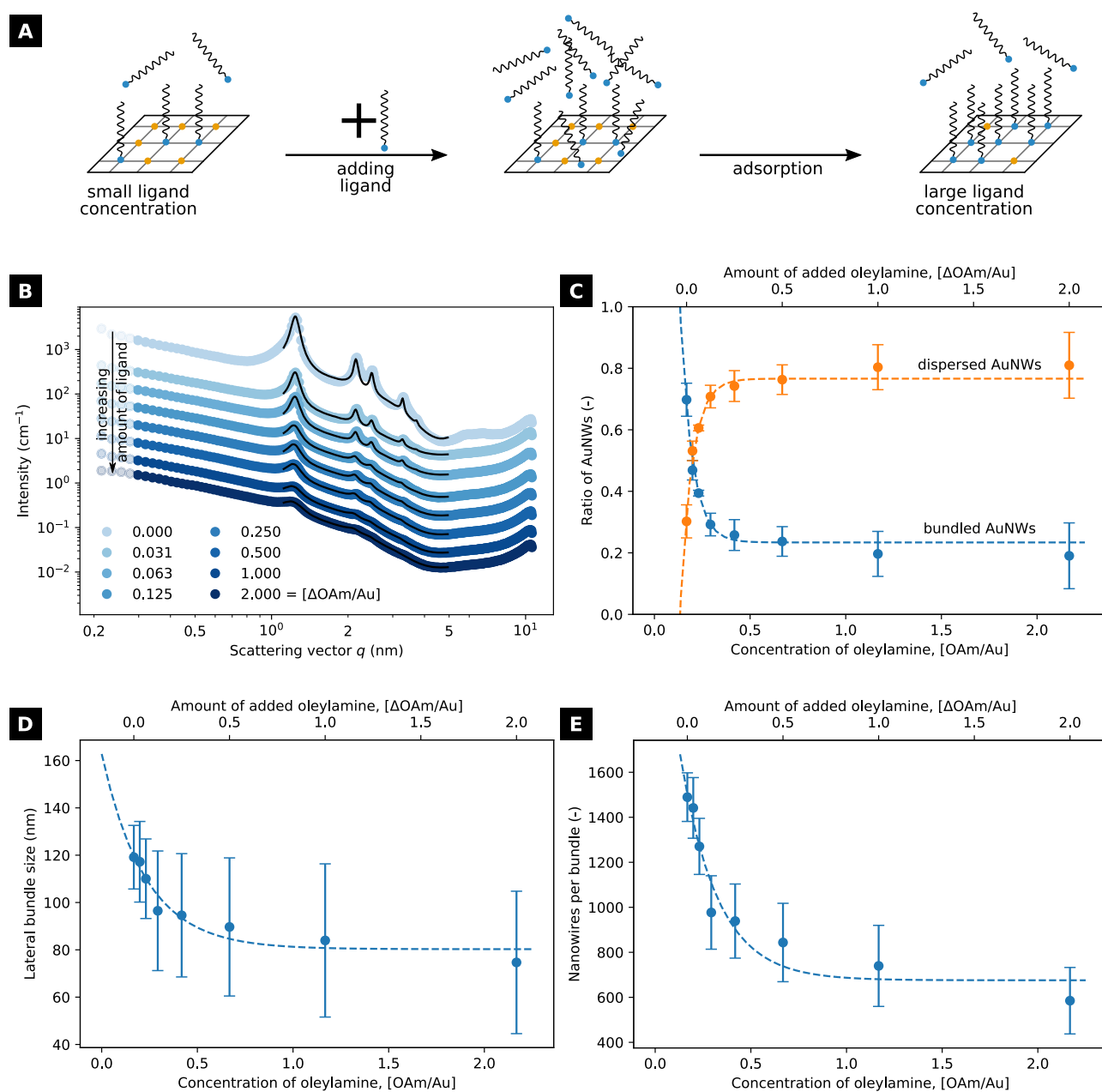


Figure 3. (A) Adding pure OAm ligand to AuNW dispersion shifts the equilibrium and leads to denser ligand shells. (B) Degree of bundling in sample 3 at a gold concentration of 2 mg/mL decreased upon addition of pure OAm. The black solid lines show fits based on a scattering model for bundled cylinders.^{16,22,23} The scattering curves (with the exception of that for $[\Delta\text{OAm}/\text{Au}] = 2.0$) are shifted for better visualization. (C) Ratios of bundled and dispersed AuNWs as obtained by the fits in part B. Error bars equal ± 1 standard deviation from three independent experiments. (D) Average lateral sizes of AuNW bundles and (E) average number of AuNWs per bundle as a function of $[\text{OAm}]$. The dashed lines are exponential fits.

number of nanowires per bundle (Figure 3E) as a function of $[\text{OAm}]/[\text{Au}]$. Small changes in $[\text{OAm}]$ strongly affected bundling: increasing $[\text{OAm}]/[\text{Au}]$ from 0.168 to 0.231 reduced the fraction of bundled AuNW from 0.7 to 0.39.

The exchange between adsorbed and unbound oleylamine is fast (on the millisecond time scale) so that AuNW dispersions rapidly reach an equilibrium.^{26,27} The maximum ligand shell density of AuNW and the change of shell density with $[\text{OAm}]$ is presently unknown. The following considerations provide useful estimates. We purified as-synthesized AuNWs three

times by centrifugation and determined $[\text{OAm}]/[\text{Au}]$ for each purification cycle. The ratio dropped from 40 ligands per gold atom to 0.708 ± 0.148 ligands per gold atom in the first purification cycle, then to 0.183 ± 0.002 , and, finally, to 0.178 ± 0.008 ligands per gold atom (see Figure S1 in the Supporting Information), which corresponds to 4.5 ligands/nm². This provides an upper limit for the ligand shell density of the AuNWs. A dense alkanethiol monolayer on a flat gold surface has been reported to contain 4 ligands/nm².²⁸ Thermodynamic data indicates a free energy of adsorption

for OAm on Au of $\Delta G_{\text{ads}} = -8.1$ kJ/mol (see details in the Supporting Information).^{19,28–34} Assuming equilibrium between unbound and adsorbed OAm and using the above numbers suggest that agglomeration was induced at a grafting density of about 90% corresponding to 4.1 ligands/nm².

Dilution-induced agglomeration of AuNWs apparently requires an incomplete ligand shell. The sparse shell induces enthalpic and/or entropic attraction between the wires. Temperature-dependent stability data can help in distinguishing enthalpic from entropic mechanisms. We diluted sample 2 to [Au] = 4 mg/mL and observed bundling with SAXS at temperatures between 25 to 65 °C. Each temperature was held for 15 min to ensure thermal equilibration. The fraction of bundles at 25 °C was minute; it increased to 45% when increasing the temperature to 65 °C. The center-to-center distance slightly increased from 5.9 to 6.1 nm. Given that Brownian motion increases with temperature, this result clearly suggests an entropic origin of dilution-induced AuNW agglomeration.

Finally, we tested whether bundle formation upon dilution is unique to cyclohexane or occurs in other solvents, too. To this end, AuNWs were synthesized and purified as for samples 1 and 3 but were redispersed in *n*-hexane instead of cyclohexane. We diluted the new samples with *n*-hexane and detected bundling via SAXS as shown in Figure S4 in the Supporting Information. The results were qualitatively similar to the situation in cyclohexane: scattering peaks indicative of bundles were only present at small [OAm]. The transition occurred at [OAm] \approx 14.2 mmol/L, which was far above that for cyclohexane (\approx 3.2 mmol/L).

DISCUSSION

The aim of the following discussion is to identify the most likely mechanism of dilution-induced bundling in AuNWs. First, we discuss and rule out well-known agglomeration mechanisms. An entropic model based on the depletion of unbound ligand is then introduced and shown to be consistent with the experimental results.

Solid particles in nonpolar dispersions attract each other due to dispersive van der Waals (vdW) forces. Stability requires opposing them with repulsive interactions; these are often entropic or “steric” forces caused by the overlap of ligand shells.^{35–37} The magnitude of such repulsive forces depends on the length of the ligands and their grafting density. Shorter ligands and smaller grafting densities reduce repulsion.^{38–41}

Reducing the grafting density of ligands on AuNWs by dilution could induce bundling by reducing steric repulsion so that vdW forces become dominant. However, several experimental observations are inconsistent with this idea. First, bundling driven by vdW forces should lead to compressed ligand shells. The measured interwire distance (center-to-center) in cyclohexane was 5.9 ± 0.2 nm, above the distance of 5.5 nm reported for neighboring nanowires whose ligand shells no longer touch.¹⁸ Second, the vdW interaction energy between two parallel gold cylinders with a diameter of 1.7 nm at a distance of 5.9 ± 0.2 nm in alkanes is very likely too small to cause agglomeration. An estimate using standard expressions (eq S2 in the Supporting Information; see, for example, Parsegian⁴²) indicates an interaction energy of approximately 1.245×10^{-3} $k_{\text{B}}T/\text{nm}$ of wire contact, below the thermal energy even if two AuNWs formed contact over several hundred nanometers. Third, raising the temperature increased bundling, which indicates an entropic rather than an

enthalpic mechanism (see Figure 4). Note that increasing temperature may affect the ligand shell density by shifting the

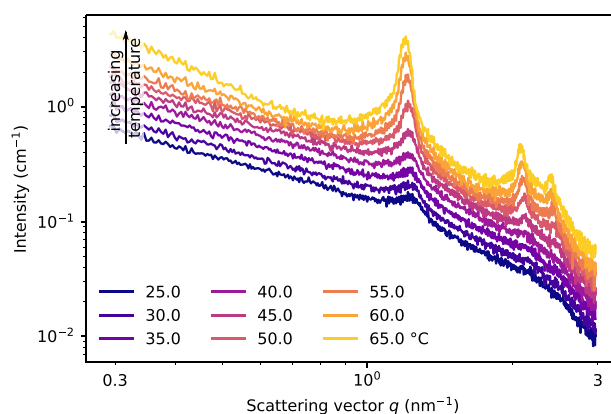


Figure 4. Temperature-dependent SAXS on sample 2 at [Au] = 4 mg/mL. Increasing temperatures led to additional bundling as visible in the growing structure peaks.

adsorption equilibrium. However, we found that AuNW spacing increased with temperature and conclude that an entropic destabilization mechanism is at play.

The bundling of AuNWs in linear alkanes has recently been explained with the depletion of ordered solvent molecules in the direct vicinity of the ligand shell.¹⁸ Dense wire packing reduces the loss in rotational entropy of solvent molecules, because the bundled wires share domains of ordered solvent. The resulting entropic force is attractive (on the order of 0.2 $k_{\text{B}}T/\text{nm}$ of wire contact) and leads to bundling. Our experiments show that this mechanism can be induced by dilution, because it requires sufficiently sparse ligand shells (Figure S4 in the Supporting Information). Could this entropic mechanism explain the effect of dilution-induced bundling in cyclic alkanes, too?

The entropic mechanism requires solvent molecules that align in the ligand shell. The structure of cyclohexane makes it difficult for the molecule to align in a way that markedly reduces entropy. The linear ligand molecule OAm, in contrast, readily aligns and is known to interdigitate into the ligand shell.⁴³ It is very likely that unbound OAm plays the role of *n*-alkanes in entropic bundling¹⁸ for the case of dilution-induced bundling in cyclohexane. Unbound OAm that interdigitates in the shell of bound OAm loses entropy (upper part of Figure 5B). When AuNWs bundle, they can share ordered OAm molecules so that the low-entropy domains overlap and some of the entropic losses are avoided (lower part of Figure 5B). Dense ligand shells prevent preferential alignment of unbound OAm and remove the driving force for bundling (Figure 5A).

It is instructive to compare this mechanism to the action of the well-known “depletion forces” that can initiate agglomeration of colloidal particles. Depletion forces can occur if a colloid contains smaller particles or molecules (the “depletants”) that cannot enter the liquid volumes in the immediate vicinity of the larger particles. The resulting gradients in depletant concentration give rise to an osmotic pressure that pushes the larger particles together.^{36,37,44} The concentration gradient can be due to steric limitations or (for anisotropic depletants) entropic constraints. For example, rod-shaped depletants that orient parallel to the surface of the larger particles lose rotational entropy and thus form a concentration

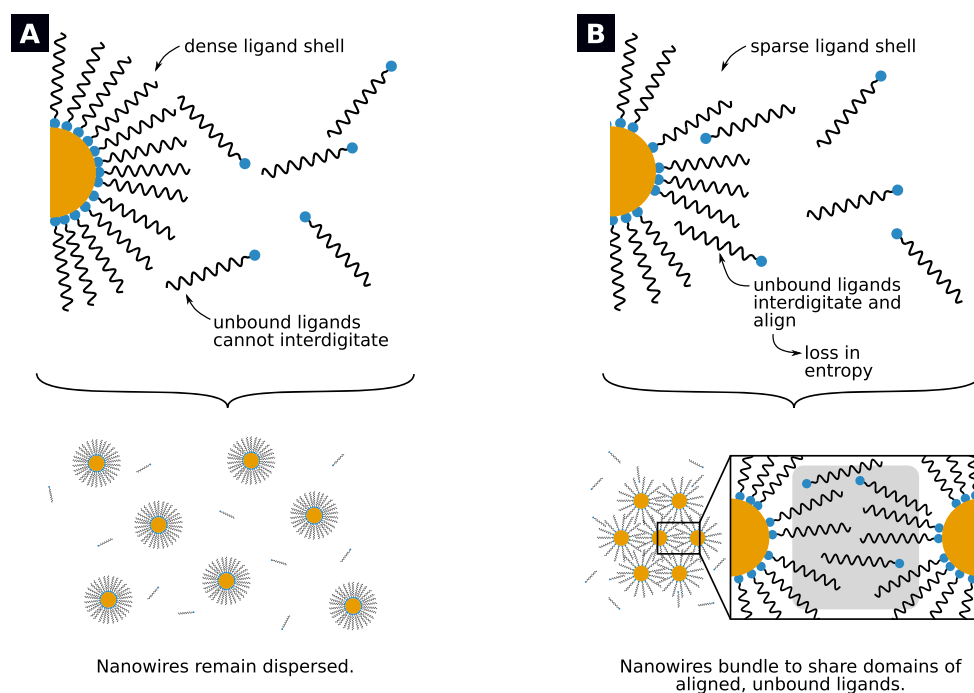


Figure 5. Illustration of the proposed mechanism. (A) Dense ligand shells preclude interdigitation of unbound ligand into the shell. (B) Sparse ligand shells provide gaps where unbound ligand can interdigitate and orient. The associated decrease in entropy is minimized if nanowires form bundles to share domains of ordered ligands (shaded area). The drawings are approximately to scale and show the cross sections of a 1 nm-long wire segment with a shell denser (4.5 ligands/nm^2) (A) and sparser (3.6 ligands/nm^2) (B) than the measured threshold for bundling (4.1 ligands/nm^2).

gradient.^{45–51} One may argue that the mechanism above involves a depletion force that is caused by alignment of the depletant OAm normal to the AuNW surface in the sparse ligand shell.

The role of unbound molecules in nonpolar dispersions has recently attracted interest more broadly. Current reports indicate that the formation of nanoparticle superlattices from nonpolar solvents can be tuned by adding unbound oleic acid or oleylamine to the dispersion, where they act as depletants.^{43,52–55} Winslow et al.⁴³ used molecular dynamics simulations to show that free oleic acid preferably interdigitates into ligand shells and associated this ligand shell swelling with a change in the crystal structure from bcc to fcc. Baranov et al.⁵² assembled semiconductor nanorods covered by phosphonate and triethylphosphine oxide into hexagonal arrays by adding oleic acid and other macromolecules. These reports highlight the role of unbound ligands and similar molecules as destabilizing agents.

CONCLUSIONS

We studied the agglomeration of AuNWs into crystalline bundles upon dilution. Only AuNWs with sufficiently sparse ligand shells exhibit this unusual type of self-assembly. We show evidence for an entropy-driven self-assembly mechanism based on the depletion of linear molecules. Linear solvent or unbound ligand molecules initiate bundling when they interdigitate into the ligand shell and lose some of their rotational entropy.

Note that unbound ligands are in a dynamic equilibrium with the adsorbed ligands on the particles. It is thus impossible to completely remove the destabilizing agent. Few cases of agglomeration by unbound ligand have been reported in

literature, possibly because it is often difficult to conclusively identify the depletant that causes entropic attraction. Note that the mechanism described here is not unique to ultrathin gold nanowires and likely to operate in other nanowires or nanoparticle dispersions with ligands of linear shape.

Our findings have several implications. First, bundling can be turned on and off by controlling the number of adsorbed and excess ligands in the system. This could be of interest for processes that require switching between dispersed and assembled AuNWs such as stamp imprinting AuNWs into transparent conductive electrodes.¹⁴ Second, the ligand grafting density is of importance to colloidal systems beyond the “simple” task of stabilizing a colloid against the van der Waals attraction. Molecular dynamics simulations by Gao et al.¹⁸ indicate that the interaction energies caused by the proposed mechanism are small (on the order of 0.1 to $1 k_B T/\text{nm}$) and can induce bundling only because the attraction accumulates along an elongated contact line of several 10 to $100 \mu\text{m}$. Equally large contact areas might be formed between assembled nanosheets or nanoplatelets^{56–58} and between larger spherical nanoparticles. In such systems, future research may have to pay more attention to grafting densities and the chemical equilibria between adsorbed and unbound ligand.

ASSOCIATED CONTENT

Supporting Information

The Supporting Information is available free of charge at <https://pubs.acs.org/doi/10.1021/acs.jpcc.0c10919>.

Additional figures on the grafting density and AuNW dispersions with added oleylamine and in *n*-hexane and additional data and rationale on the adsorption energy,

as well as calculations on the van der Waals interaction energy (PDF)

AUTHOR INFORMATION

Corresponding Author

Tobias Kraus – INM–Leibniz Institute for New Materials, 66123 Saarbrücken, Germany; Colloid and Interface Chemistry, Saarland University, 66123 Saarbrücken, Germany; orcid.org/0000-0003-2951-1704; Email: tobias.kraus@leibniz-inm.de

Authors

Simon Bettscheider – INM–Leibniz Institute for New Materials, 66123 Saarbrücken, Germany; Colloid and Interface Chemistry, Saarland University, 66123 Saarbrücken, Germany; orcid.org/0000-0001-6068-246X

Björn Kuttich – INM–Leibniz Institute for New Materials, 66123 Saarbrücken, Germany; Colloid and Interface Chemistry, Saarland University, 66123 Saarbrücken, Germany

Lukas F. Engel – INM–Leibniz Institute for New Materials, 66123 Saarbrücken, Germany; Colloid and Interface Chemistry, Saarland University, 66123 Saarbrücken, Germany

Lola González-García – INM–Leibniz Institute for New Materials, 66123 Saarbrücken, Germany; Colloid and Interface Chemistry, Saarland University, 66123 Saarbrücken, Germany

Complete contact information is available at: <https://pubs.acs.org/10.1021/acs.jpcc.0c10919>

Notes

The authors declare no competing financial interest.

ACKNOWLEDGMENTS

The authors thank Robert Drumm for performing TGA measurements, and Eduard Arzt for his continuing support of the project. S.B. thanks the Foundation of German Business for his Ph.D. scholarship.

REFERENCES

- (1) Doblas, D.; Kister, T.; Cano-Bonilla, M.; González-García, L.; Kraus, T. Colloidal Solubility and Agglomeration of Apolar Nanoparticles in Different Solvents. *Nano Lett.* **2019**, *19*, 5246–5252.
- (2) Langmuir, I. The Adsorption of Gases on Plane Surfaces of Glass, Mica and Platinum. *J. Am. Chem. Soc.* **1918**, *40*, 1361–1403.
- (3) Adamson, A. W.; Gast, A. P. *Physical Chemistry of Surfaces*; Wiley: New York, 1997.
- (4) Halder, A.; Ravishankar, N. Ultrafine Single-Crystalline Gold Nanowire Arrays by Oriented Attachment. *Adv. Mater.* **2007**, *19*, 1854–1858.
- (5) Huo, Z.; Tsung, C.-k.; Huang, W.; Zhang, X.; Yang, P. Sub-Two Nanometer Single Crystal Au Nanowires. *Nano Lett.* **2008**, *8*, 2041–2044.
- (6) Lu, X.; Yavuz, M. S.; Tuan, H.-y.; Korgel, B. A.; Xia, Y. Ultrathin Gold Nanowires Can Be Obtained by Reducing Polymeric Strands of Oleylamine-AuCl Complexes Formed via Auophilic Interaction. *J. Am. Chem. Soc.* **2008**, *130*, 8900–8901.
- (7) Pazos-Pérez, N.; Baranov, D.; Irsen, S.; Hilgendorff, M.; Liz-Marzán, L. M.; Giersig, M. Synthesis of Flexible, Ultrathin Gold Nanowires in Organic Media. *Langmuir* **2008**, *24*, 9855–9860.
- (8) Wang, C.; Hu, Y.; Lieber, C. M.; Sun, S. Ultrathin Au Nanowires and Their Transport Properties. *J. Am. Chem. Soc.* **2008**, *130*, 8902–8903.
- (9) Saitoh, M.; Kashiwagi, Y.; Chigane, M. Structural Analysis of Micrometer-Long Gold Nanowires Using a Wormlike Chain Model and Their Rheological Properties. *Soft Matter* **2017**, *13*, 3927–3935.
- (10) Gong, S.; Zhao, Y.; Shi, Q.; Wang, Y.; Yap, L. W.; Cheng, W. Self-assembled Ultrathin Gold Nanowires as Highly Transparent, Conductive and Stretchable Supercapacitor. *Electroanalysis* **2016**, *28*, 1298–1304.
- (11) Porter, A. G.; Ouyang, T.; Hayes, T. R.; Biechele-Speziale, J.; Russell, S. R.; Claridge, S. A. 1-nm-Wide Hydrated Dipole Arrays Regulate AuNW Assembly on Striped Monolayers in Nonpolar Solvent. *Chem.* **2019**, *5*, 2264–2275.
- (12) Roy, A.; Pandey, T.; Ravishankar, N.; Singh, A. K. Semiconductor-like Sensitivity in Metallic Ultrathin Gold Nanowire-Based Sensors. *J. Phys. Chem. C* **2014**, *118*, 18676–18682.
- (13) Reiser, B.; Gerstner, D.; González-García, L.; Maurer, J. H. M.; Kanelidis, I.; Kraus, T. Spinning Hierarchical Gold Nanowire Microfibers by Shear Alignment and Intermolecular Self-Assembly. *ACS Nano* **2017**, *11*, 4934–4942.
- (14) Maurer, J. H. M.; González-García, L.; Reiser, B.; Kanelidis, I.; Kraus, T. Templated Self-Assembly of Ultrathin Gold Nanowires by Nanoimprinting for Transparent Flexible Electronics. *Nano Lett.* **2016**, *16*, 2921–2925.
- (15) Feng, H.; Yang, Y.; You, Y.; Li, G.; Guo, J.; Yu, T.; Shen, Z.; Wu, T.; Xing, B. Simple and Rapid Synthesis of Ultrathin Gold Nanowires, their Self-Assembly and Application in Surface-Enhanced Raman Scattering. *Chem. Commun.* **2009**, *0*, 1984.
- (16) Loubat, A.; Impéror-Clerc, M.; Pansu, B.; Meneau, F.; Raquet, B.; Viau, G.; Lacroix, L.-M. Growth and Self-Assembly of Ultrathin Au Nanowires into Expanded Hexagonal Superlattice Studied by in Situ SAXS. *Langmuir* **2014**, *30*, 4005–4012.
- (17) Reiser, B.; Gerstner, D.; González-García, L.; Maurer, J. H. M.; Kanelidis, I.; Kraus, T. Multivalent Bonds in Self-Assembled Bundles of Ultrathin Gold Nanowires. *Phys. Chem. Chem. Phys.* **2016**, *18*, 27165–27169.
- (18) Gao, H.; Bettscheider, S.; Kraus, T.; Müser, M. H. Entropy Can Bundle Nanowires in Good Solvents. *Nano Lett.* **2019**, *19*, 6993–6999.
- (19) Nough, E. S. A.; Baquero, E. A.; Lacroix, L.-M.; Delpéch, F.; Poteau, R.; Viau, G. Surface-Engineering of Ultrathin Gold Nanowires: Tailored Self-Assembly and Enhanced Stability. *Langmuir* **2017**, *33*, 5456–5463.
- (20) Schubert, U.; Hüsing, N.; Laine, R. M., Eds. *Materials Syntheses*; Springer Vienna: Vienna, 2008; DOI: 10.1007/978-3-211-75125-1.
- (21) Förster, S.; Timmann, A.; Konrad, M.; Schellbach, C.; Meyer, A.; Funari, S. S.; Mulvaney, P.; Knott, R. Scattering Curves of Ordered Mesoscopic materials. *J. Phys. Chem. B* **2005**, *109*, 1347–1360.
- (22) Sundblom, A.; Oliveira, C. L. P.; Palmqvist, A. E. C.; Pedersen, J. S. Modeling in Situ Small-Angle X-ray Scattering Measurements Following the Formation of Mesoporous Silica. *J. Phys. Chem. C* **2009**, *113*, 7706–7713.
- (23) Manet, S.; Schmitt, J.; Impéror-Clerc, M.; Zholobenko, V.; Durand, D.; Oliveira, C. L. P.; Pedersen, J. S.; Gervais, C.; Baccile, N.; Babonneau, F.; et al. Kinetics of the Formation of 2D-Hexagonal Silica Nanostructured Materials by Nonionic Block Copolymer Templating in Solution. *J. Phys. Chem. B* **2011**, *115*, 11330–11344.
- (24) Loubat, A.; Lacroix, L.-M.; Robert, A.; Impéror-Clerc, M.; Poteau, R.; Maron, L.; Arenal, R.; Pansu, B.; Viau, G. Ultrathin Gold Nanowires: Soft-Templating versus Liquid Phase Synthesis, a Quantitative Study. *J. Phys. Chem. C* **2015**, *119*, 4422–4430.
- (25) Smith, A. M.; Johnston, K. A.; Crawford, S. E.; Marbella, L. E.; Millstone, J. E. Ligand Density Quantification on Colloidal Inorganic Nanoparticles. *Analyst* **2017**, *142*, 11–29.
- (26) Thomson, J. W.; Cademartiri, L.; MacDonald, M.; Petrov, S.; Calestani, G.; Zhang, P.; Ozin, G. A. Ultrathin Bi₂S₃ Nanowires: Surface and Core Structure at the Cluster-Nanocrystal Transition. *J. Am. Chem. Soc.* **2010**, *132*, 9058–9068.

- (27) Moreels, I.; Justo, Y.; De Geyter, B.; Hastraete, K.; Martins, J. C.; Hens, Z. Size-Tunable, Bright, and Stable PbS Quantum Dots: A Surface Chemistry Study. *ACS Nano* **2011**, *5*, 2004–2012.
- (28) Vericat, C.; Vela, M. E.; Benitez, G.; Carro, P.; Salvarezza, R. C. Self-Assembled Monolayers of Thiols and Dithiols on Gold: New Challenges for a Well-Known System. *Chem. Soc. Rev.* **2010**, *39*, 1805.
- (29) Karpovich, D. S.; Blanchard, G. J. Direct Measurement of the Adsorption Kinetics of Alkanethiolate Self-Assembled Monolayers on a Microcrystalline Gold Surface. *Langmuir* **1994**, *10*, 3315–3322.
- (30) Schessler, H. M.; Karpovich, D. S.; Blanchard, G. J. Quantitating the Balance between Enthalpic and Entropic Forces in Alkanethiol/Gold Monolayer Self Assembly. *J. Am. Chem. Soc.* **1996**, *118*, 9645–9651.
- (31) Peiretti, L. F.; Quaino, P.; Tielens, F. Competition between Two High-Density Assemblies of Poly(phenyl)thiols on Au(111). *J. Phys. Chem. C* **2016**, *120*, 25462–25472.
- (32) Grönbeck, H.; Curioni, A.; Andreoni, W. Thiols and Disulfides on the Au(111) Surface: The Headgroup-Gold Interaction. *J. Am. Chem. Soc.* **2000**, *122*, 3839–3842.
- (33) Faján, J. L. C.; Teixeira, F.; Gomes, J. R. B.; Cordeiro, M. N. D. S. Effect of van der Waals Interactions in the DFT Description of Self-Assembled Monolayers of Thiols on Gold. *Theor. Chem. Acc.* **2015**, *134*, 67.
- (34) Mete, E.; Yortanlı, M.; Danisman, M. F. A van der Waals DFT Study of Chain Length Dependence of Alkanethiol Adsorption on Au(111): Physisorption vs. Chemisorption. *Phys. Chem. Chem. Phys.* **2017**, *19*, 13756–13766.
- (35) Goubet, N.; Richardi, J.; Albouy, P. A.; Pileni, M. P. How to Predict the Growth Mechanism of Supracrystals from Gold Nanocrystals. *J. Phys. Chem. Lett.* **2011**, *2*, 417–422.
- (36) Evans, D. F.; Wennerström, H. *The Colloidal Domain: Where Physics, Chemistry, Biology, and Technology Meet*, 2nd ed.; Wiley-VCH: New York, 1999.
- (37) Israelachvili, J. N. *Intermolecular and Surface Forces*, 3rd ed.; Academic Press: Boston, MA, 2011.
- (38) Marla, K. T.; Meredith, J. C. Simulation of Interaction Forces between Nanoparticles: End-Grafted Polymer Modifiers. *J. Chem. Theory Comput.* **2006**, *2*, 1624–1631.
- (39) Khan, S. J.; Pierce, F.; Sorensen, C. M.; Chakrabarti, A. Self-Assembly of Ligated Gold Nanoparticles: Phenomenological Modeling and Computer Simulations †. *Langmuir* **2009**, *25*, 13861–13868.
- (40) Martin, T. B.; Jayaraman, A. Identifying the Ideal Characteristics of the Grafted Polymer Chain Length Distribution for Maximizing Dispersion of Polymer Grafted Nanoparticles in a Polymer Matrix. *Macromolecules* **2013**, *46*, 9144–9150.
- (41) Monego, D.; Kister, T.; Kirkwood, N.; Mulvaney, P.; Widmer-Cooper, A.; Kraus, T. Colloidal Stability of Apolar Nanoparticles: Role of Ligand Length. *Langmuir* **2018**, *34*, 12982–12989.
- (42) Parsegian, V. A. *Van der Waals Forces*; Cambridge University Press: Cambridge, U.K., 2006; DOI: 10.2277/0521839068.
- (43) Winslow, S. W.; Swan, J. W.; Tisdale, W. A. The Importance of Unbound Ligand in Nanocrystal Superlattice Formation. *J. Am. Chem. Soc.* **2020**, *142*, 9675–9685.
- (44) Lekkerkerker, H. N.; Tuinier, R. *Colloids and the Depletion Interaction*; Lecture Notes in Physics; Springer Netherlands: Dordrecht, 2011; Vol. 833; DOI: 10.1007/978-94-007-1223-2.
- (45) Auvray, L. Solutions de macromolécules rigides: effets de paroi, de confinement et d'orientation par un écoulement. *J. Phys. (Paris)* **1981**, *42*, 79–95.
- (46) Mao, Y.; Cates, M.; Lekkerkerker, H. Depletion Force in Colloidal Systems. *Phys. A* **1995**, *222*, 10–24.
- (47) Mao, Y.; Cates, M. E.; Lekkerkerker, H. N. W. Depletion Stabilization by Semidilute Rods. *Phys. Rev. Lett.* **1995**, *75*, 4548–4551.
- (48) Mao, Y.; Cates, M. E.; Lekkerkerker, H. N. W. Theory of the Depletion Force due to Rodlike Polymers. *J. Chem. Phys.* **1997**, *106*, 3721–3729.
- (49) Lin, K.-h.; Crocker, J. C.; Zeri, A. C.; Yodh, A. G. Colloidal Interactions in Suspensions of Rods. *Phys. Rev. Lett.* **2001**, *87*, No. 088301.
- (50) Helden, L.; Roth, R.; Koenderink, G. H.; Leiderer, P.; Bechinger, C. Direct Measurement of Entropic Forces Induced by Rigid Rods. *Phys. Rev. Lett.* **2003**, *90*, No. 048301.
- (51) Guu, D.; Dhont, J. K. G.; Vliegthart, G. A.; Lettinga, M. P. Depletion Induced Clustering in Mixtures of Colloidal Spheres and fd-Virus. *J. Phys.: Condens. Matter* **2012**, *24*, 464101.
- (52) Baranov, D.; Fiore, A.; van Huis, M.; Giannini, C.; Falqui, A.; Lafont, U.; Zandbergen, H.; Zanella, M.; Cingolani, R.; Manna, L. Assembly of Colloidal Semiconductor Nanorods in Solution by Depletion Attraction. *Nano Lett.* **2010**, *10*, 743–749.
- (53) Lau, C. Y.; Duan, H.; Wang, F.; He, C. B.; Low, H. Y.; Yang, J. K. W. Enhanced Ordering in Gold Nanoparticles Self-Assembly Through Excess Free Ligands. *Langmuir* **2011**, *27*, 3355–3360.
- (54) Brown, S. L.; Shah, V. D.; Morrell, M. V.; Zubich, M.; Wagner, A.; Denton, A. R.; Hobbie, E. K. Superlattice Formation in Colloidal Nanocrystal Suspensions: Hard-Sphere Freezing and Depletion Effects. *Phys. Rev. E: Stat. Phys., Plasmas, Fluids, Relat. Interdiscip. Top.* **2018**, *98*, No. 062616.
- (55) Kim, D.; Bae, W. K.; Kim, S.-H.; Lee, D. C. Depletion-Mediated Interfacial Assembly of Semiconductor Nanorods. *Nano Lett.* **2019**, *19*, 963–970.
- (56) Ithurria, S.; Tessier, M. D.; Mahler, B.; Lobo, R. P. S. M.; Dubertret, B.; Efron, A. L. Colloidal Nanoplatelets with Two-Dimensional Electronic Structure. *Nat. Mater.* **2011**, *10*, 936–941.
- (57) Sichert, J. A.; Tong, Y.; Mutz, N.; Vollmer, M.; Fischer, S.; Milowska, K. Z.; García Cortadella, R.; Nickel, B.; Cardenas-Daw, C.; Stolarczyk, J. K.; et al. Quantum Size Effect in Organometal Halide Perovskite Nanoplatelets. *Nano Lett.* **2015**, *15*, 6521–6527.
- (58) Nasilowski, M.; Mahler, B.; Lhuillier, E.; Ithurria, S.; Dubertret, B. Two-Dimensional Colloidal Nanocrystals. *Chem. Rev.* **2016**, *116*, 10934–10982.

SUPPORTING INFORMATION TO: Bundling of Nanowires Induced by Unbound Ligand

Simon Bettscheider,^{†,‡} Björn Kuttich,^{†,‡} Lukas F. Engel,^{†,‡} Lola
González-García,^{†,‡} and Tobias Kraus^{*,†,‡}

[†]*INM — Leibniz Institute for New Materials, Campus D2 2, 66123 Saarbrücken, Germany*

[‡]*Colloid and Interface Chemistry, Saarland University, Campus D2 2, 66123 Saarbrücken,
Germany*

E-mail: tobias.kraus@leibniz-inm.de

1 Ligand grafting density and the free energy of adsorption

In order to determine the grafting density of a monolayer ligand shell, we purified a dispersion of AuNWs several times (see main text). The results are shown in Fig. S1.

Besides the grafting density, we intend to approximately quantify the adsorption equilibrium between a gold surface and oleylammonium chloride. To this end, we estimate the order of magnitude of the free energy of adsorption based on data from the literature and use this value to calculate a Langmuir adsorption isotherm. Following classic adsorption isotherms,^{1,2} we expect some ligands to desorb when the amount of ligand is reduced from 28 mmol/L to 0.9 mmol/L. We further know from the experiments discussed in the main text

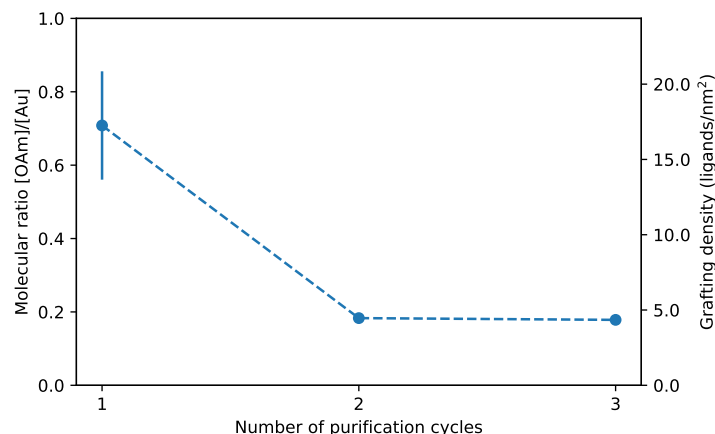


Figure S1: Amount of ligand in the system and nominal grafting density for an increasing number of purification cycles as obtained by TGA. The error bars display \pm the standard deviation of measuring three independent batches of AuNWs. For 2 and 3 purification cycles, the error bars are within the size of the marker. The dashed line is only a guide to the eye.

that the transition from dispersed to bundled AuNWs occurs at a ligand concentration of ca. 4.4 mmol/L. Above this threshold, the AuNWs are dispersed. Below, they are bundled.

We start by assessing a better-known system: the adsorption of alkanethiols onto gold. From experimental data by Karpovich and Blanchard and by Schessler *et al.*, we know that the free energy of adsorption for octadecanethiol onto gold at room temperature is $\Delta G_{\text{ads}} = -5.5$ kcal/mol, the enthalpy is $\Delta H_{\text{ads}} = -20$ kcal/mol, and the entropy is $\Delta S_{\text{ads}} = -48$ cal/(mol K).

We now estimate the free energy of adsorption for oleylammonium chloride adsorbing onto a gold surface. For the enthalpic part of the free energy, we know from DFT calculations⁵ that the enthalpy of adsorption for an amine is -23.4 kcal/mol and for an ammonium chloride end group -40.1 kcal/mol. It is difficult to directly compare these values to experimental data but we can compare to DFT values of alkanethiols. There, the reported adsorption enthalpies are on the order of -50 kcal/mol.⁶⁻¹⁰ This means that the adsorption enthalpy of the ammonium chloride group is 20% smaller than the one of a thiol group.

For the entropic part of the free energy, we make the very crude assumption that the change in entropy due to adsorption for oleylammonium chloride is the same as for 1-

octadecanethiol.^{3,4} Both molecules possess the same chain length of 18 carbon atoms. They differ in their functional group, which will not influence the entropy fundamentally, and in the double bond at the center of oleylamine. This latter difference most likely influences the entropy of adsorption since it will influence the packing of a monolayer. For the present order-of-magnitude estimation, we ignore this difference.

Given these estimates for the enthalpy and entropy of adsorption of oleylammonium chloride, we obtain the adsorption isotherm depicted in Fig. S2B with a free energy of adsorption of $\Delta G_{\text{ads}} = -1.9 \text{ kcal/mol} = -8.1 \text{ kJ/mol}$. This should be interpreted as an estimate and not as an accurate account of the adsorption isotherm of oleylammonium chloride onto a gold surface.

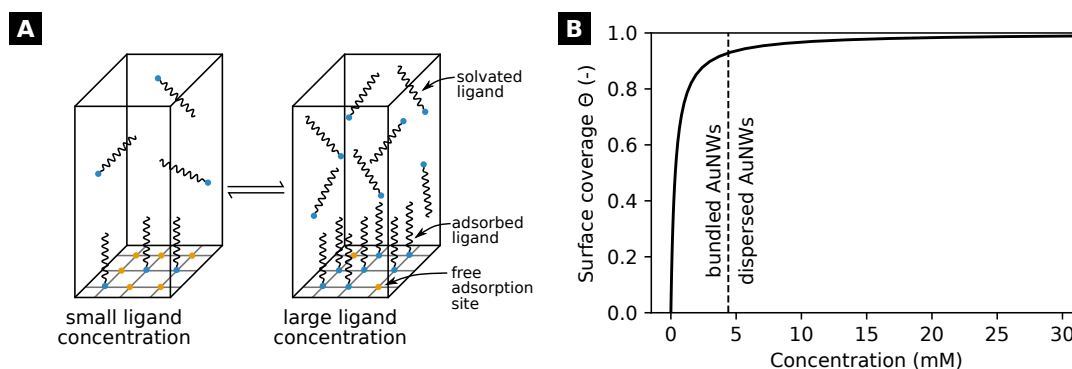


Figure S2: **A** Schematic of the adsorption equilibrium between free and adsorbed ligands and the influence of diluting a dispersion. **B** Estimated adsorption isotherm with an free energy of adsorption

2 Addition of oleylamine to dispersed AuNWs

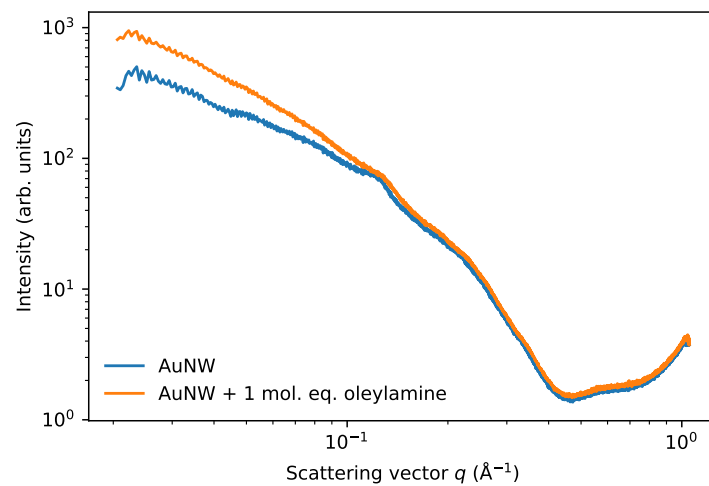


Figure S3: SAXS curve of AuNWs dispersed in cyclohexane at 6 mg/mL (blue) and the same sample with 1 mol of the ligand oleylamine added per mole of gold (orange).

3 Bundling in dependence of amount of ligand in linear alkanes

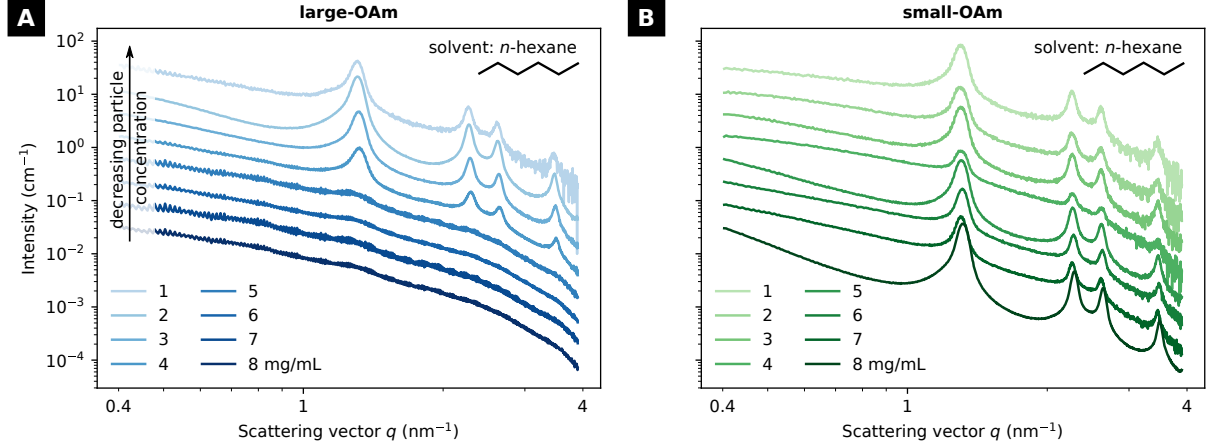


Figure S4: SAXS scattering curves of AuNWs in *n*-hexane with different amounts ligand (see Table 1 in the main text for ligand quantities) and at different nanowire concentrations. **A** In the sample centrifuged once with the larger amount of ligand, distinct scattering peaks are present in the curves with smaller nanowire concentrations of 1 to 3 mg/mL, indicating AuNWs assembled in elongated bundles. For larger concentrations, no scattering peaks can be found indicating that the AuNWs are completely dispersed. **B** In the sample centrifuged twice with the smaller amount of ligand, distinct scattering peaks indicative of bundles are present at all concentrations.

4 The van der Waals interaction between two gold cylinders

In the following, the vdW interaction is approximated by pairwise summation with the Hamaker-Lifshitz theory neglecting for retardation screening. The equations are summarized in¹¹ and.¹² The interaction energy G is given by

$$G = -\frac{2A}{3z} \sum_{i,j=1}^{\infty} \frac{\Gamma^2(i+j+\frac{1}{2})}{i!j!(i-1)!(j-1)!} \left(\frac{R_1}{z}\right)^{2i} \left(\frac{R_2}{z}\right)^{2j}, \quad (\text{S1})$$

where A is the Hamaker constant, Γ is the Gamma function, R_1 and R_2 are the radii of the cylinders, and z is the distance between the centers of the cylinders. In our case, $R_1 = R_2 = R$ so that

$$G = -\frac{2A}{3z} \sum_{i,j=1}^{\infty} \frac{\Gamma^2(i+j+\frac{1}{2})}{i!j!(i-1)!(j-1)!} \left(\frac{R}{z}\right)^{2(i+j)}. \quad (\text{S2})$$

The Hamaker constant for a body of material 1 interacting through medium 3 with a body of material 2 can be approximated by

$$A_{123} = (\sqrt{A_1} - \sqrt{A_3})(\sqrt{A_2} - \sqrt{A_3}), \quad (\text{S3})$$

which simplifies to

$$A_{121} = (\sqrt{A_1} - \sqrt{A_2})^2 \quad (\text{S4})$$

in our case where a cylinder of material 1 interacts with another cylinder of the same material through medium 2. The resulting vdW interaction energy, with Hamaker constants of 1.96×10^{-19} J for gold and 4.69×10^{-20} J for the hydrocarbons from Ref. 11 p. 64, is plotted in Fig. S5. At an interwire distance of 5.9 nm as measured in the AuNWs bundled in cyclohexane, the interaction energy due to van der Waals forces is $1.245 \times 10^{-3} k_B T/\text{nm}$.

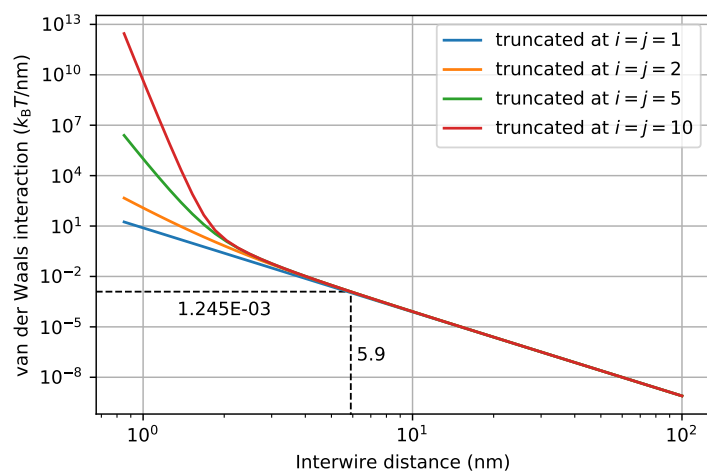


Figure S5: The van der Waals interaction between two parallel cylinders of diameter of 1.7 nm made from gold across alkanes. The marked distance of 5.9 nm is the one found in bundled AuNWs in cyclohexane. To calculate the interaction energy, Hamaker constants of 1.96×10^{-19} J for gold and 4.69×10^{-20} J for hydrocarbon from Ref. 11 p. 64 were used.

References

1. Langmuir, I. The Adsorption of Gases on Plane Surfaces of Glass, Mica and Platinum. *Journal of the American Chemical Society* **1918**, *40*, 1361–1403, DOI: 10.1021/ja02242a004.
2. Adamson, A. W.; Gast, A. P. *Physical Chemistry of Surfaces*; Wiley: New York, 1997.
3. Karpovich, D. S.; Blanchard, G. J. Direct Measurement of the Adsorption Kinetics of Alkanethiolate Self-Assembled Monolayers on a Microcrystalline Gold Surface. *Langmuir* **1994**, *10*, 3315–3322, DOI: 10.1021/1a00021a066.
4. Schessler, H. M.; Karpovich, D. S.; Blanchard, G. J. Quantitating the Balance between Enthalpic and Entropic Forces in Alkanethiol/Gold Monolayer Self Assembly. *Journal of the American Chemical Society* **1996**, *118*, 9645–9651, DOI: 10.1021/ja961565r.
5. Nouh, E. S. A.; Baquero, E. A.; Lacroix, L.-M.; Delpech, F.; Poteau, R.; Viau, G. Surface-Engineering of Ultrathin Gold Nanowires: Tailored Self-Assembly and Enhanced Stability. *Langmuir* **2017**, *33*, 5456–5463, DOI: 10.1021/acs.langmuir.7b00477.

6. Vericat, C.; Vela, M. E.; Benitez, G.; Carro, P.; Salvarezza, R. C. Self-Assembled Monolayers of Thiols and Dithiols on Gold: New Challenges for a Well-Known System. *Chemical Society Reviews* **2010**, *39*, 1805, DOI: 10.1039/b907301a.
7. Peiretti, L. F.; Quaino, P.; Tielens, F. Competition between Two High-Density Assemblies of Poly(phenyl)thiols on Au(111). *The Journal of Physical Chemistry C* **2016**, *120*, 25462–25472, DOI: 10.1021/acs.jpcc.6b08977.
8. Grönbeck, H.; Curioni, A.; Andreoni, W. Thiols and Disulfides on the Au(111) Surface: The Headgroup-Gold Interaction. *Journal of the American Chemical Society* **2000**, *122*, 3839–3842, DOI: 10.1021/ja993622x.
9. Fajín, J. L. C.; Teixeira, F.; Gomes, J. R. B.; Cordeiro, M. N. D. S. Effect of van der Waals Interactions in the DFT Description of Self-Assembled Monolayers of Thiols on Gold. *Theoretical Chemistry Accounts* **2015**, *134*, 67, DOI: 10.1007/s00214-015-1666-y.
10. Mete, E.; Yortanlı, M.; Danışman, M. F. A van der Waals DFT Study of Chain Length Dependence of Alkanethiol Adsorption on Au(111): Physisorption vs. Chemisorption. *Physical Chemistry Chemical Physics* **2017**, *19*, 13756–13766, DOI: 10.1039/C7CP01653K.
11. Parsegian, V. A. *Van der Waals Forces*; Cambridge University Press: Cambridge, 2006; DOI: 10.2277/0521839068.
12. Langbein, D. Van der Waals Attraction Between Cylinders, Rods or Fibers. *Physik der Kondensierten Materie* **1972**, *15*, 61–86, DOI: 10.1007/BF02422580.

3.3 Publication 3: On the geometric stability of an inorganic nanowire and an organic ligand shell

Reprinted with permission from:

S. Bettscheider, T. Kraus, N.A. Fleck, On the geometric stability of an inorganic nanowire and an organic ligand shell, *J. Mech. Phys. Solids.* 123 (2019) 3–19.
<https://doi.org/10.1016/j.jmps.2018.07.017>.

© 2018 The Authors. Published by Elsevier Ltd. Open access article published under [CC BY 4.0](https://creativecommons.org/licenses/by/4.0/).



Contents lists available at ScienceDirect

Journal of the Mechanics and Physics of Solids

journal homepage: www.elsevier.com/locate/jmps

On the geometric stability of an inorganic nanowire and an organic ligand shell

Simon Bettscheider^{a,b}, Tobias Kraus^{a,b}, Norman A. Fleck^{c,*}^a INM - Leibniz Institute for New Materials, Campus D2.2, 66123 Saarbrücken, Germany^b Colloid and Interface Chemistry, Saarland University, Campus, 66123 Saarbrücken, Germany^c Cambridge University Engineering Department, Trumpington Street, Cambridge CB2 1PZ, UK

ARTICLE INFO

Article history:

Received 4 July 2018

Revised 21 July 2018

Accepted 21 July 2018

Available online 23 July 2018

Keywords:

Rayleigh-Plateau instability

Colloidal nanowire

Microstructure evolution

Surface diffusion

Ligand stabilisation

Core-shell nanowire

ABSTRACT

The break-up of a nanowire with an organic ligand shell into discrete droplets is analysed in terms of the Rayleigh-Plateau instability. Explicit account is taken of the effect of the organic ligand shell upon the energetics and kinetics of surface diffusion in the wire. Both an initial perturbation analysis and a full numerical analysis of the evolution in wire morphology are conducted, and the governing non-dimensional groups are identified. The perturbation analysis is remarkably accurate in obtaining the main features of the instability, including the pinch-off time and the resulting diameter of the droplets. It is conjectured that the surface energy of the wire and surrounding organic shell depends upon both the mean and deviatoric invariants of the curvature tensor. Such a behaviour allows for the possibility of a stable nanowire such that the Rayleigh-Plateau instability is not energetically favourable. A stability map illustrates this. Maps are also constructed for the final droplet size and pinch-off time as a function of two non-dimensional groups that characterise the energetics and kinetics of diffusion in the presence of the organic shell. These maps can guide future experimental activity on the stabilisation of nanowires by organic ligand shells.

© 2018 The Authors. Published by Elsevier Ltd.
This is an open access article under the CC BY license.
(<http://creativecommons.org/licenses/by/4.0/>)

1. Introduction

Wires are prototypical components in electrical circuits; a metal wire is the simplest way of connecting two points electrically. The microelectronics industry has successfully evolved the miniaturization of metal and semiconductor wires (“interconnects”) using *subtractive* processes based on lithography. Thin films are deposited and selectively etched to give in-plane features of dimension down to 10 nm in the latest semiconductor technologies (ITRS, 2011). However, thin wires are inherently unstable. This can be traced to the fact that a circular cylinder of finite length has a larger surface area than a sphere of equal volume. The surface energy associated with this surface area is the driving force for the Rayleigh-Plateau instability: a long circular cylinder evolves into an array of spheres (Plateau, 1873; Rayleigh, 1878). The kinetic mechanism for the instability is either bulk or surface diffusion. The relative importance of these two mechanisms depends upon the relative diffusion constants and upon the wire diameter: at sufficiently small scale and at sufficiently low temperature,

* Corresponding author.

E-mail address: naf1@eng.cam.ac.uk (N.A. Fleck).<https://doi.org/10.1016/j.jmps.2018.07.017>0022-5096/© 2018 The Authors. Published by Elsevier Ltd. This is an open access article under the CC BY license. (<http://creativecommons.org/licenses/by/4.0/>)

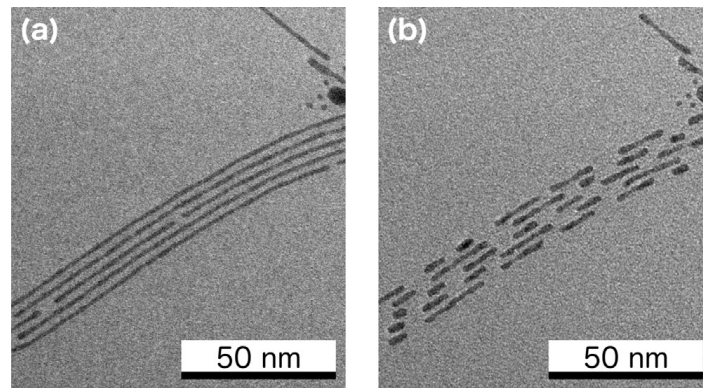


Fig. 1. Transmission Electron Microscopy (TEM) micrographs of chemically synthesised gold nanowires on a carbon-coated copper grid. The synthesis followed that of [Reiser et al. \(2016, 2017\)](#), by adaption of the original protocol of [Feng et al. \(2009\)](#). (a) Initial state, and (b) after electron beam heating for 212 s at 200 kV.

surface diffusion dominates ([Frost and Ashby, 1982](#)). The Rayleigh-Plateau instability has been observed experimentally for a wide range of materials including copper ([Toimil Molares et al., 2004](#)), silver ([Bid et al., 2005](#)), platinum ([Zhao et al., 2006](#)), gold ([Karim et al., 2006](#)), tin ([Shin et al., 2007](#)), nickel ([Zhou et al., 2009](#)), and cobalt ([Huang et al., 2010](#)). Recently, the Rayleigh-Plateau instability has also been observed in silicon nanowires ([Barwicz et al., 2012](#)). These authors argue that the surface self-diffusivity of silicon is significantly increased by the presence of a reduced hydrogen environment, which provides a kinetic path for surface diffusion at temperatures exceeding 700 °C.

Recently, a new class of nanowires of diameter below 10 nm has been made by chemical *synthesis*. Such “ultrathin” nanowires form when solutions of metal or semiconductor salts are reduced in the presence of certain organic molecules. The detailed formation mechanism of the wires is a topic of present debate ([Cademartiri and Ozin, 2009](#); [Repko and Cademartiri, 2012](#)); proposed routes involve the self-assembly of the organic molecules into micelle-like structures that template wire growth. Regardless of the precise mechanism of formation, the result is a metal core surrounded by a “ligand shell” of organic molecules. A common choice of organic ligand is oleylamine, a simple hydrocarbon chain with 18 carbon atoms and a single double bond at its centre, which forms an organic ligand shell of thickness approximately 2 nm. To date, ultrathin nanowires made from gold ([Lu et al., 2008](#); [Wang et al., 2008](#)) ([Fig. 1a](#)), iron-platinum ([Wang et al., 2007](#)), silver ([Li et al., 2015](#)), calcium phosphate ([Sadasivan et al., 2005](#)), barium sulfate ([Hopwood and Mann, 1997](#)), tellurium ([Xi et al., 2006](#)), copper sulfide ([Liu et al., 2005](#)), bismuth sulfide ([Cademartiri et al., 2008](#)), antimony trisulfide ([Malakooti et al., 2008](#)), samarium oxide ([Yu et al., 2006](#)), and ruthenium ([Zhao et al., 2016](#)) have all been synthesised in this manner. Such wires hold promise for new electronic devices such as mechanically flexible, optically transparent, or printable electronics ([Chen et al., 2013](#); [Gong et al., 2014](#); [Maurer et al., 2015](#); [2016](#); [Pazos-Perez et al., 2008](#); [Sánchez-Iglesias et al., 2012](#); [Wang et al., 2008](#)).

Ultrathin nanowires are prone to the Rayleigh-Plateau instability. Since the characteristic pinch-off time for the Rayleigh-Plateau instability scales with the fourth power of the wire radius ([Nichols and Mullins, 1965a](#); [1965b](#)), ultrathin nanowires break-up into spheres at much shorter times and at lower temperatures than thicker wires. For example, [Takahata et al. \(2016\)](#) report the break-up of ultrathin gold nanorods of diameter of 2 nm (and length of 6 nm) into spheres after 5400 s at 80 °C in liquid chloroform; similar observations have been reported by other authors ([Lacroix et al., 2014](#); [Lu et al., 2008](#); [Xu et al., 2013](#); [Xu et al., 2018](#)). Electron beam heating in a transmission electron microscope (TEM) leads to the break-up of gold nanowires into a string of nanorods within four minutes, see [Fig. 1b](#).

[Ciuculescu et al. \(2009\)](#), [Huber et al. \(2012\)](#), [Wu et al. \(2015\)](#), and [Takahata et al. \(2016\)](#) all suggest that the break-up of ultrathin nanowires is delayed by the presence of an organic ligand shell. However, the mechanism of stabilisation remains unclear: it can be energetic or kinetic in nature, or a combination of the two. This lack of understanding inhibits a systematic search for ligands that could enhance wire stability to a point where storage at room temperature does not limit their applicability. The purpose of the present paper is to provide a framework for understanding the stabilisation mechanisms and to generate guiding principles for the selection of suitable ligands.

2. Governing field equations

The evolution in shape of a circular wire into spherical droplets by surface diffusion has been analysed by [Nichols and Mullins \(1965a,b\)](#): they treated the bulk of the wire as rigid and considered diffusion along the bare surface of the wire. This surface diffusion was driven by a gradient in chemical potential associated with local surface curvature. Finite shape changes were included in the analysis such that a long cylindrical wire breaks-up into an array of droplets.

In the case of ultrathin nanowires, the wire surface has a more complex structure: the wire core is surrounded by the organic ligand shell, and the wire and shell are dispersed within an organic solvent, see [Fig. 2](#). While the mechanism for shape evolution of the nanowire remains surface diffusion (see [Fig. 2a](#)), driven by a gradient in chemical potential, the

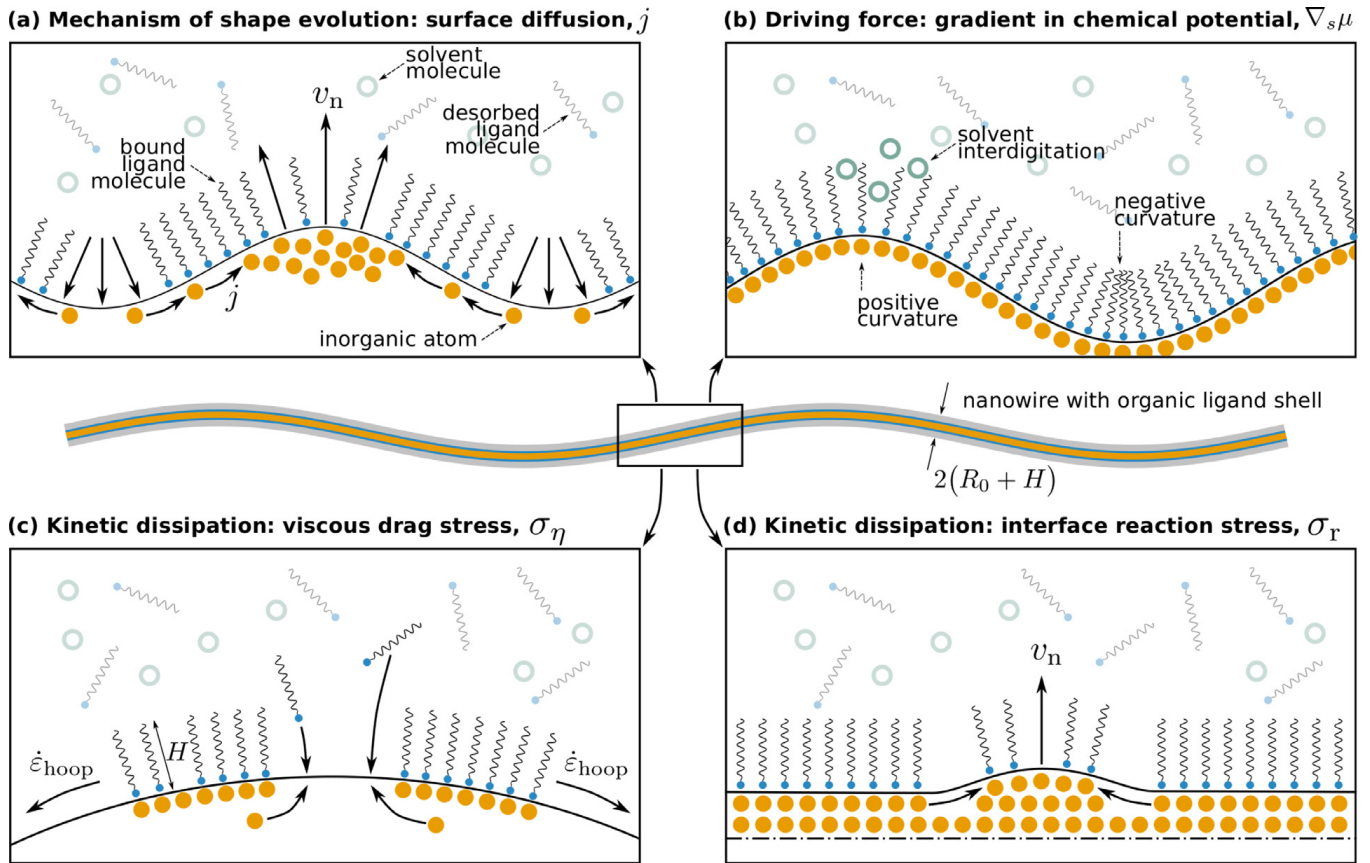


Fig. 2. An inorganic nanowire and organic ligand shell in a solvent. (a) A flux j of wire atoms diffuse along the wire surface and lead to an outward normal velocity v_n . (b) Diffusion is driven by the surface gradient in chemical potential μ . (c) Adsorption and desorption of ligands is resisted by a viscous drag stress σ_η . (d) Plating of surface atoms is resisted by an interface reaction stress σ_r .

presence of the shell introduces additional physical phenomena that need to be incorporated into the model. For example, the local packing arrangement of ligands within the shell, and thereby the free energy of the shell, depend upon local curvature (see Fig. 2b). In the present study, the surface energy γ is treated as a function of surface curvature. The organic ligand shell is of fixed thickness H but its circumference changes when the wire profile evolves. When the circumference of the shell changes, additional ligand molecules must assemble (or disassemble) into the shell and viscous losses occur, see Fig. 2c. This is modelled by a viscous drag stress σ_η that depends upon the hoop strain rate of the organic ligand shell. Additionally, the plating of surface-diffusing atoms onto the surface of the wire involves an interface reaction and an attendant viscous drag, see Fig. 2d. This is idealised as a dissipative interface reaction, involving an interface reaction stress σ_r and its work conjugate, the normal velocity of the interface v_n . These notions build upon previous models for grain growth due to surface diffusion, see for example Ashby (1969), Cocks (1992), and Cocks et al. (1998).

In order to derive the governing equations for shape evolution of a nanowire surrounded by an organic ligand shell, we first introduce the geometry and kinematics of shape evolution of a small wire. Second, the chemical potential, interface reaction stress, and viscous drag stress are described and a governing ordinary differential equation (ODE) is developed for the outward normal velocity v_n along the surface of the wire in its current configuration. An updating scheme is then given for the wire profile as a function of time.

2.1. Geometry

Consider a circular cylindrical nanowire of radius R_0 and a surrounding organic ligand shell of thickness H , see Figs. 2 and 3a. Assume that the wire and shell maintain a circular cross-section when its shape evolves by the diffusion of atoms along the surface of the wire in the axial direction. Assume that the initial radius of the wire Y depends upon the axial position X according to

$$Y = R_0 + e_0 \sin(\omega X) \quad (1)$$

in terms of an initial imperfection amplitude e_0 and wavenumber $\omega = 2\pi/\lambda$, where λ is the perturbation wavelength. It proves convenient to describe the initial shape of the wire in terms of intrinsic coordinates (S, Θ) rather than (X, Y) , where S is the arc length along the surface profile and Θ is the inclination of the surface in the initial, reference configuration. The

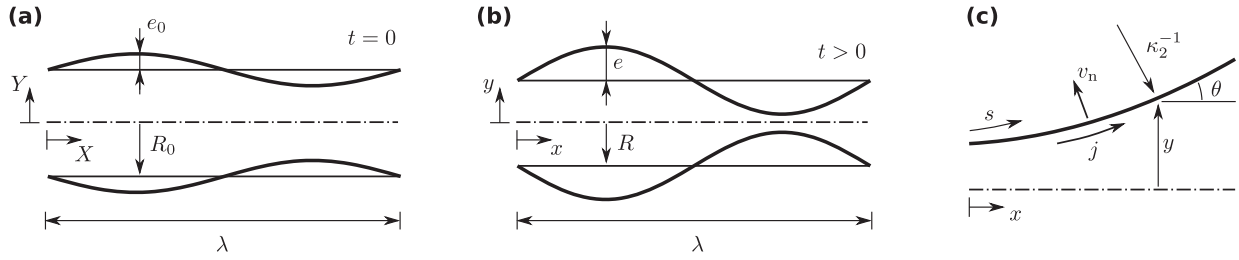


Fig. 3. (a) Nanowire of initial mean radius R_0 and sinusoidal perturbation of amplitude e_0 and wavelength λ , at time $t = 0$. (b) In the current configuration at time $t > 0$, the nanowire has a mean radius R and a sinusoidal perturbation of amplitude e . (c) Geometry of current configuration.

transformation is straightforward:

$$dS^2 = dX^2 + dY^2 \quad \text{and} \quad (2a)$$

$$\tan \Theta = \frac{dY}{dX}. \quad (2b)$$

such that

$$\frac{dX}{dS} = \cos \Theta \quad \text{and} \quad (3a)$$

$$\frac{dY}{dS} = \sin \Theta. \quad (3b)$$

Now consider the current configuration at time t . Write $y(x)$ as the deformed shape at time t , in the current configuration. The challenge is to predict $y(x, t)$, due to surface diffusion. Write s as the arc length along the wire surface and θ as the inclination of the surface of the wire, as shown in Fig. 3c. We seek $s = s(S, t)$ and $\theta = \theta(S, t)$.

The two principal curvatures of the wire surface are

$$\kappa_1 = \frac{\cos \theta}{y}, \quad \text{and} \quad (4a)$$

$$\kappa_2 = -\frac{\partial \theta}{\partial s}, \quad (4b)$$

and the stretch factor Λ relates s in the current configuration to S in the initial configuration, such that

$$\Lambda = \frac{\partial s}{\partial S}. \quad (5)$$

2.2. Nanowire shape evolution by surface diffusion

The dominant mechanism for shape evolution of a nanowire in the presence of an organic ligand shell is taken to be surface diffusion, see for example Ciuculescu et al. (2009). We begin by relating the surface gradient of the volumetric surface diffusive flux \mathbf{j} to the outward normal velocity v_n of the surface of the wire as demanded by mass conservation, such that

$$\nabla_s \cdot \mathbf{j} + v_n = 0. \quad (6)$$

Now, the force \mathbf{f} that drives surface diffusion is the surface gradient of the chemical potential μ ,

$$\mathbf{f} = \nabla_s \mu \quad (7)$$

and, in the absence of other kinetic dissipation processes, the flux \mathbf{j} scales with \mathbf{f} according to

$$\mathbf{j} = -\frac{\mathcal{D}\mathbf{f}}{\Omega}, \quad (8)$$

in terms of a mobility \mathcal{D}/Ω , where \mathcal{D} is the interface diffusion constant in units of $\text{m}^6\text{J}^{-1}\text{s}^{-1}$ and Ω is the atomic volume. \mathcal{D} is related to the interface diffusion coefficient D_b and the effective thickness of the boundary δ_b according to $\mathcal{D} = D_b \delta_b \Omega / (kT)$, where k is the Boltzmann constant and T is absolute temperature. We take $\Omega = \delta_b^3$.

Limit attention to a solid of revolution, and consequently Eqs. (6) and (7) reduce to

$$v_n = -\frac{1}{y} \frac{\partial(jy)}{\partial s}, \quad \text{and} \quad (9a)$$

$$f = \frac{\partial \mu}{\partial s}, \quad (9b)$$

respectively, as discussed by [Nichols and Mullins \(1965a\)](#).

Now, if additional dissipation processes are at play, f not only drives the diffusive flux j but also needs to drive the additional drag processes. Here, we shall assume the presence of an interface reaction associated with the outward normal velocity of the wire surface v_n , and viscous drag associated with the hoop strain rate of the wire surface, so that (8) now reads

$$j = -\frac{\mathcal{D}}{\Omega} (f - f_r - f_\eta), \quad (10)$$

where f_r and f_η are the forces needed to drive the interface reaction and the viscous dissipation, respectively. Following [Ashby \(1969\)](#), [Cocks \(1992\)](#), and [Cocks et al. \(1998\)](#), the latter two forces can be written as

$$f_r = -\Omega \frac{\partial \sigma_r}{\partial s}, \quad \text{and} \quad (11a)$$

$$f_\eta = -\Omega \frac{\partial \sigma_\eta}{\partial s}, \quad (11b)$$

where σ_r and σ_η are the stresses normal to the interface that drive the interface reaction and the viscous drag, respectively. Insert [Eqs. \(11a\)](#) and [\(11b\)](#) into [Eq. \(10\)](#) to give

$$j = -\frac{\mathcal{D}}{\Omega} \frac{\partial \mu}{\partial s} - \mathcal{D} \frac{\partial \sigma_r}{\partial s} - \mathcal{D} \frac{\partial \sigma_\eta}{\partial s}. \quad (12)$$

The remainder of this section will deal with the determination of μ , σ_r , and σ_η .

2.3. The chemical potential μ

The wire is coated by an organic ligand shell and we assume that a representative species of the wire-shell-interface comprises a surface metallic atom and a ligand molecule bound to it. The chemical potential μ is, by definition, the energy required to bring a metallic atom from the bulk to the surface of the wire and to bring its partner organic ligand molecule from remote solvent to the bound state of the metal-organic complex.

Assume that the free energy of the organic ligand molecule depends upon its local configuration, as characterised by the curvature (κ_1, κ_2) of the wire at this location. We envisage that the free energy of the organic ligand molecule is less when bound to a sphere of total curvature $2\kappa_s$ (such that $\kappa_1 = \kappa_2 = \kappa_s > 0$) than for a cylinder of total curvature κ_s (such that $\kappa_1 = \kappa_s$ and $\kappa_2 = 0$). Also, the free energy of a surface of saddle point shape with zero total curvature (such that $\kappa_1 = -\kappa_2 = \kappa_s$) is higher still. An empirical relation for the chemical potential of the metal-organic-ligand complex that captures these features is

$$\mu = 2\Omega\gamma\kappa_m, \quad (13)$$

where $\kappa_m = (\kappa_1 + \kappa_2)/2$ is the mean curvature, and the surface energy γ depends upon an effective curvature κ_e . The effective curvature is taken to be a function of the two invariants of the curvature tensor and we shall assume that it adopts the simple quadratic form

$$\kappa_e^2 = \alpha\kappa_m^2 + (1 - \alpha)\kappa_d^2, \quad (14)$$

where the deviatoric curvature reads $\kappa_d = (\kappa_1 - \kappa_2)/2$ and the “shape factor” α is between zero and unity. Note that the choice $\alpha = 1$ implies that $\kappa_e = |\kappa_m|$ while $\alpha = 0$ implies $\kappa_e = |\kappa_d|$.

It remains to stipulate a functional form for $\gamma(\kappa_e)$. We adopt the empirical choice

$$\gamma(\kappa_e) = \gamma_0 \exp\left(c\left(\frac{\kappa_e}{\kappa_0} - 1\right)\right), \quad (15)$$

where γ_0 , c , and κ_0 are material constants. The sensitivity of γ to κ_e is largely captured by the value of c and we shall assume both positive and negative values for c in our analysis below.

The authors recognise that the continuum approach loses validity as the length scales approach atomistic dimensions. However, experimental evidence on the transition from cylindrical wires to spheres suggests that the wires behave as a continuum, with a smooth surface that can be described by continuous functions, such as that used in [\(14\)](#). The present study could be complemented by molecular dynamics (MD) simulations, but it will be a challenge to match the timescales of MD simulations (on the order of picoseconds) to the timescales as observed in an experiment (on the order of 100–1000 s). The current approach is phenomenological, and it may be possible to calibrate the parameters of the model using predictions from MD simulations of the wires' interfaces.

2.4. The interface reaction stress σ_r and viscous stress σ_η

The plating/removal of atoms onto/from a surface involves local rearrangement of atoms as they change configuration from a bulk co-ordination number on the interior to a reduced co-ordination number on the surface. Such rearrangements involve viscous drag at low temperatures, modelled by an interface reaction stress. Following Cocks (1992) and Cocks et al. (1998), the reaction stress is assumed to take the form of a power law according to

$$\sigma_r = \sigma_{r0} \left(\frac{v_n}{|v_n|} \right) \left(\frac{|v_n|}{v_{r0}} \right)^M, \quad (16)$$

in terms of a reference velocity v_{r0} , a reaction strength σ_{r0} , and an exponent M . An appropriate choice for the exponent is $M = 1$ (Ashby, 1969; Cocks, 1992; Cocks et al., 1998); it leads to considerable simplification of the governing equations for shape evolution of the nanowire.

In order to obtain the viscous drag stress σ_η we consider an organic ligand shell subjected to equi-biaxial tension. A derivation of σ_η as a function of v_n is given in the appendix. Here, we simply state the results. The viscous drag stress reads

$$\sigma_\eta = \frac{\partial \phi_\eta}{\partial v_n} = 4H\eta\kappa_m^2 v_n, \quad (17)$$

where the viscosity η is taken to be a function of curvature,

$$\eta(\kappa_e) = \eta_0 \exp \left(d \left(\frac{\kappa_e}{\kappa_0} - 1 \right) \right) \quad (18)$$

in terms of the material constants η_0 , d and κ_0 .

2.5. Governing equation for normal velocity

We proceed to insert Eqs. (13), (16), and (17) into Eqs. (12) and (9a) to obtain a non-linear second order ODE in v_n ,

$$\frac{\Lambda y v_n}{\mathcal{D}} - \frac{\partial}{\partial S} \left(\frac{y}{\Lambda} \frac{\partial}{\partial S} \left[\sigma_{r0} \left(\frac{v_n}{|v_n|} \right) \left(\frac{|v_n|}{v_{r0}} \right)^M + 4H\eta\kappa_m^2 v_n + 2\gamma\kappa_m \right] \right) = 0. \quad (19)$$

3. Perturbation analysis

In order to identify the dominant non-dimensional groups and assess their relative importance in dictating wire stability, a linear perturbation analysis is now conducted. Later, the predictions of the perturbation analysis will be compared with a full numerical solution. Consider a cylindrical wire of initial shape as given by Eq. (1), and as depicted in Fig. 3a. Assume that the perturbation evolves with time t as illustrated in Fig. 3b such that

$$y(x, t) = R(t) + e(t) \sin(\omega x), \quad (20)$$

where $x = X$, and $R(t)$ and $e(t)$ are to be determined. Our aim is to re-express the ODE (19) in v_n as an ODE in de/dt . Conservation of mass dictates that

$$\int_0^\lambda Y^2 dX = \int_0^\lambda y^2(t) dx \quad (21)$$

and consequently

$$R^2 + \frac{1}{2}e^2 = R_0^2 + \frac{1}{2}e_0^2. \quad (22)$$

The two principal curvatures, as defined in Eqs. (4a) and (4b), evolve with time according to

$$\kappa_1 = \left(1 + (\omega e)^2 \cos^2(\omega x) \right)^{-1/2} \left(\left(R_0^2 + \frac{1}{2}e_0^2 - \frac{1}{2}e^2 \right)^{\frac{1}{2}} + e \sin(\omega x) \right)^{-1} \quad \text{and} \quad (23a)$$

$$\kappa_2 = \omega^2 e \sin(\omega x) \left(1 + (\omega e)^2 \cos^2(\omega x) \right)^{-3/2}, \quad (23b)$$

upon making use of the identity $\partial y / \partial x = \tan \theta$ and the relations (20) and (22). Now expand κ_1 and κ_2 in terms of increasing powers of e and neglect terms of order e^2 and higher to obtain

$$R_0 \kappa_1 = 1 - \frac{e}{R_0} \sin(\omega x) + \mathcal{O}(e^2), \quad \text{and} \quad (24a)$$

$$R_0 \kappa_2 = \frac{e}{R_0} (R_0 \omega)^2 \sin(\omega x) + \mathcal{O}(e^3), \quad (24b)$$

so that the mean curvature reads

$$2R_0\kappa_m = 1 + \frac{e}{R_0} \left((R_0\omega)^2 - 1 \right) \sin(\omega x) + \mathcal{O}(e^2), \quad (25)$$

and the effective curvature reduces to

$$2R_0\kappa_e = 1 + \frac{e}{R_0} \left((2\alpha - 1)(R_0\omega)^2 - 1 \right) \sin(\omega x) + \mathcal{O}(e^2). \quad (26)$$

Likewise, expand the surface energy $\gamma(\kappa_e)$ and the viscosity $\eta(\kappa_e)$ as defined in (15) and (18), respectively, to give

$$\gamma(\kappa_e) = \gamma_0 + \frac{\gamma_0 c e}{R_0} \left((2\alpha - 1)(R_0\omega)^2 - 1 \right) \sin(\omega x) + \mathcal{O}(e^2), \quad \text{and} \quad (27a)$$

$$\eta(\kappa_e) = \eta_0 + \frac{\eta_0 d e}{R_0} \left((2\alpha - 1)(R_0\omega)^2 - 1 \right) \sin(\omega x) + \mathcal{O}(e^2), \quad (27b)$$

upon taking $\kappa_0 = 1/(2R_0)$.

Now, for small perturbations, we may write

$$\frac{1}{y} \frac{\partial}{\partial s} \left(y \frac{\partial}{\partial s} \right) \approx \frac{\partial^2}{\partial x^2}, \quad (28)$$

so that, by limiting the analysis to cases where $M = 1$ in Eq. (16), the governing ODE (19) becomes

$$\frac{1}{\mathcal{D}} v_n - \frac{\partial^2}{\partial x^2} \left[\frac{\sigma_{r0}}{\nu_{r0}} v_n \right] - \frac{\partial^2}{\partial x^2} \left[4H\eta\kappa_m^2 v_n \right] = \frac{\partial^2}{\partial x^2} \left[2\gamma\kappa_m \right]. \quad (29)$$

The outward normal velocity v_n scales with \dot{R} and \dot{e} according to

$$v_n = \dot{R} + \dot{e} \sin(\omega x), \quad (30)$$

where $\dot{(\)}$ denotes $d(\)/dt$. Recall that \dot{R} is a function of \dot{e} as dictated by (22) such that

$$\dot{R} = -\frac{1}{2} \frac{e}{R_0} \dot{e} + \mathcal{O}(e^2). \quad (31)$$

Since we neglect terms of order e^2 and higher, we can neglect the contribution from \dot{R} to v_n , and (29) can be linearised to

$$\frac{R_0^4}{\mathcal{D}\gamma_0} \frac{\dot{e}}{R_0} \left(1 + \frac{\mathcal{D}\sigma_{r0}(R_0\omega)^2}{\nu_{r0}R_0^2} + \frac{\mathcal{D}H\eta_0(R_0\omega)^2}{R_0^4} \right) = \frac{e(R_0\omega)^2}{R_0} \left(\left[1 + (2\alpha - 1)c \right] (R_0\omega)^2 - 1 - c \right), \quad (32)$$

upon making use of (30) to (27a).

We proceed to introduce the non-dimensional geometric variables

$$\bar{\omega} = R_0\omega, \quad \bar{e} = e/R_0, \quad (33)$$

the non-dimensional time \bar{t} as

$$\bar{t} = (1 + c) \frac{\mathcal{D}\gamma_0 t}{R_0^4}, \quad (34)$$

and the non-dimensional material groups

$$\chi_1 = \frac{1 + c}{1 + (2\alpha - 1)c}, \quad \chi_2 = \bar{\sigma}_{r0} + \bar{\eta}_0, \quad \bar{\sigma}_{r0} = \frac{\mathcal{D}\sigma_{r0}}{R_0^2\nu_{r0}}, \quad \text{and} \quad \bar{\eta}_0 = \frac{\mathcal{D}H\eta_0}{R_0^4}. \quad (35)$$

Note that χ_1 contains only material parameters associated with the energetic parameter c and the shape of the $\kappa_e(\kappa_m, \kappa_d)$ locus. In contrast, χ_2 includes only the kinetic terms $\bar{\sigma}_{r0}$ and $\bar{\eta}_0$. Eq. (32) can be re-written to express the perturbation growth rate for a given perturbation wavenumber in the compact form

$$\frac{1}{\bar{e}} \frac{d\bar{e}}{d\bar{t}} = \frac{\bar{\omega}^2 - \chi_1^{-1} \bar{\omega}^4}{1 + \chi_2 \bar{\omega}^2}. \quad (36)$$

We proceed to evaluate the stability of a perturbation for any assumed wavenumber $\bar{\omega}$ by evaluating the sign of the perturbation growth rate $d\bar{e}/d\bar{t}$. A positive value of $d\bar{e}/d\bar{t}$ implies instability of the wire profile, whereas a negative value implies stability. Upon examining (36), we find that the wire is stable for all $\bar{\omega}$ provided (α, c) satisfy the values

$$0 < \alpha < \frac{1}{2} \quad \text{and} \quad c < -1, \quad \text{or} \quad (37a)$$

$$\frac{1}{2} < \alpha < 1 \quad \text{and} \quad \frac{-1}{2\alpha - 1} < c < -1, \quad (37b)$$

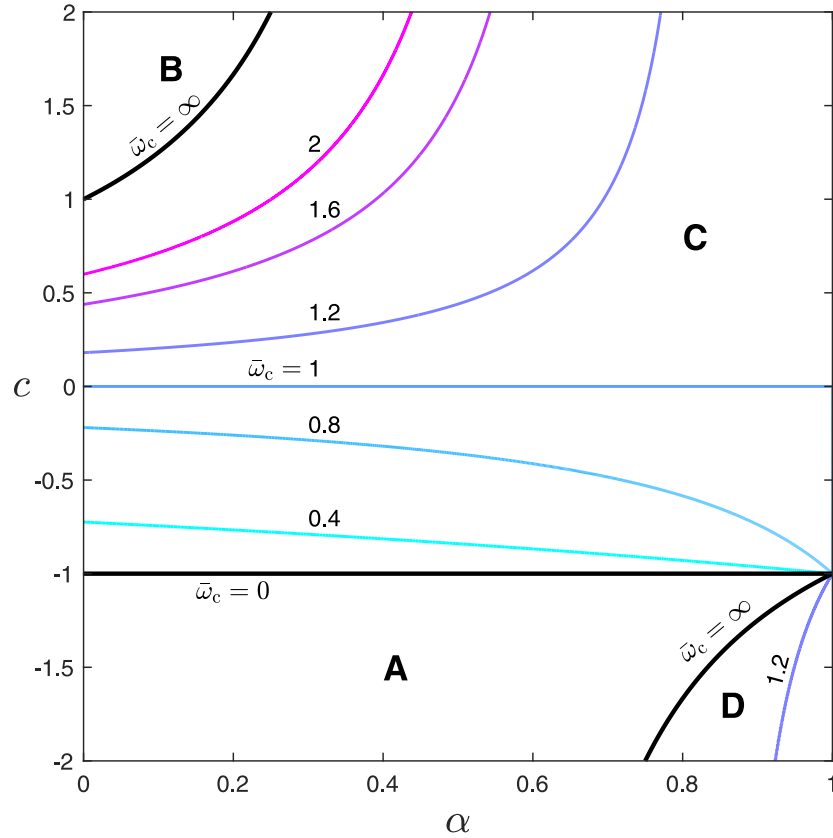


Fig. 4. The four regimes of stability, with contours of critical wavenumber $\bar{\omega}_c$. Regime A: stable such that $d\bar{e}/d\bar{r} < 0$ for all $\bar{\omega}$. Regime B: unstable such that $d\bar{e}/d\bar{r} > 0$ for all $\bar{\omega}$. Regime C: stable for $\bar{\omega} > \bar{\omega}_c$. Regime D: stable for $\bar{\omega} < \bar{\omega}_c$.

and we label this regime A in (α, c) space. The wire is unstable for all $\bar{\omega}$, when

$$0 < \alpha < \frac{1}{2} \quad \text{and} \quad c > \frac{-1}{2\alpha - 1}, \quad (38)$$

and this is labelled regime B in (α, c) space. The critical perturbation wavenumber $\bar{\omega}_c$ at which $d\bar{e}/d\bar{r} = 0$ follows immediately from (36) as

$$\bar{\omega}_c = (\chi_1)^{1/2}. \quad (39)$$

Note that the perturbation is conditionally stable for wavenumbers $\bar{\omega} > \bar{\omega}_c$ for (α, c) in regime C of (α, c) space:

$$0 < \alpha < \frac{1}{2} \quad \text{and} \quad c < \frac{-1}{2\alpha - 1}, \quad \text{or} \quad (40a)$$

$$\frac{1}{2} < \alpha < 1 \quad \text{and} \quad c > \frac{-1}{2\alpha - 1}. \quad (40b)$$

Finally, the wire is conditionally stable for wavenumbers $\bar{\omega} < \bar{\omega}_c$ in regime D, where

$$0 < \alpha < \frac{1}{2} \quad \text{and} \quad c > \frac{-1}{2\alpha - 1}, \quad \text{or} \quad (41a)$$

$$\frac{1}{2} < \alpha < 1 \quad \text{and} \quad c < \frac{-1}{2\alpha - 1}. \quad (41b)$$

The regimes A to D are marked on (α, c) space in Fig. 4 and contours of the critical perturbation wavenumber $\bar{\omega}_c$ are included.

Salient features of the map are now discussed. For the choice $c = 0$, the surface energy γ is constant and $\bar{\omega}_c = 1$, as predicted by Nichols and Mullins (1965b). The range of wavenumbers $\bar{\omega} > \bar{\omega}_c$, for which the wire is stable, shrinks as c increases, such that for sufficiently large c (and small α) regime B is entered and the wire is unconditionally unstable. Recall that a positive value of c leads to an increase in γ with increasing effective curvature κ_e , see (15). Alternatively, a negative value of c implies a reduction in γ with increasing κ_e , and this choice of value for c stabilises the wire profile. Thus, for

$c < -1$, regime A is entered and the wire is unconditionally stable for all $\bar{\omega}$. Regime D is small in extent: this regime of conditional stability for $\bar{\omega} < \bar{\omega}_c$ exists only for large negative c and large positive α .

It is emphasised that the above perturbation analysis is based on (19), which contains both kinetic and energetic terms. Simplification of (19) leads to the first order Eq. (36), and it is noted that the numerator on the r.h.s. of (36) involves only energetic terms while the denominator has only kinetic terms. Consequently, the stability regimes, as plotted in Fig. 4, depend only on the energetic terms, and are independent of the various assumptions made in the kinetic part of the model. Thus, the response plotted in Fig. 4 has broad applicability and the conclusions drawn from the perturbation analysis are rather general.

3.1. Prediction of final droplet size and pinch-off time

The above perturbation analysis can be used to estimate the radius R_s of the spherical droplet that arises from break-up of the wire from the fastest growing perturbation. Also, an estimate for the pinch-off time \bar{t}_p required to convert the wire into an array of such spherical droplets can be obtained.

It is recognised that a spherical droplet is attained only at $t \rightarrow \infty$. However, we can identify a finite pinch-off time \bar{t}_p by assuming arbitrarily that the wire pinches off when \bar{y} at any location along the wire has dropped to a selected value of $(1 - \bar{e}_p)$. The radius R_s of the final spherical droplet is set by the value of wavenumber $\bar{\omega}_E$ for which the perturbation growth rate $\bar{e}^{-1}(d\bar{e}/d\bar{t})$ is a maximum. Now, the extremum of $\bar{e}^{-1}(d\bar{e}/d\bar{t})$ with respect to $\bar{\omega}$ follows from (36) as

$$\left(\frac{1}{\bar{e}} \frac{d\bar{e}}{d\bar{t}}\right)_E = \frac{1}{\chi_1 \chi_2^2} \left(\left[1 + \chi_1 \chi_2\right]^{\frac{1}{2}} - 1 \right)^2. \quad (42)$$

and occurs at $\bar{\omega} = \bar{\omega}_E$, where

$$\bar{\omega}_E^2 = \chi_2^{-1} \left(\left[1 + \chi_1 \chi_2\right]^{\frac{1}{2}} - 1 \right). \quad (43)$$

Contours of $\bar{\omega}_E$ are shown in (χ_1, χ_2) space in Fig. 5a. Note that the fastest growing wavenumber scales as $\bar{\omega}_E = (\chi_1/2)^{1/2}$ for small χ_1 or small χ_2 . The ratio $\bar{\omega}_E/\bar{\omega}_c$ follows directly from (39) and (43) such that

$$\left(\frac{\bar{\omega}_E}{\bar{\omega}_c}\right)^2 = (\chi_1 \chi_2)^{-1} \left(\left[1 + \chi_1 \chi_2\right]^{\frac{1}{2}} - 1 \right), \quad (44)$$

as shown in Fig. 5b.

Conservation of mass between a spherical droplet of radius R_s and a wavelength λ of wire requires $3\pi R_0^2 \lambda = 4\pi R_s^3$, and consequently the ratio R_s/R_0 reads

$$\left(\frac{R_s}{R_0}\right)^6 = \left(\frac{3\pi}{2}\right)^2 \chi_2 \left(\left[1 + \chi_1 \chi_2\right]^{\frac{1}{2}} - 1 \right)^{-1}, \quad (45)$$

upon making use of (43). This dependence of (R_s/R_0) upon (χ_1, χ_2) is illustrated in Fig. 5c: (R_s/R_0) increases monotonically with increasing χ_2 and decreasing χ_1 . Note that, for small χ_1 or small χ_2 , (45) reduces to

$$\frac{R_s}{R_0} = \left(\frac{3\pi}{\sqrt{2}}\right)^{\frac{1}{3}} \chi_1^{\frac{1}{6}}, \quad (46)$$

Now consider the pinch-off time \bar{t}_p . Full numerical simulations (discussed later) reveal that the pinch-off time is dominated by the initial stage of perturbation growth at small \bar{e} : consequently, the value of $(\bar{e}^{-1}(d\bar{e}/d\bar{t}))_E$ can be used to estimate \bar{t}_p . Integration of (42) from an initial imperfection of amplitude \bar{e}_0 to an arbitrary pinch-off value \bar{e}_p gives

$$\bar{t}_p = \chi_1 \chi_2^2 \left(\left[1 + \chi_1 \chi_2\right]^{\frac{1}{2}} - 1 \right)^{-2} \ln \left(\frac{\bar{e}_p}{\bar{e}_0} \right). \quad (47)$$

The logarithmic dependence of \bar{t}_p upon \bar{e}_p/\bar{e}_0 implies that \bar{t}_p is relatively insensitive to the precise choice of \bar{e}_0 and \bar{e}_p , but for definiteness we shall take $\bar{e}_0 = 10^{-3}$ and $\bar{e}_p = 0.8$ in the presentation of numerical results below. The formula (47) is shown in graphical form in Fig. 5d; it simplifies to $\bar{t}_p = 4/\chi_1$ for small (χ_1, χ_2) .

4. Full numerical study

The above perturbation analysis considered the initial growth of a small imperfection. A full numerical solution is now obtained to study the shape evolution in both the initial and the later stages of shape evolution. The solution strategy builds upon that of Nichols and Mullins (1965a).

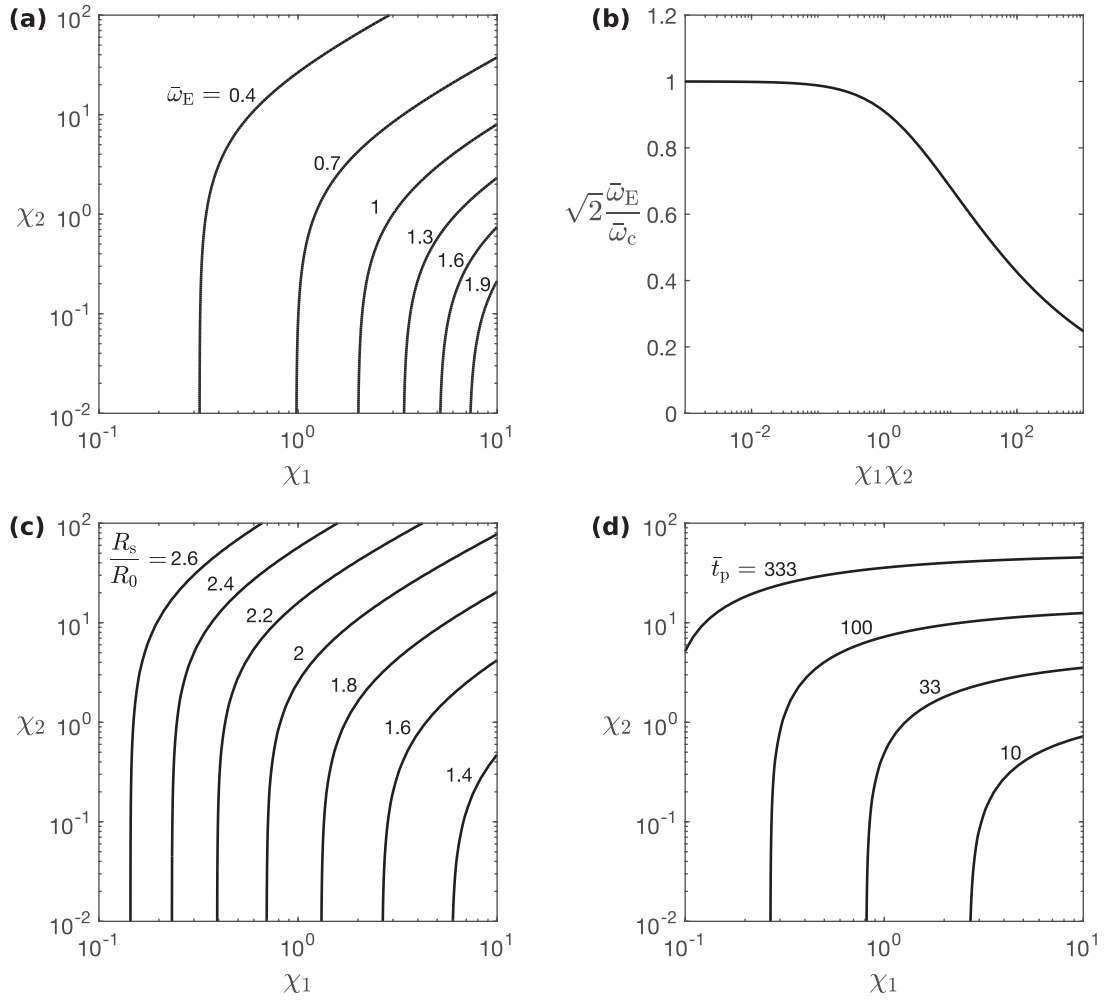


Fig. 5. (a) Contours of the fastest growing wavenumber $\bar{\omega}_E$ in the $(\chi_1 \chi_2)$ plane. (b) $\bar{\omega}_E/\bar{\omega}_c$ versus $\chi_1 \chi_2$. (c) Contours of radius of spherical droplet R_s , normalised by the initial wire radius R_0 , in the $(\chi_1 \chi_2)$ plane. (d) Contours of pinch-off time \bar{t}_p in the $(\chi_1 \chi_2)$ plane.

4.1. Numerical implementation

We proceed to obtain a numerical solution to (19). First, we non-dimensionalise the problem as follows. Lengths are non-dimensionalised by the initial wire radius R_0 , curvatures by $2R_0$, and the outward normal velocity v_n by $R_0^3/((1+c)\mathcal{D}\gamma_0)$ such that

$$\bar{x} = x/R_0; \quad \bar{y} = y/R_0; \quad \bar{S} = S/R_0; \quad \bar{\kappa}_i = 2R_0\kappa_i; \quad \bar{v}_n = \frac{R_0^3 v_n}{(1+c)\mathcal{D}\gamma_0}, \quad (48)$$

where the subscript i denotes m, d, e for the mean, deviatoric, and effective curvature, respectively. Non-dimensionalise γ and η such that $\bar{\gamma} = (1+c)^{-1}(\gamma/\gamma_0)$ and $\bar{\eta} = \eta/\eta_0$, write $\kappa_0 = 1/(2R_0)$, and again limit attention to the case of a linear viscous interface reaction, i.e. $M = 1$. Then, the governing Eq. (19) reduces to

$$\bar{v}_n - \frac{1}{\bar{y}\bar{\Lambda}} \frac{\partial}{\partial \bar{S}} \left(\frac{\bar{y}}{\bar{\Lambda}} \frac{\partial}{\partial \bar{S}} [\bar{\sigma}_{r0}\bar{v}_n + \bar{\eta}\bar{\eta}_0\bar{\kappa}_m^2\bar{v}_n] \right) = \frac{1}{\bar{y}\bar{\Lambda}} \frac{\partial}{\partial \bar{S}} \left(\frac{\bar{y}}{\bar{\Lambda}} \frac{\partial}{\partial \bar{S}} [\bar{\gamma}\bar{\kappa}_m] \right). \quad (49)$$

Note that the dependent variables \bar{y}, \bar{x} , and θ can be described as a function of $(\bar{t}, \bar{S}; \bar{\sigma}_{r0}, \bar{\eta}_0, \alpha, c, d)$ and the initial conditions $(\bar{Y}, \bar{X}, \Theta)$. To simulate the evolution of wire geometry, we use a numerical scheme based on finite differences in space and a forward Euler scheme in time, in similar manner to that of Nichols and Mullins (1965a). Our implementation differs from theirs as we employ a full Lagrangian formulation, as stated in Eqs. (5) and (19). The scheme is summarised briefly in the following paragraph.

The starting point of a simulation is the initial profile as parametrised by $\bar{y}(\bar{S})$ and $\theta(\bar{S})$, where the variable \bar{S} is discretised into equidistant steps of value \bar{h} , such that $\bar{S}_i = i\bar{h}$ for $i = 0, 1, 2, \dots$. Periodic boundary conditions are enforced over the perturbation wavelength $\bar{\lambda} = 2\pi/\bar{\omega}$. The simulation begins with the evaluation of the two principal curvatures, $\bar{\kappa}_1$ and $\bar{\kappa}_2$, by central differences. Central differences are also used to compute other spatial derivatives, as needed. For evaluation of

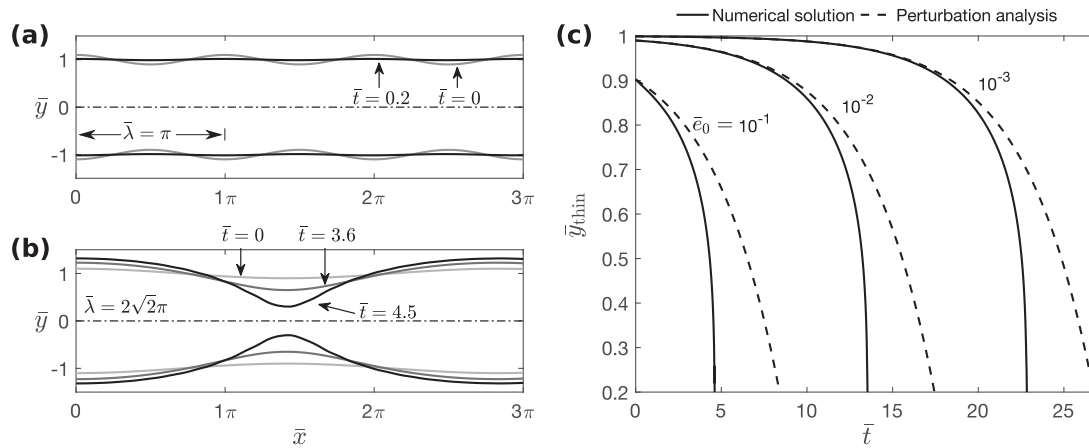


Fig. 6. Shape evolution of a bare wire with $c = 0$, $\bar{\sigma}_{r0} = 0$ and $\bar{\eta}_0 = 0$. (a) The perturbation decays for $\bar{\lambda} = \pi$, which is smaller than the critical wavelength $\bar{\lambda}_c = 2\pi$. (b) The perturbation grows for $\bar{\lambda} = 2\sqrt{2}\pi > \bar{\lambda}_c$. (c) Prediction of the time-evolution of the radius at the thinnest wire site, $\bar{y}_{\text{thin}} = \bar{y}(\bar{x} = \bar{\lambda}/2)$, for three choices of \bar{e}_0 . Full numerical solution as solid line; perturbation analysis as dashed line.

Eq. (49), this gives a system of linear equations for \bar{v}_n , which are solved by a standard solver algorithm¹. The time derivative of the stretch ratio Λ and of the inclination θ are given by

$$\dot{\Lambda}(\bar{S}_i) = -\bar{v}_n \frac{\partial \theta}{\partial \bar{S}} \quad \text{and} \quad \dot{\theta}(\bar{S}_i) = \frac{1}{\Lambda} \frac{\partial \bar{v}_n}{\partial \bar{S}}, \quad (50)$$

respectively. The forward Euler method is used to update $\Lambda(\bar{S}_i)$ and $\theta(\bar{S}_i)$. The new profile is obtained by fitting a third-order Lagrange polynomial to the function $\Lambda \sin \theta$, and the integral

$$\bar{y}(\bar{S}_i) - \bar{y}(0) = \int_0^{\bar{S}_i} \Lambda \sin(\theta) d\bar{S}', \quad (51)$$

is evaluated using a Newton-Cotes scheme. Periodic boundary conditions dictate that $\dot{\bar{y}}(0) = \bar{v}_n(0)$. Eq. (49) is then solved in finite difference form, the geometry is updated over the time step, and the process is repeated. We note in passing that $\bar{x}(\bar{S}_i)$ is not required in the simulation but its value can be tracked in a similar manner to that of $\bar{y}(\bar{S}_i)$. Numerical stability is ensured by choosing a suitably small time increment. In agreement with the comments by Nichols and Mullins (1965a), instabilities appear for time increments of $\Delta \bar{t} \gtrsim 0.8 \times \bar{h}^4$. Throughout this study, the time increment is kept at $\Delta \bar{t} = 0.4 \times \bar{h}^4$.

4.2. Prototypical results

Checks were performed to ensure that the predictions of the perturbation analysis agree with the full numerical solution in the early stages of perturbation growth. For simplicity, we consider the reference case $c = \bar{\sigma}_{r0} = \bar{\eta}_0 = 0$, corresponding to a nanowire absent the organic ligand shell, as analysed by Nichols and Mullins (1965a). Typical results for the shape evolution are given in Fig. 6 for the choices $\bar{\lambda} = \pi$ and $\bar{\lambda} = 2\sqrt{2}\pi$. Note that the critical perturbation wavelength $\bar{\lambda}_c = 2\pi/\bar{\omega}_c$ takes a value of 2π in the present case. A stable response is obtained for $\bar{\lambda} = \pi < \bar{\lambda}_c$, see Fig. 6a, whereas the perturbation grows for $\bar{\lambda} = 2\sqrt{2}\pi > \bar{\lambda}_c$, see Fig. 6b.

Now focus attention on the time-evolution of the thinnest section of the wire, \bar{y}_{thin} , again for $c = \bar{\sigma}_{r0} = \bar{\eta}_0 = 0$ and $\bar{\lambda} = 2\sqrt{2}\pi$. The full numerical solution is compared with the perturbation analysis in Fig. 6c for selected values of initial perturbation amplitude \bar{e}_0 . Recall that we have chosen to define the pinch-off time \bar{t}_p on the basis that $\bar{e}_p = 0.8$ such that $\bar{y}_{\text{thin}}(\bar{t}_p) = 1 - \bar{e}_p = 0.2$. The predicted evolution of the thinnest section of the wire from the perturbation analysis is included in Fig. 6c. Excellent agreement is obtained in the initial stage of instability growth, but there is some divergence between perturbation theory and the full numerical prediction as the wire develops a deep notch at the pinch-off location. It is evident that \bar{t}_p scales as $-\ln(\bar{e}_0)$ for both the numerical analysis and the perturbation analysis, recall (47).

4.3. Comparison of initial perturbation analysis and full numerical solution

The perturbation analysis reveals that the early growth of the Rayleigh-Plateau instability is independent of the value of d and is only controlled by χ_1 , which characterises the effective surface energy of wire and organic ligand shell, and by χ_2 , which characterises the kinetics of interface reaction and viscous drag.

How accurate is the perturbation analysis in terms of prediction of the final droplet radius and of the pinch-off time? The predictions (45) for R_s/R_0 and (47) for \bar{t}_p from the perturbation analysis are plotted in Fig. 7 using χ_1 as the ordinate and

¹ Matlab function mldivide as implemented in Matlab 2017b.

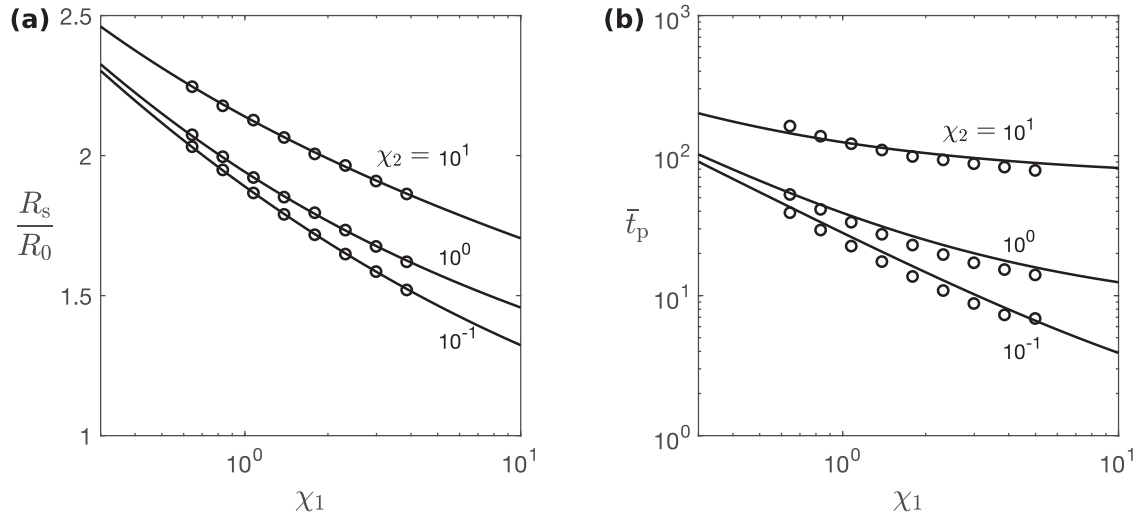


Fig. 7. (a) Comparison of analytical solution (45) (solid line) and full numerical solution (data points) for the radius of spherical droplets; (b) comparison of analytical solution (47) (solid line) and full numerical solution (data points) for the pinch-off time.

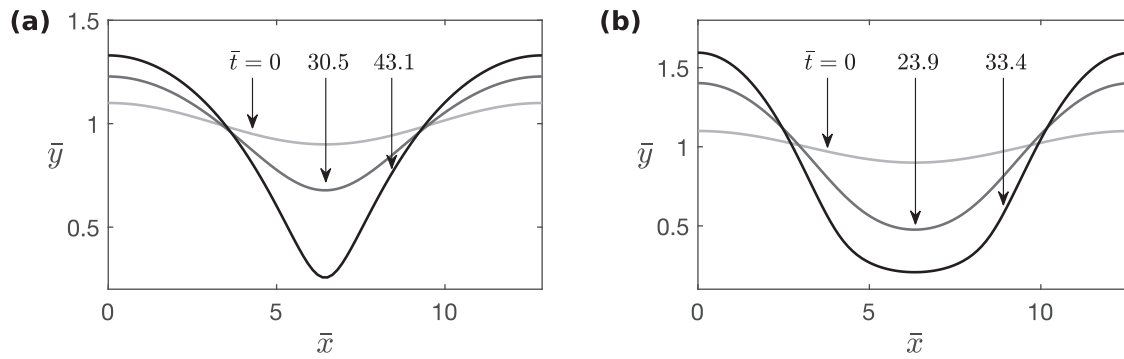


Fig. 8. Sensitivity of the wire profile to the kinetic parameters $\bar{\sigma}_{r0}$ and $\bar{\eta}_0$ for $(\chi_1, \chi_2) = (1, 10)$ and $(\alpha, c, d) = (0.5, 0, 0)$. (a) $\bar{\sigma}_{r0} = 10$ and $\bar{\eta}_0 = 0$. (b) $\bar{\sigma}_{r0} = 0$ and $\bar{\eta}_0 = 10$.

for selected values of χ_2 . Full numerical results are included on the same plots for the choice $d = 0$. Excellent agreement between the perturbation and full numerical analyses is noted for both R_s/R_0 and \bar{t}_p implying that the main features of the instability are dictated by early growth of the imperfection, with (χ_1, χ_2) playing the main role. Hence, the maps of Figs. 5c and d remain accurate beyond the initial growth phase of the instability.

4.4. Influence of the kinetic parameters upon morphology and pinch-off time

We anticipate that the later stages of the instability depend upon the various non-dimensional groups contained within χ_1 and χ_2 . For example, consider $\chi_2 = \bar{\sigma}_{r0} + \bar{\eta}_0$. What if we keep χ_2 fixed and vary the ratio $\bar{\sigma}_{r0}/\bar{\eta}_0$? To explore this, we have performed a full numerical simulation for the case $(\bar{\sigma}_{r0}, \bar{\eta}_0)$ equal to $(10, 0)$ and then equal to $(0, 10)$ such that $\chi_2 = 10$ in both simulations. The other parameters were held fixed at $\alpha = 0.5$, $c = 0$, and $d = 0$. As anticipated, the early growth of the instability is the same in both cases, see Fig. 8. But at later times, the pinch-off shape is sharper for the choice $\bar{\sigma}_{r0} = 10$ and $\bar{\eta}_0 = 0$ (Fig. 8a) than for the other choice (Fig. 8b).

It remains to explore the role of d in influencing the instability. Consider the evolution of wire shape for the choice $d = -1$ in Fig. 9a and for $d = 1$ in Fig. 9b. In both cases, we take $\alpha = 0.5$, $c = 0$, $\bar{\sigma}_{r0} = 0$, and $\bar{\eta}_0 = 10$ such that $\chi_1 = 1$ and $\chi_2 = 10$. (We note in passing that the plot in Fig. 8b is for the same parameter values, but with $d = 0$.) A sharp notch develops in the profile for $d = -1$, whereas for $d = 1$ the degree of viscous drag within the organic ligand shell has a strong stabilising influence, and the wire adopts a uniform high curvature κ_1 (with $\kappa_2 \approx 0$) over a significant portion of the wire. To gain further insight, we have plotted $\bar{\eta}$ versus $\bar{\kappa}_e$, as defined in Eq. (18), in Fig. 9c. The choice of $d = 1$ leads to a steep increase in $\bar{\eta}$ with increasing curvature $\bar{\kappa}_e$, thereby stabilising the wire against continued pinch-off. The dependence of \bar{t}_p upon d is shown explicitly in Fig. 9d for $\chi_1 = 1$ and for three selected values of χ_2 . Consider the case $\chi_2 = 10$, as discussed in reference to Fig. 9a and b. As d increases from -1 to 1 , there is a moderate increase in \bar{t}_p due to the increase in $\bar{\eta}$ at high local curvature.

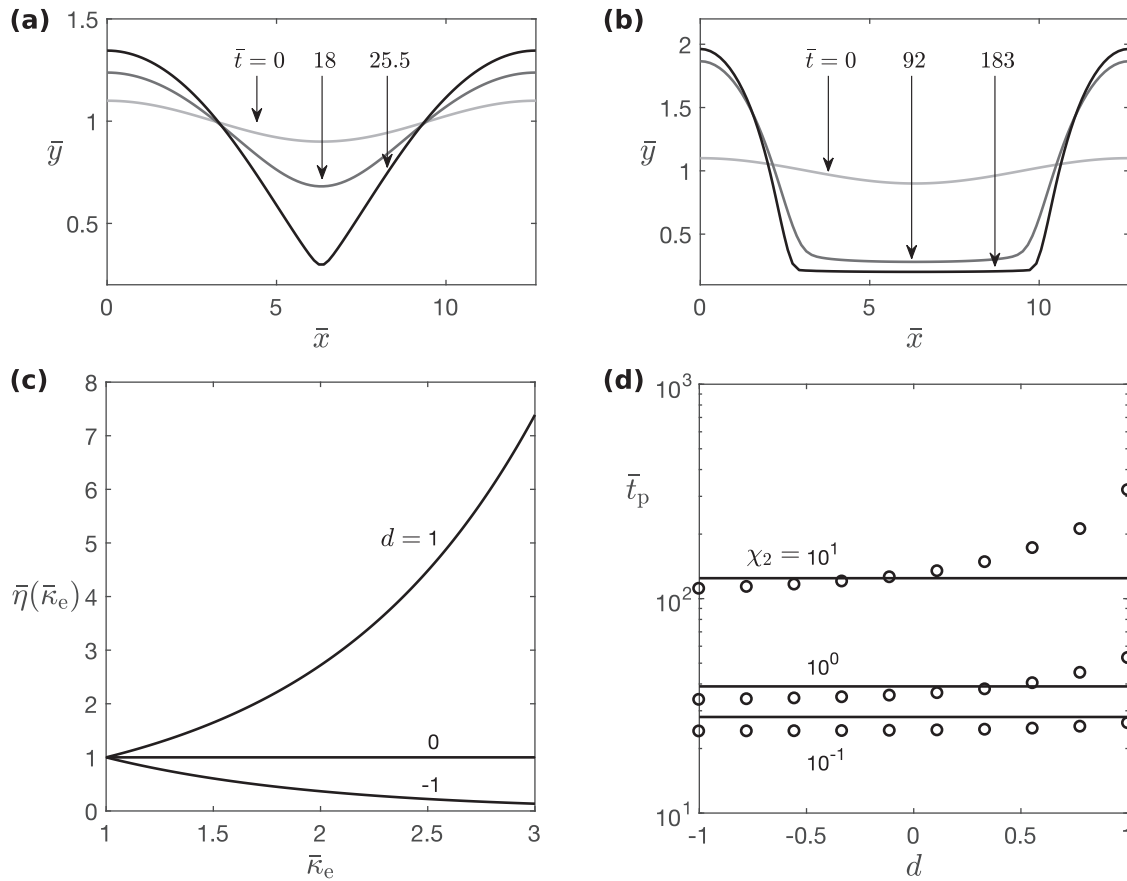


Fig. 9. (a) Wire evolution for $(\chi_1, \chi_2) = (1, 10)$ and $d = -1$. (b) Wire evolution for $(\chi_1, \chi_2) = (1, 10)$ and $d = +1$. (c) Sensitivity of $\bar{\eta}_0$ to d for increasing effective curvature $\bar{\kappa}_e$. (d) Sensitivity of the pinch-off time \bar{t}_p to d for $\chi_1 = 1$ and $\chi_2 = (0.1, 1, 10)$. The prediction by the initial perturbation analysis is shown as a solid line and is insensitive to d . The numerical results are shown as circles.

5. Concluding discussion

The present study reveals the significant role played by an organic ligand shell in the Rayleigh-Plateau instability for nanowires. It assumes an axisymmetric response which is appropriate for isotropic behaviour. Additionally, functional forms for the surface energy and the viscosity are assumed and a measure for the effective curvature is introduced. We anticipate that the general behaviour of the organic ligand shell can be adequately captured by the effective curvature and these functionals. Future modelling at the molecular length scale can give further insight into appropriate continuum descriptions.

Before summarising how our findings can guide the development of geometrically stable nanowires, we shall first show how our findings can be used to broaden our understanding of the Rayleigh-Plateau instability of currently available nanowires. The maps of Fig. 5 highlight the dependence of pinch-off time \bar{t}_p and final droplet radius R_s/R_0 upon the two dominant non-dimensional groups χ_1 and χ_2 . In order to deduce information about currently available nanowires, it is instructive to replot these maps as contours of χ_1 and χ_2 with R_s/R_0 and \bar{t}_p as axes, see Fig. 10. We note in passing the formulae (45) and (47) can be inverted algebraically to give

$$\chi_1 = \left(\frac{3\pi}{2}\right)^4 \left(\ln\left(\frac{\bar{e}_p}{\bar{e}_0}\right)\right)^{-1} \left(\frac{R_s}{R_0}\right)^{-12} \bar{t}_p \quad (52)$$

and

$$\chi_2 = \left(\ln\left(\frac{\bar{e}_p}{\bar{e}_0}\right)\right)^{-1} \bar{t}_p - \left(\frac{2\sqrt{2}}{3\pi}\right)^2 \left(\frac{R_s}{R_0}\right)^6, \quad (53)$$

as depicted in Fig. 10. Recall that both χ_1 and χ_2 are non-negative. This restricts the contour plot of χ_2 in Fig. 10b as illustrated by the shaded region. The revised map of Fig. 10a may be used to deduce information about χ_1 and thereby the energetics of the organic ligand shell from measurements of R_s/R_0 and \bar{t}_p . Likewise, the map of Fig. 10b can be used to deduce a value for χ_2 , and consequently the kinetics of the organic ligand shell, again from observed values of R_s/R_0 and \bar{t}_p .

Our findings can guide the selection of organic ligands that render nanowires more stable. The above results confirm that nanowires can be stabilised energetically against break-up into discrete droplets, and the relevant parameter range in (α, c) space is given in Fig. 4. Stabilisation requires the combined surface energy of wire and organic ligand shell to decrease with increasing effective curvature. When break-up is inevitable on energetic grounds, there is still the opportunity to delay its

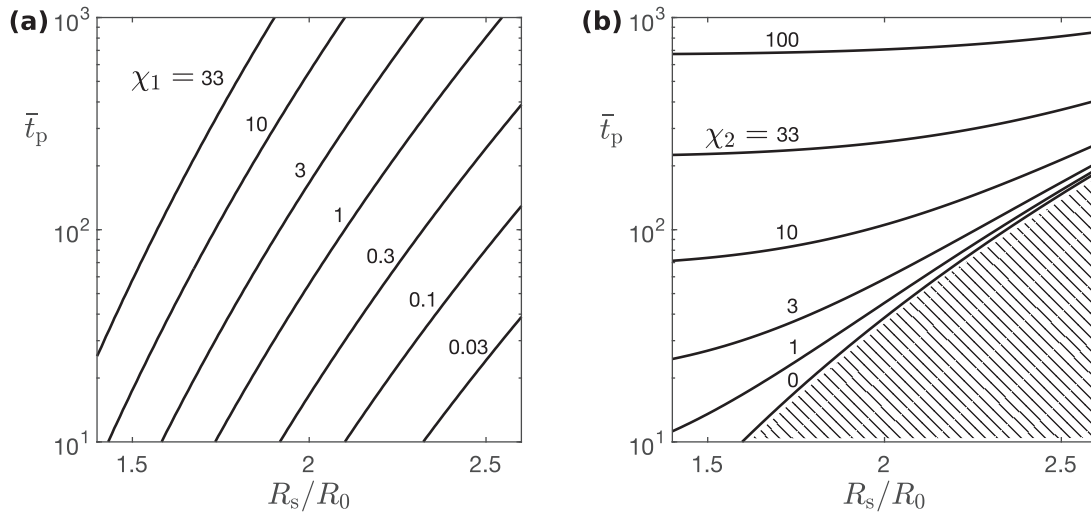


Fig. 10. The inverse problem of extraction of the magnitude of (a) χ_1 and (b) χ_2 from given values of R_s/R_0 and \bar{t}_p .

occurrence by judicious control of the kinetics of diffusion, of the interface reaction, and of the viscous dissipation within the organic ligand shell. Suitable ligands should thus minimise surface energy, maximise the viscous dissipation captured by the non-dimensional group χ_2 , and cause an increase in the shell's viscosity with increasing effective curvature. Molecular dynamics simulations and systematic experimentation can help to find suitable molecules.

Acknowledgements

The authors are grateful for financial support of this work in the form of an [ERC MULTILAT grant 669764](#), and to the Humboldt Society (NAF was the recipient of a Humboldt award). SB gratefully acknowledges the Cambridge Centre for Micromechanics, the [INM](#), and the [German Academic Exchange Service](#) for funding a number of research stays at the University of Cambridge. SB and TK would like to thank Eduard Arzt for his continuing support of the project. The authors would like to thank Louis V. Weber and Lola González-García for recording TEM micrographs of the nanowires.

Appendix A. Determination of viscous drag stress

Consider a metallic sphere of radius R and a surrounding organic ligand shell of thickness H . A change in radius at rate \dot{R} leads to a hoop strain at $\dot{\epsilon}_{\text{hoop}}$ of the shell and, in turn, to viscous dissipation within the shell due to its shear viscosity η . Upon writing $v_n = \dot{R}$ the hoop strain rate is

$$\dot{\epsilon}_{\text{hoop}} = \frac{v_n}{R} \quad (54)$$

The von Mises strain rate $\dot{\epsilon}_e$ reads

$$\dot{\epsilon}_e = \frac{2}{\sqrt{3}} |\dot{\epsilon}_{\text{hoop}}| \quad (55)$$

and the von Mises stress σ_e is related to $\dot{\epsilon}_e$ by the normal relation

$$\sigma_e = 3\eta\dot{\epsilon}_e, \quad (56)$$

in terms of a shear viscosity η . The work rate per unit volume is given by

$$\sigma_e\dot{\epsilon}_e = 3\eta\dot{\epsilon}_e^2 = 4\eta\dot{\epsilon}_{\text{hoop}}^2, \quad (57)$$

and the dissipation potential per unit area is

$$\phi_\eta = \frac{1}{2}H\sigma_e\dot{\epsilon}_e = 2H\eta\left(\frac{v_n}{R}\right)^2. \quad (58)$$

Differentiate (58) with respect to v_n to obtain the viscous drag stress

$$\sigma_\eta = \frac{\partial\phi_\eta}{\partial v_n} = 4H\eta\kappa_m^2 v_n \quad (59)$$

upon recalling that $\kappa_m = 1/R$ for a sphere.

Appendix B. List of symbols

Variable	Description (units)
α	“Shape” parameter in effective curvature (-)
γ	Surface energy (N/m)
γ_0	Material parameter in surface energy (N/m)
δ_b	Thickness of boundary layer (m)
$\dot{\epsilon}$	Strain rate (s^{-1})
$\dot{\epsilon}_e$	Von Mises strain rate (s^{-1})
$\dot{\epsilon}_{hoop}$	Hoop strain rate (s^{-1})
η	Viscosity ($Nm^{-2}s$)
η_0	Material parameter in viscosity ($Nm^{-2}s$)
θ	Inclination of surface in current configuration (-)
Θ	Inclination of surface in initial configuration (-)
κ_1	Principal curvature in 1-direction (m^{-1})
κ_2	Principle curvature in 2-direction (m^{-1})
κ_m	Mean curvature (m^{-1})
κ_d	Deviatoric curvature (m^{-1})
κ_e	Effective curvature (m^{-1})
λ	Perturbation wavelength (m)
λ_c	Critical perturbation wavelength (m)
Λ	Stretch ratio of surface (-)
μ	Chemical potential per atom (J)
σ_r	Interface reaction stress (Nm^{-2})
σ_{r0}	Material parameter in interface reaction stress (Nm^{-2})
σ_η	Viscous drag stress (Nm^{-2})
χ_1	Non-dimensional group containing energetic terms (-)
χ_2	Non-dimensional group containing dissipative terms (-)
ω	Perturbation wavenumber (m^{-1})
ω_c	Critical perturbation wavenumber (m^{-1})
ω_E	Perturbation wavenumber of fastest growing perturbation (m^{-1})
Ω	Atomic volume (m^3)
c	Material constant in surface energy (-) (Eq. 15)
d	Material constant in viscosity (-) (Eq. 18)
D_b	Interface diffusivity (m^2s^{-1})
\mathcal{D}	Interface diffusion constant ($J^{-1}m^6s^{-1}$)
e	Perturbation amplitude (m)
e_0	Initial perturbation amplitude (m)
e_p	Perturbation amplitude at pinch-off (m)
f	Driving force for kinetic dissipation (N)
f_r	Driving force for interface reaction (N)
f_η	Driving force for viscous dissipation (N)
h	Step size in finite difference scheme (m)
H	Layer thickness of the organic ligand shell (m)
j	Surface diffusion flux (m^2s^{-1})
k	Boltzmann constant (JK^{-1})
M	Power law exponent in interface reaction (-)
R	Wire radius (m)
R_0	Initial wire radius (m)
R_s	Radius of spherical droplets (m)
s	Arc length coordinate (m)
S	Arc length coordinate in the initial configuration (m)
t	Time (s)
t_p	Pinch-off time (s)
T	Absolute temperature (K)
v_n	Outward normal velocity of surface (ms^{-1})
v_{r0}	Reference velocity in interface reaction (ms^{-1})
x	Cylindrical coordinate along wire-axis (m)
X	Cylindrical coordinate along wire-axis in initial configuration (m)
y	Cylindrical coordinate perpendicular to wire-axis (m)
Y	Cylindrical coordinate perpendicular to wire-axis in initial configuration (m)
-	Non-dimensional versions of symbols are marked with a bar on top of the original symbol.

References

- Ashby, M.F., 1969. On interface-reaction control of nabarro-Herring creep and sintering. *Scr. Metall.* 3 (11), 837–842. doi:10.1016/0036-9748(69)90191-4.
- Barwicz, T., Cohen, G.M., Reuter, K.B., Bangsaruntip, S., Sleight, J.W., 2012. Anisotropic capillary instability of silicon nanostructures under hydrogen anneal. *Appl. Phys. Lett.* 100 (9), 093109. doi:10.1063/1.3690869.
- Bid, A., Bora, A., Raychaudhuri, A.K., 2005. Experimental study of Rayleigh instability in metallic nanowires using resistance fluctuations measurements from 77K to 375K. In: Svedlindh, P., Popovic, D., Weissman, M.B. (Eds.), *Fluctuations and Noise in Materials II*, Vol. 5843, p. 147. doi:10.1117/12.609419.
- Cademartiri, L., Malakooti, R., O'Brien, P.G., Migliori, A., Petrov, S., Kherani, N.P., Ozin, G.A., 2008. Large-Scale synthesis of ultrathin bi2s3 necklace nanowires. *Angew. Chem. Int. Ed.* 47 (20), 3814–3817. doi:10.1002/anie.200705034.
- Cademartiri, L., Ozin, G.A., 2009. Ultrathin nanowires-A materials chemistry perspective. *Adv. Mater.* 21 (9), 1013–1020. doi:10.1002/adma.200801836.
- Chen, Y., Ouyang, Z., Gu, M., Cheng, W., 2013. Mechanically strong, optically transparent, giant metal superlattice nanomembranes from ultrathin gold nanowires. *Adv. Mater.* 25 (1), 80–85. doi:10.1002/adma.201202241.
- Ciuculescu, D., Dumestre, F., Comesana-Hermo, M., Chaudret, B., Spasova, M., Farle, M., Amiens, C., 2009. Single-Crystalline co nanowires: synthesis, thermal stability, and carbon coating. *Chem. Mater.* 21 (17), 3987–3995. doi:10.1021/cm901349y.
- Cocks, A.C.F., 1992. Interface reaction controlled creep. *Mech. Mater.* 13 (2), 165–174. doi:10.1016/0167-6636(92)90044-E.
- Cocks, A.C.F., Gill, S.P.A., Pan, J., 1998. Modeling Microstructure Evolution in Engineering Materials. In: van der Giessen, E., Wu, T. (Eds.), *Advances in Applied Mechanics Volume 36*. Academic Press, pp. 82–162. URL: <https://www.elsevier.com/books/advances-in-applied-mechanics/unknown/978-0-12-002036-2>
- Feng, H., Yang, Y., You, Y., Li, G., Guo, J., Yu, T., Shen, Z., Wu, T., Xing, B., 2009. Simple and rapid synthesis of ultrathin gold nanowires, their self-assembly and application in surface-enhanced raman scattering. *Chem. Commun.* 0 (15), 1984. doi:10.1039/b822507a.
- Frost, H.J., Ashby, M.F., 1982. *Deformation-Mechanism Maps: The Plasticity and Creep of Metals and Ceramics*. Pergamon Press, Oxford, New York, Sydney.
- Gong, S., Schwalb, W., Wang, Y., Chen, Y., Tang, Y., Si, J., Shirinzadeh, B., Cheng, W., 2014. A wearable and highly sensitive pressure sensor with ultrathin gold nanowires. *Nat. Commun.* 5 (1), 3132. doi:10.1038/ncomms4132.
- Hopwood, J.D., Mann, S., 1997. Synthesis of barium sulfate nanoparticles and nanofilaments in reverse micelles and microemulsions. *Chem. Mater.* 9 (8), 1819–1828. doi:10.1021/cm970113q.
- Huang, X.H., Zhan, Z.Y., Wang, X., Zhang, Z., Xing, G.Z., Guo, D.L., Leusink, D.P., Zheng, L.X., Wu, T., 2010. Rayleigh-instability-driven simultaneous morphological and compositional transformation from co nanowires to CoO octahedra. *Appl. Phys. Lett.* 97 (20), 203112. doi:10.1063/1.3518470.
- Huber, S.E., Warakulwit, C., Limtrakul, J., Tsukuda, T., Probst, M., 2012. Thermal stabilization of thin gold nanowires by surfactant-coating: a molecular dynamics study. *Nanoscale* 4 (2), 585–590. doi:10.1039/C1NR11282A.
- ITRS, 2011. International Technology Roadmap for Semiconductors. ITRS 2011 Edition.. Technical Report. World Semiconductor Council. URL: <http://www.itrs2.net/2011-itrs.html>
- Karim, S., Toimil-Molares, M.E., Balogh, A.G., Ensinger, W., Cornelius, T.W., Khan, E.U., Neumann, R., 2006. Morphological evolution of au nanowires controlled by Rayleigh instability. *Nanotechnology* 17 (24), 5954–5959. doi:10.1088/0957-4484/17/24/009.
- Lacroix, L.-M., Arenal, R., Viau, G., 2014. Dynamic HAADF-STEM observation of a single-Atom chain as the transient state of gold ultrathin nanowire breakdown. *J. Am. Chem. Soc.* 136 (38), 13075–13077. doi:10.1021/ja507728j.
- Li, B., Ye, S., Stewart, I.E., Alvarez, S., Wiley, B.J., 2015. Synthesis and purification of silver nanowires to make conducting films with a transmittance of 99%. *Nano Lett.* 15 (10), 6722–6726. doi:10.1021/acs.nanolett.5b02582.
- Liu, Z., Xu, D., Liang, J., Shen, J., Zhang, S., Qian, Y., 2005. Growth of cu 2 s ultrathin nanowires in a binary surfactant solvent. *J. Phys. Chem. B* 109 (21), 10699–10704. doi:10.1021/jp050332w.
- Lu, X., Yavuz, M.S., Tuan, H.-y., Korgel, B.A., Xia, Y., 2008. Ultrathin gold nanowires can be obtained by reducing polymeric strands of oleylamine/uc complexes formed via aurophilic interaction. *J. Am. Chem. Soc.* 130 (28), 8900–8901. doi:10.1021/ja803343m.
- Malakooti, R., Cademartiri, L., Migliori, A., Ozin, G.A., 2008. Ultrathin Sb 2 S 3 nanowires and nanoplatelets. *J. Mater. Chem.* 18 (1), 66–69. doi:10.1039/B713383A.
- Maurer, J.H.M., González-García, L., Reiser, B., Kanelidis, I., Kraus, T., 2015. Sintering of ultrathin gold nanowires for transparent electronics. *ACS Appl. Mater. Interf.* 7 (15), 7838–7842. doi:10.1021/acsami.5b02088.
- Maurer, J.H.M., González-García, L., Reiser, B., Kanelidis, I., Kraus, T., 2016. Templated self-assembly of ultrathin gold nanowires by nanoimprinting for transparent flexible electronics. *Nano Lett.* 16 (5), 2921–2925. doi:10.1021/acs.nanolett.5b04319.
- Nichols, F.A., Mullins, W.W., 1965. Morphological changes of a surface of revolution due to capillarity-induced surface diffusion. *J. Appl. Phys.* 36 (6), 1826–1835. doi:10.1063/1.1714360.
- Nichols, F.A., Mullins, W.W., 1965. Surface- (interface-) and volume diffusion contributions to morphological changes driven by capillarity. *AIME Metall. Soc. Trans.* 233 (10), 1840–1848. URL: <http://www.onemine.org/document/abstract.cfm?docid=26784>
- Pazos-Perez, N., Baranov, D., Irsen, S., Hilgendorff, M., Liz-Marzan, L.M., Giersig, M., 2008. Synthesis of flexible, ultrathin gold nanowires in organic media. *Langmuir* 24 (17), 9855–9860. doi:10.1021/la801675d.
- Plateau, J.A.F., 1873. *Statique experimentale et theorique des liquides soumis aux seules forces moleculaires*. Gauthiers-Villars, Paris.
- Rayleigh, J.W.S., 1878. On the instability of jets. *Proc. London Math. Soc.* 10 (4).
- Reiser, B., Gerstner, D., Gonzalez-Garcia, L., Maurer, J.H.M., Kanelidis, I., Kraus, T., 2016. Multivalent bonds in self-assembled bundles of ultrathin gold nanowires. *Phys. Chem. Chem. Phys.* 18 (39), 27165–27169. doi:10.1039/C6CP05181B.
- Reiser, B., Gerstner, D., Gonzalez-Garcia, L., Maurer, J.H.M., Kanelidis, I., Kraus, T., 2017. Spinning hierarchical gold nanowire microfibers by shear alignment and intermolecular self-Assembly. *ACS Nano* 11 (5), 4934–4942. doi:10.1021/acsnano.7b01551.
- Repko, A., Cademartiri, L., 2012. Recent advances in the synthesis of colloidal nanowires. *Can J Chem* 90 (12), 1032–1047. doi:10.1139/v2012-077.
- Sadasivan, S., Khushalani, D., Mann, S., 2005. Synthesis of calcium phosphate nanofilaments in reverse micelles. *Chem. Mater.* 17 (10), 2765–2770. doi:10.1021/cm047926g.
- Sánchez-Iglesias, A., Rivas-Murias, B., Grzelczak, M., Pérez-Juste, J., Liz-Marzán, L.M., Rivadulla, F., Correa-Duarte, M.A., 2012. Highly transparent and conductive films of densely aligned ultrathin au nanowire monolayers. *Nano Lett.* 12 (12), 6066–6070. doi:10.1021/nl3021522.
- Shin, H.S., Yu, J., Song, J.Y., 2007. Size-dependent thermal instability and melting behavior of sn nanowires. *Appl. Phys. Lett.* 91 (17), 173106. doi:10.1063/1.2801520.
- Takahata, R., Yamazoe, S., Warakulwit, C., Limtrakul, J., Tsukuda, T., 2016. Rayleigh instability and surfactant-Mediated stabilization of ultrathin gold nanorods. *J. Phys. Chem. C* 120 (30), 17006–17010. doi:10.1021/acs.jpcc.6b03113.
- Toimil Molares, M.E., Balogh, A.G., Cornelius, T.W., Neumann, R., Trautmann, C., 2004. Fragmentation of nanowires driven by rayleigh instability. *Appl. Phys. Lett.* 85 (22), 5337–5339. doi:10.1063/1.1826237.
- Wang, C., Hou, Y., Kim, J., Sun, S., 2007. A general strategy for synthesizing fept nanowires and nanorods. *Angew. Chem. Int. Ed.* 46 (33), 6333–6335. doi:10.1002/anie.200702001.
- Wang, C., Hu, Y., Lieber, C.M., Sun, S., 2008. Ultrathin au nanowires and their transport properties. *J. Am. Chem. Soc.* 130 (28), 8902–8903. doi:10.1021/ja803408f.
- Wu, J., Pan, Y.-T., Su, D., Yang, H., 2015. Ultrathin and stable agau alloy nanowires. *Sci. China Mater.* 58 (8), 595–602. doi:10.1007/s40843-015-0072-z.
- Xi, G., Liu, Y., Wang, X., Liu, X., Peng, Y., Qian, Y., 2006. Large-Scale synthesis, growth mechanism, and photoluminescence of ultrathin te nanowires. *Crystal Growth Des.* 6 (11), 2567–2570. doi:10.1021/cg0603218.
- Xu, J., Zhu, Y., Zhu, J., Jiang, W., 2013. Ultralong gold nanoparticle/block copolymer hybrid cylindrical micelles: a strategy combining surface templated self-assembly and rayleigh instability. *Nanoscale* 5 (14), 6344. doi:10.1039/c3nr01296d.

- Xu, S., Li, P., Lu, Y., 2018. In situ atomic-scale analysis of rayleigh instability in ultrathin gold nanowires. *Nano Res.* 11 (2), 625–632. doi:[10.1007/s12274-017-1667-3](https://doi.org/10.1007/s12274-017-1667-3).
- Yu, T., Joo, J., Park, Y.I., Hyeon, T., 2006. Single unit cell thick samaria nanowires and nanoplates. *J. Am. Chem. Soc.* 128 (6), 1786–1787. doi:[10.1021/ja057264b](https://doi.org/10.1021/ja057264b).
- Zhao, K., Averbach, R.S., Cahill, D.G., 2006. Patterning of metal nanowires by directed ion-induced dewetting. *Appl. Phys. Lett.* 89 (5), 053103. doi:[10.1063/1.2261271](https://doi.org/10.1063/1.2261271).
- Zhao, W., Huang, D., Yuan, Q., Wang, X., 2016. Sub-2.0-nm ru and composition-tunable rupt nanowire networks. *Nano Res.* 9 (10), 3066–3074. doi:[10.1007/s12274-016-1189-4](https://doi.org/10.1007/s12274-016-1189-4).
- Zhou, Z., Zhou, Y., Pan, Y., Lei, W., Xu, C., 2009. Overheating and undercooling of Ni polycrystalline nanowires. *Scr. Mater.* 60 (7), 512–515. doi:[10.1016/j.scriptamat.2008.11.044](https://doi.org/10.1016/j.scriptamat.2008.11.044).

3.4 Publication 4: Stabilization of ultrathin nanowires by self-assembly into bundles

Reprinted with permission from:

S. Bettscheider, T. Kraus, N.A. Fleck, Stabilization of ultrathin nanowires by self-assembly into bundles, *Acta Mater.* 231 (2022) 117799. <https://doi.org/10.1016/j.actamat.2022.117799>.

© 2022 Acta Materialia Inc. Published by Elsevier Ltd.



Full length article

Stabilization of ultrathin nanowires by self-assembly into bundles

Simon Bettscheider^{a,b}, Tobias Kraus^{a,b,*}, Norman A. Fleck^{c,**}^a INM – Leibniz Institute for New Materials, Campus D2.2, Saarbrücken 66123, Germany^b Colloid and Interface Chemistry, Saarland University, Campus D2.2, Saarbrücken 66123, Germany^c Cambridge University Engineering Department, Trumpington Street, Cambridge CB2 1PZ, UK

ARTICLE INFO

Article history:

Received 2 January 2022

Revised 19 February 2022

Accepted 24 February 2022

Available online 26 February 2022

Keywords:

Rayleigh instability

Nanowire

Nanoparticle

Diffusion

Agglomeration

ABSTRACT

The relative tendency of freely dispersed and bundled gold nanowires to break up along their length by the Rayleigh–Plateau instability is investigated both experimentally and theoretically. Small angle X-ray scattering, in combination with transmission electron microscopy, reveal that the bundling of nanowires can enhance their stability. The experimental observation is rationalized by a linear perturbation analysis of a representative unit cell of bundled wires. A stability map is constructed for a bundle of nanowires to display the sensitivity of the Rayleigh–Plateau instability to the number and size of contacts with nearest neighbors per nanowire, and to the ratio of interfacial energy to surface energy. Stabilisation is enhanced by allowing the bundle of wires to sinter freely: a criterion for this kinetically-based stabilisation is given in terms of the ratio of pinch-off time for the instability to the sintering time to form the necks between nanowires.

© 2022 Acta Materialia Inc. Published by Elsevier Ltd. All rights reserved.

1. Introduction

Ultrathin nanowires of length to diameter aspect ratio exceeding 10^3 are now readily available. They are prepared by chemically reducing a metal or semiconductor salt in the presence of an organic ligand [1]. The ligand directs one-dimensional growth of the nanowire by binding to the nanowire surface; additionally, the ligand stabilizes the nanowire core and the colloidal dispersion [2–6]. To date, ultrathin nanowires have been made from metals and their alloys (gold [3,7–10], iron–platinum [11], silver [12], ruthenium [13]) and semiconductors (copper sulfide [14], bismuth sulfide [15], antimony sulfide [16]). The nanowires are flexible and can spontaneously form continuous 2D and 3D superstructures; this tendency has been exploited to assemble opto-electronic devices [17–19]. Ultrathin nanowires have also been used in stretchable and optically transparent supercapacitors [17], in electrocatalytic membranes [20], and in the printed electrodes of bendable touchscreens [18].

A fundamental challenge for nanowire manufacture and use is their stability. Cylindrical wires are thermodynamically unfavorable in shape: a circular cylinder has a greater surface area, and conse-

quently greater interfacial energy, than an array of spheres of the same overall volume, provided the ratio of the radius of spheres to that of the cylinder exceeds $(3\pi/2)^{1/3}$ [21,22]. This difference in surface energy drives the so-called Rayleigh–Plateau instability [23,24], also known as the morphological, geometric, shape, or Rayleigh instability. The evolution in shape of a circular cylindrical wire into spherical droplets by surface diffusion has been analyzed by Nichols and Mullins [21,22]; the bulk of the wire is taken to be rigid and diffusional flow occurs in the axial direction along the surface of the wire. The time required for break-up is proportional to the fourth power of the cylinder radius so that thin wires are particularly prone to degradation [21,22]. In practice, ultrathin gold nanowires in a dispersion fragment over a few weeks at room temperature, and over a few minutes at 100 °C.

Both energetic and kinetic considerations play a role in stabilizing nanowires against the Rayleigh–Plateau instability [25]. Stabilization by energetic contributions can be enhanced by the presence of a substrate [26–29], by anisotropy of the nanowire's surface energy [30–33], and by geometrical confinement in a matrix [34–36]. The addition of a ligand shell can enhance stability both energetically and kinetically [25]. For example, the ligand shell can reduce the nanowire's surface energy and slow down diffusion [25,34,37–40].

Surprisingly little is known about the stabilization of nanowires by their self-assembly into a bundle. Commonly, ultrathin nanowires are synthesized as colloids, and the resulting dispersion can comprise individual wires or wires that have self-assembled

* Corresponding author at: INM – Leibniz Institute for New Materials, Campus D2.2, Saarbrücken 66123, Germany.

** Corresponding author.

E-mail addresses: simon.bettscheider@leibniz-inm.de (S. Bettscheider), tobias.kraus@leibniz-inm.de (T. Kraus), naf1@eng.cam.ac.uk (N.A. Fleck).

into close-packed bundles [1,19,41]. The size and relative density (also called packing density) of the bundles depend upon the choice of solvent [41], ligand type [40], and ligand shell density [42]. For example, the bundling of ultrathin gold nanowires (AuNWs) can be driven by a phase separation between the ligand shell and the solvent, or by depletion forces induced by the solvent or unbound ligand molecules [42,43]. Bundles also form when the nanowire dispersions are dried [18,44]. The center-to-center spacing of the wires ranges from 4.1 nm [43] to 5.9 nm [42], depending upon the method of self-assembly.

In the following, we show that the formation of bundles affects the shape stability of nanowires. The break-up of both fully dispersed and bundled nanowires is observed *in situ* by small-angle X-ray scattering. An analytical model is introduced to predict the influence of bundling upon shape stability. Stability maps are generated using a linear perturbation analysis, and are compared with the experimental results of the present study and with those reported in the literature. The adopted approach has a wide applicability: both the experimental approach (X-ray scattering and transmission microscopy, along with a scattering model), and the micromechanical model of the Rayleigh–Plateau instability for a bundle of nanowires are applicable for a broad range of nanowire composition and diameter.

2. Experimental methods

2.1. Synthesis of ultrathin gold nanowires

Chemicals and materials All chemicals used are listed in Table S1 in the supplementary information.

Synthesis Ultrathin gold nanowires (AuNWs) were synthesized using a protocol based upon that of Feng et al. [45] and Nohu et al. [40]. In a typical synthesis, 60 mg of the dry precursor $\text{HAuCl}_4 \cdot n\text{H}_2\text{O}$ was placed in a glass vial and quickly covered with a volume of 9.9 ml of *n*-hexane; 2.04 ml of the ligand oleylamine was added while flushing with Ar. The mixture was vortexed for 5 min to dissolve the precursor. Finally, 3.06 ml of the reducing agent triisopropylsilane was added while flushing with Ar. The mixture was again vortexed for 30 s and the solution was rested, without stirring, at 25 °C for 24 h.

Purification The reaction product was purified twice by adding two volumes of ethanol (30 ml each), centrifugating at 100 rcf for 1 min to precipitate the AuNWs, and redispersing in *n*-hexane after the first purification cycle and cyclooctane after the second purification cycle.

2.2. Heating of nanowires and *in situ* small-angle X-ray scattering

The break-up of nanowires was monitored *in situ* by small-angle X-ray scattering (SAXS). Samples for observation in SAXS were kept at room temperature for at least 16 h after purification before transferring them into glass capillaries with an inner diameter of 1.5 mm. To accelerate the break-up, the samples were heated *in situ* to either 60 °C or 70 °C. The heating stage was pre-heated to the desired temperature, and measurements were taken at 2 min intervals in the beamline of a $\text{Cu K}\alpha$ X-ray source (SAXS setup XEUSS 2.0, XENOCs, France). The scattered intensity was captured by a detector at a distance of approximately 1.2 m from the sample. The sample-to-detector distance was calibrated with a standard of silver behenate prior to each measurement. The two-dimensional scattering images were integrated (azimuthal integration) using the software Foxtrott (Synchrotron Soleil, France) to obtain scattering curves.

The (center-to-center) interwire distance d inside bundles of AuNWs was determined assuming Bragg scattering [46] using the

formula

$$d = \frac{4\pi}{\sqrt{3}q_{uv}} \sqrt{u^2 + uv + v^2} \quad (1)$$

where q_{uv} is the value of the q -vector of the Bragg scattering peak of a two-dimensional hexagonal lattice of Miller indices u and v [46].

2.3. Scattering model fits

The volume fractions of gold in the form of bundled nanowires, freely dispersed nanowires, and spherical particles in the dispersion were obtained by fitting a scattering model to the SAXS data. The model was based on the work of Sundblom et al. [47], Manet et al. [48], and Loubat et al. [19] and used the form factors of cylinders and spheres and the structure factor of crystalline cylinders. The authors emphasize that the novelty of the present study is not in the choice of scattering model, but rather in the measurement (and prediction) of breakup of bundled and freely dispersed nanowires. Freely dispersed nanowires were modeled using the form factor of a cylinder convoluted with a Schulz–Zimm distribution to account for the distribution of their diameters. Bundles of nanowires were modeled by multiplying this form factor with the structure factor of a 2D hexagonal lattice. The structure factor was approximated by a sum of Lorentzian functions at the positions of the Bragg peaks. A Debye–Waller factor accounted for disorder in the 2D hexagonal lattice, for example caused by thermal fluctuations. Spherical nanoparticles were modeled by convoluting the form factor of spheres with a Schulz–Zimm distribution. All spherical particles (formed during the synthesis and during break-up) were consolidated in a single, broadly distributed function whose mean diameter was allowed to evolve with time. The overall scattered intensity was the volume-weighted sum of the scattered intensity of freely dispersed nanowires, bundled nanowires, and spherical nanoparticles. Details on the model can be found in the supplementary information. The fits were implemented in Python using the library LMFIT [49].

2.4. Transmission electron microscopy

Transmission Electron Microscopy (TEM) was used in order to help interpret the scattering data from SAXS. Ideally, high magnification TEM images of bundles would be used to reveal the necessary physical detail. However, high-resolution TEM is yet unable to probe a liquid dispersion at sufficient resolution, and the energy of the electron beam can disrupt the nanostructures. High-resolution TEM images of single nanowires do exist in the literature [50–53], and these studies suggest that wire break-up is by a Rayleigh–Plateau instability. The advantage of SAXS measurements in the present study is the generation of statistically meaningful information over many nanowires.

Small aliquots of the heated samples were prepared for *ex situ* observation by transmission electron microscopy. To this end, the aliquots were diluted to a concentration of approximately $[\text{Au}] = 0.05 \text{ mg/ml}$ and 5 μl of the diluted sample was drop cast on a perforated carbon-coated grid (Plano, Germany). The perforated grid reduced drying artefacts when compared to standard carbon-coated grids. The samples were observed at an acceleration voltage of 200 kV in a JEM 2010 (JEOL, Japan) transmission electron microscope (TEM).

3. Experimental results

3.1. *Ex situ* transmission electron micrographs

Ultrathin gold nanowires (AuNWs) were chemically synthesized using the protocol detailed above, dried on carbon-coated grids,

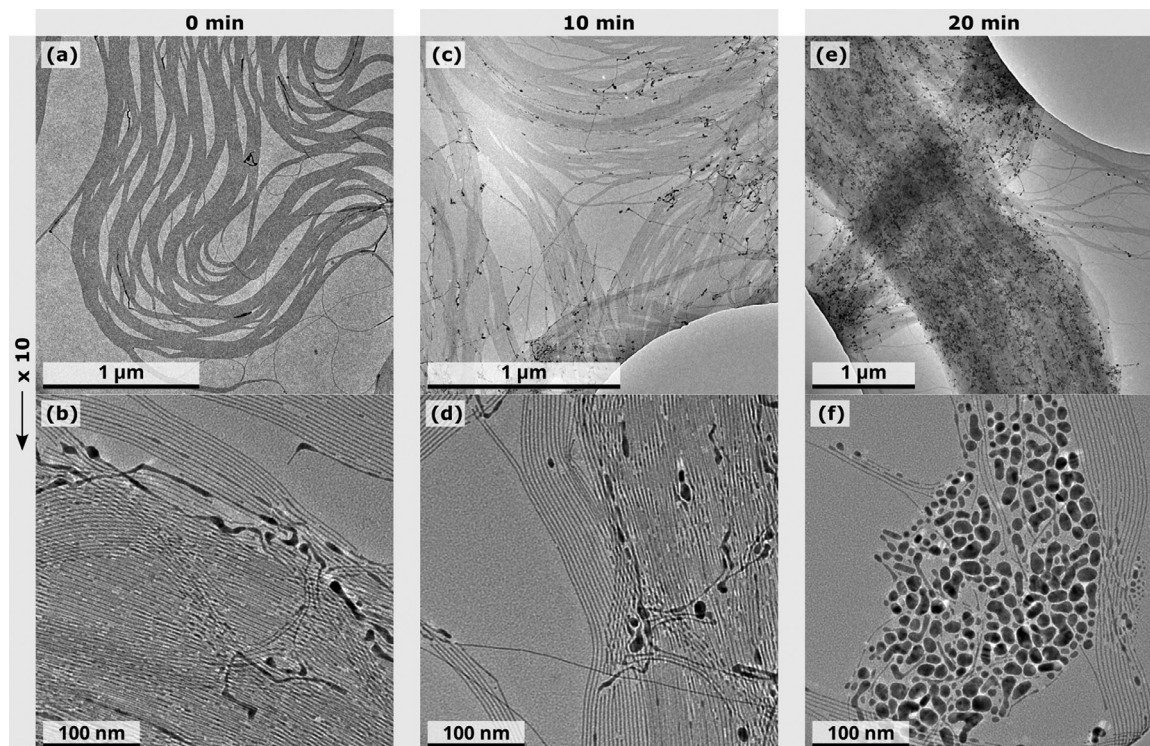


Fig. 1. Transmission electron micrographs of ultrathin gold nanowires after drying at room temperature (a) and (b); and after heating them to 60 °C for 10 min (c) and (d); and 20 min (e) and (f). The wires fragmented into spherical particles.

and analyzed in a Transmission Electron Microscope (TEM). A typical micrograph (Fig. 1a,b) shows nanowires with uniform gold cores and diameters of 1.6 nm and a spacing of 4.4 nm that is caused by a monolayer of the ligand oleylamine on the metal. The length of the nanowires exceeded the field of view and was estimated to be above 1 μm; lengths of 1 to 4 μm have been reported previously [54].

Heating of the AuNW dispersions to 60 °C resulted in fragmentation of the nanowires. Samples that were kept at 60 °C for 10 min contained an increased fraction of spheres (Fig. 1c,d) that further grew after 20 min at 60 °C, whereupon much of the micrograph was covered with spherical particles (Fig. 1e,f).

The fragmentation of gold nanowires has been explained in terms of the Rayleigh–Plateau instability [25,39]. Here, we are interested in the relative stability of bundled and freely dispersed wires. We used X-ray scattering to quantify the volume fractions of intact and fragmented wires at elevated temperatures.

3.2. In situ small-angle X-ray scattering

Small-angle X-ray scattering (SAXS) from the AuNWs in cyclooctane at 20 °C is shown in Fig. 2b. The scattered intensity depends on the shape of the particles ('form factor') and their relative arrangement ('structure factor') [46]. A dispersion of free AuNW has its scattering determined only by the form factor, as reported in [41,42], for example.

Scattering from the samples used here (Fig. 2b) was dominated by the form factor for scattering vectors $q < 1 \text{ nm}^{-1}$, while the structure factor dominated for $q > 1 \text{ nm}^{-1}$. Hexagonally packed AuNW bundles caused distinct peaks in the scattered intensity at 1.27 nm^{-1} , 2.20 nm^{-1} , and 2.52 nm^{-1} . Such bundles have been reported previously [19,41,45]. They are caused by attractive, entropic interactions that are due to unbound ligands and linear solvent molecules that align between the wires [42,43]. The peak positions indicate a center-to-center spacing of the wires of $d = 5.7 \text{ nm}$.

Scattering models (discussed in the next section) revealed that the dispersion contained a fraction of approximately 55 % in dispersed nanowires and 40 % in nanowire bundles.

The fragmentation of wires through the Rayleigh–Plateau instability was initiated by heating the dispersion of wires and bundles to 60 °C and tracked via SAXS. Scattering measurements at 2 min intervals are shown in Fig. 2. The scattered intensity initially scaled with q^{-1} in the region dominated by the form factor ($q < 1 \text{ nm}^{-1}$), which is typical for cylindrical objects. The overall scattering in this region gradually increased, indicating the formation of spherical particles. The overall scattering in the region dominated by the structure factor ($q > 1 \text{ nm}^{-1}$) remained unchanged, indicating that the bundles did not fragment.

3.3. Interpretation of scattering data

The scattering model described in Section 2.3 was used to extract quantitative volume fractions of the gold contained in dispersed nanowires, bundled nanowires, and spherical particles from the time-dependent SAXS (Fig. 2d,e). The original gold volume fractions were $54.8 \pm 1.8 \%$ in freely dispersed nanowires, $40.4 \pm 1.2 \%$ in bundled nanowires, and $4.7 \pm 0.5 \%$ in spherical nanoparticles. The fraction of gold in freely dispersed nanowires decreased linearly to $39.0 \pm 1.3 \%$ over 20 min at 60 °C, while that of spherical particles increased to $21.2 \pm 0.3 \%$. This corresponds to a fragmentation rate of approximately $6.5 \text{ km.s}^{-1}.\text{ml}^{-1}$ of freely dispersed nanowires.

The volume fraction of bundled nanowires remained constant (Fig. 2e). Heating to 70 °C led to the same qualitative results (Fig. S1 in the supplementary information): freely dispersed nanowires broke up and bundled nanowires remained mainly intact. Note that an elevated temperature can induce the formation of bundles, too [42]. The formation and dissociation of bundles occurs over a time scales of hours [41], and is hence independent of the break-up that is observed over minutes.

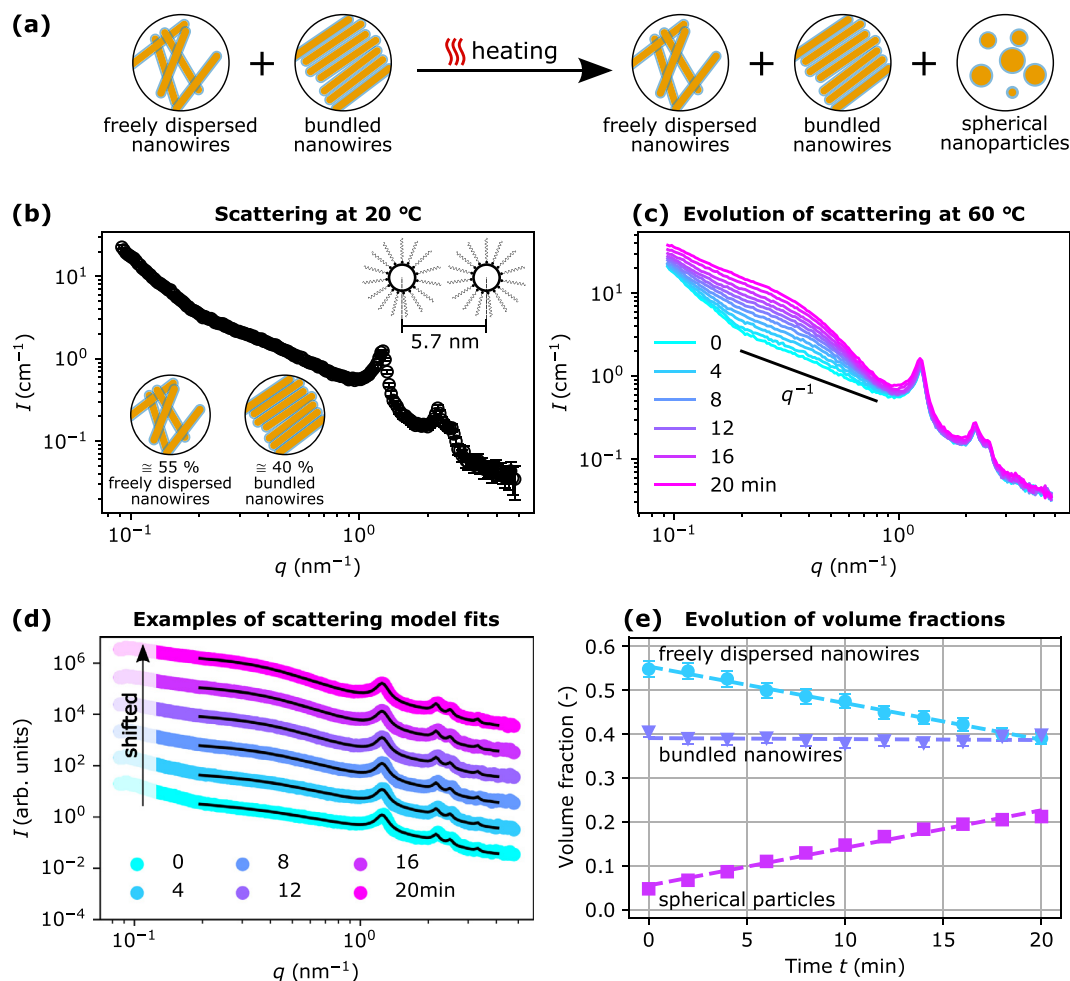


Fig. 2. Analysis of nanowire shape stability via X-ray scattering. **(a)** The fragmentation of wires was induced by heating a dispersion to 60 °C and was observed via *in situ* Small-Angle X-ray Scattering (SAXS). **(b)** Distinct scattering maxima indicate that 40 % of the gold existed in bundles and 55 % in dispersed nanowires. The remaining 5 % were in spherical nanoparticles, a by-product of the synthesis. The interwire (center to center) distance inside the bundles was 5.7 nm. **(c)** Heating to 60 °C increased scattering at small q -values, indicating the formation of spheres. **(d)** Scattering models (solid lines) were fitted to the scattering (dots) at selected times to quantify the change in volume fractions. The scattering curves are shifted vertically for better visualization. **(e)** Volume fractions of gold in freely dispersed nanowires, bundled nanowires, and spherical particles from the scattering models. Error bars denote the standard errors of the fits. The dashed lines are linear fits.

The results of SAXS and TEM analysis, taken together, indicated the rapid fragmentation of dispersed AuNWs, but not of AuNWs in bundle form. We conclude that AuNWs stabilize each other in bundles. The following sections provide an analytical model for the stability of nanowires in bundles to provide additional insights into this observation.

4. Analytical model for Rayleigh–Plateau instability of a bundle of nanowires

The prototypical problem is sketched in Fig. 3, showing the progressive breakdown of a cylindrical wire into discrete droplets. The wire resides in a vertical stack of fixed height and so the necks between neighboring wires can be idealized by fixed planes. The model is based on the notion that the interaction between neighboring wires can be treated kinematically as the appearance of flats at contacting necks. This geometry is accurate in the absence of a ligand shell surrounding each wire but becomes an idealization when a ligand shell surrounds each wire. The model assumes that the center-to-center spacing of neighboring wires remains constant during the fragmentation of the bundled nanowires, and disintegration proceeds by the axial diffusion of surface atoms of each wire.

4.1. Geometry

A representative nanowire within a bundle is modeled as a circular cylinder of radius R truncated by $n \geq 2$ flat surfaces, each representing the neck with a neighboring wire, as shown in Fig. 4. Values of n for tessellation are $n = 2, 3, 4, 6$.

Our aim is to explore the possibility of diffusional flow of atoms along the surface of the wire in the axial direction in order to perturb the shape from prismatic to one where the cross-section varies with the axial coordinate z . Assume that the radius $R(z, t)$ evolves with time t and varies harmonically with axial position z . Suppose that the radius of the cylinder is perturbed from the uniform reference state $R = R_0$ to the state

$$R(z, t) = R_0 + \Delta R(t) + a(t) \cos(kz), \quad (2)$$

where $a(t)$ is the perturbation amplitude, λ is the perturbation wavelength, and $k = 2\pi/\lambda$ is the corresponding wavenumber (Fig. 5b). The term $\Delta R(t)$ results from the constraint that the cylinder maintains a constant overall mass. The shape (2) has the following interpretation. In general, assume that an initial imperfection exists at $t_1 = 0$, and is of amplitude $a(t_1 = 0) > 0$ and wavelength λ . Our aim is to seek an expression for the rate of growth of the imperfection $\dot{a}(t)$.

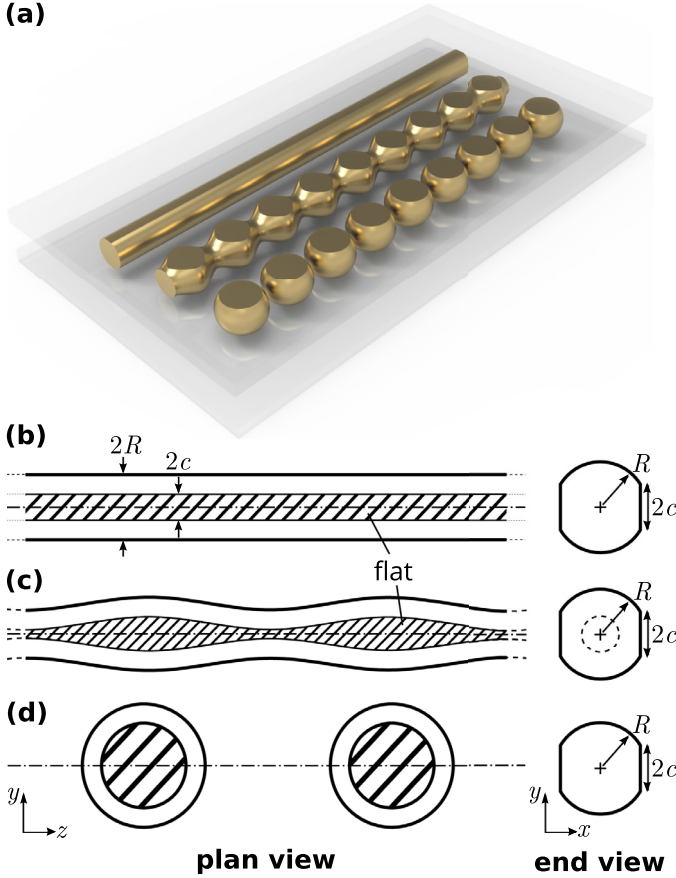


Fig. 3. The prototypical problem showing a stacked nanowire. (a) Rendered view of three states. The nanowire may remain (b) prismatic in shape (stable), or it may evolve into (c) a non-uniform shape and thence into (d) discrete droplets.

The evolution in shape of the wire occurs at fixed value of relative density of the bundle of wires. Thus, the center-to-center spacing of adjacent wires $2H$ is held constant, and the contact angle $\omega(z, t)$ evolves with $R(z, t)$ such that

$$\cos \omega = \frac{H}{R}. \quad (3)$$

In the unperturbed reference state, $R = R_0$, the contact angle equals ω_0 , where $\cos \omega_0 = H/R_0$. Note that ω is *not* the local contact angle as dictated by local equilibrium of surface energies for the wire. Rather, ω is a macroscopic measure of the wire inclination at the edge of the contact. This approximation has been justified by Parhami et al. [55] for the sintering of a row of spherical particles. Example configurations for a bundle of wires are shown in Fig. S2, and the relative density as a function of ω_0 is given in Fig. S3 for the unperturbed state, $a = 0$. The perturbation analysis of the present study builds upon that of Gill [28]; he considered the case of a single wire on a surface, for which H is free to evolve with time.

4.2. Conservation of cylinder mass

The term $\Delta R(t)$ in (2) is determined from conservation of volume over the wavelength λ as follows. The cross-section of the wire A_z^0 in the unperturbed state is

$$A_z^0 = \pi f_0 R_0^2, \quad (4)$$

where

$$f_0 \equiv 1 - \frac{n}{\pi} \left(\omega_0 - \frac{1}{2} \sin(2\omega_0) \right). \quad (5)$$

Consequently, the volume V_0 of a length λ of the wire in the unperturbed state is $V_0 = A_z^0 \lambda$. Now consider the perturbed state. The cross-sectional area A_z of the cylinder at any axial position z is

$$A_z(z, t) = \pi f R^2, \quad (6)$$

where

$$f(\omega, n) \equiv 1 - \frac{n}{\pi} \left(\omega - \frac{1}{2} \sin(2\omega) \right). \quad (7)$$

Now write $\omega(z) = \omega_0 + \Delta\omega(z)$ to give, via (3),

$$\Delta\omega = \left(\frac{\Delta R}{R_0} + \frac{a}{R_0} \cos(kz) - \frac{a^2}{R_0^2} \cos^2(kz) \right) \cot \omega_0 + \mathcal{O}(a^3). \quad (8)$$

We use (8) to re-write $f(\omega, n)$ as

$$f(\omega, n) = f_0 - \frac{n}{\pi} \left(\Delta\omega(1 - \cos(2\omega_0)) + \Delta\omega^2 \sin(2\omega_0) \right). \quad (9)$$

Introduce the compact notation

$$\xi_1(\omega_0, n) \equiv \pi - n \left(\omega_0 - \frac{1}{2} \sin(2\omega_0) \right) = \pi f_0 \quad (10)$$

$$\xi_2(\omega_0) \equiv 1 - \cos(2\omega_0), \quad (11)$$

to write the current cross-sectional area $A_z(z, t)$ as

$$A_z = \pi R_0^2 \left(f_0 + \frac{\Delta\omega}{\pi} (2\xi_1 \tan \omega_0 - n\xi_2) + \frac{\Delta\omega^2}{\pi} (3\xi_1 \tan^2 \omega_0 - 2n\xi_2 \tan \omega_0 - n \sin(2\omega_0)) \right). \quad (12)$$

Conservation of volume dictates that the current volume of the cylinder over one wavelength, $V = \int_0^\lambda A_z dz$, equals the volume $V_0 = \pi R_0^2 f_0 \lambda$ in the unperturbed state, and consequently

$$\frac{\Delta R}{R_0} = \xi_3(\omega_0) \left(\frac{a}{R_0} \right)^2, \quad (13)$$

where

$$\xi_3(\omega_0, n) \equiv \frac{-\xi_1 + n\xi_2 \cot \omega_0 + n \sin(2\omega_0) \cot^2 \omega_0}{4\xi_1 - 2n\xi_2 \cot \omega_0}. \quad (14)$$

Note that ΔR is $\mathcal{O}(a^2)$.

4.3. Energetics: surface energy as driving force

The driving force for the Rayleigh-Plateau instability is the reduction in total surface energy that accompanies growth of the perturbation. The interface between neighboring wires possesses an interfacial free energy per unit area γ_c , and the free surface of the wire has a surface energy per unit area γ_s .

In the present study, the ligand shell is not considered separately. Instead, the stability analysis adopts the simple and general approach of ascribing an effective surface energy to the interaction between the ligand shell and the adjacent nanowire. Effective values could be obtained from advanced quantum chemical simulations [56]. Our earlier work showed how such atomistic and molecular information can be incorporated into the effective surface energy and diffusivity values [25]. A much more sophisticated model is needed in order to predict the effect of temperature, for example, upon the effective surface energy of nanowires with a ligand shell.

4.4. Kinematics: shape evolution by surface diffusion

The shape of each nanowire evolves by surface diffusion in the axial direction [21,22]. Conservation of mass requires that the surface divergence of the surface diffusive flux \mathbf{j} and the normal velocity of matter deposited onto the surface v_n sum to zero,

$$\nabla_s \cdot \mathbf{j} + v_n = 0, \quad (15)$$

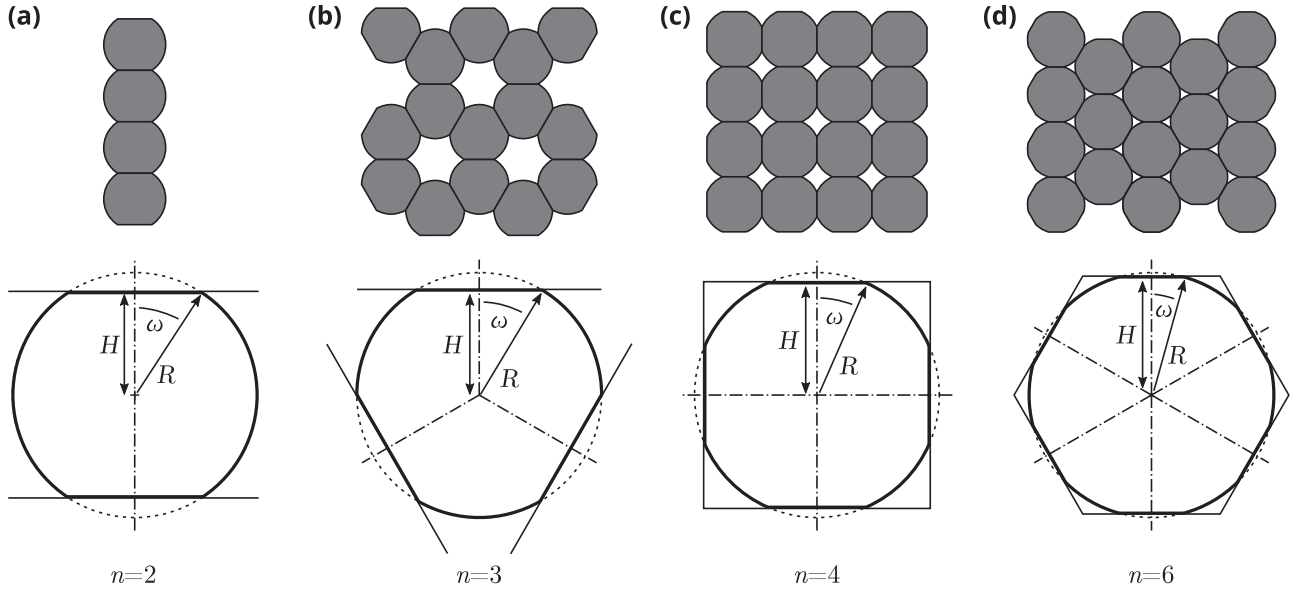


Fig. 4. Geometry of a nanowire truncated by $n = 2, 3, 4,$ or 6 flat surfaces that represent necks of neighboring wires. (a) $n = 2$, (b) $n = 3$, (c) $n = 4$, (d) $n = 6$.

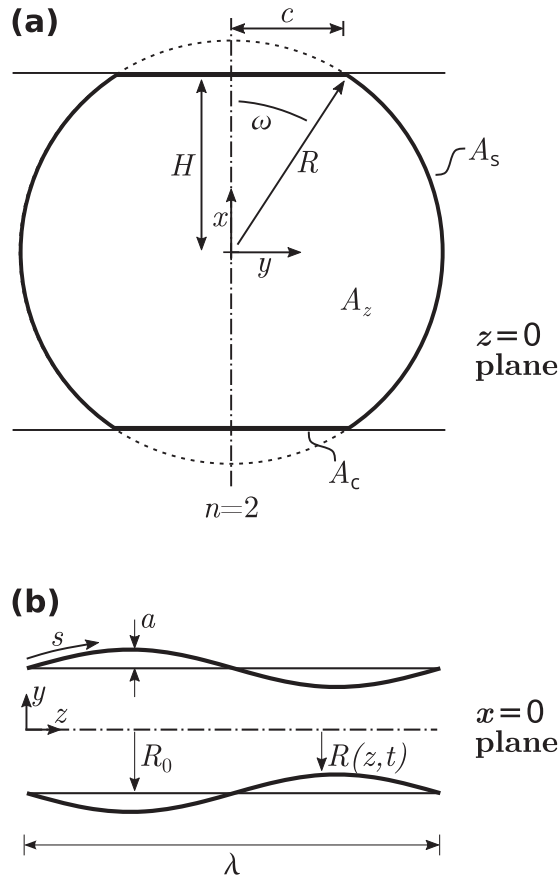


Fig. 5. Cylindrical coordinate system and geometry of a perturbed nanowire. (a) The (x, y) -plane. (b) the (y, z) -plane.

where ∇_s is the usual surface divergence operator, and a bold symbol denotes a vector throughout this paper. Assume that the dominant surface flux is in the axial direction and is of magnitude j . Then, (15) simplifies to

$$\frac{1}{R} \frac{\partial (Rj)}{\partial s} + v_n = 0, \quad (16)$$

where s is the arc length along the free surface (see Fig. 5b). The normal velocity of matter deposited on the surface must equal the rate of change in radius, $v_n = \dot{R} = \dot{a} \cos(kz) + \mathcal{O}(a^2)$. For small perturbations ($a \ll R$), we may write $R^{-1} \partial (Rj) / \partial s \approx \partial j / \partial z$ for the derivative in (16). Consequently, the surface flux j is

$$j = -\frac{\dot{a}}{k} \sin(kz) + \mathcal{O}(a^2). \quad (17)$$

5. Linearised perturbation analysis

5.1. Stability map and critical wavenumber

The presence of a perturbation changes the Gibb's free energy of the wire over one wavelength λ by ΔG , where

$$\Delta G = \gamma_s (A_s - A_s^0) + \gamma_c (A_c - A_c^0). \quad (18)$$

Here, A_s is the area of the free surface and A_c is the area at the constraining neck over one wavelength, as shown in Fig. 5a. The superscript 0 denotes the respective area in the unperturbed state.

The free surface area of the wire over one wavelength λ of the perturbation is

$$A_s = \int_0^\lambda 2(\pi - n\omega)R \, ds. \quad (19)$$

For small perturbations, we can write

$$ds = \left(1 + \frac{1}{2}(ak)^2 \sin^2(kz) + \mathcal{O}(a^4)\right) dz. \quad (20)$$

Now make use of (8) to obtain

$$A_s = A_s^0 \left(1 + \left(\xi_3 \xi_4 + \frac{1}{4}(R_0 k)^2\right) \frac{a^2}{R_0^2}\right), \quad (21)$$

where ξ_4 is defined by

$$\xi_4(\omega_0, n) \equiv \frac{\pi - n\omega_0 - n \cot \omega_0}{\pi - n\omega_0} \quad (22)$$

and $A_s^0 = 2(\pi - n\omega_0)R_0\lambda$ is the surface area of the free surface of the unperturbed cylinder. Note from (21) that $(A_s - A_s^0)$ is second-order in a/R_0 .

The contact area A_c over one wavelength is

$$A_c = 2n \int_0^\lambda R \sin \omega \, dz, \quad (23)$$

and can be re-written in terms of a/R_0 by making use of the expression

$$\frac{\sin \omega}{\sin \omega_0} = 1 + \Delta\omega \cot \omega_0 - \frac{1}{2} \Delta\omega^2 + \mathcal{O}(\Delta\omega^3), \quad (24)$$

and by expressing the radius R in terms of $\Delta\omega$ via (3), such that

$$\frac{R}{R_0} = 1 + \Delta\omega \tan \omega_0 + \Delta\omega^2 \tan^2 \omega_0. \quad (25)$$

Now make use of (8), along with (24) and (25) to express (23) as

$$A_c = A_c^0 \left(1 + \xi_5 \frac{a^2}{R_0^2} \right), \quad (26)$$

where

$$\xi_5(\omega_0, n) \equiv \xi_3 + \xi_3 \cot^2 \omega_0 - \frac{1}{4} \cot^2 \omega_0 \quad (27)$$

and $A_c^0 = 2nR_0\lambda \sin \omega_0$ is the contact area in the unperturbed, reference state over one wavelength. The result for A_c is also second-order in a/R_0 .

Substitute the expressions (21) and (26) into the definition of Gibb's free energy change (18), and introduce the ratio of interfacial free energies $\tilde{\gamma} = \gamma_c/\gamma_s$, to obtain

$$\Delta G = \gamma_s A_s^0 \left(\frac{a}{R_0} \right)^2 \left(\xi_3 \xi_4 + \frac{1}{4} (R_0 k)^2 + \frac{\tilde{\gamma} \xi_5 n \sin \omega_0}{\pi - n\omega_0} \right). \quad (28)$$

The nanowire is stable against the formation of a perturbation of amplitude a and wavelength λ if $\Delta G \geq 0$. This is satisfied for wavelengths $\lambda \leq \lambda_c$, where the critical perturbation wavelength λ_c for which $\Delta G = 0$ is given in non-dimensional form by

$$\tilde{\lambda} \equiv \frac{\lambda_c}{2\pi R_0} = \frac{1}{2} \left(-\xi_3 \xi_4 - \frac{\tilde{\gamma} \xi_5 n \sin \omega_0}{\pi - n\omega_0} \right)^{-\frac{1}{2}}. \quad (29)$$

We note in passing that $\xi_3 > 0$, $\xi_4 < 0$, and $\xi_5 > 0$ and consequently $\tilde{\lambda}$ is real in (29). The wavenumber corresponding to λ_c is $k_c = 2\pi/\lambda_c$, and for later use, we emphasize that the tilde over the symbol λ denotes the non-dimensional quantity $\tilde{\lambda} \equiv \lambda/(2\pi R_0)$. The stability maps in Fig. 6 illustrate (29) in graphical form, and show the sensitivity of $\tilde{\lambda}_c$ to n , $\tilde{\gamma}$, and ω_0 . We emphasize that the co-ordinates of the stability maps are independent of nanowire radius; in contrast, the timescale for the progression of an instability is highly sensitive to length scale, as discussed below.

It is evident from Fig. 6 that a region ($\tilde{\lambda}_c = \infty$) exists in the top-right of each map for which the bundle is stable against break-up into discrete droplets. Stability is enhanced by a large value of $\tilde{\gamma}$, a large value of ω_0 (corresponding to a high relative density of the bundle), and by a small co-ordination number n . For reference, a free standing circular cylindrical wire is unstable for all wavelengths exceeding $\lambda_c = 2\pi R_0$, as discussed by Nichols and Mullins [21,22]: thus, $\tilde{\lambda}_c$ equals unity for the free standing wire.

5.2. Perturbation growth rate and fastest growing perturbation

We proceed to use the Cocks-Suo variational principle [28,55,57] to derive the wavenumber of the fastest growing perturbation. The variational functional is defined as $\Pi(\dot{a}) = \Delta\dot{G}(\dot{a}) + \Psi(\dot{a})$, where $\Psi(\dot{a})$ is a dissipation potential due to surface diffusion. A stationary value of Π with respect to \dot{a} gives the solution that satisfies the constitute law for surface diffusion,

$$\delta\Pi \equiv \delta(\Delta\dot{G}) + \delta\Psi = 0. \quad (30)$$

The variation in change of Gibb's free energy, $\delta(\Delta\dot{G})$, with respect to a variation $\delta\dot{a}$ is obtained from (28) as

$$\delta(\Delta\dot{G}) = \gamma_s A_s \left(\frac{2a\delta\dot{a}}{R_0^2} \right) \left(\xi_3 \xi_4 + \frac{1}{4} (R_0 k)^2 + \frac{\tilde{\gamma} \xi_5 n \sin \omega_0}{\pi - n\omega_0} \right). \quad (31)$$

The dissipation potential $\Psi(\dot{a})$ is defined as

$$\Psi = \int_{A_s} \frac{j^2}{2D_s} dA_s, \quad (32)$$

where $D_s = \delta_s D_s \Omega_s / (R_G T)$ is the surface diffusion constant, δ_s is the thickness over which surface diffusion occurs, D_s is the surface diffusivity, Ω_s is the molar volume of the wire material, R_G is the universal gas constant, and T is absolute temperature. To first order accuracy in a/R_0 , we may write $dA_s = R_0 d\varphi dz$, so that (32) simplifies to

$$\Psi = \frac{nR_0}{D_s} \int_0^\lambda \int_0^{\frac{\pi}{n} - \omega_0} j^2 d\varphi dz. \quad (33)$$

Now substitute the expression (17) for j into (33), and integrate to obtain

$$\Psi = \frac{\dot{a}^2 A_s^0}{4D_s k^2}. \quad (34)$$

Upon making use of (31) and (34), the variational statement (30) reduces to

$$\frac{\dot{a}}{a} = -\frac{4D_s \gamma_s}{R_0^4} (kR_0)^2 \left(\xi_3 \xi_4 + \frac{1}{4} (kR_0)^2 + \frac{\tilde{\gamma} \xi_5 n \sin \omega_0}{\pi - n\omega_0} \right) \quad (35)$$

for any assumed wavenumber k . The fastest growing perturbation has a wavelength that maximizes \dot{a} in (35); by setting $\partial(\dot{a}/a)/(\partial k)$ to zero, the fastest growing wavelength is $\lambda_{\max} = \sqrt{2}\lambda_c$, where λ_c has already been defined in (29). The wavenumber k_{\max} that corresponds to λ_{\max} follows immediately as

$$k_{\max} = \frac{\sqrt{2}\pi}{\lambda_{\max}} = \frac{k_c}{\sqrt{2}}, \quad (36)$$

and the fastest growth rate $(\dot{a}/a)_{\max}$ of the bundle at $\lambda = \lambda_{\max}$ follows directly from (35) as

$$\left(\frac{R_0^4}{\gamma_s D_s} \frac{\dot{a}}{a} \right)_{\max} = (k_{\max} R_0)^4. \quad (37)$$

Note that the expression (36) for k_{\max} is the same as that derived previously for the classical Rayleigh-Plateau instability of a single free-standing wire [21,22].

5.3. Topology of wires after pinch-off

The wavelength of the fastest growing imperfection $\lambda_{\max} = \sqrt{2}\lambda_c$ is given by (29) and can be written in the non-dimensional form $\tilde{\lambda}_{\max} = \lambda_{\max}/(2\pi R_0) = \sqrt{2}\tilde{\lambda}_c$. The value of $\tilde{\lambda}_{\max}$ dictates the asymptotic shape of the final, pinched-off particles: (a) discrete sphere at small $\tilde{\lambda}_{\max}$, (b) truncated sphere at intermediate $\tilde{\lambda}_{\max}$, and (c) rod at large $\tilde{\lambda}_{\max}$. Consider each in turn.

(a) Discrete sphere

A small value of $\tilde{\lambda}_{\max}$ leads to break-up into an array of spherical droplets of final radius R_s . Conservation of mass dictates that

$$\frac{R_s}{H} = \frac{1}{\cos \omega_0} \left(\frac{3}{2} \xi_1 \tilde{\lambda} \right)^{1/3}. \quad (38)$$

This geometry occurs provided $R_s < H$, and consequently $\tilde{\lambda}_{\max} < \tilde{\lambda}_1$, where

$$\tilde{\lambda}_1 \equiv \frac{2 \cos^3 \omega_0}{3 \xi_1} \quad (39)$$

upon suitable rearrangement of (38).

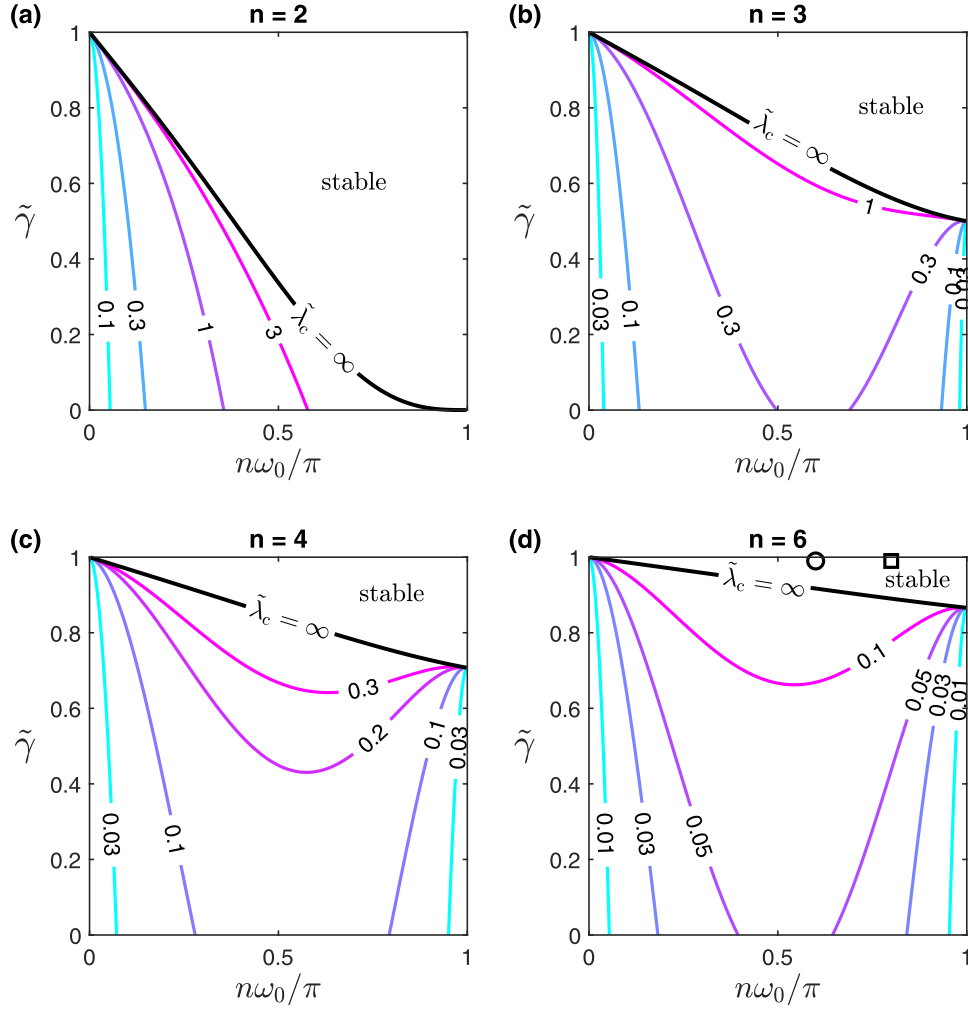


Fig. 6. Contours of the critical perturbation wavelength $\tilde{\lambda}_c = \lambda_c/(2\pi R_0)$ as a function of the surface energies $\tilde{\gamma}$ and the initial contact angle ω_0 for a cylinder constrained by (a) $n = 2$, (b) $n = 3$, (c) $n = 4$, and (d) $n = 6$ necks. The black line separates the regime in which shape stability depends on the perturbation wavelength from the regime in which the cylinder is always stable regardless of the perturbation wavelength. The circle locates our experimental material and system properties and the square that of Nouh et al. [40].

(b) Truncated sphere

Now consider the case $\tilde{\lambda}_{\max} > \tilde{\lambda}_1$. Then, the discrete droplets are truncated spheres with flat circular necks between immediate neighbors, see Fig. 7a. The height of each particle is $2H$, and its radius external to the necks is R_s . The radius of each neck is $R_s \cos \omega_s$, where $2\omega_s$ is the angle subtended by the neck at the center of the particle. The radius R_s is related to R_0 via the identity from (3):

$$H = R_s \cos \omega_s = R_0 \cos \omega_0 \quad (40)$$

once ω_s has been obtained from ω_0 by conservation of volume between the reference, unperturbed volume V_0 and the final volume of the truncated sphere. Routine algebra gives

$$V_0 = \xi_1 R_0^2 \lambda_{\max} = \frac{4}{3} \pi R_0^3 \xi_6 \cos^3 \omega_0, \quad (41)$$

where

$$\xi_6(\omega_s, n) \equiv (\cos \omega_s)^{-3} \left(1 - \frac{n}{4} (2 + \cos \omega_s) (1 - \cos \omega_s)^2 \right). \quad (42)$$

A standard root-finding algorithm ('fzero' in Matlab R2021a) is used to solve (41) and (42) for ω_s in terms of $(n, \omega_0, \tilde{\lambda}_{\max})$. Truncated spheres are obtained for an intermediate value of $\tilde{\lambda}_{\max}$. When $\tilde{\lambda}_{\max}$ attains a transition value of $\tilde{\lambda}_2$, adjacent necks touch. This occurs at $n\omega_s = 2\pi$, and the associated value of $\xi_6(\omega_s =$

$\frac{2\pi}{n}, n)$ is obtained from (42). Upon substitution into (41), we find

$$\tilde{\lambda}_2 = \frac{2 \cos^3 \omega_0}{3 \xi_1(\omega_0, n)} \xi_6 \left(\frac{2\pi}{n}, n \right). \quad (43)$$

In summary, truncated spheres are the pinched-off final shape when $\tilde{\lambda}_1 < \tilde{\lambda}_{\max} < \tilde{\lambda}_2$.

(c) Rods

The discrete droplets adopt a rod-like shape for $\tilde{\lambda}_{\max} > \tilde{\lambda}_2$, as shown in Fig. 7a.

5.4. Pinch-off time

Our linear perturbation analysis describes the initial stage of shape evolution. It does not accurately capture the details of the nanowire pinch-off into discrete spheres. However, previous numerical calculations have shown that the initial perturbation growth rate is a good predictor for the pinch-off time [25]. Assume that a nanowire of initial perturbation amplitude a_1 at time t_1 pinches off when the perturbation amplitude reaches a value a_p at time t_p . The pinch-off time t_p is related to the perturbation growth rate $\dot{a}(t_1)$ via the approximation [25],

$$\ln \left(\frac{a_p}{a_1} \right) = \int_{t_1}^{t_p} \frac{\dot{a}}{a} (t') dt' \approx (t_p - t_1) \frac{\dot{a}}{a} (t_1). \quad (44)$$

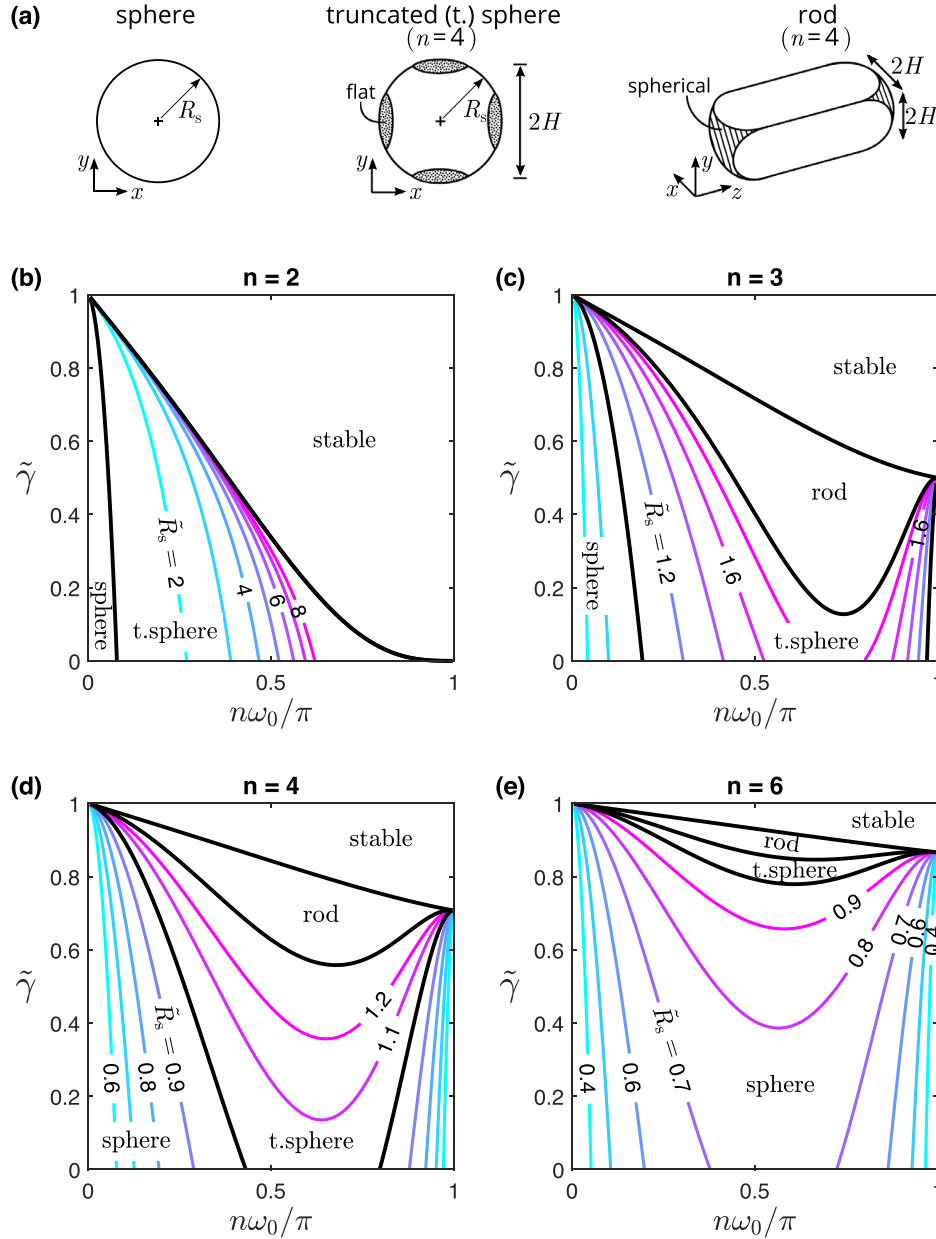


Fig. 7. (a) The discrete particles emerging from pinch-off take the final form of spheres, truncated spheres (t. spheres), and rods. (b) to (e) Contours of the final, pinched-off radius of particle $\tilde{R}_s = R_s/H$ as a function of the surface energy ratio $\tilde{\gamma}$ and the initial contact angle ω_0 for a cylinder constrained by (b) $n = 2$, (c) $n = 3$, (d) $n = 4$, and (e) $n = 6$ necks. The topologies of the final particles are marked on the maps.

By setting $t_1 = 0$ and inserting the fastest growth rate from (37), the pinch-off time is predicted as

$$\frac{\gamma_s D_s t_p}{R_0^4} = (k_{\max} R_0)^{-4} \ln \left(\frac{a_p}{a_i} \right), \quad (45)$$

which is again consistent with the results obtained by Nichols and Mullins [22] for an isolated metal nanowire. Note that $k_{\max} = 2\pi/\lambda_{\max}$ is directly related to $k_c = 2\pi/\lambda_c$ via (36) and consequently $k_{\max} = \sqrt{2}\pi/\lambda_c$. Also recall that $\tilde{\lambda}_c = \lambda_c/(2\pi R_0)$ is a function of $(n, \tilde{\gamma}, \omega_0)$ as given by (29) and Fig. 6. Assume that all wavelengths of perturbation are present in the wire so that the pinch-off time is dictated by the fastest growing perturbation of wavelength $\lambda_{\max} = \sqrt{2}\lambda_c$. Thus, upon making use of (45), the pinch-off time t_p scales as $\tilde{\lambda}_c^4$; some broad conclusions can be deduced immediately from Fig. 6. Consider a close-packed, fully triangulated arrangement of wires ($n = 6$), with $\tilde{\gamma} < 0.8$. Then, pinch-off is fastest for small contacts ($\omega_0 \approx 0$) corresponding to low relative

density and for large contacts ($\omega_0 \approx \pi/6$) corresponding to almost vanishing porosity. A large drop in surface energy from the surface value γ_s to the interfacial, contact value γ_c (that is, a small value of $\tilde{\gamma} \equiv \gamma_c/\gamma_s$) leads to a faster pinch-off.

The formula (45) also applies to the case of a free-standing wire, with $k_{\max} = \sqrt{2}\pi/\lambda_c$ and $\lambda_c = 2\pi R_0$, such that $\tilde{\lambda}_c = 1$. Thus, the plots of Fig. 6 can be used immediately to determine whether bundling reduces or increases pinch-off time. In broad terms, a bundle of wires is more stable than the isolated wire in regimes of the map for which $\tilde{\lambda}_c > 1$.

6. Discussion

6.1. Comparison of experiment and perturbation analysis

The experiments reported above indicate that a bundle of ultrathin gold nanowires fragments more slowly than freely dis-

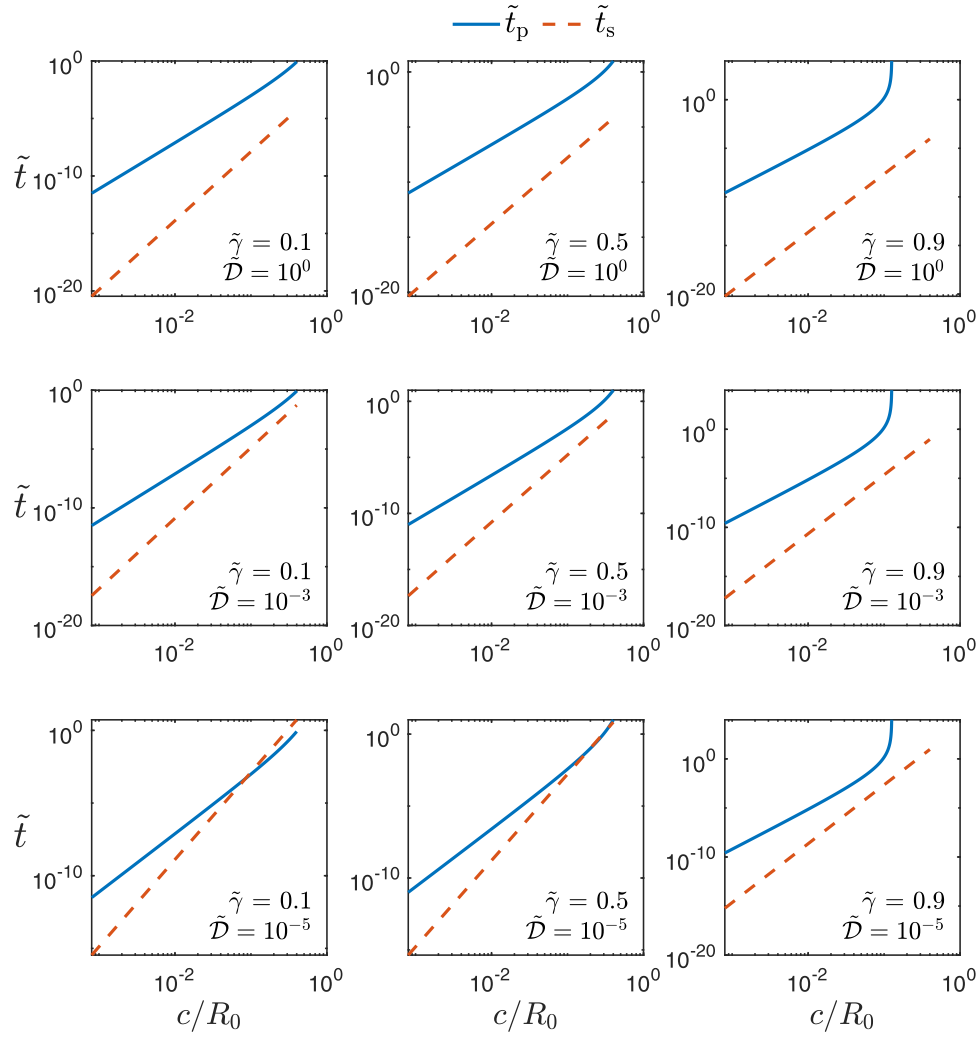


Fig. 8. Pinch-off time $\tilde{t}_p = D_c \gamma_s t_p / R_0^3$ of cylinders of contact width c/R_0 compared to the time $\tilde{t}_s = D_s \gamma_s t_s / R_0^3$ to sinter a row of cylinders to establish the same value of c/R_0 . Predictions are shown for selected combinations of relative diffusivity $\tilde{D} = D_c/D_s$ and relative surface energy $\tilde{\gamma} = \gamma_c/\gamma_s$.

persed nanowires. Our perturbation analysis shows that stabilization arises from the presence of necks between wires. Whether stabilization occurs or not depends upon the number of necks n , surface energy ratio $\tilde{\gamma}$, and initial contact angle ω_0 as shown in the stability maps of Fig. 6. It is instructive to make use of the material properties and geometric parameters of the present experimental study in order to assess whether the predictions match the observed stabilization due to bundle formation.

The measured radius of gold nanowires was approximately 0.84 nm and the thickness of the ligand shell was 2.2 nm [58,59]. The AuNWs formed fully-triangulated bundles with $n = 6$ and a center-to-center distance of 5.7 nm, giving $\omega_0 \approx \pi/10$. The surface energy γ_s is set by the interaction between ligand and solvent molecules, and the interfacial energy γ_c by the interaction of ligand shells. The spacing indicates that solvent was always present between the ligand shells, implying $\tilde{\gamma} \approx 1$. These parameters put the system at the operating point $(n, \tilde{\gamma}, n\omega_0/\pi) \approx (6, 1, 0.6)$ in the maps of Fig. 6, inside a region of unconditional stability. This explains why the bundled AuNWs were observed to be more stable than the freely dispersed ones.

Nouh et al. [40] exchanged the ligand oleylamine with tri-octylphosphine and observed that the wires' stability increased, but did not provide an explanation for this finding. It was not stated whether stabilization was due to the different bond chemistry, the steric properties of the ligands, or the tighter bundling at

an interwire distance of 3.75 nm [40]. We locate their material and geometric parameters to be at the operating point $(n, \tilde{\gamma}, n\omega_0/\pi) \approx (6, 1, 0.8)$ in Fig. 6 in a region of unconditional stability, consistent with their experimental observations.

6.2. Comparison of pinch-off time and free sintering time

The analysis of the Rayleigh–Plateau pinch-off instability of a bundle of wires assumes that the center-to-center spacing of the wires remains constant, with the instability driven by surface diffusion in the axial direction. In addition, free sintering can occur such that the bundle of wires densifies by in-plane surface diffusion, and the center-to-center spacing of neighboring nanowires reduces. We emphasize that, in the present study, the nanowires were surrounded by a ligand shell and sintering was not observed. In contrast, sintering is observed in other nanowire systems, see for example [18,44,60]; it is then instructive to obtain an expression for the sintering time t_s to achieve a given contact size c between adjoining wires, and to compare this sintering time with the pinch-off time t_p for this same value of c . Sintering stabilizes against pinch-off when t_s is less than t_p . Alternatively, when t_s exceeds t_p the Rayleigh–Plateau instability occurs with break-up of the wires into discrete particles.

The sintering time t_s is calculated as follows. We focus attention on the early stages of sintering involving initial neck forma-

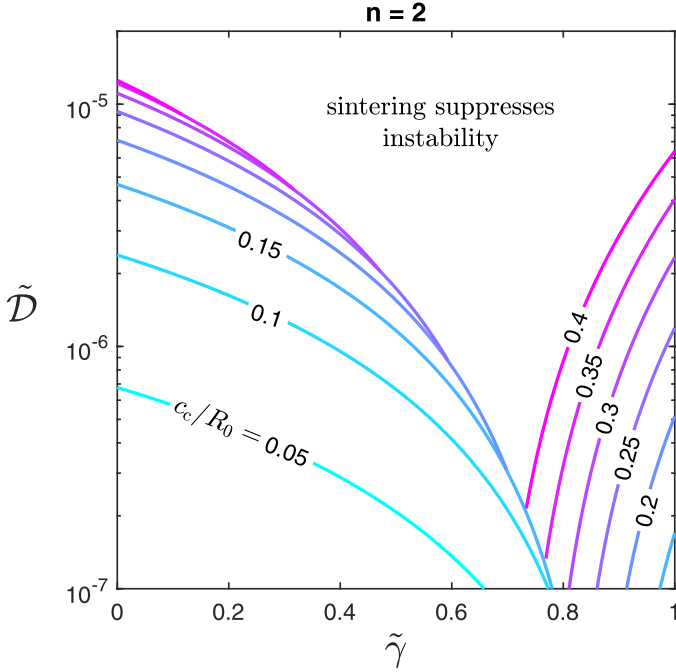


Fig. 9. Contours of critical contact width c_c as a function of relative diffusivity $\tilde{D} = D_c/D_s$ and relative surface energy $\tilde{\gamma} = \gamma_c/\gamma_s$. For $c > c_c$, the pinch-off time t_p is shorter than the sintering time t_s . A region exists in the map where sintering is always faster than pinch-off, regardless of the contact width c , and consequently sintering suppresses the instability.

tion and neck growth (stage I sintering) [55,61]. Consider a row of cylinders with an initial contact length $c = 0$ (see Fig. A1). Sintering increases c and decreases H , as shown in Fig. A1. We follow Parhami et al. [55] and determine, for the 2D plane strain case, the dependence of c upon sintering time t_s , such that

$$c^6 = \frac{81}{2} D_c R_0^2 (2\gamma_s - \gamma_c) t_s. \quad (46)$$

Here, D_c is the diffusion constant in the contact zone (grain boundary). The derivation is given in Appendix A.

The sintering time t_s to achieve a neck size c is compared in Fig. 8 with the pinch-off time t_p for the same value of c , for selected values of $\tilde{\gamma}$ and $\tilde{D} = D_c/D_s$. Sintering is sufficiently fast to stabilize the nanowire shape at large $\tilde{\gamma}$ and large \tilde{D} . These conditions are typically satisfied for metals, for which $\tilde{\gamma} \approx 0.3$ to 0.4 [62] and $\tilde{D} \approx 10^{-3}$ to 10^{-1} [63]. Note that, for the choice $\tilde{\gamma} = 0.1$ and $\tilde{D} = 10^{-5}$, pinch-off is anticipated at $c/R_0 \approx 0.1$ since $t_p = t_s$ at this value of contact size between neighboring wires.

A critical neck size c_c can be defined for which $t_s = t_p$. Then, the sintering time is smaller than the pinch-off time for $c < c_c$. For $c > c_c$, the instability is faster than sintering and the wires break up into discrete droplets. Contours of c_c are plotted in Fig. 9: c_c increases with increasing relative diffusivity \tilde{D} . For sufficiently large \tilde{D} , sintering is always faster than pinch-off and thereby stabilizes the wire.

7. Concluding remarks

Ultrathin nanowires can self-assemble into bundles. *In situ* SAXS and *ex situ* TEM reveal that bundling delays the Rayleigh–Plateau instability. An analytical model, based on interfacial energy, geometrical confinement and axial surface diffusion, indicates that bundle formation can render the nanowire unconditionally stable. Stability depends upon the number and size of necks between neighboring wires, and upon the surface and interfacial energies.

An optimal neck size maximizes pinch-off time for packings with more than two neighbors.

Pressureless sintering, in its early stages, is much more rapid than the rate of pinch-off by the Rayleigh–Plateau instability. However, the rate of sintering decreases sharply with increasing time, $\dot{c} \propto t^{-5/6}$ as given directly from (46), and consequently the Rayleigh–Plateau instability may ensue.

Declaration of Competing Interest

The authors declare that they have no known competing financial interests or personal relationships that could have appeared to influence the work reported in this paper.

Acknowledgments

SB and TK would like to thank Eduard Arzt for his continuing support of the project. The authors would like to thank Louis V. Weber for recording TEM micrographs of the nanowires and Björn Kutlich for help with the scattering models.

Funding: This work was supported by the European Research Council (MULTILAT, grant number 669764), the Humboldt Society (NAF was the recipient of a Humboldt award), and the Foundation of German Business (SB was awarded with a Ph.D. scholarship).

Appendix A. Stage I sintering of an array of circular cylinders

Our analysis of stage I sintering of an array of circular cylinders parallels that of Parhami et al. [55] who analyzed sintering of spheres. Consider an array of circular cylinders of initial radius R_0 with a center-to-center spacing of initial value $2H = 2R_0$ at time $t = 0$, as depicted in Fig. A1. In stage I sintering, the cylinders maintain a constant radius R_0 , the cylinder centers approach each other and a neck of width $2c$ grows. The driving force is the reduction in overall free energy associated with surface and interfacial energies. Assume a surface energy per unit area γ_s of the free surface of the cylinders and an interfacial energy per unit area γ_c of the contact zone. We proceed to obtain $c(t)$.

The initial cross-section of the cylinders in a unit cell at $t = 0$ is $A_z^0 = \pi R_0^2$, and after a time $t > 0$, it evolves to

$$A_z = \pi R_0^2 - \frac{4}{3} \frac{c^3}{R_0} + 4hc. \quad (A.1)$$

Conservation of mass requires $A_z = A_z^0$, and consequently

$$h = \frac{1}{3} \frac{c^2}{R_0} \quad (A.2)$$

and

$$H = R_0 - \frac{c^2}{6R_0}. \quad (A.3)$$

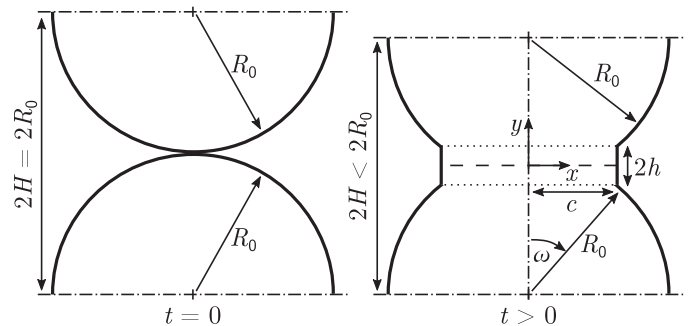


Fig. A1. Geometry of an array of circular cylinders undergoing stage I sintering.

We use the same variational principle as defined in (30) with the definition of ΔG given in (18) in order to obtain \dot{c} . Assume that the dissipation in the grain boundary in stage I sintering dominates that over the free surface. Consequently, the dissipation potential reads

$$\Psi = \int_{A_c} \frac{j_c^2}{2\mathcal{D}_c} dA_c, \quad (\text{A.4})$$

where we consider unit depth along the axis of the cylinder.

Now obtain expressions for the surface and interface areas per unit depth. For the surface area, we have

$$A_s = 2\pi R_0 - 4c + \mathcal{O}(c^2), \quad (\text{A.5})$$

and $A_s^0 = 2\pi R_0$ for the initial surface area. For the contact area, we have $A_c = 2c$, and $A_c^0 = 0$. Upon inserting these areas into (18), we obtain

$$\Delta G = 2(\gamma_c - 2\gamma_s)c. \quad (\text{A.6})$$

Consider the kinematics of the diffusive flux. Conservation of mass requires that the divergence of the flux in the grain boundary and the velocity of matter into the grain boundary v_c sum to zero,

$$\nabla_s \cdot \mathbf{j}_c + v_c = 0, \quad (\text{A.7})$$

where ∇_s is the surface divergence operator. This relation simplifies to $\partial j_c / \partial x + v_c = 0$ for the in-plane problem. The velocity v_c is related directly to the rate of change in height $2\dot{H}$ by $v_n = 2\dot{H}$, where

$$\dot{H} = -\frac{c\dot{c}}{3R_0}, \quad (\text{A.8})$$

via (48) and (49). Consequently, the diffusive flux is

$$j_c = \frac{2c\dot{c}x}{3R_0} \quad (\text{A.9})$$

and (50) reduces to

$$\Psi = \frac{4c^5\dot{c}^2}{27\mathcal{D}_c R_0^2}. \quad (\text{A.10})$$

It remains to substitute (52) and (56) into (30), and to integrate with respect to time t to obtain

$$c^6 = \frac{81}{2} \mathcal{D}_c R_0^2 (2\gamma_s - \gamma_c)t, \quad (\text{A.11})$$

which is the same result as that obtained by [55] for an array of spheres, except for a small difference in pre-factor.

Supplementary material

Supplementary material associated with this article can be found, in the online version, at doi:10.1016/j.actamat.2022.117799.

References

- [1] L. Cademartiri, G.A. Ozin, Ultrathin nanowires—A materials chemistry perspective, *Adv. Mater.* 21 (9) (2009) 1013–1020, doi:10.1002/adma.200801836.
- [2] J. Gao, C.M. Bender, C.J. Murphy, Dependence of the gold nanorod aspect ratio on the nature of the directing surfactant in aqueous solution, *Langmuir* 19 (21) (2003) 9065–9070, doi:10.1021/la034919i.
- [3] N. Pazos-Pérez, D. Baranov, S. Irsen, M. Hilgendorff, L.M. Liz-Marzán, M. Giersig, Synthesis of flexible, ultrathin gold nanowires in organic media, *Langmuir* 24 (17) (2008) 9855–9860, doi:10.1021/la801675d.
- [4] T.K. Sau, A.L. Rogach, Nonspherical noble metal nanoparticles: colloid-chemical synthesis and morphology control, *Adv. Mater.* 22 (16) (2010) 1781–1804, doi:10.1002/adma.200901271.
- [5] H. You, X. Liu, H. Liu, J. Fang, Theoretical description of the role of amine surfactant on the anisotropic growth of gold nanocrystals, *CrystEngComm* 18 (21) (2016) 3934–3941, doi:10.1039/C6CE00550K.
- [6] M.J. Kim, S. Alvarez, Z. Chen, K.A. Fichtorn, B.J. Wiley, Single-crystal electrochemistry reveals why metal nanowires grow, *J. Am. Chem. Soc.* 140 (44) (2018) 14740–14746, doi:10.1021/jacs.8b08053.
- [7] A. Halder, N. Ravishanker, Ultrafine single-crystalline gold nanowire arrays by oriented attachment, *Adv. Mater.* 19 (14) (2007) 1854–1858, doi:10.1002/adma.200602325.
- [8] Z. Huo, C.-k. Tsung, W. Huang, X. Zhang, P. Yang, Sub-two nanometer single crystal Au nanowires, *Nano Lett.* 8 (7) (2008) 2041–2044, doi:10.1021/nl8013549.
- [9] C. Wang, Y. Hu, C.M. Lieber, S. Sun, Ultrathin Au nanowires and their transport properties, *J. Am. Chem. Soc.* 130 (28) (2008) 8902–8903, doi:10.1021/ja803408f.
- [10] X. Lu, M.S. Yavuz, H.-y. Tuan, B.A. Korgel, Y. Xia, Ultrathin gold nanowires can be obtained by reducing polymeric strands of oleylamine-AuCl complexes formed via aurophilic interaction, *J. Am. Chem. Soc.* 130 (28) (2008) 8900–8901, doi:10.1021/ja803343m.
- [11] Z. Wang, Y. Hou, J. Kim, S. Sun, A general strategy for synthesizing FePt nanowires and nanorods, *Angew. Chem. Int. Ed.* 46 (33) (2007) 6333–6335, doi:10.1002/anie.200702001.
- [12] B. Li, S. Ye, I.E. Stewart, S. Alvarez, B.J. Wiley, Synthesis and purification of silver nanowires to make conducting films with a transmittance of 99%, *Nano Lett.* 15 (10) (2015) 6722–6726, doi:10.1021/acs.nanolett.5b02582.
- [13] W. Zhao, D. Huang, Q. Yuan, X. Wang, Sub-2.0-nm Ru and composition-tunable RuPt nanowire networks, *Nano Res.* 9 (10) (2016) 3066–3074, doi:10.1007/s12274-016-1189-4.
- [14] Z. Liu, D. Xu, J. Liang, J. Shen, S. Zhang, Y. Qian, Growth of Cu₂S ultrathin nanowires in a binary surfactant solvent, *J. Phys. Chem. B* 109 (21) (2005) 10699–10704, doi:10.1021/jp050332w.
- [15] L. Cademartiri, R. Malakooti, P.G. O'Brien, A. Migliori, S. Petrov, N.P. Kherani, G.A. Ozin, Large-scale synthesis of ultrathin Bi₂S₃ necklace nanowires, *Angew. Chem. Int. Ed.* 47 (20) (2008) 3814–3817, doi:10.1002/anie.200705034.
- [16] R. Malakooti, L. Cademartiri, A. Migliori, G.A. Ozin, Ultrathin Sb₂S₃ nanowires and nanoplatelets, *J. Mater. Chem.* 18 (1) (2008) 66–69, doi:10.1039/B713383A.
- [17] S. Gong, Y. Zhao, Q. Shi, Y. Wang, L.W. Yap, W. Cheng, Self-assembled ultrathin gold nanowires as highly transparent, conductive and stretchable supercapacitor, *Electroanalysis* 28 (6) (2016) 1298–1304, doi:10.1002/elan.201600081.
- [18] J.H.M. Maurer, L. González-García, B. Reiser, I. Kanelidis, T. Kraus, Templated self-assembly of ultrathin gold nanowires by nanoimprinting for transparent flexible electronics, *Nano Lett.* 16 (5) (2016) 2921–2925, doi:10.1021/acs.nanolett.5b04319.
- [19] A. Loubat, M. Impéror-Clerc, B. Pansu, F. Meneau, B. Raquet, G. Viau, L.-M. Lacroix, Growth and self-assembly of ultrathin Au nanowires into expanded hexagonal superlattice studied by in situ SAXS, *Langmuir* 30 (14) (2014) 4005–4012, doi:10.1021/la500549z.
- [20] B.Y. Xia, H.B. Wu, Y. Yan, X.W.D. Lou, X. Wang, Ultrathin and ultralong single-crystal platinum nanowire assemblies with highly stable electrocatalytic activity, *J. Am. Chem. Soc.* 135 (25) (2013) 9480–9485, doi:10.1021/ja402955t.
- [21] F.A. Nichols, W.W. Mullins, Morphological changes of a surface of revolution due to capillarity-induced surface diffusion, *J. Appl. Phys.* 36 (6) (1965a) 1826–1835, doi:10.1063/1.1714360.
- [22] F.A. Nichols, W.W. Mullins, Surface- (interface-) and volume diffusion contributions to morphological changes driven by capillarity, *AIME Metall. Soc. Trans.* 233 (10) (1965b) 1840–1848.
- [23] J.A.F. Plateau, *Statique Experimentale et Theorique des Liquides Soumis aux Seules Forces Moleculaires*, Gauthiers-Villars, Paris, 1873.
- [24] L. Rayleigh, On the instability of jets, *Proc. Lond. Math. Soc.* s1-10 (1) (1878) 4–13, doi:10.1112/plms/s1-10.1.4.
- [25] S. Bettscheider, T. Kraus, N.A. Fleck, On the geometric stability of an inorganic nanowire and an organic ligand shell, *J. Mech. Phys. Solids* 123 (2019) 3–19, doi:10.1016/j.jmps.2018.07.017.
- [26] M.S. McCallum, P.W. Voorhees, M.J. Miksis, S.H. Davis, H. Wong, Capillary instabilities in solid thin films: lines, *J. Appl. Phys.* 79 (10) (1996) 7604–7611, doi:10.1063/1.362343.
- [27] K.F. Gurski, G.B. McFadden, M.J. Miksis, The effect of contact lines on the Rayleigh instability with anisotropic surface energy, *SIAM J. Appl. Math.* 66 (4) (2006) 1163–1187, doi:10.1137/050626946.
- [28] S.P.A. Gill, Controlling the Rayleigh instability of nanowires, *Appl. Phys. Lett.* 102 (14) (2013) 143108, doi:10.1063/1.4801766.
- [29] G. Boussinot, E.A. Brener, Inhibition of Rayleigh-Plateau instability on a unidirectionally patterned substrate, *Phys. Rev. E* 92 (3) (2015) 032408, doi:10.1103/PhysRevE.92.032408.
- [30] J. Cahn, Stability of rods with anisotropic surface free energy, *Scr. Metall.* 13 (11) (1979) 1069–1071, doi:10.1016/0036-9748(79)90205-9.
- [31] A.M. Glaeser, Model studies of Rayleigh instabilities via microdesigned interfaces, *Interface Sci.* 9 (1/2) (2001) 65–82, doi:10.1023/A:1011279015039.
- [32] K.F. Gurski, G.B. McFadden, The effect of anisotropic surface energy on the Rayleigh instability, *Proc. R. Soc. A Math. Phys. Eng. Sci.* 459 (2038) (2003) 2575–2598, doi:10.1098/rspa.2003.1144.
- [33] G.H. Kim, C.V. Thompson, Effect of surface energy anisotropy on Rayleigh-like solid-state dewetting and nanowire stability, *Acta Mater.* 84 (2015) 190–201, doi:10.1016/j.actamat.2014.10.028.
- [34] Y. Imura, S. Hojo, C. Morita, T. Kawai, Preparation of silica-coated ultrathin gold nanowires with high morphological stability, *Langmuir* 30 (7) (2014) 1888–1892, doi:10.1021/la403681w.
- [35] S.P.O. Danielsen, J. Choi, R.J. Composto, Retardation of shape change of Au nanorods using photo-cross-linkable ligands, *J. Polym. Sci. Part B Polym. Phys.* 54 (2) (2016) 301–307, doi:10.1002/polb.23929.

- [36] W.J. Kennedy, S. Izor, B.D. Anderson, G. Frank, V. Varshney, G.J. Ehlert, Thermal reshaping dynamics of gold nanorods: influence of size, shape, and local environment, *ACS Appl. Mater. Interfaces* 10 (50) (2018) 43865–43873, doi:10.1021/acsami.8b12965.
- [37] Y. Imura, H. Tanuma, H. Sugimoto, R. Ito, S. Hojo, H. Endo, C. Morita, T. Kawai, Water-dispersible ultrathin Au nanowires prepared using a lamellar template of a long-chain amidoamine derivative, *Chem. Commun.* 47 (22) (2011) 6380, doi:10.1039/c0cc05545j.
- [38] S.E. Huber, C. Warakulwit, J. Limtrakul, T. Tsukuda, M. Probst, Thermal stabilization of thin gold nanowires by surfactant-coating: a molecular dynamics study, *Nanoscale* 4 (2) (2012) 585–590, doi:10.1039/C1NR11282A.
- [39] R. Takahata, S. Yamazoe, C. Warakulwit, J. Limtrakul, T. Tsukuda, Rayleigh instability and surfactant-mediated stabilization of ultrathin gold nanorods, *J. Phys. Chem. C* 120 (30) (2016) 17006–17010, doi:10.1021/acs.jpcc.6b03113.
- [40] E.S.A. Nouh, E.A. Baquero, L.-M. Lacroix, F. Delpech, R. Poteau, G. Viau, Surface-engineering of ultrathin gold nanowires: tailored self-assembly and enhanced stability, *Langmuir* 33 (22) (2017) 5456–5463, doi:10.1021/acs.langmuir.7b00477.
- [41] B. Reiser, D. Gerstner, L. Gonzalez-Garcia, J.H.M. Maurer, I. Kanelidis, T. Kraus, Multivalent bonds in self-assembled bundles of ultrathin gold nanowires, *PCCP* 18 (39) (2016) 27165–27169, doi:10.1039/C6CP05181B.
- [42] S. Bettscheider, B. Kuttich, L.F. Engel, L. González-García, T. Kraus, Bundling of nanowires induced by unbound ligand, *J. Phys. Chem. C* 125 (6) (2021) 3590–3598, doi:10.1021/acs.jpcc.0c10919.
- [43] H. Gao, S. Bettscheider, T. Kraus, M.H. Müser, Entropy can bundle nanowires in good solvents, *Nano Lett.* 19 (10) (2019) 6993–6999, doi:10.1021/acs.nanolett.9b02379.
- [44] J.H.M. Maurer, L. González-García, B. Reiser, I. Kanelidis, T. Kraus, Sintering of ultrathin gold nanowires for transparent electronics, *ACS Appl. Mater. Interfaces* 7 (15) (2015) 7838–7842, doi:10.1021/acsami.5b02088.
- [45] H. Feng, Y. Yang, Y. You, G. Li, J. Guo, T. Yu, Z. Shen, T. Wu, B. Xing, Simple and rapid synthesis of ultrathin gold nanowires, their self-assembly and application in surface-enhanced Raman scattering, *Chem. Commun.* 0 (15) (2009) 1984, doi:10.1039/b822507a.
- [46] S. Förster, A. Timmann, M. Konrad, C. Schellbach, A. Meyer, S.S. Funari, P. Mulvaney, R. Knott, Scattering curves of ordered mesoscopic materials, *J. Phys. Chem. B* 109 (4) (2005) 1347–1360, doi:10.1021/jp0467494.
- [47] A. Sundblom, C.L.P. Oliveira, A.E.C. Palmqvist, J.S. Pedersen, Modeling in situ small-angle X-ray scattering measurements following the formation of mesostructured silica, *J. Phys. Chem. C* 113 (18) (2009) 7706–7713, doi:10.1021/jp809798c.
- [48] S. Manet, J. Schmitt, M. Impéror-Clerc, V. Zholobenko, D. Durand, C.L.P. Oliveira, J.S. Pedersen, C. Gervais, N. Baccile, F. Babonneau, I. Grillo, F. Meneau, C. Rochas, Kinetics of the formation of 2D-hexagonal silica nanostructured materials by nonionic block copolymer templating in solution, *J. Phys. Chem. B* 115 (39) (2011) 11330–11344, doi:10.1021/jp200213k.
- [49] M. Newville, R. Otten, A. Nelson, A. Ingargiola, T. Stensitzki, D. Allan, A. Fox, F. Carter, Michał, D. Pustakhod, Lneuhhaus, S. Weigand, R.O. Glenn, C.D. Mark, A.L.R. Hansen, G. Pasquevich, L. Foks, N. Zobrist, O. Frost, A. Beelen, Stuermer, Kwertyops, A. Polloreno, S. Caldwell, A. Almarza, A. Persaud, B. Gamari, B.F. Maier, *Imfit*, 2021, doi:10.5281/zenodo.4516651.
- [50] Y. Yu, F. Cui, J. Sun, P. Yang, Atomic structure of ultrathin gold nanowires, *Nano Lett.* 16 (5) (2016) 3078–3084, doi:10.1021/acs.nanolett.6b00233.
- [51] S. Xu, P. Li, Y. Lu, In situ atomic-scale analysis of Rayleigh instability in ultrathin gold nanowires, *Nano Res.* 11 (2) (2018) 625–632, doi:10.1007/s12274-017-1667-3.
- [52] P. Li, Y. Han, X. Zhou, Z. Fan, S. Xu, K. Cao, F. Meng, L. Gao, J. Song, H. Zhang, Y. Lu, Thermal effect and Rayleigh instability of ultrathin 4H hexagonal gold nanoribbons, *Matter* 2 (3) (2020a) 658–665, doi:10.1016/j.matt.2019.10.003.
- [53] P. Li, W. Liao, L. Yue, Z. Fan, F. Rao, Key factors affecting Rayleigh instability of ultrathin 4H hexagonal gold nanoribbons, *Nanoscale Adv.* 2 (7) (2020b) 3027–3032, doi:10.1039/D0NA00186D.
- [54] M. Saitoh, Y. Kashiwagi, M. Chigane, Structural analysis of micrometer-long gold nanowires using a wormlike chain model and their rheological properties, *Soft Matter* 13 (21) (2017) 3927–3935, doi:10.1039/C7SM00284J.
- [55] F. Parhami, R. McMeeking, A. Cocks, Z. Suo, A model for the sintering and coarsening of rows of spherical particles, *Mech. Mater.* 31 (1) (1999) 43–61, doi:10.1016/S0167-6636(98)00049-0.
- [56] A.J.R. Hensley, K. Ghale, C. Rieg, T. Dang, E. Anderst, F. Studt, C.T. Campbell, J.-S. McEwen, Y. Xu, DFT-Based Method for more accurate adsorption energies: an adaptive sum of energies from RPBE and vdW density functionals, *J. Phys. Chem. C* 121 (9) (2017) 4937–4945, doi:10.1021/acs.jpcc.6b10187.
- [57] A.C.F. Cocks, S.P.A. Gill, J. Pan, Modeling microstructure evolution in engineering materials, in: E. van der Giessen, T. Wu (Eds.), *Advances in Applied Mechanics*, 36, Academic Press, 1998, pp. 82–162.
- [58] J. Borges, J.A. Ribeiro, E.M. Pereira, C.A. Carreira, C.M. Pereira, F. Silva, Preparation and characterization of DNA films using oleylamine modified Au surfaces, *J. Colloid Interface Sci.* 358 (2) (2011) 626–634, doi:10.1016/j.jcis.2011.03.039.
- [59] S. Mourdikoudis, L.M. Liz-Marzán, Oleylamine in nanoparticle synthesis, *Chem. Mater.* 25 (9) (2013) 1465–1476, doi:10.1021/cm4000476.
- [60] J.H.M. Maurer, L. Gonzalez-Garcia, B. Reiser, I. Kanelidis, T. Kraus, Ultrathin gold nanowires for transparent electronics: soft sintering and temperature stability, *Phys. Status Solidi (A)* 213 (9) (2016) 2336–2340, doi:10.1002/pssa.201532874.
- [61] R.L. Coble, Initial sintering of alumina and hematite, *J. Am. Ceram. Soc.* 41 (2) (1958) 55–62, doi:10.1111/j.1151-2916.1958.tb13519.x.
- [62] T. Roth, The surface and grain boundary energies of iron, cobalt and nickel, *Mater. Sci. Eng.* 18 (2) (1975) 183–192, doi:10.1016/0025-5416(75)90168-8.
- [63] T. Wejrzanowski, K.J. Kurzydowski, Modeling of size effects in diffusion driven processes at nanoscale - large atomic and mesoscale methods, *Diffus. Found.* 12 (2017) 38–73, doi:10.4028/www.scientific.net/DF.12.38.

Supplementary Information to: Stabilization of ultrathin nanowires by self-assembly into bundles

Simon Bettscheider^{a,c}, Norman A. Fleck^{b,*}, Tobias Kraus^{a,c,*}

^a*INM – Leibniz Institute for New Materials, Campus
D2.2, Saarbrücken, 66123, Germany*

^b*Cambridge University Engineering Department, Trumpington Street, Cambridge, CB2
1PZ, UK*

^c*Colloid and Interface Chemistry, Saarland University, Campus
D2.2, Saarbrücken, 66123, Germany*

1. Chemicals

All chemicals used are listed in Tab. S1. Oleylamine was filtered prior to use (Millex filter, 0.45 μm , hydrophobic PTFE). All other chemicals were used as received.

Chemical	Purity	Manufacturer
Oleylamine	80-90 % C18	Acros Organics, PA, US
Hydrogen tetrachloroaurate trihydrate ($\text{HAuCl}_4 \cdot n\text{H}_2\text{O}$ with $n \approx 3$)	Au content $\geq 49\%$	Acros Organics, PA, US
Triisopropylsilane	$\geq 98\%$	abcr, Germany
<i>n</i> -hexane	$\geq 99\%$	abcr, Germany
Absolute ethanol	$\geq 99.8\%$	Fisher Scientific, PA, US
Cyclooctane	$\geq 99\%$	Alfa Aesar, MA, US

Table S1: Chemicals and manufacturers.

*Authors to whom correspondence should be addressed.

Email addresses: simon.bettscheider@leibniz-inm.de (Simon Bettscheider), naf1@eng.cam.ac.uk (Norman A. Fleck), tobias.kraus@leibniz-inm.de (Tobias Kraus)

5 2. Scattering model

6 This section follows the work of Förster et al. [1], Sundblom et al. [2], Manet
7 et al. [3], and Loubat et al. [4]. The total scattered intensity is the sum of
8 the scattering contribution from spheres I_s , freely dispersed cylinders I_c , and
9 bundled cylinders I_b . Consider each in turn.

10 2.1. Spheres

11 The intensity I_s scattered by a number n_s spheres is given by

$$I_s(q) = n_s(\rho_s - \rho_0)^2 P_s(q), \quad (1)$$

12 where ρ_s is the scattering length density of the sphere and ρ_0 that of the
13 solvent. The term $P_s(q) = \langle F_s(q)^2 \rangle$ is the averaged form factor of the spheres,
14 obtained by convoluting the form factor F_s of the spheres with a Schulz-Zimm
15 distribution. The form factor $F_s(q)$ of the spheres is given by

$$F_s(q) = \left(\frac{4}{3} \pi R_s^2 \right) \frac{3(\sin(qR_s) - qR_s \cos(qR_s))}{(qR_s)^3}. \quad (2)$$

16 The number of spheres n_s is related to the volume fraction of spheres ϕ_s via
17 $n_s = \phi_s / \langle V_s \rangle$, where $\langle V_s \rangle$ is the average volume of a sphere. The intensity of
18 the spheres can then be written as

$$I_s(q) = \phi_s(\rho_s - \rho_0)^2 \frac{\langle F_s^2(q) \rangle}{\langle V_s \rangle} \quad (3)$$

19 2.2. Freely dispersed nanowires

20 Freely dispersed nanowires were modeled as cylinders of radius R_c and length
21 L with a scattered intensity of

$$I_c(q) = n_c(\rho_c - \rho_0)^2 P_c(q), \quad (4)$$

22 where n_c is the number of cylinders, ρ_c the scattering length density of the
23 cylinder material, and $P_c(q)$ the averaged form factor of the cylinder. The
24 averaged form factor of the cylinder $P_c(q)$ depends on the form factors of
25 an infinitesimally thin cylinder $F_{\text{thin}}(q)$ and a disk's cross-section $F_{\text{cs}}(q)$ as
26 $P_c(q) = F_{\text{thin}}(q) \langle F_{\text{cs}}^2(q) \rangle$. The form factor of the cross-section $F_{\text{cs}}(q)$ is given
27 by

$$F_{\text{cs}}(q) = \pi R_c^2 \frac{2J_1(qR_c)}{qR_c}, \quad (5)$$

28 where J_1 is the Bessel function of the first kind. The form factor of the
 29 infinitesimally thin cylinder is given by

$$F_{\text{thin}}(q) = L^2 \left(\frac{2}{qL} \int_0^{qL} \frac{\sin(x)}{x} dx - \left(\frac{2 \sin(qL/2)}{qL} \right)^2 \right) \quad (6)$$

30 In the case of $q \gg 1/L$, which is valid in our scattering experiments, the
 31 integral may be approximated by $\int_0^{qL} \frac{\sin(x)}{x} dx \approx \frac{\pi}{2}$ so that the form factor
 32 $F_{\text{thin}}(q)$ simplifies to

$$F_{\text{thin}}(q) = L^2 \left(\frac{\pi}{qL} - \left(\frac{2 \sin(qL/2)}{qL} \right)^2 \right) \quad (7)$$

33 In analogy to the spheres, the number of cylinders n_c is related to the volume
 34 fraction of freely dispersed cylinders ϕ_c via $n_c = \phi_c / \langle V_c \rangle$, where $\langle V_c \rangle$ is the
 35 average volume of a cylinder. The scattered intensity of the freely dispersed
 36 cylinders can hence be written as

$$I_c(q) = \phi_c (\rho_c - \rho_0)^2 \frac{F_{\text{thin}}(q) \langle F_{\text{cs}}^2(q) \rangle}{\langle V_c \rangle}. \quad (8)$$

37 2.3. Bundled nanowires

38 Bundled nanowires were modeled as the average over a 2D close-packed
 39 (hexagonal) lattice of cylinders. The scattered intensity is the one of cylin-
 40 ders given in (8), multiplied by lattice factor of a disordered lattice $Z(q)$ as
 41 given by

$$I_d(q) = \phi_d (\rho_c - \rho_0)^2 \frac{F_{\text{thin}}(q) \langle F_{\text{cs}}^2(q) \rangle}{\langle V_c \rangle} Z(q). \quad (9)$$

42 The lattice factor of the disordered lattice is given by

$$Z(q) = \beta(q)G(q)Z_0(q) + (1 - \beta(q))G(q), \quad (10)$$

43 where $Z_0(q)$ is the lattice factor of an ideal lattice, $\beta(q)$ accounts for disorder
 44 in the lattice due to polydispersity of the cylinder radius, and $G(q)$ if the
 45 Debye-Waller factor accounting for disorder caused by thermal fluctuations.
 46 The lattice factor of an ideal lattice of unit cell area A_{unit} , peak multiplicites
 47 m_{hk} , and peak positions q_{hk} is given by

$$Z_0(q) = \frac{1}{A_{\text{unit}}} \frac{2\pi}{q} \sum_{hk} m_{hk} L_{hk}(q, q_{hk}, \sigma). \quad (11)$$

48 Here, $L_{hk}(q, q_{hk}, \sigma)$ is the normalized Lorentz function with a peak width of
 49 2σ . The term accounting for lattice disorder due to polydispersity in the
 50 cylinder radius $\beta(q)$ is given by

$$\beta(q) = \frac{\langle F_{cs} \rangle^2}{\langle F_{cs}^2 \rangle} \quad (12)$$

51 and the Debye-Waller factor $G(q)$ is given by

$$G(q) = \exp(-\sigma_{\text{DW}}^2 a^2 q^2), \quad (13)$$

52 where σ_{DW} is the relative mean-square displacement for the positional disorder,
 53 and a is the distance between the nearest neighbors, which is identical
 54 to the lattice constant in the close-packed, hexagonal lattice.

55 3. Additional figures

56 The relative density (also called packing density) $\bar{\rho}$ can be calculated for
 57 $n \geq 3$ and is given by

$$\bar{\rho} = \frac{\cot(\pi/n)}{\cos^2 \omega_0} \left(\frac{\pi}{n} - \frac{1}{2} (2\omega_0 - \sin(2\omega_0)) \right). \quad (14)$$

58 Values of the relative density $\bar{\rho}$ are given for example configurations in S2,
 59 and $\bar{\rho}$ is plotted as a function of n and ω_0 in S3a.

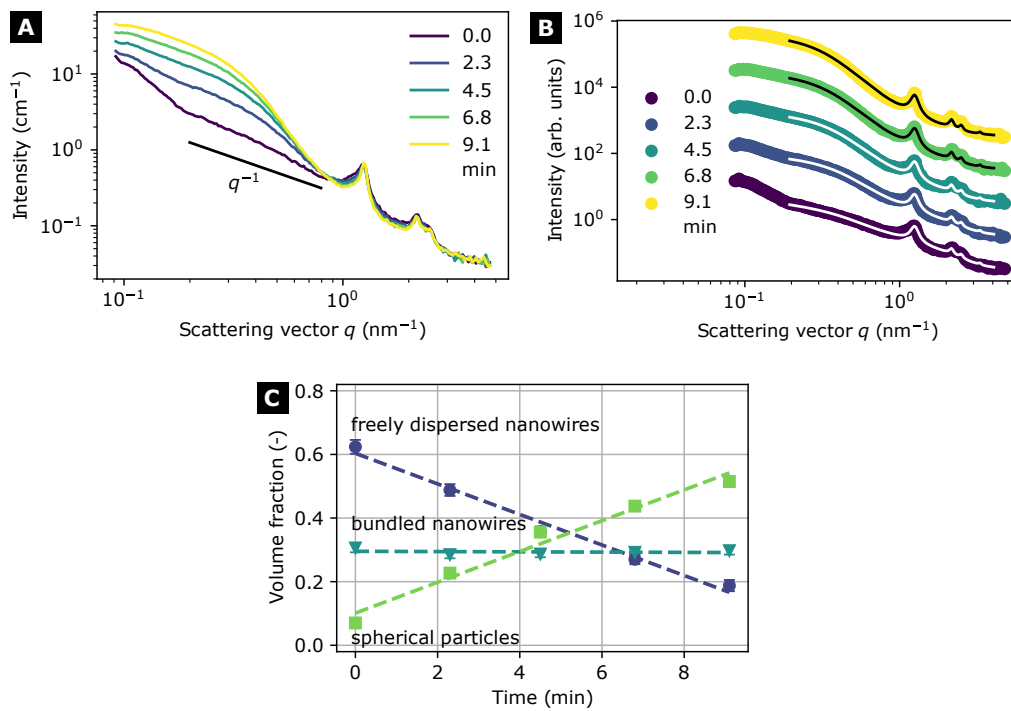


Figure S1: (a) Evolution of small-angle X-ray scattering from fragmenting AuNWs at 70 °C. At small q -values, the scattering signal bulges upwards, indicating that nanowires have broken-up into spheroidal particles. (b) Scattering models fitted to the scattering from (a) at selected times. Dots show experimental data points and solid lines the fits; the scattering curves are shifted vertically for better visualisation. (c) Volume fractions of gold in freely dispersed nanowires, bundled nanowires, and spherical particles. Error bars denote the standard error of the fits. The dashed line are linear fits.

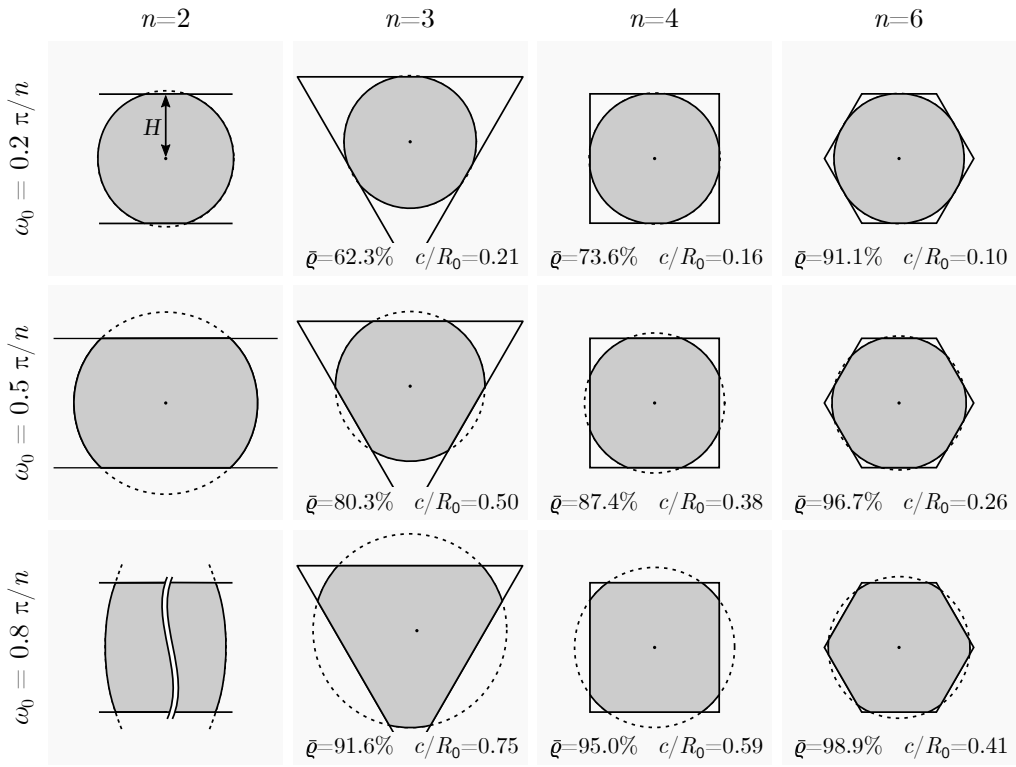


Figure S2: Example configurations a cylinder truncated by n facets at three different contact angles ω_0 . The height H , which is the distance between the cylinders centre and the truncating surfaces, is constant among all shown configurations. For $n \geq 3$, the relative density (also called packing density) $\bar{\rho}$ and the contact width c/R_0 are shown.

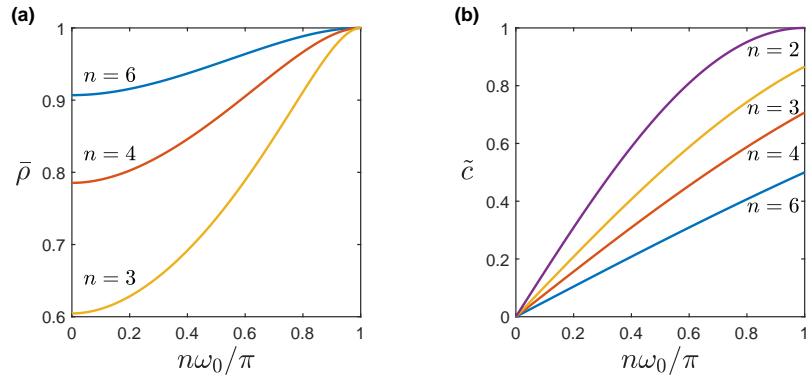


Figure S3: **(a)** Packing density $\bar{\rho}$ as a function of the contact angle ω_0 for the tessellated arrangements of truncated cylinders as shown in Fig. S2. **(b)** The contact width $\tilde{c} = c/R_0$ as a function of contact angle ω_0 .

60 **References**

- 61 [1] S. Förster, A. Timmann, M. Konrad, C. Schellbach, A. Meyer,
62 S. S. Funari, P. Mulvaney, R. Knott, Scattering Curves of Ordered
63 Mesoscopic Materials, *Journal of Physical Chemistry B* 109 (2005)
64 1347–1360. URL: <http://pubs.acs.org/doi/abs/10.1021/jp0467494>.
65 doi:10.1021/jp0467494.
- 66 [2] A. Sundblom, C. L. P. Oliveira, A. E. C. Palmqvist, J. S. Pedersen, Mod-
67 eling in Situ Small-Angle X-ray Scattering Measurements Following the
68 Formation of Mesoporous Silica, *The Journal of Physical Chemistry*
69 *C* 113 (2009) 7706–7713. URL: <https://pubs.acs.org/doi/10.1021/jp809798c>. doi:10.1021/jp809798c.
- 71 [3] S. Manet, J. Schmitt, M. Impéror-Clerc, V. Zholobenko, D. Durand,
72 C. L. P. Oliveira, J. S. Pedersen, C. Gervais, N. Baccile, F. Babon-
73 neau, I. Grillo, F. Meneau, C. Rochas, Kinetics of the Formation of 2D-
74 Hexagonal Silica Nanostructured Materials by Nonionic Block Copolymer
75 Templating in Solution, *The Journal of Physical Chemistry B* 115 (2011)
76 11330–11344. URL: <https://pubs.acs.org/doi/10.1021/jp200213k>.
77 doi:10.1021/jp200213k.
- 78 [4] A. Loubat, M. Impéror-Clerc, B. Pansu, F. Meneau, B. Raquet, G. Viau,
79 L.-M. Lacroix, Growth and Self-Assembly of Ultrathin Au Nanowires
80 into Expanded Hexagonal Superlattice Studied by in Situ SAXS, *Lang-*
81 *muir* 30 (2014) 4005–4012. URL: [https://pubs.acs.org/doi/10.1021/](https://pubs.acs.org/doi/10.1021/la500549z)
82 [la500549z](https://pubs.acs.org/doi/10.1021/la500549z). doi:10.1021/la500549z.

Chapter 4

Discussion

The goal of this dissertation is to investigate the shape stability of ultrathin, ligand-coated nanowires, elucidate the mechanisms that induce the bundling of these nanowires, and assess whether bundling influences shape stability. The mechanisms of bundle formation were studied in AuNWs in alcohols and alkanes, using both experiments and MD simulations in [Publication 1](#) and [Publication 2](#). The shape stability of ligand-capped nanowires was investigated in a linear perturbation analysis in [Publication 3](#). Whether bundling influences the shape stability was studied experimentally in the model system of AuNWs with a ligand shell of OAm and more broadly with a micromechanical model in [Publication 4](#).

4.1 Mechanisms of bundle formation

Ultrathin nanowires can exist as single, freely dispersed nanowires, or they can self-assemble into elongated, close-packed (hexagonal) bundles during drying and in dispersion. [Publication 1](#) and [Publication 2](#) investigated why and when such bundles form in AuNW dispersions in three solvent types: while hydrophobic interactions caused bundling in alcohols, entropic interactions induced bundling in linear and cyclic alkanes.

Insight 1: OAm-capped AuNWs in alcohols form bundles due to hydrophobic segregation ([Publication 1](#)). Bundles were denser than those previously found in arenes and linear and cyclic alkanes, with a center-to-center distance of 4.1 nm as measured by SAXS, corresponding to a surface-to-surface spacing of 2.4 nm. Given that the ligand OAm has a length of approximately 2.2 nm, this spacing implies that the ligand shells must have collapsed or interdigitated. MD simulations in [Publication 1](#) revealed that the shells did not collapse; rather, they strongly interdigitated into the shells of neighboring nanowires, thus expelling the solvent from the space between two nanowires. This hydrophobic segregation caused the bundling of OAm-capped AuNWs in alcohols: the ligands have a stronger affinity to other ligands than to solvent molecules, and vdW forces between the gold cores add to the

attractive force. This mechanism is equivalent to that described for ligand-capped nanoparticles in other poor solvents, see Section 2.2.1 [152, 158–160]. Note that the center-to-center distance of OAm-capped AuNWs in ethanol was previously reported to be 3.6 nm by Reiser et al. [199], differing from the value of 4.1 nm reported in Publication 1. The peak positions measured in Publication 1 match those of Reiser et al. [199], so the discrepancy must be due to differences in the analysis between Publication 1 and Ref. [199]. Based on re-analyzing both data sets, I, as the author of this thesis, take the position that the value of 4.1 nm reported in Publication 1 is correct.

Insight 2: Bundling of OAm-capped AuNWs in linear alkanes is driven by entropic interactions: solvent orders in the proximity of the ligand shell. AuNWs purified twice and re-dispersed in *n*-hexane were confirmed to bundle with a center-to-center distance of 5.5 nm, corresponding to a surface-to-surface spacing of 3.8 nm, as reported earlier by Reiser et al. [45]. MD simulations in Publication 1 showed that the ligand shells were well solvated. The total interactions energy was $0.2k_{\text{B}}T/\text{nm}$. VdW forces accounted for only one-tenth of this interaction energy, so another interaction must have been responsible for bundling. An analysis of molecular orientations by Herman's orientation function revealed that *n*-hexane molecules within and in the proximity of the ligand shell aligned perpendicular to the nanowire surface, whereby they lost entropy. By forming bundles, the system can avoid this loss in entropy because bundled nanowires share domains of ordered solvent.

This entropic mechanism shares similarities with the depletion force outlined in Section 2.2.1. Rod-shaped depletants in the proximity of larger spherical particles must orient their backbone parallel to the surface of these larger particles, whereby they lose entropy (see Fig. 2.6C) [184–190]. The entropic mechanism proposed here is similar to depletion forces with two differences. First, the depletants orient their backbone perpendicular to the nanowire surface. Second, the depletants are not separate colloidal constituents; instead, they are solvent molecules that are necessary constituents of any colloidal dispersion.

The findings contradict the proposition by Loubat et al. [44] that bundling of OAm-capped AuNWs in *n*-hexane is dominated by vdW forces (Section 2.2.2) and show that ligand phase transitions observed in nanoparticles of similar size neither play a role (Section 2.2.1). Bundling is instead driven by a type of depletion interaction, an idea first proposed by Loubat et al. [44] but previously not substantiated. Publication 1 provides this evidence. The proposed mechanism could be of practical relevance. If bundling was to be controlled, it could be switched on and off by small changes in the solvent's ability to order.

Insight 3: Bundling of OAm-capped AuNWs in cyclic alkanes is also driven

by entropic interactions: unbound ligand orders in proximity of the ligand shell. Bundles in cyclohexane formed at small nanowire concentrations with a center-to-center distance of 5.9 nm, larger than in *n*-hexane, implying that the ligand shells of neighboring nanowires did not touch and solvent must always have been present between the shells (Publication 2). The percentage of bundled AuNWs increased with increasing temperature, indicating that the underlying interaction is entropic. In contrast to the case of *n*-hexane, the solvent cyclohexane could not be responsible for bundling because it lacks a linear or planar structure. It was proposed that unbound ligand orders in the proximity of the ligand shell and thereby loses entropy, thus acting as a depletant. By analogy to the case of *n*-hexane, the AuNWs form bundles because bundles allow sharing domains of ordered, unbound ligand.

This finding is in line with the recent notion that nanorods and other particles can agglomerate when linearly shaped molecules such as oleic acid or OAm are added to the dispersion, see Section 2.2.1 [183, 192–195]. Publication 2 extends this knowledge by showing that unbound ligand itself can act as a depletant and induce agglomeration. The mechanism itself is not specific to AuNWs; future research will show if this entropic mechanism is also responsible for agglomeration in other non-polar colloidal dispersions, such as two-dimensional nanoplatelets in *n*-hexane [235].

Insight 4: Entropy-driven bundling occurs only at small nanowire concentrations because it requires a sufficiently sparse ligand shell. Scattering experiments of OAm-capped AuNWs in cyclohexane in Publication 2 revealed that bundles only appear in dilute samples. Dilution lowers the overall ligand concentration and—since there is always a dynamic equilibrium between adsorbed and unbound ligand—thins the ligand shell. Systematic variations of the overall amount of ligand in the system revealed that bundles form only at small concentrations of ligand and with sparse ligand shells. A dense ligand shell hinders the unbound ligand from aligning with the shell, the entropic mechanism cannot be effective, and the nanowires remain dispersed. When the sample is diluted, the ligand grafting density decreases, and the nanowires bundle. Bundling in linear alkanes required a sparse ligand shell, too.

The phenomenon of bundles forming only at small nanowire concentrations is opposite to the behavior of other colloids. For example, octanethiol-stabilized gold nanoparticles with a diameter of 3.4 nm only agglomerated above a specific nanoparticle concentration, see Section 2.2.1 [166]. The present case differs because the entropic mechanism requires sparse ligand shells. The mechanism opens a new route to stabilize and destabilize colloids by controlling the overall ligand concentration in the system. There may be potential use cases for such behavior, for example, in

recycling dispersed nanomaterials. More broadly, the study highlights that the ligand shell's density is essential not only in stabilizing colloids and maximizing their steric repulsion but also in tuning the entropic attraction of ultrathin AuNWs.

Future research could support the evidence from [Publication 1](#) and [Publication 2](#). A shortcoming of the present MD simulations is that they did not distinguish between enthalpic and entropic contributions nor between interactions of the core, the ligand, or the solvent. The conclusion that entropic interactions drive bundling had to be drawn indirectly via the analysis of molecular orientations. These conclusions could be drawn more straightforwardly by future MD simulations that directly probe the interaction between the constituents and that allow deriving enthalpic and entropic terms, such as those carried out by Kister et al. [155] and Monego et al. [157]. The second point of improvement is the notion proposed in [Publication 2](#) that unbound ligand can act as a depletant, a theory that cannot be easily proved experimentally. Prospective MD simulations explicitly treating unbound ligand would enable us to verify this theory.

Taken together, the insights from [Publication 1](#) and [Publication 2](#) highlight that future research on colloidal interactions may have to pay closer attention to the role of small molecules, at least when the colloidal particles are also of molecular length scale. The entropic mechanism found in OAm-capped AuNWs with a diameter of 1.7 nm might also be important in non-polar dispersions of other nanowires (e.g., OAm-capped Bi₂S₃ nanowires [77, 236]) or nanoplatelets (e.g. oleic-acid-capped CdSe nanoplatelets [235]), which could be clarified in future studies.

4.2 Shape stability of ligand-coated nanowires

Nanowires are prone to fragmentation due to a Plateau-Rayleigh instability. [Publication 3](#) studies the role of the ligand shell in the shape stability of ultrathin nanowires.

Insight 5: The ligand shell can stabilize and destabilize the nanowire shape. The ligand shell was included in the Plateau-Rayleigh theory by considering a nanowire whose surface energy depends on local surface curvature, see [Publication 3](#). The shape stability of such a nanowire was studied in a linearized perturbation analysis. Two parameters determine the critical perturbation wavelength: the parameter c describes the sensitivity of the ligand shell's free energy on the local surface curvature, and the parameter α weighs the mean and deviatoric contributions to the surface curvature. Ligand-capped nanowires were less stable than bare ones for $c > 0$ and more stable for $c < 0$, implying that ligand shells are stabilizing if their free energy decreases with increasing surface curvature. Nanowires were more stable for

small α , i.e. when the ligand shell's free energy depended on deviatoric rather than mean contributions to the surface curvature.

The model builds upon and extends previous research on the Plateau-Rayleigh instability of wires with anisotropic surface energy. Cahn [206] and Gurski and McFadden [207] assumed that the surface energy is a function of crystal orientation (see Section 2.3.3). Publication 3 is similar in that it assumes non-constant surface energy; it extends the previous models in that the surface energy depends on local curvature.

The model in Publication 3 shows that energetic properties of the ligand shell can both impair and improve the shape stability, which might explain some of the earlier experimental findings reported in the literature (see Section 2.3.4). Exchanging the ligand OAm on AuNWs with TOP [47] and ethyl 11-(4-mercaptobenzamido) undecanoate [68] increased the shape stability, while 1-dodecanethiol [47] and 3-mercaptopropanoic acid [65, 67] decreased stability. We do not yet understand why some of these ligands impair and others improve the shape stability. The model now allows assessing whether these differences are due to energetic reasons. If so, the parameters c and α , which could be determined by MD simulations, for example, will differ between the ligands.

Insight 6: The ligand shell can slow down the break-up and prolong nanowire lifetime. Kinetic contributions of the ligand shell were considered in the model in Publication 3 by interface reaction stresses and viscous stresses. The interface reaction stress accounted for the kinetic dissipation in rearranging atoms at the wire surface, and the viscous stress accounted for the kinetic dissipation arising from ligands ad- and desorbing from the wire surface. The pinch-off time increased with increasing viscous stresses, implying that the shelf-life of nanowires is prolonged when there is a strong kinetic barrier in ad- and desorbing ligands.

This extension of the Plateau-Rayleigh theory might give a reason for the observations by Takahata et al. [69]. They experimentally observed that a denser ligand shell delays the Plateau-Rayleigh instability in AuNRs. Since a denser ligand shell increases the adsorption energy [85], the model might explain their observation by linking molecular adsorption energies to the dissipation processes in the Plateau-Rayleigh theory.

Insight 7: The linearized perturbation analysis is a good predictor of pinch-off time. Publication 3 studied the pinch-off time of ligand-capped nanowires with a numerical finite difference solver alongside the predictions of the linearized perturbation analysis. Although the analytical solution cannot capture the details of break-up at later stages, they were a good predictor of the overall pinch-off time. This finding strengthens earlier notions by Nichols and Mullins [61] that the linearized perturbation analysis is a suitable tool to study the Plateau-Rayleigh instability.

To sum up, the model in [Publication 3](#) provides a general framework that allows studying various combinations of ligand and core material and linking the shape stability with the molecular behavior of the ligand shell. Energetic information can be linked to the framework by determining a ligand shell's free energy as a function of mean and deviatoric surface curvatures. This data could be obtained from MD simulations of ligand shells on curved surfaces. For example, the free energy could be simulated of those ligand molecules that were already studied experimentally and were found to influence shape stability (see Section 2.3.4). The parameters α and c could be extracted from these simulations, allowing us to locate the systems on the stability maps in [Publication 3](#) and verify whether energetic contributions alone explain the impact on shape stability. Kinetic information can be incorporated into the framework by studying ligand adsorption energies. For example, density functional theory could be used to quantify the adsorption energies of OAm on AuNWs in dependence on shell density. The framework could subsequently be used to test whether differences in adsorption energies account for the stabilization by denser ligand shells observed by Takahata et al. [69].

4.3 Influence of bundling on shape stability

Nanowires in dispersion can either be freely dispersed or agglomerate into bundles. [Publication 4](#) answers whether and to what extent bundling influences the shape stability of nanowires.

Insight 8: Bundled AuNWs are more stable than freely dispersed AuNWs. Dispersions containing both freely dispersed and bundled AuNWs were heated in experiments in [Publication 4](#) to accelerate the Plateau-Rayleigh instability, and the shape of the nanowires was tracked by SAXS and TEM. A scattering model was used to extract the fraction of freely dispersed AuNWs, bundled AuNWs, and particles resulting from fragmentation. The scattering model and TEM revealed that bundled nanowires fragmented more slowly than freely dispersed ones.

The finding implies that the shelf-life of nanowires can be prolonged if their dispersions contain bundled instead of freely dispersed nanowires. Care must be taken to account for competing effects, though. For example, bundling in linear and cyclic alkanes occurs only with sufficiently sparse ligand shells. However, a sparse ligand shell might be detrimental to shape stability, see Section 2.3.4 [69]. We need further experimental data to quantify such competing effects.

Insight 9: Bundling stabilizes nanowires by constraining their shape. The Plateau-Rayleigh instability of bundled nanowires was studied by a linear perturbation analysis in [Publication 4](#). The contact between neighboring nanowires was

modeled as flats, and the center-to-center spacing inside bundles was assumed to remain constant, thus constraining the space available to each nanowire. Stability maps showed the critical perturbation wavelength in dependence on the number of nearest neighbors, contact width, and the ratio of interfacial to surface energy.

The theoretical predictions in [Publication 4](#) matched the experimental data, showing that this simplified model can explain the stabilizing effect of bundling. The theoretical predictions were also compared to the work of Nouh et al. [47], who reported that AuNWs capped by TOP were more stable than those capped by OAm (also see Section 2.3.4). Nouh et al. [47] did not explain whether this stabilization was due to the properties of the ligand or the tighter bundles formed from the TOP-capped AuNWs. Because the model correctly predicted the stabilization solely based on the effect of bundling without considering any properties of the ligand shell, the stabilization was likely caused by bundling.

The model in [Publication 4](#) builds upon and extends two ideas introduced in Section 2.3.3. First, the interface between neighboring nanowires being modeled as fixed planes implies that the nanowire shape can only evolve inside the space confined by the bundle; and the influence of confinement on the Plateau-Rayleigh instability has already been studied experimentally and was shown to stabilize the nanowire shape [65, 66] (see Section 2.3.3). Second, the notion that the nanowire is in contact with these fixed planes resembles a nanowire contacting a substrate, which was analyzed by Gill [204] and others [64, 212, 213] (see Section 2.3.3). These previous models allowed the centerline of the wire to move relative to the substrate. The present model in [Publication 4](#) treats the case of the centerline being at a fixed distance to the constraining necks, better reflecting the geometry of bundles.

The main limitation of the analysis in [Publication 4](#) is that any elasticity of the ligand shell was omitted. The interface between neighboring nanowires was treated as fixed planes, whereas in reality, it consists of two ligand shells that exhibit some compliance. This compliance of the ligand shell could be included in the model in the future, for example, by considering a rigid core surrounded by a (visco-)elastic shell.

Insight 10: Bundling can destabilize nanowires. The model in [Publication 4](#) showed that the shape stability of bundled wires depends on the number of nearest neighbors n , the neck size between neighboring nanowires c , and the ratio of interfacial to surface energy $\tilde{\gamma}$. For sufficiently large $\tilde{\gamma}$ and c , bundled nanowires were stable against the Plateau-Rayleigh instability, regardless of the perturbation wavelength. For smaller $\tilde{\gamma}$ and c , stability decreased with increasing n , decreasing $\tilde{\gamma}$, and small or large c ; and bundled nanowires were less stable than freely dispersed ones.

These predictions differ from the Plateau-Rayleigh theory of nanowires on substrates discussed in Section 2.3.3. McCallum et al. [64], Gill [204], and Boussinot and Brener [213] theoretically showed that a nanowire on a substrate is always more stable than a free-standing nanowire, regardless of the contact angle. In contrast, the present model shows that bundles are less stable than free-standing nanowires if the ratio of interfacial to surface energy $\tilde{\gamma}$ is small.

The fact that bundling can also destabilize nanowires shows that attention is necessary if one wants to engineer bundles of improved shape stability. Stabilization requires tightly interdigitating ligand shells, and the interfacial energy between nanowires should equal the surface energy. This requirement implies that bundles formed due to hydrophobic forces, such as AuNWs in alcohols discussed in Section 2.2.2 and Publication 1, are not necessarily more stable than freely dispersed nanowires. Their interfacial energy is smaller than the surface energy. Bundles driven by entropic interactions, as discussed in Publication 1 and Publication 2, appear to be better candidates.

Insight 11: Bundled nanowires can fragment into spheres, truncated spheres, or rods. The final equilibrium shape of a fragmenting free-standing nanowire is a sphere. In contrast, other topologies can emerge from fragmenting bundles, since the space inside the bundles is constrained. Publication 4 showed that discrete spheres emerge from fragmenting bundles at small perturbation wavelengths. At larger wavelengths, the resulting particles make contact with the constraining necks and acquire the shape of a truncated sphere. At even larger wavelengths, the volume of the resulting particles no longer fits into a truncated sphere, and the final particles adopt a rod-like shape.

The model helps to interpret earlier experimental findings on the resulting particle shape. Rods as the final particle shape have already been observed in experiments of confined cylinders, see Section 2.3.3. For example, tin and polystyrene wires confined by aluminum oxide and PDMS templates broke into rods [219, 221–223]. The current model allows predicting when such nanorods form and can thus provide an explanation for these experimental observations.

Insight 12: Sintering stabilizes nanowires against the Plateau-Rayleigh instability. Publication 4 analyzes the competing effects of in-plane diffusion associated with sintering and out-of-plane diffusion associated with the Plateau-Rayleigh instability. Sintering is relevant when the nanowires are no longer capped by ligands, for example, in manufacturing transparent electrodes where the ligand shell is deliberately removed to form electrical contacts between the wires [71, 92, 237]. Sintering generally stabilized the cylindrical shape since it increased the neck size between neighboring wires. For surface and interfacial energies and diffusivities typically

found in metals, sintering was sufficiently fast to inhibit break-up. Yet, when the grain boundary energy was much smaller than the surface energy and the diffusivity in the grain boundary much slower than along the free surface, the Plateau-Rayleigh instability could still be dominant and lead to the eventual break-up of bundled wires.

Many models on the Plateau-Rayleigh instability implicitly assume that in-plane diffusion is always faster than out-of-plane diffusion along the cylinder axis [61, 62, 204]. While this assumption is valid in the case of a free-standing wire, [Publication 4](#) takes a closer look at wires on substrates as studied by McCallum et al. [64] and Gill [204] (see Section 2.3.3). For wires on substrates, the assumption still holds as long as the grain boundary energy is sufficiently large and the grain boundary diffusion is sufficiently fast.

The practical implication is that sintering is beneficial for nanowire shape stability. Such stabilization by sintering has already been exploited. To improve the conductivity and shape stability of transparent films made from AuNWs, Maurer et al. [71] removed the ligand shell around dried AuNW bundles and sintered them by plasma treatment. [Publication 4](#) explains why sintering is beneficial: sintering increases the neck size between adjacent nanowires, which stabilizes their shape.

Chapter 5

Conclusion and Outlook

In this dissertation, the shape stability of ultrathin, ligand-coated nanowires was investigated, the mechanisms that induce bundling of these nanowires were elucidated, and whether and to what extent bundling influences the shape stability was assessed.

The bundling mechanism of nanowires depended on the type of solvent. In ethanol, the ligand shells of neighboring nanowires interdigitated, expelling the polar solvent from the non-polar ligand shells. Bundling was driven by hydrophobic forces: the ligands had a higher affinity to other ligands than solvent molecules. The free energy gained in the formation of bundles was $1.52 k_B T/\text{nm}$.

In alkane solvents, an entropic mechanism similar to depletion forces drove bundling. MD simulations revealed that the ligand shells in *n*-hexane were well solvated and barely touched each other. Linear alkane solvent inside and in the proximity of the ligand shell tended to orient its backbone perpendicular to the wire surface, whereby the system lost entropy. This loss in entropy was reduced by forming bundles, allowing neighboring nanowires to share domains of ordered solvent. The interaction energy was $0.20 k_B T/\text{nm}$, indicating that only nanowires exceeding a critical length of the order of 10 nm to 100 nm can form bundles via such an entropic mechanism.

Bundles also formed in cyclohexane at small nanowire concentrations. The center-to-center distance was greater than in *n*-hexane with a distance of 5.9 nm, implying there was no contact between the ligand shells of neighboring nanowires. Temperature-dependent scattering data revealed that the underlying bundling mechanism was entropic. In contrast to *n*-hexane, cyclohexane, with its chair-like conformation, cannot be aligned in a way that it substantially loses rotational entropy. Instead, unbound ligand must have aligned in proximity to the ligand shell and induced bundling.

The entropic mechanism in linear and cyclic alkanes required a sufficiently sparse ligand shell. If the ligand shell was too dense, solvent or unbound ligand could not

be aligned, and the entropic mechanism was ineffective. This requirement gives rise to an unusual colloidal phenomenon: while colloidal particles typically remain dispersed at smaller particle concentrations and agglomerate at larger concentrations, nanowires in linear and cyclic alkanes bundled at smaller concentrations. Lowering the wire concentrations shifted the adsorption equilibrium of the ligand so that the ligand shell became less dense.

Future research on the bundling of nanowires could focus on proving that it is indeed the unbound ligand that drives bundling in cyclohexane. To date, we lack direct evidence that unbound OAm aligns with the ligand shell, and it is challenging to obtain such evidence experimentally. Instead, MD simulations of a nanowire surrounded by solvent and unbound ligand could show whether unbound ligand aligns with the shell. The associated loss in entropy could be quantified, and a critical concentration of unbound ligand necessary to induce bundling could be determined to validate the critical shell density obtained experimentally.

The shape stability of an individual, freely dispersed nanowire was studied theoretically in a linear perturbation analysis by extending the Plateau-Rayleigh theory to include the ligand shell. Energetic contributions of the ligand shell were accounted for by making the surface energy dependent on the local surface curvature. Kinetic contributions were modeled by an interface reaction stress that reflects the dissipation associated with rearranging atoms at the wire surface and a viscous stress that reflects the dissipation associated with adsorption and desorption of ligands. A ligand-coated nanowire was potentially more or less stable than a bare metal nanowire, depending on the energetic parameters of the ligand shell. The ligand shell stabilized if its free energy decreased with increasing effective curvature. From a kinetic viewpoint, the ligand shell could slow the Plateau-Rayleigh instability if it generated considerable viscous stresses. Such viscous stresses occur if there are kinetic barriers in rearranging atoms at the core-shell interface and in adsorbing and desorbing ligands onto the core surface.

Experiments showed that bundling influenced the shape stability of ligand-capped nanowires. In a dispersion containing both bundled and freely dispersed AuNWs, the freely dispersed AuNWs fragmented faster than the bundled ones, indicating that bundling stabilized the AuNWs.

A linear perturbation analysis of a continuum model helped interpret the stabilizing effect of bundling. The model considered lattices of $n = 2, 3, 4,$ or 6 nearest neighbors and treated the contact between neighboring nanowires as fixed planes. Stability maps showed the critical perturbation wavelength dependent on the number of nearest neighbors, the ratio of interfacial to surface energy, and the initial contact width between the wires. Based on these parameters, bundled nanowires

were more or less stable than freely-dispersed ones. In general, stability increased with an increasing ratio of interfacial to surface energy and decreasing number of nearest neighbors. For a sufficiently large ratio of interfacial to surface energy, bundled nanowires were stable against initial perturbations of any wavelength. In other cases, the bundled nanowires would eventually pinch off into discrete particles with three characteristic topologies. For small perturbation wavelengths, pinch-off resulted in discrete spheres, truncated spheres emerged for intermediate wavelengths, and nanorods for larger wavelengths. The model predictions agreed with the experimental observations and could explain the stabilizing effect of bundling. The theory predicts that sintering enhances shape stability. For the material parameters typically found in metals, the stabilizing effect of sintering outweighed the Plateau-Rayleigh instability. However, the Plateau-Rayleigh instability can dominate for slow grain boundary diffusion and small grain boundary energy, and wires will eventually pinch off.

Future research on the shape stability of ligand-coated nanowires could focus on comparing the theoretical model with experimental and simulated data. The pinch-off time of AuNWs could be studied by SAXS while the ligand is varied systematically. Ligands that render the AuNWs more or less stable could then be studied by MD simulations by calculating their free energy in dependence of surface curvature. Feeding this data back into the analytical model would allow linking the behavior of the ligand shell on the molecular length scale with break-up on the nano- and microscale.

The influence of bundling on the shape stability could be studied by focusing on the role of the initial neck size in experiments and the role of the ligand shell in theory. The initial neck size is determined by the center-to-center distance inside bundles, which can be modulated from 4.1 nm to 5.9 nm in OAm-capped AuNWs by varying the solvent. Studying the pinch-off time by SAXS in dependence on this center-to-center distance would allow for further validation of the model. Regarding theory, the current analytical model did not explicitly incorporate the ligand shell and treated the interface between neighboring nanowires as rigid planes. In reality, the interface consists of two compliant ligand shells. The ligand shell and its compliance could be modeled as a (visco-)elastic shell around the inelastic cylinder.

Overall, this thesis elucidated the mechanisms that induce bundling in ultrathin, ligand-coated nanowires, described the influence of the ligand shell on the shape stability of these nanowires, and assessed whether bundling influences the shape stability. Bundling in non-polar solvents is due to a new type of entropic depletion force. Understanding these molecular forces lays the foundation for exploiting bundling in applications. Future research will show whether the force is also present

in other nanoparticle systems, such as nanoplatelets. Nanowire shape stability was studied by extending the theory on the Plateau-Rayleigh instability to allow linking molecular length scale information of the ligand shell to nanowire break-up on the nano- and microscale. This newly presented framework will allow for the development of more stabilizing ligand shells. Finally, the influence of bundling on shape stability was studied experimentally and theoretically, showing that bundling can stabilize the nanowire shape. This knowledge will enable us to design colloidal systems that use bundling to stabilize nanowires further.

Bibliography

- [1] Liz Allen et al. "Publishing: Credit where credit is due". In: *Nature* 508.7496 (Apr. 2014), pp. 312–313. ISSN: 0028-0836. DOI: [10.1038/508312a](https://doi.org/10.1038/508312a). URL: <https://www.nature.com/articles/508312a>.
- [2] Amy Brand et al. "Beyond authorship: Attribution, contribution, collaboration, and credit". In: *Learned Publishing* 28.2 (2015), pp. 151–155. ISSN: 17414857. DOI: [10.1087/20150211](https://doi.org/10.1087/20150211).
- [3] Liz Allen, Alison O'Connell, and Veronique Kiermer. "How can we ensure visibility and diversity in research contributions? How the Contributor Role Taxonomy (CRediT) is helping the shift from authorship to contributorship". In: *Learned Publishing* 32.1 (Jan. 2019), pp. 71–74. ISSN: 09531513. DOI: [10.1002/leap.1210](https://doi.org/10.1002/leap.1210). URL: <https://onlinelibrary.wiley.com/doi/10.1002/leap.1210>.
- [4] Mélanie Auffan et al. "Towards a definition of inorganic nanoparticles from an environmental, health and safety perspective". In: *Nature Nanotechnology* 4.10 (Oct. 2009), pp. 634–641. ISSN: 1748-3387. DOI: [10.1038/nnano.2009.242](https://doi.org/10.1038/nnano.2009.242). URL: <http://www.nature.com/articles/nnano.2009.242>.
- [5] Wolfgang G. Kreyling, Manuela Semmler-Behnke, and Qasim Chaudhry. "A complementary definition of nanomaterial". In: *Nano Today* 5.3 (June 2010), pp. 165–168. ISSN: 17480132. DOI: [10.1016/j.nantod.2010.03.004](https://doi.org/10.1016/j.nantod.2010.03.004). URL: <http://dx.doi.org/10.1016/j.nantod.2010.03.004%20https://linkinghub.elsevier.com/retrieve/pii/S1748013210000460>.
- [6] Ibrahim Khan, Khalid Saeed, and Idrees Khan. "Nanoparticles: Properties, applications and toxicities". In: *Arabian Journal of Chemistry* 12.7 (Nov. 2019), pp. 908–931. ISSN: 18785352. DOI: [10.1016/j.arabjc.2017.05.011](https://doi.org/10.1016/j.arabjc.2017.05.011). URL: <https://doi.org/10.1016/j.arabjc.2017.05.011%20https://linkinghub.elsevier.com/retrieve/pii/S1878535217300990>.
- [7] Andy Brunning. "Periodic graphics: The chemistry of nanotechnology". In: *C&EN Global Enterprise* 94.40 (Oct. 2016), pp. 29–29. ISSN: 2474-7408. DOI: [10.1021/cen-09440-scitech2](https://doi.org/10.1021/cen-09440-scitech2). URL: <https://pubs.acs.org/doi/abs/10.1021/cen-09440-scitech2>.
- [8] Xucheng Hou et al. "Lipid nanoparticles for mRNA delivery". In: *Nature Reviews Materials* 6.12 (Dec. 2021), pp. 1078–1094. ISSN: 2058-8437. DOI: [10.1038/s41578-021-00358-0](https://doi.org/10.1038/s41578-021-00358-0). URL: <https://www.nature.com/articles/s41578-021-00358-0>.
- [9] Ryan Cross. "Without these lipid shells, there would be no mRNA vaccines for COVID-19". In: *Chemical & Engineering News* 99.8 (Mar. 2021), pp. 16–19. ISSN: 1520-605X. DOI: [10.47287/cen-09908-feature1](https://doi.org/10.47287/cen-09908-feature1). URL: <https://cen.acs.org/pharmaceuticals/drug-delivery/Without-lipid-shells-mRNA-vaccines/99/i8>.

- [10] Chao Huang et al. "Rapid Detection of IgM Antibodies against the SARS-CoV-2 Virus via Colloidal Gold Nanoparticle-Based Lateral-Flow Assay". In: *ACS Omega* 5.21 (June 2020), pp. 12550–12556. ISSN: 2470-1343. DOI: [10.1021/acsomega.0c01554](https://doi.org/10.1021/acsomega.0c01554). URL: <https://pubs.acs.org/doi/10.1021/acsomega.0c01554>.
- [11] Tian Wen et al. "Development of a lateral flow immunoassay strip for rapid detection of IgG antibody against SARS-CoV-2 virus". In: *The Analyst* 145.15 (2020), pp. 5345–5352. ISSN: 0003-2654. DOI: [10.1039/DOAN00629G](https://doi.org/10.1039/DOAN00629G). URL: <http://xlink.rsc.org/?DOI=DOAN00629G>.
- [12] Boris G. Andryukov. "Six decades of lateral flow immunoassay: from determining metabolic markers to diagnosing COVID-19". In: *AIMS Microbiology* 6.3 (2020), pp. 280–304. ISSN: 2471-1888. DOI: [10.3934/microbiol.2020018](https://doi.org/10.3934/microbiol.2020018). URL: <http://www.aimspress.com/article/10.3934/microbiol.2020018>.
- [13] Masashi Saitoh, Yukiyasu Kashiwagi, and Masaya Chigane. "Structural Analysis of Micrometer-Long Gold Nanowires Using a Wormlike Chain Model and Their Rheological Properties". In: *Soft Matter* 13.21 (2017), pp. 3927–3935. ISSN: 1744-683X. DOI: [10.1039/C7SM00284J](https://doi.org/10.1039/C7SM00284J). URL: <http://xlink.rsc.org/?DOI=C7SM00284J>.
- [14] Ludovico Cademartiri and Geoffrey A. Ozin. "Ultrathin Nanowires-A Materials Chemistry Perspective". In: *Advanced Materials* 21.9 (Mar. 2009), pp. 1013–1020. ISSN: 09359648. DOI: [10.1002/adma.200801836](https://doi.org/10.1002/adma.200801836). URL: <http://doi.wiley.com/10.1002/adma.200801836>.
- [15] Jae Yeon Yi and Gyeong Man Choi. "Percolation behavior of conductor-insulator composites with varying aspect ratio of conductive fiber". In: *Journal of Electroceramics* 3.4 (1999), pp. 361–369. ISSN: 13853449. DOI: [10.1023/A:1009913913732](https://doi.org/10.1023/A:1009913913732). URL: <https://link.springer.com/article/10.1023/A:1009913913732>.
- [16] L. Berhan and A. M. Sastry. "Modeling percolation in high-aspect-ratio fiber systems. I. Soft-core versus hard-core models". In: *Physical Review E* 75.4 (Apr. 2007), p. 041120. ISSN: 1539-3755. DOI: [10.1103/PhysRevE.75.041120](https://doi.org/10.1103/PhysRevE.75.041120). URL: <https://link.aps.org/doi/10.1103/PhysRevE.75.041120>.
- [17] Tanja Schilling, Mark A. Miller, and Paul van der Schoot. "Percolation in suspensions of hard nanoparticles: From spheres to needles". In: *EPL (Europhysics Letters)* 111.5 (Sept. 2015), p. 56004. ISSN: 0295-5075. DOI: [10.1209/0295-5075/111/56004](https://doi.org/10.1209/0295-5075/111/56004). URL: <https://iopscience.iop.org/article/10.1209/0295-5075/111/56004>.
- [18] Ana Sánchez-Iglesias et al. "Highly Transparent and Conductive Films of Densely Aligned Ultrathin Au Nanowire Monolayers". In: *Nano Letters* 12.12 (Dec. 2012), pp. 6066–6070. ISSN: 1530-6984. DOI: [10.1021/nl3021522](https://doi.org/10.1021/nl3021522). URL: <http://pubs.acs.org/doi/10.1021/nl3021522>.
- [19] Thomas Sannicolo et al. "Metallic Nanowire-Based Transparent Electrodes for Next Generation Flexible Devices: a Review". In: *Small* 12.44 (Nov. 2016), pp. 6052–6075. ISSN: 16136810. DOI: [10.1002/smll.201602581](https://doi.org/10.1002/smll.201602581). URL: <http://doi.wiley.com/10.1002/smll.201602581>.
- [20] Jin-Long Wang et al. "Nanowire Assemblies for Flexible Electronic Devices: Recent Advances and Perspectives". In: *Advanced Materials* 1803430 (Oct. 2018), p. 1803430. ISSN: 09359648. DOI: [10.1002/adma.201803430](https://doi.org/10.1002/adma.201803430). URL: <http://doi.wiley.com/10.1002/adma.201803430>.

- [21] Ludovico Cademartiri et al. "Cross-Linking Bi₂S₃ Ultrathin Nanowires: A Platform for Nanostructure Formation and Biomolecule Detection". In: *Nano Letters* 9.4 (Apr. 2009), pp. 1482–1486. ISSN: 1530-6984. DOI: [10.1021/nl803417v](https://doi.org/10.1021/nl803417v). URL: <https://pubs.acs.org/doi/10.1021/nl803417v>.
- [22] Dan Wen et al. "Ultrathin Pd nanowire as a highly active electrode material for sensitive and selective detection of ascorbic acid". In: *Biosensors and Bioelectronics* 26.3 (Nov. 2010), pp. 1056–1061. ISSN: 09565663. DOI: [10.1016/j.bios.2010.08.054](https://doi.org/10.1016/j.bios.2010.08.054). URL: <https://linkinghub.elsevier.com/retrieve/pii/S0956566310005580>.
- [23] Ning Wang et al. "Detection of H₂O₂ at the Nanomolar Level by Electrode Modified with Ultrathin AuCu Nanowires". In: *Analytical Chemistry* 87.1 (Jan. 2015), pp. 457–463. ISSN: 0003-2700. DOI: [10.1021/ac502682n](https://doi.org/10.1021/ac502682n). URL: <https://pubs.acs.org/doi/10.1021/ac502682n>.
- [24] Huajie Yin et al. "Ultrathin platinum nanowires grown on single-layered nickel hydroxide with high hydrogen evolution activity". In: *Nature Communications* 6.1 (May 2015), p. 6430. ISSN: 2041-1723. DOI: [10.1038/ncomms7430](https://doi.org/10.1038/ncomms7430). URL: <http://www.nature.com/articles/ncomms7430>.
- [25] Huanlei Lin et al. "Cobalt-Doping in Molybdenum-Carbide Nanowires Toward Efficient Electrocatalytic Hydrogen Evolution". In: *Advanced Functional Materials* 26.31 (Aug. 2016), pp. 5590–5598. ISSN: 1616301X. DOI: [10.1002/adfm.201600915](https://doi.org/10.1002/adfm.201600915). URL: <https://onlinelibrary.wiley.com/doi/10.1002/adfm.201600915>.
- [26] Hao Lv et al. "Ultrathin PdPt bimetallic nanowires with enhanced electrocatalytic performance for hydrogen evolution reaction". In: *Applied Catalysis B: Environmental* 238 (Dec. 2018), pp. 525–532. ISSN: 09263373. DOI: [10.1016/j.apcatb.2018.07.060](https://doi.org/10.1016/j.apcatb.2018.07.060). URL: <https://linkinghub.elsevier.com/retrieve/pii/S0926337318306787>.
- [27] Zhaojun Liu et al. "Aqueous Synthesis of Ultrathin Platinum/Non-Noble Metal Alloy Nanowires for Enhanced Hydrogen Evolution Activity". In: *Angewandte Chemie International Edition* 57.36 (Sept. 2018), pp. 11678–11682. ISSN: 1433-7851. DOI: [10.1002/anie.201806194](https://doi.org/10.1002/anie.201806194). URL: <https://onlinelibrary.wiley.com/doi/10.1002/anie.201806194>.
- [28] Jaya Sarkar, Gobinda Gopal Khan, and A. Basumallick. "Nanowires: properties, applications and synthesis via porous anodic aluminium oxide template". In: *Bulletin of Materials Science* 30.3 (June 2007), pp. 271–290. ISSN: 0250-4707. DOI: [10.1007/s12034-007-0047-0](https://doi.org/10.1007/s12034-007-0047-0). URL: <http://link.springer.com/10.1007/s12034-007-0047-0>.
- [29] Richard G. Hobbs, Nikolay Petkov, and Justin D. Holmes. "Semiconductor Nanowire Fabrication by Bottom-Up and Top-Down Paradigms". In: *Chemistry of Materials* 24.11 (June 2012), pp. 1975–1991. ISSN: 0897-4756. DOI: [10.1021/cm300570n](https://doi.org/10.1021/cm300570n). URL: <http://pubs.acs.org/doi/10.1021/cm300570n>.
- [30] Neil P. Dasgupta et al. "25th Anniversary Article: Semiconductor Nanowires - Synthesis, Characterization, and Applications". In: *Advanced Materials* 26.14 (Apr. 2014), pp. 2137–2184. ISSN: 09359648. DOI: [10.1002/adma.201305929](https://doi.org/10.1002/adma.201305929). URL: <https://onlinelibrary.wiley.com/doi/10.1002/adma.201305929>.

- [31] Chao Wang and Shouheng Sun. "Facile Synthesis of Ultrathin and Single-Crystalline Au Nanowires". In: *Chemistry - An Asian Journal* 4.7 (July 2009), pp. 1028–1034. ISSN: 18614728. DOI: [10.1002/asia.200900002](https://doi.org/10.1002/asia.200900002). URL: <https://onlinelibrary.wiley.com/doi/10.1002/asia.200900002>.
- [32] Ryo Takahata and Tatsuya Tsukuda. "Ultrathin Gold Nanowires and Nanorods". In: *Chemistry Letters* 48.8 (Aug. 2019), pp. 906–915. ISSN: 0366-7022. DOI: [10.1246/cl.190313](https://doi.org/10.1246/cl.190313). URL: <http://www.journal.csj.jp/doi/10.1246/cl.190313>.
- [33] Aditi Halder and N. Ravishankar. "Ultrafine Single-Crystalline Gold Nanowire Arrays by Oriented Attachment". In: *Advanced Materials* 19.14 (July 2007), pp. 1854–1858. ISSN: 09359648. DOI: [10.1002/adma.200602325](https://doi.org/10.1002/adma.200602325). URL: <https://onlinelibrary.wiley.com/doi/10.1002/adma.200602325>.
- [34] Ziyang Huo et al. "Sub-Two Nanometer Single Crystal Au Nanowires". In: *Nano Letters* 8.7 (July 2008), pp. 2041–2044. ISSN: 1530-6984. DOI: [10.1021/nl8013549](https://doi.org/10.1021/nl8013549). URL: <https://pubs.acs.org/doi/10.1021/nl8013549>.
- [35] Chao Wang et al. "Ultrathin Au Nanowires and Their Transport Properties". In: *Journal of the American Chemical Society* 130.28 (July 2008), pp. 8902–8903. ISSN: 0002-7863. DOI: [10.1021/ja803408f](https://doi.org/10.1021/ja803408f). URL: <https://pubs.acs.org/doi/10.1021/ja803408f>.
- [36] Xianmao Lu et al. "Ultrathin Gold Nanowires Can Be Obtained by Reducing Polymeric Strands of Oleylamine-AuCl Complexes Formed via Auophilic Interaction". In: *Journal of the American Chemical Society* 130.28 (July 2008), pp. 8900–8901. ISSN: 0002-7863. DOI: [10.1021/ja803343m](https://doi.org/10.1021/ja803343m). URL: <https://pubs.acs.org/doi/10.1021/ja803343m>.
- [37] Nicolás Pazos-Pérez et al. "Synthesis of Flexible, Ultrathin Gold Nanowires in Organic Media". In: *Langmuir* 24.17 (Sept. 2008), pp. 9855–9860. ISSN: 0743-7463. DOI: [10.1021/la801675d](https://doi.org/10.1021/la801675d). URL: <http://pubs.acs.org/doi/abs/10.1021/la801675d>.
- [38] João Borges et al. "Preparation and characterization of DNA films using oleylamine modified Au surfaces". In: *Journal of Colloid and Interface Science* 358.2 (2011), pp. 626–634. ISSN: 00219797. DOI: [10.1016/j.jcis.2011.03.039](https://doi.org/10.1016/j.jcis.2011.03.039).
- [39] Stefanos Mourdikoudis and Luis M. Liz-Marzán. "Oleylamine in Nanoparticle Synthesis". In: *Chemistry of Materials* 25.9 (May 2013), pp. 1465–1476. ISSN: 0897-4756. DOI: [10.1021/cm4000476](https://doi.org/10.1021/cm4000476). URL: <https://pubs.acs.org/doi/10.1021/cm4000476>.
- [40] Cheng Qian et al. "Solution-Phase Synthesis of Single-Crystalline Iron Phosphide Nanorods/Nanowires". In: *Journal of the American Chemical Society* 126.4 (Feb. 2004), pp. 1195–1198. ISSN: 0002-7863. DOI: [10.1021/ja038401c](https://doi.org/10.1021/ja038401c). URL: <https://pubs.acs.org/doi/10.1021/ja038401c>.
- [41] James W. Grebinski et al. "Solution-Based Straight and Branched CdSe Nanowires". In: *Chemistry of Materials* 16.25 (Dec. 2004), pp. 5260–5272. ISSN: 0897-4756. DOI: [10.1021/cm048498h](https://doi.org/10.1021/cm048498h). URL: <https://pubs.acs.org/doi/10.1021/cm048498h>.
- [42] Zhaoping Liu et al. "Growth of Cu₂S Ultrathin Nanowires in a Binary Surfactant Solvent". In: *The Journal of Physical Chemistry B* 109.21 (June 2005), pp. 10699–10704. ISSN: 1520-6106. DOI: [10.1021/jp050332w](https://doi.org/10.1021/jp050332w). URL: <http://pubs.acs.org/doi/abs/10.1021/jp050332w>.

- [43] Huajun Feng et al. "Simple and Rapid Synthesis of Ultrathin Gold Nanowires, their Self-Assembly and Application in Surface-Enhanced Raman Scattering". In: *Chemical Communications* 0.15 (2009), p. 1984. ISSN: 1359-7345. DOI: [10.1039/b822507a](https://doi.org/10.1039/b822507a). URL: <http://xlink.rsc.org/?DOI=b822507a>.
- [44] Anaïs Loubat et al. "Growth and Self-Assembly of Ultrathin Au Nanowires into Expanded Hexagonal Superlattice Studied by in Situ SAXS". In: *Langmuir* 30.14 (Apr. 2014), pp. 4005–4012. ISSN: 0743-7463. DOI: [10.1021/la500549z](https://doi.org/10.1021/la500549z). URL: <https://pubs.acs.org/doi/10.1021/la500549z>.
- [45] B. Reiser et al. "Multivalent bonds in self-assembled bundles of ultrathin gold nanowires". In: *Physical Chemistry Chemical Physics* 18.39 (2016), pp. 27165–27169. ISSN: 1463-9076. DOI: [10.1039/C6CP05181B](https://doi.org/10.1039/C6CP05181B). URL: <http://xlink.rsc.org/?DOI=C6CP05181B>.
- [46] Pierre Moutet et al. "Directed Assembly of Single Colloidal Gold Nanowires by AFM Nanoxerography". In: *Langmuir* 31.14 (Apr. 2015), pp. 4106–4112. ISSN: 0743-7463. DOI: [10.1021/acs.langmuir.5b00299](https://doi.org/10.1021/acs.langmuir.5b00299). URL: <http://pubs.acs.org/doi/10.1021/acs.langmuir.5b00299>.
- [47] El Said A. Nouh et al. "Surface-Engineering of Ultrathin Gold Nanowires: Tailored Self-Assembly and Enhanced Stability". In: *Langmuir* 33.22 (June 2017), pp. 5456–5463. ISSN: 0743-7463. DOI: [10.1021/acs.langmuir.7b00477](https://doi.org/10.1021/acs.langmuir.7b00477). URL: <https://pubs.acs.org/doi/10.1021/acs.langmuir.7b00477>.
- [48] M. E. Toimil Molares et al. "Fragmentation of nanowires driven by Rayleigh instability". In: *Applied Physics Letters* 85.22 (Nov. 2004), pp. 5337–5339. ISSN: 0003-6951. DOI: [10.1063/1.1826237](https://doi.org/10.1063/1.1826237). URL: <http://aip.scitation.org/doi/10.1063/1.1826237>.
- [49] S Karim et al. "Morphological evolution of Au nanowires controlled by Rayleigh instability". In: *Nanotechnology* 17.24 (Dec. 2006), pp. 5954–5959. ISSN: 0957-4484. DOI: [10.1088/0957-4484/17/24/009](https://doi.org/10.1088/0957-4484/17/24/009). URL: <http://stacks.iop.org/0957-4484/17/i=24/a=009?key=crossref.ace7f89b491888e67281fa4095ad9a42>.
- [50] M. Rauber et al. "Thermal stability of electrodeposited platinum nanowires and morphological transformations at elevated temperatures". In: *Nanotechnology* 23.47 (Nov. 2012), p. 475710. ISSN: 0957-4484. DOI: [10.1088/0957-4484/23/47/475710](https://doi.org/10.1088/0957-4484/23/47/475710). URL: <http://stacks.iop.org/0957-4484/23/i=47/a=475710?key=crossref.ea49844ee5ffd7ce43ac4c74a20722a1>.
- [51] Shang Xu, Peifeng Li, and Yang Lu. "In situ atomic-scale analysis of Rayleigh instability in ultrathin gold nanowires". In: *Nano Research* 11.2 (Feb. 2018), pp. 625–632. ISSN: 1998-0124. DOI: [10.1007/s12274-017-1667-3](https://doi.org/10.1007/s12274-017-1667-3). URL: <http://link.springer.com/10.1007/s12274-017-1667-3>.
- [52] Peifeng Li et al. "Key factors affecting Rayleigh instability of ultrathin 4H hexagonal gold nanoribbons". In: *Nanoscale Advances* 2.7 (2020), pp. 3027–3032. ISSN: 2516-0230. DOI: [10.1039/D0NA00186D](https://doi.org/10.1039/D0NA00186D). URL: <http://xlink.rsc.org/?DOI=D0NA00186D>.
- [53] Joysurya Basu et al. "Nanopatterning by solid-state dewetting on reconstructed ceramic surfaces". In: *Applied Physics Letters* 94.17 (Apr. 2009), p. 171114. ISSN: 0003-6951. DOI: [10.1063/1.3127442](https://doi.org/10.1063/1.3127442). URL: <http://aip.scitation.org/doi/10.1063/1.3127442>.

- [54] Qiangfei Xia and Stephen Y. Chou. "The fabrication of periodic metal nanodot arrays through pulsed laser melting induced fragmentation of metal nanogratings". In: *Nanotechnology* 20.28 (July 2009), p. 285310. ISSN: 0957-4484. DOI: [10.1088/0957-4484/20/28/285310](https://doi.org/10.1088/0957-4484/20/28/285310). URL: <https://iopscience.iop.org/article/10.1088/0957-4484/20/28/285310>.
- [55] J. A. F. Plateau. *Statique experimentale et theorique des liquides soumis aux seules forces moleculaires*. Paris: Gauthiers-Villars, 1873.
- [56] Lord Rayleigh. "On The Instability Of Jets". In: *Proceedings of the London Mathematical Society* s1-10.1 (Nov. 1878), pp. 4–13. ISSN: 00246115. DOI: [10.1112/plms/s1-10.1.4](https://doi.org/10.1112/plms/s1-10.1.4). URL: <http://doi.wiley.com/10.1112/plms/s1-10.1.4>.
- [57] J.S Stölken and A.M Glaeser. "The morphological evolution of cylindrical rods with anisotropic surface free energy via surface diffusion". In: *Scripta Metallurgica et Materialia* 27.4 (Aug. 1992), pp. 449–454. ISSN: 0956716X. DOI: [10.1016/0956-716X\(92\)90209-W](https://doi.org/10.1016/0956-716X(92)90209-W). URL: <http://www.sciencedirect.com/science/article/pii/0956716X9290209W>.
- [58] J Colin, J. Grilhé, and N Junqua. "Morphological instabilities of a stressed pore channel". In: *Acta Materialia* 45.9 (Sept. 1997), pp. 3835–3841. ISSN: 13596454. DOI: [10.1016/S1359-6454\(97\)00068-2](https://doi.org/10.1016/S1359-6454(97)00068-2). URL: <https://linkinghub.elsevier.com/retrieve/pii/S1359645497000682>.
- [59] MA Qian. "Non-linear capillary shape evolution of rod morphologies via interfacial diffusion". In: *Acta Materialia* 46.5 (Mar. 1998), pp. 1669–1681. ISSN: 13596454. DOI: [10.1016/S1359-6454\(97\)00337-6](https://doi.org/10.1016/S1359-6454(97)00337-6). URL: <http://linkinghub.elsevier.com/retrieve/pii/S1359645497003376>.
- [60] Melissa K. Santala and Andreas M. Glaeser. "Surface-energy-anisotropy-induced orientation effects on Rayleigh instabilities in sapphire". In: *Surface Science* 600.4 (Feb. 2006), pp. 782–792. ISSN: 00396028. DOI: [10.1016/j.susc.2005.11.038](https://doi.org/10.1016/j.susc.2005.11.038). URL: <https://linkinghub.elsevier.com/retrieve/pii/S0039602805013129>.
- [61] F. A. Nichols and W. W. Mullins. "Morphological Changes of a Surface of Revolution due to Capillarity-Induced Surface Diffusion". In: *Journal of Applied Physics* 36.6 (June 1965), pp. 1826–1835. ISSN: 0021-8979. DOI: [10.1063/1.1714360](https://doi.org/10.1063/1.1714360). URL: <http://aip.scitation.org/doi/10.1063/1.1714360>.
- [62] F A Nichols and W W Mullins. "Surface- (interface-) and volume diffusion contributions to morphological changes driven by capillarity". In: *AIME Metallurgical Society Transactions* 233.10 (Oct. 1965), pp. 1840–1848. URL: <http://www.onemine.org/document/abstract.cfm?docid=26784>.
- [63] Melissa K. Santala and Andreas M. Glaeser. "Rayleigh instabilities in crystalline solids: Evolution of finite-aspect-ratio pore channels in sapphire". In: *Acta Materialia* 56.9 (May 2008), pp. 1967–1980. ISSN: 13596454. DOI: [10.1016/j.actamat.2007.12.054](https://doi.org/10.1016/j.actamat.2007.12.054). URL: <https://linkinghub.elsevier.com/retrieve/pii/S1359645408000098>.
- [64] Matthew S. McCallum et al. "Capillary instabilities in solid thin films: Lines". In: *Journal of Applied Physics* 79.10 (May 1996), pp. 7604–7611. ISSN: 0021-8979. DOI: [10.1063/1.362343](https://doi.org/10.1063/1.362343). URL: <http://aip.scitation.org/doi/10.1063/1.362343>.

- [65] Yoshiro Imura et al. "Preparation of Silica-Coated Ultrathin Gold Nanowires with High Morphological Stability". In: *Langmuir* 30.7 (Feb. 2014), pp. 1888–1892. ISSN: 0743-7463. DOI: [10.1021/la403681w](https://doi.org/10.1021/la403681w). URL: <https://pubs.acs.org/doi/10.1021/la403681w>.
- [66] William Joshua Kennedy et al. "Thermal Reshaping Dynamics of Gold Nanorods: Influence of Size, Shape, and Local Environment". In: *ACS Applied Materials & Interfaces* 10.50 (Dec. 2018), pp. 43865–43873. ISSN: 1944-8244. DOI: [10.1021/acsami.8b12965](https://doi.org/10.1021/acsami.8b12965). URL: <https://pubs.acs.org/doi/10.1021/acsami.8b12965>.
- [67] Yoshiro Imura et al. "Water-dispersible ultrathin Au nanowires prepared using a lamellar template of a long-chain amidoamine derivative". In: *Chemical Communications* 47.22 (2011), p. 6380. ISSN: 1359-7345. DOI: [10.1039/c0cc05545j](https://doi.org/10.1039/c0cc05545j). URL: <http://xlink.rsc.org/?DOI=c0cc05545j>.
- [68] Mirko Maturi et al. "Surface-Stabilization of Ultrathin Gold Nanowires for Capacitive Sensors in Flexible Electronics". In: *ACS Applied Nano Materials* 4.9 (Sept. 2021), pp. 8668–8673. ISSN: 2574-0970. DOI: [10.1021/acsanm.1c01849](https://doi.org/10.1021/acsanm.1c01849). URL: <https://pubs.acs.org/doi/10.1021/acsanm.1c01849>.
- [69] Ryo Takahata et al. "Rayleigh Instability and Surfactant-Mediated Stabilization of Ultrathin Gold Nanorods". In: *The Journal of Physical Chemistry C* 120.30 (Aug. 2016), pp. 17006–17010. ISSN: 1932-7447. DOI: [10.1021/acs.jpcc.6b03113](https://doi.org/10.1021/acs.jpcc.6b03113). URL: <https://pubs.acs.org/doi/10.1021/acs.jpcc.6b03113>.
- [70] Scott P. O. Danielsen, Jihoon Choi, and Russell J. Composto. "Retardation of shape change of Au nanorods using photo-cross-linkable ligands". In: *Journal of Polymer Science Part B: Polymer Physics* 54.2 (Jan. 2016), pp. 301–307. ISSN: 08876266. DOI: [10.1002/polb.23929](https://doi.org/10.1002/polb.23929). URL: <https://onlinelibrary.wiley.com/doi/10.1002/polb.23929>.
- [71] Johannes H. M. Maurer et al. "Sintering of Ultrathin Gold Nanowires for Transparent Electronics". In: *ACS Applied Materials & Interfaces* 7.15 (Apr. 2015), pp. 7838–7842. ISSN: 1944-8244. DOI: [10.1021/acsami.5b02088](https://doi.org/10.1021/acsami.5b02088). URL: <https://pubs.acs.org/doi/10.1021/acsami.5b02088>.
- [72] Bo Li et al. "Synthesis and Purification of Silver Nanowires To Make Conducting Films with a Transmittance of 99%". In: *Nano Letters* 15.10 (Oct. 2015), pp. 6722–6726. ISSN: 1530-6984. DOI: [10.1021/acs.nanolett.5b02582](https://doi.org/10.1021/acs.nanolett.5b02582). URL: <http://pubs.acs.org/doi/10.1021/acs.nanolett.5b02582>.
- [73] Weiyue Zhao et al. "Sub-2.0-nm Ru and composition-tunable RuPt nanowire networks". In: *Nano Research* 9.10 (Oct. 2016), pp. 3066–3074. ISSN: 1998-0124. DOI: [10.1007/s12274-016-1189-4](https://doi.org/10.1007/s12274-016-1189-4). URL: <http://link.springer.com/10.1007/s12274-016-1189-4>.
- [74] Taekyung Yu et al. "Single Unit Cell Thick Samaria Nanowires and Nanoplates". In: *Journal of the American Chemical Society* 128.6 (Feb. 2006), pp. 1786–1787. ISSN: 0002-7863. DOI: [10.1021/ja057264b](https://doi.org/10.1021/ja057264b). URL: <http://pubs.acs.org/doi/abs/10.1021/ja057264b>.
- [75] Chao Wang et al. "A General Strategy for Synthesizing FePt Nanowires and Nanorods". In: *Angewandte Chemie International Edition* 46.33 (Aug. 2007), pp. 6333–6335. ISSN: 14337851. DOI: [10.1002/anie.200702001](https://doi.org/10.1002/anie.200702001). URL: <http://doi.wiley.com/10.1002/anie.200702001>.

- [76] R. Malakooti et al. "Ultrathin Sb₂S₃ nanowires and nanoplatelets". In: *J. Mater. Chem.* 18.1 (2008), pp. 66–69. ISSN: 0959-9428. DOI: [10.1039/B713383A](https://doi.org/10.1039/B713383A). URL: <http://xlink.rsc.org/?DOI=B713383A>.
- [77] Ludovico Cademartiri et al. "Large-Scale Synthesis of Ultrathin Bi₂S₃ Necklace Nanowires". In: *Angewandte Chemie International Edition* 47.20 (May 2008), pp. 3814–3817. ISSN: 14337851. DOI: [10.1002/anie.200705034](https://doi.org/10.1002/anie.200705034). URL: <http://doi.wiley.com/10.1002/anie.200705034>.
- [78] Hui-Hui Li et al. "Scalable Bromide-Triggered Synthesis of Pd@Pt Core–Shell Ultrathin Nanowires with Enhanced Electrocatalytic Performance toward Oxygen Reduction Reaction". In: *Journal of the American Chemical Society* 137.24 (June 2015), pp. 7862–7868. ISSN: 0002-7863. DOI: [10.1021/jacs.5b03877](https://doi.org/10.1021/jacs.5b03877). URL: <https://pubs.acs.org/doi/10.1021/jacs.5b03877>.
- [79] D Fenske et al. "Colloidal Synthesis of Pt Nanoparticles: On the Formation and Stability of Nanowires". In: *Langmuir* 24.16 (Aug. 2008), pp. 9011–9016. ISSN: 0743-7463. DOI: [10.1021/la800259y](https://doi.org/10.1021/la800259y). URL: <http://pubs.acs.org/doi/abs/10.1021/la800259y>.
- [80] Boon-Kin Pong et al. "New Insights on the Nanoparticle Growth Mechanism in the Citrate Reduction of Gold(III) Salt: Formation of the Au Nanowire Intermediate and Its Nonlinear Optical Properties". In: *The Journal of Physical Chemistry C* 111.17 (May 2007), pp. 6281–6287. ISSN: 1932-7447. DOI: [10.1021/jp068666o](https://doi.org/10.1021/jp068666o). URL: <http://pubs.acs.org/doi/abs/10.1021/jp068666o>.
- [81] Fernando Pschunder et al. "New Insights into the Growth Mechanism of Ultrathin Au Nanowires from Combined in Situ EXAFS and SAXS Studies". In: *The Journal of Physical Chemistry C* 122.50 (Dec. 2018), pp. 29051–29061. ISSN: 1932-7447. DOI: [10.1021/acs.jpcc.8b10449](https://doi.org/10.1021/acs.jpcc.8b10449). URL: <https://pubs.acs.org/doi/10.1021/acs.jpcc.8b10449>.
- [82] Myung Jun Kim et al. "Single-Crystal Electrochemistry Reveals Why Metal Nanowires Grow". In: *Journal of the American Chemical Society* 140.44 (Nov. 2018), pp. 14740–14746. ISSN: 0002-7863. DOI: [10.1021/jacs.8b08053](https://doi.org/10.1021/jacs.8b08053). URL: <https://pubs.acs.org/doi/10.1021/jacs.8b08053>.
- [83] Anaïs Loubat et al. "Ultrathin Gold Nanowires: Soft-Templating versus Liquid Phase Synthesis, a Quantitative Study". In: *The Journal of Physical Chemistry C* 119.8 (Feb. 2015), pp. 4422–4430. ISSN: 1932-7447. DOI: [10.1021/acs.jpcc.5b00242](https://doi.org/10.1021/acs.jpcc.5b00242). URL: <http://pubs.acs.org/doi/10.1021/acs.jpcc.5b00242>.
- [84] Naoya Miyajima et al. "Water-Phase Synthesis of Ultrathin Au Nanowires with a Two-Dimensional Parallel Array Structure". In: *Bulletin of the Chemical Society of Japan* 93.11 (Nov. 2020), pp. 1372–1377. ISSN: 0009-2673. DOI: [10.1246/bcsj.20200183](https://doi.org/10.1246/bcsj.20200183). URL: <http://www.journal.csj.jp/doi/10.1246/bcsj.20200183>.
- [85] Hongjun You et al. "Theoretical description of the role of amine surfactant on the anisotropic growth of gold nanocrystals". In: *CrystEngComm* 18.21 (2016), pp. 3934–3941. ISSN: 1466-8033. DOI: [10.1039/C6CE00550K](https://doi.org/10.1039/C6CE00550K). URL: <http://xlink.rsc.org/?DOI=C6CE00550K>.
- [86] Myung Jun Kim et al. "Modulating the Growth Rate, Aspect Ratio, and Yield of Copper Nanowires with Alkylamines". In: *Chemistry of Materials* 30.8 (Apr. 2018), pp. 2809–2818. ISSN: 0897-4756. DOI: [10.1021/acs.chemmater.8b00760](https://doi.org/10.1021/acs.chemmater.8b00760). URL: <https://pubs.acs.org/doi/10.1021/acs.chemmater.8b00760>.

- [87] Yawen Wang et al. "Effect of Thiolated Ligands in Au Nanowire Synthesis". In: *Small* 13.40 (Oct. 2017), p. 1702121. ISSN: 16136810. DOI: [10.1002/sml1.201702121](https://doi.org/10.1002/sml1.201702121). URL: <http://doi.wiley.com/10.1002/sml1.201702121>.
- [88] Jorge A. Vargas et al. "Ultrathin Gold Nanowires with the Polytetrahedral Structure of Bulk Manganese". In: *ACS Nano* 12.9 (Sept. 2018), pp. 9521–9531. ISSN: 1936-0851. DOI: [10.1021/acsnano.8b05036](https://doi.org/10.1021/acsnano.8b05036). URL: <https://pubs.acs.org/doi/10.1021/acsnano.8b05036>.
- [89] Piera Sabatino et al. "Nanowire iron(III) coordination polymer based on 1,2,4-triazolo[1,5-a]pyrimidine and chloride ligands". In: *Polyhedron* 162.Iii (Apr. 2019), pp. 45–51. ISSN: 02775387. DOI: [10.1016/j.poly.2019.01.049](https://doi.org/10.1016/j.poly.2019.01.049). URL: <https://linkinghub.elsevier.com/retrieve/pii/S0277538719300646>.
- [90] Yi Chen et al. "Mechanically Strong, Optically Transparent, Giant Metal Superlattice Nanomembranes From Ultrathin Gold Nanowires". In: *Advanced Materials* 25.1 (Jan. 2013), pp. 80–85. ISSN: 09359648. DOI: [10.1002/adma.201202241](https://doi.org/10.1002/adma.201202241). URL: <http://doi.wiley.com/10.1002/adma.201202241>.
- [91] Fan Cui et al. "Synthesis of Ultrathin Copper Nanowires Using Tris(trimethylsilyl)silane for High-Performance and Low-Haze Transparent Conductors". In: *Nano Letters* 15.11 (Nov. 2015), pp. 7610–7615. ISSN: 1530-6984. DOI: [10.1021/acs.nanolett.5b03422](https://doi.org/10.1021/acs.nanolett.5b03422). URL: <https://pubs.acs.org/doi/10.1021/acs.nanolett.5b03422>.
- [92] Johannes H. M. Maurer et al. "Templated Self-Assembly of Ultrathin Gold Nanowires by Nanoimprinting for Transparent Flexible Electronics". In: *Nano Letters* 16.5 (May 2016), pp. 2921–2925. ISSN: 1530-6984. DOI: [10.1021/acs.nanolett.5b04319](https://doi.org/10.1021/acs.nanolett.5b04319). URL: <http://pubs.acs.org/doi/10.1021/acs.nanolett.5b04319>.
- [93] Shu Gong et al. "Fabrication of Highly Transparent and Flexible NanoMesh Electrode via Self-assembly of Ultrathin Gold Nanowires". In: *Advanced Electronic Materials* 2.7 (July 2016), p. 1600121. ISSN: 2199160X. DOI: [10.1002/aelm.201600121](https://doi.org/10.1002/aelm.201600121). URL: <http://doi.wiley.com/10.1002/aelm.201600121>.
- [94] Zhiqiang Niu et al. "Ultrathin Epitaxial Cu@Au Core-Shell Nanowires for Stable Transparent Conductors". In: *Journal of the American Chemical Society* 139.21 (May 2017), pp. 7348–7354. ISSN: 0002-7863. DOI: [10.1021/jacs.7b02884](https://doi.org/10.1021/jacs.7b02884). URL: <https://pubs.acs.org/doi/10.1021/jacs.7b02884>.
- [95] Xiaowei Li et al. "Mesoporous NiO ultrathin nanowire networks topotactically transformed from α -Ni(OH)₂ hierarchical microspheres and their superior electrochemical capacitance properties and excellent capability for water treatment". In: *Journal of Materials Chemistry* 22.28 (2012), p. 14276. ISSN: 0959-9428. DOI: [10.1039/c2jm32559d](https://doi.org/10.1039/c2jm32559d). URL: <http://xlink.rsc.org/?DOI=c2jm32559d>.
- [96] Hyun-Wook Lee et al. "Ultrathin Spinel LiMn₂O₄ Nanowires as High Power Cathode Materials for Li-Ion Batteries". In: *Nano Letters* 10.10 (Oct. 2010), pp. 3852–3856. ISSN: 1530-6984. DOI: [10.1021/nl101047f](https://doi.org/10.1021/nl101047f). URL: <https://pubs.acs.org/doi/10.1021/nl101047f>.
- [97] Genqiang Zhang et al. "Rational synthesis of ultrathin n-type Bi₂Te₃ nanowires with enhanced thermoelectric properties". In: *Nano Letters* 12.1 (2012), pp. 56–60. ISSN: 15306984. DOI: [10.1021/nl202935k](https://doi.org/10.1021/nl202935k).

- [98] Jian-Wei Liu et al. "Mesostuctured Assemblies of Ultrathin Superlong Tellurium Nanowires and Their Photoconductivity". In: *Journal of the American Chemical Society* 132.26 (July 2010), pp. 8945–8952. ISSN: 0002-7863. DOI: [10.1021/ja910871s](https://pubs.acs.org/doi/10.1021/ja910871s). URL: <https://pubs.acs.org/doi/10.1021/ja910871s>.
- [99] By Jian-Wei Liu et al. "Ultrathin W 18 O 49 Nanowire Assemblies for Electrochromic Devices". In: *Nano Letters* 13.8 (Aug. 2013), pp. 3589–3593. ISSN: 1530-6984. DOI: [10.1021/nl401304n](https://pubs.acs.org/doi/10.1021/nl401304n). URL: <https://pubs.acs.org/doi/10.1021/nl401304n>.
- [100] Jin Yang et al. "Ultrathin BaTiO₃ Nanowires with High Aspect Ratio: A Simple One-Step Hydrothermal Synthesis and Their Strong Microwave Absorption". In: *ACS Applied Materials & Interfaces* 5.15 (Aug. 2013), pp. 7146–7151. ISSN: 1944-8244. DOI: [10.1021/am4014506](https://pubs.acs.org/doi/10.1021/am4014506). URL: <https://pubs.acs.org/doi/10.1021/am4014506>.
- [101] Tae Il Lee et al. "High-Power Density Piezoelectric Energy Harvesting Using Radially Strained Ultrathin Trigonal Tellurium Nanowire Assembly". In: *Advanced Materials* 25.21 (June 2013), pp. 2920–2925. ISSN: 09359648. DOI: [10.1002/adma.201300657](https://onlinelibrary.wiley.com/doi/10.1002/adma.201300657). URL: <https://onlinelibrary.wiley.com/doi/10.1002/adma.201300657>.
- [102] Guozhen Shen et al. "Ultrathin In₂O₃ Nanowires with Diameters below 4 nm: Synthesis, Reversible Wettability Switching Behavior, and Transparent Thin-Film Transistor Applications". In: *ACS Nano* 5.8 (Aug. 2011), pp. 6148–6155. ISSN: 1936-0851. DOI: [10.1021/nn2014722](https://pubs.acs.org/doi/10.1021/nn2014722). URL: <https://pubs.acs.org/doi/10.1021/nn2014722>.
- [103] Jun Xu et al. "Mechanical Nanosprings: Induced Coiling and Uncoiling of Ultrathin Au Nanowires". In: *Journal of the American Chemical Society* 132.34 (Sept. 2010), pp. 11920–11922. ISSN: 0002-7863. DOI: [10.1021/ja105433d](https://pubs.acs.org/doi/10.1021/ja105433d). URL: <https://pubs.acs.org/doi/10.1021/ja105433d>.
- [104] Shu Gong et al. "A wearable and highly sensitive pressure sensor with ultrathin gold nanowires". In: *Nature Communications* 5.1 (May 2014), p. 3132. ISSN: 2041-1723. DOI: [10.1038/ncomms4132](http://www.nature.com/articles/ncomms4132). URL: <http://www.nature.com/articles/ncomms4132>.
- [105] Xinchuan Liu et al. "A highly sensitive pressure sensor using a Au-patterned polydimethylsiloxane membrane for biosensing applications". In: *Journal of Micromechanics and Microengineering* 23.2 (Feb. 2013), p. 025022. ISSN: 0960-1317. DOI: [10.1088/0960-1317/23/2/025022](https://iopscience.iop.org/article/10.1088/0960-1317/23/2/025022). URL: <https://iopscience.iop.org/article/10.1088/0960-1317/23/2/025022>.
- [106] Dong-Weon Lee and Young-Soo Choi. "A novel pressure sensor with a PDMS diaphragm". In: *Microelectronic Engineering* 85.5-6 (May 2008), pp. 1054–1058. ISSN: 01679317. DOI: [10.1016/j.mee.2008.01.074](https://linkinghub.elsevier.com/retrieve/pii/S0167931708000865). URL: <https://linkinghub.elsevier.com/retrieve/pii/S0167931708000865>.
- [107] Po-Jui Chen et al. "Microfabricated Implantable Parylene-Based Wireless Passive Intraocular Pressure Sensors". In: *Journal of Microelectromechanical Systems* 17.6 (Dec. 2008), pp. 1342–1351. ISSN: 1057-7157. DOI: [10.1109/JMEMS.2008.2004945](http://ieeexplore.ieee.org/document/4660282/). URL: <http://ieeexplore.ieee.org/document/4660282/>.

- [108] Hyung-Kew Lee, Sun-Il Chang, and Euisik Yoon. "A Flexible Polymer Tactile Sensor: Fabrication and Modular Expandability for Large Area Deployment". In: *Journal of Microelectromechanical Systems* 15.6 (Dec. 2006), pp. 1681–1686. ISSN: 1057-7157. DOI: [10.1109/JMEMS.2006.886021](https://doi.org/10.1109/JMEMS.2006.886021). URL: <http://ieeexplore.ieee.org/document/4020266/>.
- [109] My Duyen Ho et al. "Percolating Network of Ultrathin Gold Nanowires and Silver Nanowires toward "Invisible" Wearable Sensors for Detecting Emotional Expression and Apexcardiogram". In: *Advanced Functional Materials* 27.25 (July 2017), p. 1700845. ISSN: 1616-301X. DOI: [10.1002/adfm.201700845](https://doi.org/10.1002/adfm.201700845). URL: <https://onlinelibrary.wiley.com/doi/10.1002/adfm.201700845>.
- [110] Zhigang Chen et al. "Ultrathin PEGylated W₁₈O₄₉ Nanowires as a New 980 nm-Laser-Driven Photothermal Agent for Efficient Ablation of Cancer Cells In Vivo". In: *Advanced Materials* 25.14 (Apr. 2013), pp. 2095–2100. ISSN: 09359648. DOI: [10.1002/adma.201204616](https://doi.org/10.1002/adma.201204616). URL: <https://onlinelibrary.wiley.com/doi/10.1002/adma.201204616>.
- [111] Qiang Yuan et al. "Seed Displacement, Epitaxial Synthesis of Rh/Pt Bimetallic Ultrathin Nanowires for Highly Selective Oxidizing Ethanol to CO₂". In: *Chemistry of Materials* 22.7 (Apr. 2010), pp. 2395–2402. ISSN: 0897-4756. DOI: [10.1021/cm903844t](https://doi.org/10.1021/cm903844t). URL: <https://pubs.acs.org/doi/10.1021/cm903844t>.
- [112] Wenlei Zhu et al. "Active and Selective Conversion of CO₂ to CO on Ultrathin Au Nanowires". In: *Journal of the American Chemical Society* 136.46 (Nov. 2014), pp. 16132–16135. ISSN: 0002-7863. DOI: [10.1021/ja5095099](https://doi.org/10.1021/ja5095099). URL: <https://pubs.acs.org/doi/10.1021/ja5095099>.
- [113] Christopher Koenigsmann et al. "Size-Dependent Enhancement of Electrocatalytic Performance in Relatively Defect-Free, Processed Ultrathin Platinum Nanowires". In: *Nano Letters* 10.8 (Aug. 2010), pp. 2806–2811. ISSN: 1530-6984. DOI: [10.1021/nl100718k](https://doi.org/10.1021/nl100718k). URL: <https://pubs.acs.org/doi/10.1021/nl100718k>.
- [114] Christopher Koenigsmann et al. "Enhanced Electrocatalytic Performance of Processed, Ultrathin, Supported Pd–Pt Core–Shell Nanowire Catalysts for the Oxygen Reduction Reaction". In: *Journal of the American Chemical Society* 133.25 (June 2011), pp. 9783–9795. ISSN: 0002-7863. DOI: [10.1021/ja111130t](https://doi.org/10.1021/ja111130t). URL: <https://pubs.acs.org/doi/10.1021/ja111130t>.
- [115] Shaojun Guo et al. "Synthesis of Ultrathin FePtPd Nanowires and Their Use as Catalysts for Methanol Oxidation Reaction". In: *Journal of the American Chemical Society* 133.39 (Oct. 2011), pp. 15354–15357. ISSN: 0002-7863. DOI: [10.1021/ja207308b](https://doi.org/10.1021/ja207308b). URL: <https://pubs.acs.org/doi/10.1021/ja207308b>.
- [116] Guangcheng Xi et al. "Ultrathin W₁₈O₄₉ Nanowires with Diameters below 1 nm: Synthesis, Near-Infrared Absorption, Photoluminescence, and Photochemical Reduction of Carbon Dioxide". In: *Angewandte Chemie International Edition* 51.10 (Mar. 2012), pp. 2395–2399. ISSN: 14337851. DOI: [10.1002/anie.201107681](https://doi.org/10.1002/anie.201107681). URL: <https://onlinelibrary.wiley.com/doi/10.1002/anie.201107681>.
- [117] Longgai Zhang et al. "Insulin Amyloid Fibrils: An Excellent Platform for Controlled Synthesis of Ultrathin Superlong Platinum Nanowires with High Electrocatalytic Activity". In: *Journal of the American Chemical Society* 134.28 (July 2012), pp. 11326–11329. ISSN: 0002-7863. DOI: [10.1021/ja302959e](https://doi.org/10.1021/ja302959e). URL: <https://pubs.acs.org/doi/10.1021/ja302959e>.

- [118] Hui-Hui Li et al. "Ultrathin PtPdTe Nanowires as Superior Catalysts for Methanol Electrooxidation". In: *Angewandte Chemie International Edition* 52.29 (July 2013), pp. 7472–7476. ISSN: 14337851. DOI: [10.1002/anie.201302090](https://doi.org/10.1002/anie.201302090). URL: <https://onlinelibrary.wiley.com/doi/10.1002/anie.201302090>.
- [119] Lingyan Ruan et al. "Biomimetic Synthesis of an Ultrathin Platinum Nanowire Network with a High Twin Density for Enhanced Electrocatalytic Activity and Durability". In: *Angewandte Chemie International Edition* 52.48 (Nov. 2013), pp. 12577–12581. ISSN: 14337851. DOI: [10.1002/anie.201304658](https://doi.org/10.1002/anie.201304658). URL: <https://onlinelibrary.wiley.com/doi/10.1002/anie.201304658>.
- [120] Yi Wang et al. "Polyol Synthesis of Ultrathin Pd Nanowires via Attachment-Based Growth and Their Enhanced Activity towards Formic Acid Oxidation". In: *Advanced Functional Materials* 24.1 (Jan. 2014), pp. 131–139. ISSN: 1616301X. DOI: [10.1002/adfm.201302339](https://doi.org/10.1002/adfm.201302339). URL: <https://onlinelibrary.wiley.com/doi/10.1002/adfm.201302339>.
- [121] Bao Yu Xia et al. "Ultrathin and Ultralong Single-Crystal Platinum Nanowire Assemblies with Highly Stable Electrocatalytic Activity". In: *Journal of the American Chemical Society* 135.25 (June 2013), pp. 9480–9485. ISSN: 0002-7863. DOI: [10.1021/ja402955t](https://doi.org/10.1021/ja402955t). URL: <https://pubs.acs.org/doi/10.1021/ja402955t>.
- [122] Hongying Liu et al. "Control of surface ligand density on PEGylated gold nanoparticles for optimized cancer cell uptake". In: *Particle and Particle Systems Characterization* (2014), pp. 197–204. ISSN: 09340866. DOI: [10.1002/ppsc.201400067](https://doi.org/10.1002/ppsc.201400067).
- [123] Megan E. Scofield et al. "Tailoring the composition of ultrathin, ternary alloy PtRuFe nanowires for the methanol oxidation reaction and formic acid oxidation reaction". In: *Energy & Environmental Science* 8.1 (2015), pp. 350–363. ISSN: 1754-5692. DOI: [10.1039/C4EE02162B](https://doi.org/10.1039/C4EE02162B). URL: <http://xlink.rsc.org/?DOI=C4EE02162B>.
- [124] Zhaoyu Jin, Panpan Li, and Dan Xiao. "Metallic Co₂P ultrathin nanowires distinguished from CoP as robust electrocatalysts for overall water-splitting". In: *Green Chemistry* 18.6 (2016), pp. 1459–1464. ISSN: 1463-9262. DOI: [10.1039/C5GC02462E](https://doi.org/10.1039/C5GC02462E). URL: <http://xlink.rsc.org/?DOI=C5GC02462E>.
- [125] Megan E. Scofield et al. "Role of Chemical Composition in the Enhanced Catalytic Activity of Pt-Based Alloyed Ultrathin Nanowires for the Hydrogen Oxidation Reaction under Alkaline Conditions". In: *ACS Catalysis* 6.6 (June 2016), pp. 3895–3908. ISSN: 2155-5435. DOI: [10.1021/acscatal.6b00350](https://doi.org/10.1021/acscatal.6b00350). URL: <https://pubs.acs.org/doi/10.1021/acscatal.6b00350>.
- [126] Hongwen Huang et al. "Achieving Remarkable Activity and Durability toward Oxygen Reduction Reaction Based on Ultrathin Rh-Doped Pt Nanowires". In: *Journal of the American Chemical Society* 139.24 (June 2017), pp. 8152–8159. ISSN: 0002-7863. DOI: [10.1021/jacs.7b01036](https://doi.org/10.1021/jacs.7b01036). URL: <https://pubs.acs.org/doi/10.1021/jacs.7b01036>.
- [127] Junjie Mao et al. "Design of ultrathin Pt-Mo-Ni nanowire catalysts for ethanol electrooxidation". In: *Science Advances* 3.8 (Aug. 2017), pp. 1–10. ISSN: 2375-2548. DOI: [10.1126/sciadv.1603068](https://doi.org/10.1126/sciadv.1603068). URL: <https://www.science.org/doi/10.1126/sciadv.1603068>.

- [128] Yifan Li et al. "Structure-Sensitive CO₂ Electroreduction to Hydrocarbons on Ultrathin 5-fold Twinned Copper Nanowires". In: *Nano Letters* 17.2 (Feb. 2017), pp. 1312–1317. ISSN: 1530-6984. DOI: [10.1021/acs.nanolett.6b05287](https://doi.org/10.1021/acs.nanolett.6b05287). URL: <https://pubs.acs.org/doi/10.1021/acs.nanolett.6b05287>.
- [129] Luhong Fu et al. "Ultrathin Ir nanowires as high-performance electrocatalysts for efficient water splitting in acidic media". In: *Nanoscale* 10.4 (2018), pp. 1892–1897. ISSN: 2040-3364. DOI: [10.1039/C7NR09377B](https://doi.org/10.1039/C7NR09377B). URL: <http://xlink.rsc.org/?DOI=C7NR09377B>.
- [130] Honggen Peng et al. "Confined Ultrathin Pd-Ce Nanowires with Outstanding Moisture and SO₂ Tolerance in Methane Combustion". In: *Angewandte Chemie International Edition* 57.29 (July 2018), pp. 8953–8957. ISSN: 1433-7851. DOI: [10.1002/anie.201803393](https://doi.org/10.1002/anie.201803393). URL: <https://onlinelibrary.wiley.com/doi/10.1002/anie.201803393>.
- [131] Hao Lv et al. "Ultrathin PdAg single-crystalline nanowires enhance ethanol oxidation electrocatalysis". In: *Applied Catalysis B: Environmental* 249 (July 2019), pp. 116–125. ISSN: 09263373. DOI: [10.1016/j.apcatb.2019.02.068](https://doi.org/10.1016/j.apcatb.2019.02.068). URL: <https://linkinghub.elsevier.com/retrieve/pii/S0926337319301924>.
- [132] Weiyu Zhang et al. "Ultrathin PtNiM (M = Rh, Os, and Ir) Nanowires as Efficient Fuel Oxidation Electrocatalytic Materials". In: *Advanced Materials* 31.15 (Apr. 2019), p. 1805833. ISSN: 0935-9648. DOI: [10.1002/adma.201805833](https://doi.org/10.1002/adma.201805833). URL: <https://onlinelibrary.wiley.com/doi/10.1002/adma.201805833>.
- [133] Lei Gao et al. "Unconventional p–d Hybridization Interaction in PtGa Ultrathin Nanowires Boosts Oxygen Reduction Electrocatalysis". In: *Journal of the American Chemical Society* 141.45 (Nov. 2019), pp. 18083–18090. ISSN: 0002-7863. DOI: [10.1021/jacs.9b07238](https://doi.org/10.1021/jacs.9b07238). URL: <https://pubs.acs.org/doi/10.1021/jacs.9b07238>.
- [134] D. Fennell Evans and Håkan Wennerström. *The Colloidal Domain: Where Physics, Chemistry, Biology, and Technology Meet*. 2nd. New York: Wiley-VCH, 1999. ISBN: 978-0-471-24247-5. URL: <https://www.wiley.com/en-us/The+Colloidal+Domain%3A+Where+Physics%2C+Chemistry%2C+Biology%2C+and+Technology+Meet%2C+2nd+Edition-p-9780471242475>.
- [135] George M Whitesides. "Self-Assembly at All Scales". In: *Science* 295.5564 (Mar. 2002), pp. 2418–2421. ISSN: 00368075. DOI: [10.1126/science.1070821](https://doi.org/10.1126/science.1070821). URL: <http://www.sciencemag.org/content/295/5564/2418.full%0Apapers3://publication/doi/10.1126/science.1070821%20http://www.sciencemag.org/cgi/doi/10.1126/science.1070821>.
- [136] G. M. Whitesides and M. Boncheva. "Beyond molecules: Self-assembly of mesoscopic and macroscopic components". In: *Proceedings of the National Academy of Sciences* 99.8 (Apr. 2002), pp. 4769–4774. ISSN: 0027-8424. DOI: [10.1073/pnas.082065899](https://doi.org/10.1073/pnas.082065899). URL: <http://www.pnas.org/cgi/doi/10.1073/pnas.082065899>.
- [137] Helmut Cölfen and Stephen Mann. "Higher-Order Organization by Mesoscale Self-Assembly and Transformation of Hybrid Nanostructures". In: *Angewandte Chemie International Edition* 42.21 (May 2003), pp. 2350–2365. ISSN: 14337851. DOI: [10.1002/anie.200200562](https://doi.org/10.1002/anie.200200562). URL: <http://doi.wiley.com/10.1002/anie.200200562>.

- [138] S. C. Glotzer, M. J. Solomon, and N. A. Kotov. "Self-assembly: From nanoscale to microscale colloids". In: *AIChE Journal* 50.12 (2004), pp. 2978–2985. ISSN: 00011541. DOI: [10.1002/aic.10413](https://doi.org/10.1002/aic.10413).
- [139] Kyle J. M. Bishop et al. "Nanoscale Forces and Their Uses in Self-Assembly". In: *Small* 5.14 (July 2009), pp. 1600–1630. ISSN: 16136810. DOI: [10.1002/smll.200900358](https://doi.org/10.1002/smll.200900358). URL: <http://doi.wiley.com/10.1002/smll.200900358>.
- [140] Geoffrey A. Ozin et al. "Nanofabrication by self-assembly". In: *Materials Today* 12.5 (2009), pp. 12–23. ISSN: 13697021. DOI: [10.1016/S1369-7021\(09\)70156-7](https://doi.org/10.1016/S1369-7021(09)70156-7). URL: [http://dx.doi.org/10.1016/S1369-7021\(09\)70156-7](http://dx.doi.org/10.1016/S1369-7021(09)70156-7).
- [141] L. Cademartiri et al. "Using shape for self-assembly". In: *Philosophical Transactions of the Royal Society A: Mathematical, Physical and Engineering Sciences* 370.1969 (2012), pp. 2824–2847. ISSN: 1364-503X. DOI: [10.1098/rsta.2011.0254](https://doi.org/10.1098/rsta.2011.0254). URL: <http://rsta.royalsocietypublishing.org/cgi/doi/10.1098/rsta.2011.0254>.
- [142] Ludovico Cademartiri and Kyle J.M. Bishop. "Programmable self-assembly". In: *Nature Materials* 14.1 (2015), pp. 2–9. ISSN: 14764660. DOI: [10.1038/nmat4184](https://doi.org/10.1038/nmat4184). URL: <http://dx.doi.org/10.1038/nmat4184>.
- [143] Joseph B. Tracy and Thomas M. Crawford. "Magnetic field-directed self-assembly of magnetic nanoparticles". In: *MRS Bulletin* 38.11 (Nov. 2013), pp. 915–920. ISSN: 0883-7694. DOI: [10.1557/mrs.2013.233](https://doi.org/10.1557/mrs.2013.233). URL: <http://link.springer.com/10.1557/mrs.2013.233>.
- [144] Ashlin G. Porter et al. "1-nm-Wide Hydrated Dipole Arrays Regulate AuNW Assembly on Striped Monolayers in Nonpolar Solvent". In: *Chem* 5.8 (Aug. 2019), pp. 2264–2275. ISSN: 24519294. DOI: [10.1016/j.chempr.2019.07.002](https://doi.org/10.1016/j.chempr.2019.07.002). URL: <https://doi.org/10.1016/j.chempr.2019.07.002> <https://linkinghub.elsevier.com/retrieve/pii/S2451929419303109>.
- [145] Suchetan Pal et al. "DNA-Origami-Directed Self-Assembly of Discrete Silver-Nanoparticle Architectures". In: *Angewandte Chemie International Edition* 49.15 (Apr. 2010), pp. 2700–2704. ISSN: 14337851. DOI: [10.1002/anie.201000330](https://doi.org/10.1002/anie.201000330). URL: <https://onlinelibrary.wiley.com/doi/10.1002/anie.201000330>.
- [146] R. Klajn, K. J. M. Bishop, and B. A. Grzybowski. "Light-controlled self-assembly of reversible and irreversible nanoparticle suprastructures". In: *Proceedings of the National Academy of Sciences* 104.25 (June 2007), pp. 10305–10309. ISSN: 0027-8424. DOI: [10.1073/pnas.0611371104](https://doi.org/10.1073/pnas.0611371104). URL: <http://www.pnas.org/cgi/doi/10.1073/pnas.0611371104>.
- [147] V. Adrian Parsegian. *Van der Waals Forces*. Cambridge: Cambridge University Press, 2006. ISBN: 9780521839068. DOI: [10.2277/0521839068](https://doi.org/10.2277/0521839068). URL: <http://www.cambridge.org/catalogue/catalogue.asp?isbn=0521839068>.
- [148] D. Langbein. "Van der Waals Attraction Between Cylinders, Rods or Fibers". In: *Physik der Kondensierten Materie* 15.1 (Sept. 1972), pp. 61–86. ISSN: 1434-6028. DOI: [10.1007/BF02422580](https://doi.org/10.1007/BF02422580). URL: <http://link.springer.com/10.1007/BF02422580>.
- [149] Nicolas Goubet et al. "Which Forces Control Supracrystal Nucleation in Organic Media?" In: *Advanced Functional Materials* 21.14 (July 2011), pp. 2693–2704. ISSN: 1616301X. DOI: [10.1002/adfm.201100382](https://doi.org/10.1002/adfm.201100382). URL: <http://doi.wiley.com/10.1002/adfm.201100382>.

- [150] Jacob N. Israelachvili. *Intermolecular and Surface Forces*. 3rd. Boston: Elsevier, 2011. ISBN: 9780123751829. DOI: [10 . 1016 / C2009 - 0 - 21560 - 1](https://doi.org/10.1016/C2009-0-21560-1). URL: <https://linkinghub.elsevier.com/retrieve/pii/C20090215601>.
- [151] Ronald P. Danner and Martin S. High. *Handbook of Polymer Solution Thermodynamics*. Hoboken, NJ, USA: John Wiley & Sons, Inc., Jan. 1993. ISBN: 9780470938232. DOI: [10 . 1002 / 9780470938232](https://doi.org/10.1002/9780470938232). URL: <http://doi.wiley.com/10.1002/9780470938232>.
- [152] Gregory Von White, Fiaz S. Mohammed, and Christopher L. Kitchens. "Small-Angle Neutron Scattering Investigation of Gold Nanoparticle Clustering and Ligand Structure Under Antisolvent Conditions". In: *The Journal of Physical Chemistry C* 115.38 (Sept. 2011), pp. 18397–18405. ISSN: 1932-7447. DOI: [10 . 1021 / jp112020r](https://doi.org/10.1021/jp112020r). URL: <https://pubs.acs.org/doi/10.1021/jp112020r>.
- [153] Philipp Schapotschnikow, René Pool, and Thijs J. H. Vlugt. "Molecular Simulations of Interacting Nanocrystals". In: *Nano Letters* 8.9 (Sept. 2008), pp. 2930–2934. ISSN: 1530-6984. DOI: [10 . 1021 / nl8017862](https://doi.org/10.1021/nl8017862). URL: <https://pubs.acs.org/doi/10.1021/nl8017862>.
- [154] Mark Z. Griffiths and Wataru Shinoda. "Analyzing the Role of Surfactants in the Colloidal Stability of Nanoparticles in Oil through Coarse-Grained Molecular Dynamics Simulations". In: *The Journal of Physical Chemistry B* 125.23 (June 2021), pp. 6315–6321. ISSN: 1520-6106. DOI: [10 . 1021 / acs . jpcc . 1c 01148](https://doi.org/10.1021/acs.jpcc.1c01148). URL: <https://pubs.acs.org/doi/10.1021/acs.jpcc.1c01148>.
- [155] Thomas Kister et al. "Colloidal Stability of Apolar Nanoparticles: The Role of Particle Size and Ligand Shell Structure". In: *ACS Nano* 12.6 (June 2018), pp. 5969–5977. ISSN: 1936-0851. DOI: [10 . 1021 / acsnano . 8b02202](https://doi.org/10.1021/acsnano.8b02202). URL: <http://pubs.acs.org/doi/10.1021/acsnano.8b02202>.
- [156] Debora Monego et al. "Colloidal Stability of Apolar Nanoparticles: Role of Ligand Length". In: *Langmuir* 34.43 (Oct. 2018), pp. 12982–12989. ISSN: 0743-7463. DOI: [10 . 1021 / acs . langmuir . 8b02883](https://doi.org/10.1021/acs.langmuir.8b02883). URL: <http://pubs.acs.org/doi/10.1021/acs.langmuir.8b02883>.
- [157] Debora Monego et al. "When Like Destabilizes Like: Inverted Solvent Effects in Apolar Nanoparticle Dispersions". In: *ACS Nano* 14.5 (May 2020), pp. 5278–5287. ISSN: 1936-0851. DOI: [10 . 1021 / acsnano . 9b03552](https://doi.org/10.1021/acsnano.9b03552). URL: <https://pubs.acs.org/doi/10.1021/acsnano.9b03552>.
- [158] Madhu Anand et al. "Thermodynamic Analysis of Nanoparticle Size Selective Fractionation Using Gas-Expanded Liquids". In: *Industrial & Engineering Chemistry Research* 47.3 (Feb. 2008), pp. 553–559. ISSN: 0888-5885. DOI: [10 . 1021 / ie070981p](https://doi.org/10.1021/ie070981p). URL: <https://pubs.acs.org/doi/10.1021/ie070981p>.
- [159] Steven R Saunders et al. "Total Interaction Energy Model to Predict Nanoparticle Dispersability in CO₂-Expanded Solvents". In: *Computer Aided Chemical Engineering*. Vol. 28. January. 2010, pp. 1651–1672.
- [160] Byeongdu Lee et al. "Revealing the Effects of the Non-solvent on the Ligand Shell of Nanoparticles and Their Crystallization". In: *Journal of the American Chemical Society* 141.42 (Oct. 2019), pp. 16651–16662. ISSN: 0002-7863. DOI: [10 . 1021 / jacs . 9b06010](https://doi.org/10.1021/jacs.9b06010). URL: <https://pubs.acs.org/doi/10.1021/jacs.9b06010>.

- [161] Siyam M. Ansar et al. "Effect of Postsynthesis Purifications on Gold and Silver Nanoparticle Ligand Coverage". In: *The Journal of Physical Chemistry C* 120.12 (Mar. 2016), pp. 6842–6850. ISSN: 1932-7447. DOI: [10.1021/acs.jpcc.5b12423](https://doi.org/10.1021/acs.jpcc.5b12423). URL: <https://pubs.acs.org/doi/10.1021/acs.jpcc.5b12423>.
- [162] Jingru He et al. "The Remote Light Emission Modulated by Local Surface Plasmon Resonance for the CdSe NW–Au NP Hybrid Structure". In: *Advanced Materials Interfaces* 6.2 (2019), pp. 1–9. ISSN: 21967350. DOI: [10.1002/admi.201801418](https://doi.org/10.1002/admi.201801418).
- [163] C. B. Murray, C. R. Kagan, and M. G. Bawendi. "Synthesis and Characterization of Monodisperse Nanocrystals and Close-Packed Nanocrystal Assemblies". In: *Annual Review of Materials Science* 30.1 (Aug. 2000), pp. 545–610. ISSN: 0084-6600. DOI: [10.1146/annurev.matsci.30.1.545](https://doi.org/10.1146/annurev.matsci.30.1.545). URL: <https://www.annualreviews.org/doi/10.1146/annurev.matsci.30.1.545>.
- [164] A.L. Rogach et al. "Organization of Matter on Different Size Scales: Monodisperse Nanocrystals and Their Superstructures". In: *Advanced Functional Materials* 12.10 (Oct. 2002), pp. 653–664. ISSN: 1616301X. DOI: [10.1002/1616-3028\(20021016\)12:10<653::AID-ADFM653>3.0.CO;2-V](https://doi.org/10.1002/1616-3028(20021016)12:10<653::AID-ADFM653>3.0.CO;2-V). URL: [https://onlinelibrary.wiley.com/doi/10.1002/1616-3028\(20021016\)12:10%3C653::AID-ADFM653%3E3.0.CO;2-V](https://onlinelibrary.wiley.com/doi/10.1002/1616-3028(20021016)12:10%3C653::AID-ADFM653%3E3.0.CO;2-V).
- [165] Yu Yang et al. "Entropic Ligands for Nanocrystals: From Unexpected Solution Properties to Outstanding Processability". In: *Nano Letters* 16.4 (Apr. 2016), pp. 2133–2138. ISSN: 1530-6984. DOI: [10.1021/acs.nanolett.6b00730](https://doi.org/10.1021/acs.nanolett.6b00730). URL: <https://pubs.acs.org/doi/10.1021/acs.nanolett.6b00730>.
- [166] David Doblas et al. "Colloidal Solubility and Agglomeration of Apolar Nanoparticles in Different Solvents". In: *Nano Letters* 19.8 (Aug. 2019), pp. 5246–5252. ISSN: 1530-6984. DOI: [10.1021/acs.nanolett.9b01688](https://doi.org/10.1021/acs.nanolett.9b01688). URL: <https://pubs.acs.org/doi/10.1021/acs.nanolett.9b01688>.
- [167] Wei Gao et al. "Order-Disorder Transitions in Self-Assembled Monolayers: A ¹³C Solid-State NMR Study". In: *Langmuir* 13.2 (Jan. 1997), pp. 115–118. ISSN: 0743-7463. DOI: [10.1021/la960808q](https://doi.org/10.1021/la960808q). URL: <https://pubs.acs.org/doi/10.1021/la960808q>.
- [168] Antonella Badia, R Bruce Lennox, and Linda Reven. "A Dynamic View of Self-Assembled Monolayers". In: *Accounts of Chemical Research* 33.7 (July 2000), pp. 475–481. ISSN: 0001-4842. DOI: [10.1021/ar9702841](https://doi.org/10.1021/ar9702841). URL: <https://pubs.acs.org/doi/10.1021/ar9702841>.
- [169] Asaph Widmer-Cooper and Phillip Geissler. "Orientational Ordering of Passivating Ligands on CdS Nanorods in Solution Generates Strong Rod–Rod Interactions". In: *Nano Letters* 14.1 (Jan. 2014), pp. 57–65. ISSN: 1530-6984. DOI: [10.1021/nl403067p](https://doi.org/10.1021/nl403067p). URL: <https://pubs.acs.org/doi/10.1021/nl403067p>.
- [170] Asaph Widmer-Cooper and Phillip L. Geissler. "Ligand-Mediated Interactions between Nanoscale Surfaces Depend Sensitive and Nonlinearly on Temperature, Facet Dimensions, and Ligand Coverage". In: *ACS Nano* 10.2 (Feb. 2016), pp. 1877–1887. ISSN: 1936-0851. DOI: [10.1021/acsnano.5b05569](https://doi.org/10.1021/acsnano.5b05569). URL: <http://pubs.acs.org/doi/10.1021/acsnano.5b05569>.

- [171] Alex K. Chew and Reid C. Van Lehn. "Effect of Core Morphology on the Structural Asymmetry of Alkanethiol Monolayer-Protected Gold Nanoparticles". In: *The Journal of Physical Chemistry C* 122.45 (Nov. 2018), pp. 26288–26297. ISSN: 1932-7447. DOI: [10.1021/acs.jpcc.8b09323](https://doi.org/10.1021/acs.jpcc.8b09323). URL: <https://pubs.acs.org/doi/10.1021/acs.jpcc.8b09323>.
- [172] Arunima D. Balan et al. "Unsaturated Ligands Seed an Order to Disorder Transition in Mixed Ligand Shells of CdSe/CdS Quantum Dots". In: *ACS Nano* 13.12 (Dec. 2019), pp. 13784–13796. ISSN: 1936-0851. DOI: [10.1021/acsnano.9b03054](https://doi.org/10.1021/acsnano.9b03054). URL: <https://pubs.acs.org/doi/10.1021/acsnano.9b03054>.
- [173] Alex K. Chew, Bradley C. Dallin, and Reid C. Van Lehn. "The Interplay of Ligand Properties and Core Size Dictates the Hydrophobicity of Monolayer-Protected Gold Nanoparticles". In: *ACS Nano* 15.3 (Mar. 2021), pp. 4534–4545. ISSN: 1936-0851. DOI: [10.1021/acsnano.0c08623](https://doi.org/10.1021/acsnano.0c08623). URL: <https://pubs.acs.org/doi/10.1021/acsnano.0c08623>.
- [174] Tianyu Yan and Kristen A. Fichthorn. "Self-Assembly of a Linear Alkylamine Bilayer around a Cu Nanocrystal: Molecular Dynamics". In: *The Journal of Physical Chemistry B* 125.16 (Apr. 2021), pp. 4178–4186. ISSN: 1520-6106. DOI: [10.1021/acs.jpcc.1c02043](https://doi.org/10.1021/acs.jpcc.1c02043). URL: <https://pubs.acs.org/doi/10.1021/acs.jpcc.1c02043>.
- [175] Pradip Kr Ghorai and Sharon C. Glotzer. "Molecular Dynamics Simulation Study of Self-Assembled Monolayers of Alkanethiol Surfactants on Spherical Gold Nanoparticles". In: *The Journal of Physical Chemistry C* 111.43 (Nov. 2007), pp. 15857–15862. ISSN: 1932-7447. DOI: [10.1021/jp0746289](https://doi.org/10.1021/jp0746289). URL: <https://pubs.acs.org/doi/10.1021/jp0746289>.
- [176] Alicia M. Jackson, Jacob W. Myerson, and Francesco Stellacci. "Spontaneous assembly of subnanometre-ordered domains in the ligand shell of monolayer-protected nanoparticles". In: *Nature Materials* 3.5 (May 2004), pp. 330–336. ISSN: 1476-1122. DOI: [10.1038/nmat1116](https://doi.org/10.1038/nmat1116). URL: <http://www.nature.com/articles/nmat1116>.
- [177] Mauro Moglianetti et al. "Scanning tunneling microscopy and small angle neutron scattering study of mixed monolayer protected gold nanoparticles in organic solvents". In: *Chemical Science* 5.3 (2014), p. 1232. ISSN: 2041-6520. DOI: [10.1039/c3sc52595c](https://doi.org/10.1039/c3sc52595c). URL: <http://xlink.rsc.org/?DOI=c3sc52595c>.
- [178] Takaaki Tomai et al. "Solvent accommodation effect on dispersibility of metal oxide nanoparticle with chemisorbed organic shell". In: *Journal of Colloid and Interface Science* 587 (Apr. 2021), pp. 574–580. ISSN: 00219797. DOI: [10.1016/j.jcis.2020.11.014](https://doi.org/10.1016/j.jcis.2020.11.014). URL: <https://linkinghub.elsevier.com/retrieve/pii/S0021979720315174>.
- [179] Jonathan De Roo et al. "Probing Solvent–Ligand Interactions in Colloidal Nanocrystals by the NMR Line Broadening". In: *Chemistry of Materials* 30.15 (Aug. 2018), pp. 5485–5492. ISSN: 0897-4756. DOI: [10.1021/acs.chemmater.8b02523](https://doi.org/10.1021/acs.chemmater.8b02523). URL: <https://pubs.acs.org/doi/10.1021/acs.chemmater.8b02523>.
- [180] Samuel W. Winslow et al. "Repulsive, Densely Packed Ligand-Shells Mediate Interactions between PbS Nanocrystals in Solution". In: *The Journal of Physical Chemistry C* 125.14 (Apr. 2021), pp. 8014–8020. ISSN: 1932-7447. DOI: [10.1021/acs.jpcc.1c02430](https://doi.org/10.1021/acs.jpcc.1c02430). URL: <https://pubs.acs.org/doi/10.1021/acs.jpcc.1c02430>.

- [181] Henk N.W. Lekkerkerker and Remco Tuinier. *Colloids and the Depletion Interaction*. Vol. 833. Lecture Notes in Physics. Dordrecht: Springer Netherlands, 2011. ISBN: 978-94-007-1222-5. DOI: [10.1007/978-94-007-1223-2](https://doi.org/10.1007/978-94-007-1223-2). URL: <http://link.springer.com/10.1007/978-94-007-1223-2>.
- [182] S. Sacanna et al. "Lock and key colloids". In: *Nature* 464.7288 (Mar. 2010), pp. 575–578. ISSN: 0028-0836. DOI: [10.1038/nature08906](https://doi.org/10.1038/nature08906). URL: <http://www.nature.com/articles/nature08906>.
- [183] Dahin Kim et al. "Depletion-Mediated Interfacial Assembly of Semiconductor Nanorods". In: *Nano Letters* 19.2 (Feb. 2019), pp. 963–970. ISSN: 1530-6984. DOI: [10.1021/acs.nanolett.8b04198](https://doi.org/10.1021/acs.nanolett.8b04198). URL: <https://pubs.acs.org/doi/10.1021/acs.nanolett.8b04198>.
- [184] L. Auvray. "Solutions de macromolécules rigides : effets de paroi, de confinement et d'orientation par un écoulement". In: *Journal de Physique* 42.1 (1981), pp. 79–95. ISSN: 0302-0738. DOI: [10.1051/jphys:0198100420107900](https://doi.org/10.1051/jphys:0198100420107900). URL: <http://www.edpsciences.org/10.1051/jphys:0198100420107900>.
- [185] Y. Mao, M.E. Cates, and H.N.W. Lekkerkerker. "Depletion force in colloidal systems". In: *Physica A: Statistical Mechanics and its Applications* 222.1-4 (Dec. 1995), pp. 10–24. ISSN: 03784371. DOI: [10.1016/0378-4371\(95\)00206-5](https://doi.org/10.1016/0378-4371(95)00206-5). URL: <https://linkinghub.elsevier.com/retrieve/pii/0378437195002065>.
- [186] Y. Mao, M. E. Cates, and H. N. W. Lekkerkerker. "Depletion Stabilization by Semidilute Rods". In: *Physical Review Letters* 75.24 (Dec. 1995), pp. 4548–4551. ISSN: 0031-9007. DOI: [10.1103/PhysRevLett.75.4548](https://doi.org/10.1103/PhysRevLett.75.4548). URL: <https://link.aps.org/doi/10.1103/PhysRevLett.75.4548>.
- [187] Y. Mao, M. E. Cates, and H. N. W. Lekkerkerker. "Theory of the Depletion Force due to Rodlike Polymers". In: *The Journal of Chemical Physics* 106.9 (Mar. 1997), pp. 3721–3729. ISSN: 0021-9606. DOI: [10.1063/1.473424](https://doi.org/10.1063/1.473424). URL: <http://aip.scitation.org/doi/10.1063/1.473424>.
- [188] Keng-hui Lin et al. "Colloidal Interactions in Suspensions of Rods". In: *Physical Review Letters* 87.8 (Aug. 2001), p. 088301. ISSN: 0031-9007. DOI: [10.1103/PhysRevLett.87.088301](https://doi.org/10.1103/PhysRevLett.87.088301). URL: <https://link.aps.org/doi/10.1103/PhysRevLett.87.088301>.
- [189] L. Helden et al. "Direct Measurement of Entropic Forces Induced by Rigid Rods". In: *Physical Review Letters* 90.4 (Jan. 2003), p. 048301. ISSN: 0031-9007. DOI: [10.1103/PhysRevLett.90.048301](https://doi.org/10.1103/PhysRevLett.90.048301). URL: <https://link.aps.org/doi/10.1103/PhysRevLett.90.048301>.
- [190] D. Guu et al. "Depletion Induced Clustering in Mixtures of Colloidal Spheres and fd-Virus". In: *Journal of Physics: Condensed Matter* 24.46 (Nov. 2012), p. 464101. ISSN: 0953-8984. DOI: [10.1088/0953-8984/24/46/464101](https://doi.org/10.1088/0953-8984/24/46/464101). URL: <https://iopscience.iop.org/article/10.1088/0953-8984/24/46/464101>.
- [191] Seymour S. Cohen. "The Isolation and Crystallization of Plant Viruses and Other Protein Macromolecules by Means of Hydrophilic Colloids". In: *Journal of Biological Chemistry* 144.2 (July 1942), pp. 353–362. ISSN: 00219258. DOI: [10.1016/S0021-9258\(18\)72516-7](https://doi.org/10.1016/S0021-9258(18)72516-7). URL: <https://linkinghub.elsevier.com/retrieve/pii/S0021925818725167>.
- [192] Dmitry Baranov et al. "Assembly of Colloidal Semiconductor Nanorods in Solution by Depletion Attraction". In: *Nano Letters* 10.2 (Feb. 2010), pp. 743–749. ISSN: 1530-6984. DOI: [10.1021/nl903946n](https://doi.org/10.1021/nl903946n). URL: <https://pubs.acs.org/doi/10.1021/nl903946n>.

- [193] Cindy Y. Lau et al. "Enhanced Ordering in Gold Nanoparticles Self-Assembly Through Excess Free Ligands". In: *Langmuir* 27.7 (2011), pp. 3355–3360. ISSN: 07437463. DOI: [10.1021/la104786z](https://doi.org/10.1021/la104786z).
- [194] Samuel L. Brown et al. "Superlattice Formation in Colloidal Nanocrystal Suspensions: Hard-Sphere Freezing and Depletion Effects". In: *Physical Review E* 98.6 (Dec. 2018), p. 062616. ISSN: 2470-0045. DOI: [10.1103/PhysRevE.98.062616](https://doi.org/10.1103/PhysRevE.98.062616). URL: <https://link.aps.org/doi/10.1103/PhysRevE.98.062616>.
- [195] Samuel W. Winslow, James W. Swan, and William A. Tisdale. "The Importance of Unbound Ligand in Nanocrystal Superlattice Formation". In: *Journal of the American Chemical Society* 142.21 (May 2020), jacs.0c01809. ISSN: 0002-7863. DOI: [10.1021/jacs.0c01809](https://doi.org/10.1021/jacs.0c01809). URL: <https://pubs.acs.org/doi/10.1021/jacs.0c01809>.
- [196] Mirijam Zobel, Reinhard B. Neder, and Simon A. J. Kimber. "Universal solvent restructuring induced by colloidal nanoparticles". In: *Science* 347.6219 (Jan. 2015), pp. 292–294. ISSN: 0036-8075. DOI: [10.1126/science.1261412](https://doi.org/10.1126/science.1261412). URL: <https://www.science.org/doi/10.1126/science.1261412>.
- [197] Dandan Zhang et al. "Ultrathin Colloidal Cesium Lead Halide Perovskite Nanowires". In: *Journal of the American Chemical Society* 138.40 (Oct. 2016), pp. 13155–13158. ISSN: 0002-7863. DOI: [10.1021/jacs.6b08373](https://doi.org/10.1021/jacs.6b08373). URL: <https://pubs.acs.org/doi/10.1021/jacs.6b08373>.
- [198] Erin N. Lang et al. "Oleylamine Impurities Regulate Temperature-Dependent Hierarchical Assembly of Ultranarrow Gold Nanowires on Biotemplated Interfaces". In: *ACS Nano* 15.6 (June 2021), pp. 10275–10285. ISSN: 1936-0851. DOI: [10.1021/acsnano.1c02414](https://doi.org/10.1021/acsnano.1c02414). URL: <https://pubs.acs.org/doi/10.1021/acsnano.1c02414>.
- [199] Beate Reiser et al. "Spinning Hierarchical Gold Nanowire Microfibers by Shear Alignment and Intermolecular Self-Assembly". In: *ACS Nano* 11.5 (May 2017), pp. 4934–4942. ISSN: 1936-0851. DOI: [10.1021/acsnano.7b01551](https://doi.org/10.1021/acsnano.7b01551). URL: <http://pubs.acs.org/doi/10.1021/acsnano.7b01551>.
- [200] Lulu Wang, Haiying Huang, and Tianbai He. "Rayleigh Instability Induced Cylinder-to-Sphere Transition in Block Copolymer Micelles: Direct Visualization of the Kinetic Pathway". In: *ACS Macro Letters* 3.5 (May 2014), pp. 433–438. ISSN: 2161-1653. DOI: [10.1021/mz500158f](https://doi.org/10.1021/mz500158f). URL: <http://pubs.acs.org/doi/10.1021/mz500158f>. URL: <https://pubs.acs.org/doi/10.1021/mz500158f>.
- [201] Pierre-Gilles de Gennes, Françoise Brochard-Wyart, and David Quéré. *Capillarity and Wetting Phenomena*. New York, NY: Springer New York, 2004, pp. 118–122. ISBN: 978-1-4419-1833-8. DOI: [10.1007/978-0-387-21656-0](https://doi.org/10.1007/978-0-387-21656-0). URL: <http://link.springer.com/10.1007/978-0-387-21656-0>.
- [202] Bastian E. Rapp. "Chapter 23: Plateau-Rayleigh Instability". In: *Microfluidics: Modeling, Mechanics, and Mathematics*. Elsevier, 2016. Chap. 23. ISBN: 978-1-4557-3141-1. URL: <https://www.elsevier.com/books/microfluidics-modeling-mechanics-and-mathematics/rapp/978-1-4557-3141-1>.
- [203] Alan C. F. Cocks, Simon P. A. Gill, and Jingzhe Pan. "Modeling Microstructure Evolution in Engineering Materials". In: *Advances in Applied Mechanics Volume 36*. Ed. by Erik van der Giessen and Theodore Wu. Academic Press, 1998, pp. 82–162. ISBN: 9780120020362. URL: <https://www.elsevier.com/books/advances-in-applied-mechanics/unknown/978-0-12-002036-2>.

- [204] S. P. A. Gill. "Controlling the Rayleigh instability of nanowires". In: *Applied Physics Letters* 102.14 (Apr. 2013), p. 143108. ISSN: 0003-6951. DOI: [10.1063/1.4801766](https://doi.org/10.1063/1.4801766). URL: <http://aip.scitation.org/doi/10.1063/1.4801766>.
- [205] F. Parhami et al. "A model for the sintering and coarsening of rows of spherical particles". In: *Mechanics of Materials* 31.1 (Jan. 1999), pp. 43–61. ISSN: 01676636. DOI: [10.1016/S0167-6636\(98\)00049-0](https://doi.org/10.1016/S0167-6636(98)00049-0). URL: <https://linkinghub.elsevier.com/retrieve/pii/S0167663698000490>.
- [206] J.W. Cahn. "Stability of rods with anisotropic surface free energy". In: *Scripta Metallurgica* 13.11 (Nov. 1979), pp. 1069–1071. ISSN: 00369748. DOI: [10.1016/0036-9748\(79\)90205-9](https://doi.org/10.1016/0036-9748(79)90205-9). URL: <http://linkinghub.elsevier.com/retrieve/pii/0036974879902059>.
- [207] K. F. Gurski and G. B. McFadden. "The effect of anisotropic surface energy on the Rayleigh instability". In: *Proceedings of the Royal Society A: Mathematical, Physical and Engineering Sciences* 459.2038 (2003), pp. 2575–2598. ISSN: 1364-5021. DOI: [10.1098/rspa.2003.1144](https://doi.org/10.1098/rspa.2003.1144). URL: <http://rspa.royalsocietypublishing.org/cgi/doi/10.1098/rspa.2003.1144>.
- [208] Andreas M. Glaeser. "Model Studies of Rayleigh Instabilities via Microdesigned Interfaces". In: *Interface Science* 9.1/2 (2001), pp. 65–82. ISSN: 09277056. DOI: [10.1023/A:1011279015039](https://doi.org/10.1023/A:1011279015039). URL: <http://link.springer.com/10.1023/A:1011279015039>.
- [209] Gye Hyun Kim and Carl V. Thompson. "Effect of surface energy anisotropy on Rayleigh-like solid-state dewetting and nanowire stability". In: *Acta Materialia* 84 (Feb. 2015), pp. 190–201. ISSN: 13596454. DOI: [10.1016/j.actamat.2014.10.028](https://doi.org/10.1016/j.actamat.2014.10.028). URL: <http://linkinghub.elsevier.com/retrieve/pii/S1359645414007800>.
- [210] Vyacheslav Gorshkov and Vladimir Privman. "Kinetic Monte Carlo model of breakup of nanowires into chains of nanoparticles". In: *Journal of Applied Physics* 122.20 (Nov. 2017), p. 204301. ISSN: 0021-8979. DOI: [10.1063/1.5002665](https://doi.org/10.1063/1.5002665). URL: <http://aip.scitation.org/doi/10.1063/1.5002665>.
- [211] Vyacheslav N. Gorshkov et al. "Dynamics of Anisotropic Break-Up in Nanowires of FCC Lattice Structure". In: *Advanced Theory and Simulations* 2.9 (Sept. 2019), p. 1900118. ISSN: 2513-0390. DOI: [10.1002/adts.201900118](https://doi.org/10.1002/adts.201900118). URL: <https://onlinelibrary.wiley.com/doi/10.1002/adts.201900118>.
- [212] K. F. Gurski, G. B. McFadden, and M. J. Miksis. "The Effect of Contact Lines on the Rayleigh Instability with Anisotropic Surface Energy". In: *SIAM Journal on Applied Mathematics* 66.4 (Jan. 2006), pp. 1163–1187. ISSN: 0036-1399. DOI: [10.1137/050626946](https://doi.org/10.1137/050626946). URL: <http://epubs.siam.org/doi/10.1137/050626946>.
- [213] G. Boussinot and Efim A. Brener. "Inhibition of Rayleigh-Plateau instability on a unidirectionally patterned substrate". In: *Physical Review E* 92.3 (Sept. 2015), p. 032408. ISSN: 1539-3755. DOI: [10.1103/PhysRevE.92.032408](https://doi.org/10.1103/PhysRevE.92.032408). URL: <https://link.aps.org/doi/10.1103/PhysRevE.92.032408>.
- [214] E B Dussan. "On the Spreading of Liquids on Solid Surfaces: Static and Dynamic Contact Lines". In: *Annual Review of Fluid Mechanics* 11.1 (Jan. 1979), pp. 371–400. ISSN: 0066-4189. DOI: [10.1146/annurev.fl.11.010179.002103](https://doi.org/10.1146/annurev.fl.11.010179.002103). URL: <http://www.annualreviews.org/doi/10.1146/annurev.fl.11.010179.002103>.

- [215] Stephen H. Davis. "Moving contact lines and rivulet instabilities. Part 1. The static rivulet". In: *Journal of Fluid Mechanics* 98.2 (May 1980), pp. 225–242. ISSN: 0022-1120. DOI: [10.1017/S0022112080000110](https://doi.org/10.1017/S0022112080000110). URL: https://www.cambridge.org/core/product/identifier/S0022112080000110/type/journal_article.
- [216] Marco Salvalaglio et al. "Morphological evolution of Ge/Si nano-strips driven by Rayleigh-like instability". In: *Applied Physics Letters* 112.2 (Jan. 2018), p. 022101. ISSN: 0003-6951. DOI: [10.1063/1.5007937](https://doi.org/10.1063/1.5007937). URL: <http://aip.scitation.org/doi/10.1063/1.5007937>.
- [217] Jeong-yong Park et al. "Anisotropic rupture of polymer strips driven by Rayleigh instability". In: *The Journal of Chemical Physics* 124.21 (June 2006), p. 214710. ISSN: 0021-9606. DOI: [10.1063/1.2206580](https://doi.org/10.1063/1.2206580). URL: <http://aip.scitation.org/doi/10.1063/1.2206580>.
- [218] Hongwei Li et al. "Thermal stability of Cu nanowires on a sapphire substrate". In: *Journal of Applied Physics* 103.2 (2008). ISSN: 00218979. DOI: [10.1063/1.2837053](https://doi.org/10.1063/1.2837053).
- [219] Ho Sun Shin, Jin Yu, and Jae Yong Song. "Size-dependent thermal instability and melting behavior of Sn nanowires". In: *Applied Physics Letters* 91.17 (Oct. 2007), p. 173106. ISSN: 0003-6951. DOI: [10.1063/1.2801520](https://doi.org/10.1063/1.2801520). URL: <http://aip.scitation.org/doi/10.1063/1.2801520>.
- [220] Jiun-Tai Chen, Mingfu Zhang, and Thomas P. Russell. "Instabilities in Nanoporous Media". In: *Nano Letters* 7.1 (Jan. 2007), pp. 183–187. ISSN: 1530-6984. DOI: [10.1021/nl0621241](https://doi.org/10.1021/nl0621241). URL: <https://pubs.acs.org/doi/10.1021/nl0621241>.
- [221] Chia-Chan Tsai and Jiun-Tai Chen. "Effect of the Polymer Concentration on the Rayleigh-Instability-Type Transformation in Polymer Thin Films Coated in the Nanopores of Anodic Aluminum Oxide Templates". In: *Langmuir* 31.8 (Mar. 2015), pp. 2569–2575. ISSN: 0743-7463. DOI: [10.1021/la504901h](https://doi.org/10.1021/la504901h). URL: <https://pubs.acs.org/doi/10.1021/la504901h>.
- [222] Zhi-Xuan Fang et al. "Rayleigh-Instability-Induced Transformation for Confined Polystyrene Nanotubes Prepared Using the Solvent-Vapor-Induced Wetting Method". In: *Macromolecular Materials and Engineering* 305.1 (Jan. 2020), p. 1900465. ISSN: 1438-7492. DOI: [10.1002/mame.201900465](https://doi.org/10.1002/mame.201900465). URL: <https://onlinelibrary.wiley.com/doi/10.1002/mame.201900465>.
- [223] K. Y. Suh and Hong H. Lee. "Anisotropic hole formation in thin polymer films confined by walls". In: *The Journal of Chemical Physics* 115.17 (Nov. 2001), pp. 8204–8208. ISSN: 0021-9606. DOI: [10.1063/1.1409540](https://doi.org/10.1063/1.1409540). URL: <http://aip.scitation.org/doi/10.1063/1.1409540>.
- [224] V. Schmidt, P. C. McIntyre, and U. Gösele. "Morphological instability of misfit-strained core-shell nanowires". In: *Physical Review B* 77.23 (June 2008), p. 235302. ISSN: 1098-0121. DOI: [10.1103/PhysRevB.77.235302](https://doi.org/10.1103/PhysRevB.77.235302). URL: <https://link.aps.org/doi/10.1103/PhysRevB.77.235302>.
- [225] Akihiro Tomioka et al. "Role of polyvinylpyrrolidone bound on silver nanowire surface: Balancing among electrical conductance, sulfuration resistance, and flexibility". In: *physica status solidi (b)* 254.6 (June 2017), p. 1600717. ISSN: 03701972. DOI: [10.1002/pssb.201600717](https://doi.org/10.1002/pssb.201600717). URL: <https://onlinelibrary.wiley.com/doi/10.1002/pssb.201600717>.

- [226] Yue Chau Garen Kwan, Quang Luan Le, and Cheng Hon Alfred Huan. "Time to failure modeling of silver nanowire transparent conducting electrodes and effects of a reduced graphene oxide over layer". In: *Solar Energy Materials and Solar Cells* 144 (2016), pp. 102–108. ISSN: 09270248. DOI: [10.1016/j.solmat.2015.08.005](https://doi.org/10.1016/j.solmat.2015.08.005). URL: <http://dx.doi.org/10.1016/j.solmat.2015.08.005>.
- [227] Jianbo Wu et al. "Ultrathin and stable AgAu alloy nanowires". In: *Science China Materials* 58.8 (Aug. 2015), pp. 595–602. ISSN: 2095-8226. DOI: [10.1007/s40843-015-0072-z](https://doi.org/10.1007/s40843-015-0072-z). URL: <http://link.springer.com/10.1007/s40843-015-0072-z>.
- [228] Stefan E. Huber et al. "Thermal stabilization of thin gold nanowires by surfactant-coating: a molecular dynamics study". In: *Nanoscale* 4.2 (2012), pp. 585–590. ISSN: 2040-3364. DOI: [10.1039/C1NR11282A](https://doi.org/10.1039/C1NR11282A). URL: <http://xlink.rsc.org/?DOI=C1NR11282A>.
- [229] Diana Ciuculescu et al. "Single-Crystalline Co Nanowires: Synthesis, Thermal Stability, and Carbon Coating". In: *Chemistry of Materials* 21.17 (Sept. 2009), pp. 3987–3995. ISSN: 0897-4756. DOI: [10.1021/cm901349y](https://doi.org/10.1021/cm901349y). URL: <http://pubs.acs.org/doi/abs/10.1021/cm901349y>.
- [230] Lise-Marie Lacroix, Raul Arenal, and Guillaume Viau. "Dynamic HAADF-STEM Observation of a Single-Atom Chain as the Transient State of Gold Ultrathin Nanowire Breakdown". In: *Journal of the American Chemical Society* 136.38 (Sept. 2014), pp. 13075–13077. ISSN: 0002-7863. DOI: [10.1021/ja507728j](https://doi.org/10.1021/ja507728j). URL: <http://pubs.acs.org/doi/10.1021/ja507728j>.
- [231] P. Pawlow. "Ober die Abhängigkeit des Schmelzpunktes von der Oberflächenenergie eines festen Körpers (Zusatz.)" In: *Zeitschrift für Physikalische Chemie* 65U.1 (Dec. 1909), pp. 545–548. ISSN: 2196-7156. DOI: [10.1515/zpch-1909-6532](https://doi.org/10.1515/zpch-1909-6532). URL: <https://www.degruyter.com/document/doi/10.1515/zpch-1909-6532/html>.
- [232] J. P. Borel. "Thermodynamical size effect and the structure of metallic clusters". In: *Surface Science* 106.1-3 (1981), pp. 1–9. ISSN: 00396028. DOI: [10.1016/0039-6028\(81\)90173-4](https://doi.org/10.1016/0039-6028(81)90173-4).
- [233] Johannes H. M. Maurer et al. "Direct Nanoimprinting of a Colloidal Self-Organizing Nanowire Ink for Flexible, Transparent Electrodes". In: *Advanced Materials Technologies* 2.6 (June 2017), p. 1700034. ISSN: 2365709X. DOI: [10.1002/admt.201700034](https://doi.org/10.1002/admt.201700034). URL: <http://doi.wiley.com/10.1002/admt.201700034>.
- [234] Shan Jiang et al. "Design colloidal particle morphology and self-assembly for coating applications". In: *Chemical Society Reviews* 46.12 (2017), pp. 3792–3807. ISSN: 0306-0012. DOI: [10.1039/C6CS00807K](https://doi.org/10.1039/C6CS00807K). URL: <http://xlink.rsc.org/?DOI=C6CS00807K>.
- [235] Santanu Jana et al. "Ligand-induced twisting of nanoplatelets and their self-assembly into chiral ribbons". In: *Science Advances* 3.9 (2017). ISSN: 23752548. DOI: [10.1126/sciadv.1701483](https://doi.org/10.1126/sciadv.1701483).
- [236] Ludovico Cademartiri et al. "Polymer-like Conformation and Growth Kinetics of Bi₂S₃ Nanowires". In: *Journal of the American Chemical Society* 134.22 (June 2012), pp. 9327–9334. ISSN: 0002-7863. DOI: [10.1021/ja301855z](https://doi.org/10.1021/ja301855z). URL: <https://pubs.acs.org/doi/10.1021/ja301855z>.

- [237] Johannes H. M. Maurer et al. "Ultrathin gold nanowires for transparent electronics: Soft sintering and temperature stability". In: *physica status solidi (a)* 213.9 (Sept. 2016), pp. 2336–2340. ISSN: 18626300. DOI: [10.1002/pssa.201532874](https://doi.org/10.1002/pssa.201532874). URL: <http://doi.wiley.com/10.1002/pssa.201532874>.